Theoretische Physik

On the dynamics of surfactant covered thin liquid films and the formation of stripe patterns in Langmuir-Blodgett transfer

Inaugural-Dissertation
zur Erlangung des Doktorgrades
der Naturwissenschaften im Fachbereich Physik
der Mathematisch-Naturwissenschaftlichen Fakultät
der Westfälischen Wilhelms-Universität Münster

vorgelegt von
Michael Hubert Köpf
aus Münster
Mai 2011

institut für
theoretische physik

revised online version: 04.09.2011

Dekan:	Prof. Dr. Tilmann Kuhn
Erster Gutachter:	Prof. Dr. Rudolf Friedrich
Zweiter Gutachter:	Prof. Dr. Andreas Heuer
Tag der mündlichen Prüfung:	08.07.2011
Tag der Promotion:	08.07.2011

Zusammenfassung

Die Langmuir-Blodgett-Methode stellt ein bewährtes Verfahren zur Beschichtung von Oberflächen mit monomolekularen Schichten organischer Moleküle, wie z.B. Phospholipiden, dar. Diese Moleküle sind amphiphil, d.h., sie haben ein hydrophiles und ein hydrophobes Ende. Bringt man sie mit Wasser in Kontakt, so bilden sie eine einmolekulare Schicht an der Wasseroberfläche, da dort die hydrophile Seite am Wasser adsorbieren und das hydrophobe Ende sich gleichzeitig vom Wasser abwenden kann.

Die Monoschicht kann nun auf einen in das Wasser getauchten Festkörper, das sogenannte Substrat, übertragen werden, indem man diesen langsam aus dem Wasser zieht. Bei diesem Vorgang, dem eigentlichen Langmuir-Blodgett-Transfer, werden die Lipidmoleküle mit herausgezogen und bedecken schließlich das gesamte Substrat mit einer einmolekularen Schicht.

Zunächst würde man annehmen, dass dieser Prozess die Monoschicht eins zu eins homogen von der Wasseroberfläche auf den Festkörper transferiert. Faszinierenderweise lassen sich die experimentellen Bedingungen jedoch so einstellen, dass stattdessen äußerst reguläre Muster mit typischen Wellenlängen von nur wenigen hundert Nanometern übertragen werden. Diese Muster bestehen aus streifenförmigen Domänen von Lipidmolekülen, die abwechselnd in zwei unterschiedlichen thermodynamischen Zuständen, nämlich der sogenannten Liquid-Expanded (LE) und der Liquid-Condensed (LC) Phase vorliegen. Interessanterweise jedoch befinden sich die Moleküle vor dem Transfer, also auf der Wasseroberfläche, in der reinen LE-Phase. Zur Entstehung des beobachteten Streifenmusters muss demnach während des Übertragungsvorgangs eine partielle und wohlgeordnete Kondensation der Monoschicht stattfinden. Dieser Effekt wurde von seinen Entdeckern als Substrate-Mediated-Condensation (SMC) bezeichnet.

Die zentrale Problemstellung der Dissertation bestand darin, eine mathematische Beschreibung der experimentell beobachteten Strukturbildungsphänomene zu entwickeln. Dazu wurde ein Modell aufgestellt, welches zunächst die Dynamik des Systems aus Wasser und Monoschicht an die Thermodynamik, insbesondere den LE-LC-Phasenübergang, koppelt und darüber hinaus die Wechselwirkung zwischen Substrat und Monoschicht, also den als SMC bekannten Effekt, erstmals theoretisch beschreibt.

Die mathematische Beschreibung der Strukturbildung erfolgt im Rahmen der sogenannten Schmiermittelapproximation, einer Näherung der hydrodynamischen Grundgleichungen, also der Navier-Stokes'schen Gleichungen, für dünne Flüssigkeitsfilme. Bei dieser Herangehensweise werden zwei zentrale Größen betrachtet: die Dichte Γ der Phospholipid-Monoschicht sowie das Höhenprofil H des darunter liegenden Wasserfilms, der sogenannten Subphase. Die zeitliche Veränderung von Γ und H lässt sich mit Hilfe zweier gekoppelter nichtlinearer partieller Differenzialgleichungen beschreiben. Um dieses Modell an die Thermodynamik der Lipid-Monoschicht zu koppeln, wird die freie Energie in der Nähe des LE-LC-Phasenübergangs formuliert und daraus eine Zustandsgleichung für Γ abgeleitet. Diese Zustandsgleichung gibt an, wie die Oberflächenspannung von der lokalen Dichte der Monoschicht abhängt. Die Interaktion zwischen Substrat und Monoschicht wird in Form eines äußeren Wechselwirkungsfeldes in der freien Energie mod-

elliert. Die Stärke dieses Feldes hängt vom Abstand zwischen Substrat und Lipidschicht ab und bewirkt für kleine Abstände eine Verkippung der freien Energie zugunsten der dichteren LC-Phase. Dadurch wird die Kondensation am Substrat energetisch bevorzugt, was den experimentell beobachteten Abfall des LE-LC-Koexistenzdruckes am Substrat erklärt.

Vor der Anwendung des Modell auf den vergleichsweise komplizierten Transferprozess werden die Gleichungen zunächst mit periodischen Randbedingungen betrachtet. Eine lineare Stabilitätsanalyse homogener Filme ermöglicht, die Abhängigkeit der Wellenlänge auftretender Strukturen von Materialparametern zu erfassen. Dabei wird zusätzlich eine Untersuchung der Oberflächensteifigkeit und eine Abschätzung ihres Einflusses in der Nähe des LE-LC-Phasenüberganges durchgeführt. Die auftretenden Gleichungen werden mit Hilfe eines selbst entwickelten Programms numerisch gelöst, wobei die räumliche Diskretisierung mit finiten Differenzen und die Zeitintegration mit Hilfe eines adaptiven Runge-Kutta-Verfahrens erfolgt. Teilweise werden die entsprechenden Simulationen parallelisiert auf modernen Grafikkarten durchgeführt.

Danach wird der Transfervorgang mit den erprobten numerischen Methoden simuliert, indem die Modellgleichungen unter geeigneten Randbedingungen gelöst werden. Die experimentell beobachteten Strukturbildungsprozesse können so erfolgreich reproduziert werden. Schließlich wird das Modell erweitert, um den Transfer auf chemisch vorstrukturierte Substrate zu beschreiben. Dabei zeigt sich, dass eine periodische Vorstrukturierung zu Synchronisationsphänomenen verschiedener Ordnungen und damit zur Entstehung komplexerer periodischer Streifenmuster führt. Zudem werden Mischzustände aus kombinierten zirkularen und streifenförmigen Domänen beobachtet, wodurch neue Perspektiven zur gezielten Nanostrukturierung von Oberflächen eröffnet werden.

Eingehend auf aktuelle Experimente wird zudem die Abhängigkeit der beobachten Strukturbildung von der Subphasentemperatur untersucht. Das dazu entwickelte Modell berücksichtigt Verschiebungen der Isothermen der Monoschicht und steht im Einklang mit den experimentellen Ergebnissen.

Zur tieferen theoretischen Analyse wird letztlich ein vereinfachtes Modell des Transfervorgangs erstellt. Semi-analytische Rechnungen ermöglichen eine lineare Stabilitätsanalyse der inhomogenen stationären Lösungen, die sich unter den Transferrandbedingungen ergeben. In Verbindung mit numerischen Kontinuierungsmethoden können die Lösungszweige verfolgt und die genauen Bifurkationspunkte, welche das Auftreten der raumzeitlichen Strukturbildung markieren, ermittelt werden. Eine alternative Berechnung eines der Bifurkationspunkte zeigt, dass die beobachteten Phänomene als Strukturbildung hinter einer laufenden Front verstanden werden können.

Summary

The Langmuir-Blodgett method is an established technique to coat solid substrates with monomolecular layers of organic molecules such as phospholipids. These molecules are amphiphilic, that is, they have a hydrophilic and a hydrophobic end. Brought into contact with water, they assemble a monomolecular layer at the water surface where the hydrophilic side can adsorb to the water while the hydrophobic part can turn away from it.

The monolayer can then be transfered onto a partly submerged solid, the so-called substrate, by withdrawing it slowly from the water. During this process that constitutes the actual Langmuir-Blodgett transfer, the lipid layer is pulled out along with the substrate and covers it with a monomolecular layer.

At first one would assume the process to result in a homogeneous one-to-one transfer of the monolayer from the water surface to the substrate. Fascinatingly, however, the experimental conditions can be adjusted to obtain highly regular patterns with typical wavelengths of a few hundred nanometers, instead. These patterns consist of alternating stripe-like domains of lipid molecules in two different thermodynamic phases, the so-called liquid-expanded (LE) and liquid-condensed (LC) phases. Interestingly, before the transfer, the molecules on the water surface are in the pure LE phase. According to that, a partial and well-ordered condensation has to take place during the transfer process. This effect has been termed substrate-mediated condensation (SMC) by its discoverers.

The central problem treated in the present thesis is the development of a mathematical description of the experimentally observed pattern formation phenomena. To this end, a model is established that couples the dynamics of the system comprised by the water and the monolayer to thermodynamics, that is, in particular the LE-LC phase transition. Moreover, the interaction between the substrate and the monolayer, that is, the effect of SMC is theoretically described.

The mathematical description of the pattern formation is carried out using the framework of the lubrication approximation, an approximation of the basic equations of fluid flow, the Navier-Stokes equations, for thin liquid films. The central quantities in this approach are the density of the phospholipid monolayer Γ and the height profile of the water film H. The temporal evolution of Γ and H is described by two coupled nonlinear partial differential equations. To couple the model to the thermodynamics of the lipid monolayer, the free energy in vicinity of the LE-LC phase transition is formulated and an equation of state for Γ is derived. This equation of state determines the dependence of the surface tension on the local density of the monolayer. The interaction between substrate and monolayer is modeled in form of an external field in the free energy. The strength of this field depends on the distance between the substrate and the monolayer and yields a tilt of the free energy in favor of the LC phase at small distances. Thus, the condensation is energetically favored close to the substrate, explaining the experimentally observed drop of the LE-LC coexistence pressure at the substrate.

Before the model is applied to the relatively complicated transfer process, the equations are first considered under periodic boundary conditions. A linear stability analysis of homogeneous films

allows to determine the dependence of the wavelengths of the occurring patterns on material parameters. Additionally, an investigation of the surface rigidity and an estimation of its influence in vicinity to the LE-LC phase transition is conducted. The model equations are solved numerically whereupon the domain is spatially discretized using finite differences and an adaptive Runge-Kutta scheme is used for time integration. In part, the corresponding simulations are parallelized and performed on modern graphics devices.

Subsequently, the transfer process is numerically simulated using the approved methods. To this end, the model equations are subjected to suitable boundary conditions. The experimentally observed pattern formation processes can be successfully reproduced. Finally, the model is extended to describe the transfer onto chemically prestructured substrates. Thereby it can be shown that a periodic prestructure leads to synchronization phenomena of various orders resulting in the appearance of complex periodic stripe patterns. Moreover, new two-dimensional structures are observed, such as patterns consisting of a combination of circular and stripe-like domains. These results provide new perspectives for the purposeful nanopatterning of surfaces.

Addressing recent experiments, the dependence of the observed pattern formation on the temperature of the water subphase is investigated. The model developed for this purpose takes the shift of the isothermal curve of the monolayer into account and is in accordance with the experimental findings.

Finally, in the course of a deeper theoretical analysis, a reduced model of the transfer process is proposed. By means of semi-analytical calculations, a linear stability analysis of the inhomogeneous stationary solutions obtained due to the transfer boundary conditions is performed. In combination with numerical continuation methods the solution branches are traced and the bifurcation points corresponding to the onset of the spatiotemporal pattern formation are detected. An alternative calculation of one of the bifurcation points shows that the observed phenomena can be conceived as pattern formation behind a propagating front.

Contents

Introduction

Without doubt the last decade was marked by significant scientific and technological progress in nanoscience. Although it is nowadays possible to compose small-scale structures even by manipulation of single atoms [ES90], it is expensive and time consuming to structure large areas by direct manipulation. Therefore, more and more attention is paid to a promising alternative: self-assembly and pattern formation. Physicists, physical chemists, and material scientists have developed methods to harness nature's tendency to create regular patterns and structures for purposeful application. This interdisciplinary field is very important for further technological advances and poses challenging questions for fundamental science. In particular, concepts such as pattern formation, bifurcations, and chaos have to be applied and further developed to tackle the new issues arising on the micro- and nanoscale.

Controlled dewetting processes of complex fluids play a special role in this interdisciplinary field as they are employed in a large number of experiments to obtain various micro- and nanoscopic patterns at receding contact lines. Observations comprise ring- or stripe-like depositions of nanoparticles [DBD+97, DBD+00, YS05, BLN+06], nanowires [THY08], regular microscopic stripe patterns of metallic monolayers like gold and silver [HKT+05], and microstripes of organic semiconductors [LGS+10]. The present thesis is devoted to the theoretical description of a particularly interesting example of such processses: the formation of regular stripe patterns during the transfer of monomolecular layers of phospholipids from a water surface onto solid substrates [GCF00].

With the proper recipe, it is astonishingly simple to create layers which are no more than a single molecule thick. The ingredients are just water and a small volume of an amphiphilic substance. One end hydrophilic, the other hydrophobic, amphiphilic molecules seek the liquid-vapor interface to assume a state of energetic optimum. In many cases the result is a truly monomolecular layer, a structure that - depending on the density of the molecules - represents a two-dimensional gaseous, liquid, or crystalline state. Since the surface tension of the supporting air-water interface is lowered due to the presence of the layer[1] the adsorbed substances are referred to as **surf**ace **act**ive **a**ge**nts**, a term commonly abbreviated to *surfactants*. Probably the most important group of surfactants is comprised by phospholipids like dipalmitoylphophatidylcholine (DPPC, see fig. 0.1). They are the basic building blocks of cell membranes and therefore phospholipid monolayers have been extensively investigated as biophysical model systems.

The standard technique used to transfer the monolayers onto solid substrates is the Langmuir-Blodgett-method which has been developed by Nobel price winner Irving Langmuir together with Katherine Blodgett in the twenties and thirties of the twentieth century [Blo34, Lan34]. Their work continued the systematic investigation of surface tension and surfactants which was

[1] In fact, it is this property which assures the proverbial easiness of breathing: A surfactant film primarily consisting of the phospholipid dipalmitoylphosphatidylcholine (DPPC, see fig. 0.1), the very same substance used in the patterning experiments by Chi et al. [GCF00, CLZ+06, CLH+07, HFC08], lowers the surface tension of the air-water interface in the pulmonary alveoli by more than 80%. Without this film, every breath would take an insurmountable effort.

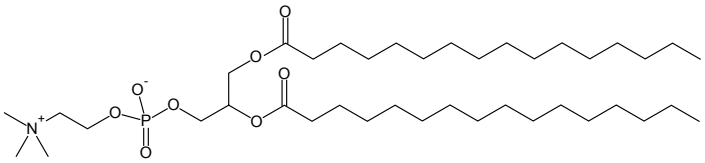

Fig. 0.1: The structure formula of lung surfactant dipalmitoylphosphatidylcholine (DPPC).

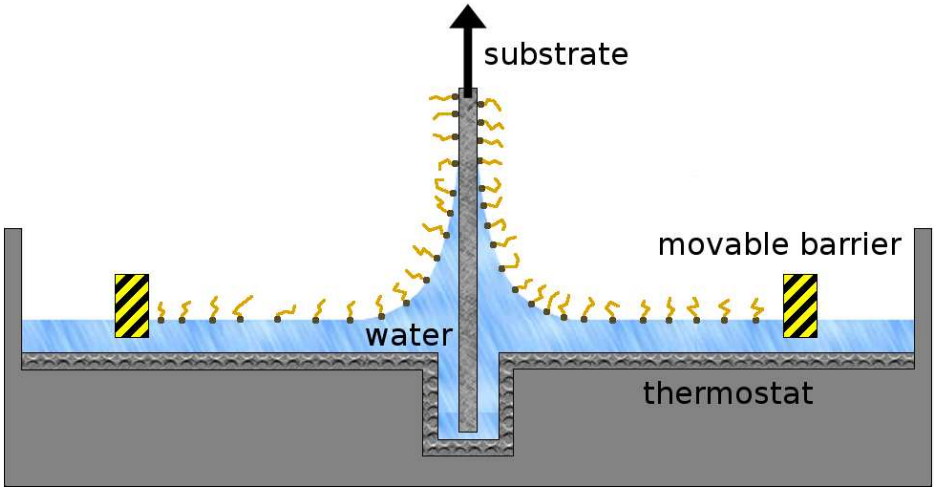

Fig. 0.2: Schematic drawing of a Langmuir-Blodgett trough. The monolayer is prepared between two movable barriers that are used to adjust the surfactant density.

established by illustrious researchers like Benjamin Franklin, Lord Rayleigh, and the ingenious "kitchen scientist" Agnes Pockels [Poc91]. Before the transfer, the surfactant monolayer is prepared in a Langmuir-Blodgett trough, as is schematically shown in fig. 0.2. In such a device, a small volume of water is kept at a constant temperature. The amphiphile is - usually together with a quickly evaporating solvent - dropped onto the water surface and spreads out over the whole area between two movable barriers, which can be used to adjust the surfactant density. The monolayer is then transfered onto a partially submerged solid substrate by slowly withdrawing it from the water. During this procedure, the barriers can be coupled to a Wilhelmy plate, a device to measure surface tension. Since the surface tension depends on the monolayer density, the trough can then automatically adjust the barriers to provide constant surface tension and monolayer density throughout the whole transfer process, if desired.

Fascinatingly, this experimental procedure does not always result in a one-to-one homogeneous transfer of the monolayer. Instead, under certain experimental conditions, highly regular stripe patterns are obtained (see figure 0.3). Wavelength and orientation of the observed stripes depend on the transfer velocity, that is, the speed of substrate removal, and on the density of the monolayer on the trough.

The observed pattern formation phenomena are directly related to the thermodynamics of the surfactant layer as the stripe pattern consists of alternating domains of different thermodynamic phases: the liquid-expanded (LE) and the liquid-condensed (LC) phase as visualized in figure 0.4.

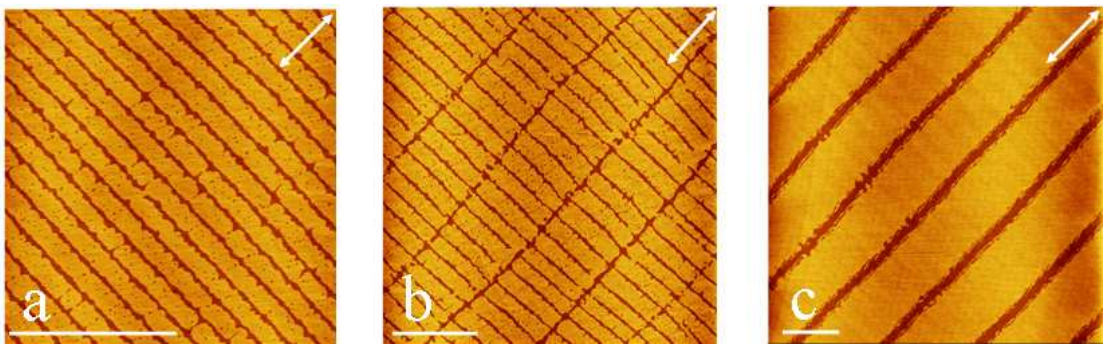

Fig. 0.3: AFM images of patterns obtained by Langmuir-Blodgett transfer of the phospholipid dipalmitoylsphosphatidylcholine (DPPC) onto mica substrates. The white double arrow indicates the pull direction. The transfer velocities were (a) 60 mm/min, (b) 40 mm/min, and (c) 10 mm/min. The lateral pressure, measured at the water surface of the trough was 3 mN/m in all three cases. Source: [CLH+07]

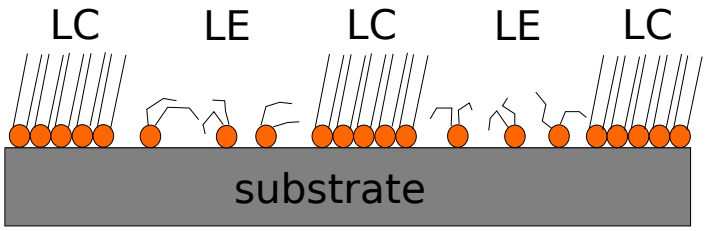

Fig. 0.4: Schematic illustration of the molecular composition of the DPPC stripe patterns: Liquid condensed stripes are divided by liquid expanded grooves.

The density of the LC is rather high, so that the molecules are closely packed and their tailgroups are aligned with each other and pointing straightly upward. In contrast, the LE phase is less dense, leaving the molecules enough space not to align their tailgroups. This leads to a measurable height difference of about 2 nm between LE and LC domains, which can be resolved by atomic force microscopy (AFM) [Gle00]. Due to this height-difference, stripe-like LE domains are often referred to as channels or grooves in the literature. It is remarkable, that the monolayer on the water surface are in the pure LE phase before the transfer. As the patterns consist of alternating LE and LC domains, a partial and well-ordered condensation has to take place during the transfer process. This effect has been termed **s**ubstrate-**m**ediated **c**ondensation (SMC) by its discoveres Riegler and Spratte [RS92, SCR94, SR94, GR98]. In subsequent experiments by Chi and coworkers the method could be refined to produce highly regular stripe patterns with typical wavelengths of no more than a few hundred nanometers that were accordingly termed nanochannel lattices [GCF00, CLZ$^+$06, CLH$^+$07, HFC08]. Typical transfer speeds are on the order of 1 mm/s and as there is in principle no limitation to the lateral width of the used substrates, the method of Langmuir-Blodgett patterning provides a fast and inexpensive way to endue substrates with a well-controlled nanostructured surface.

However, despite its great technological value, the most remarkable feature of Langmuir-Blodgett patterning is that the patterns form in a *self-organized manner*, that is, without any kind of external template. The question why a large number of interacting subsystems, in our case the single surfactant molecules, assemble themselves a structure on a scale much larger than the individual subsystem, has attracted the attention of many great scientists in the last century (see [CH93] for an overview). Hermann Haken recognized self-organization as a universal feature relevant for physics, chemistry, biology, information science, and even the social sciences [Hak04]. Most notably, he introduced the *slaving principle* that provides a systematic way to describe the collective behavior of many subsystems by means of a few order parameters.

The objective of the work summarized in this thesis is to develop a theoretical description of the experimentally observed pattern formation during Langmuir-Blodgett transfer. To this end, a model is devised that couples the dynamics of the subphase and the monolayer to the surfactant thermodynamics in vicinity of the LE-LC phase transition, and further describes the interaction between the substrate and the monolayer, that is, the SMC effect.

Following a brief historical introduction to the science of surfactant monolayers and Langmuir-Blodgett transfer, the basic theory of monolayer thermodynamics is developed in chapter 1. As a central result of these considerations, an equation of state is formulated, that links the surface tension of the monolayer covered liquid to the density of the monolayer. This equation is then modified to incorporate SMC.

A hydrodynamic model describing the liquid subphase as well as the surfactant layer at its surface is then derived in chapter 2. By means of the lubrication approximation [ODB97] two central evolution equations, one for the height profile of the liquid film and one for the surfactant density are derived. The flow is coupled to the thermodynamics of the monolayer via the surface tension that is determined by the surfactant equation of state. The resulting model is the first dynamical description of thin liquid films in the vicinity of a surfactant phase transition [KGF09] and represents one of the main achievements presented in this thesis.

Before the model is applied to the relatively complicated problem of monolayer transfer, the equations are first considered under periodic boundary conditions in chapter 3. To understand how the surfactant monolayer and the phase transition affect the dynamics of a liquid film, the

chapter begins with a description of clean film not contaminated by any surfactants. Subsequently, this case is then compared to the dynamics of surfactant covered films. A linear stability analysis of flat films is performed and allows to determine the dependence of the wavelengths of the occurring patterns on material parameters. Furthermore, the effect of surface rigidity is investigated to estimate its influence in the vicinity of the LE-LC phase transition [KGF11].

In chapter 4, monolayer transfer is numerically simulated by subjecting the derived model equations to suitable boundary conditions. The formation of periodic stripe patterns within a certain transfer velocity range is successfully reproduced by the model and the dependence of the wavenumber of the patterns on the velocity is obtained from the simulations [KGFC10]. Furthermore, the dependence of the stripe formation on the subphase temperature, that has recently been investigated experimentally [Har11], is examined, yielding results in accordance with the experimental findings.

As outlined in chapter 5, the model can be generalized to the case of chemically prepatterned substrates, which have been endued with a periodically modulated wettability [KGF11]. Upon transfer, such a prestructure translates into a spatiotemporal forcing of the pattern formation process at the meniscus. If the wavelength of the forcing is of the same order of magnitude as the natural wavelength of the pattern, synchronization of various orders can be observed. The dependence of the resulting complex periodic patterns on wavelength and amplitude of the wetting contrast can be quantified and summarized graphically in terms of the so-called *Arnold tongues* (see [PRK03]).

In chapter 6, the final chapter of this thesis, a reduced model of the transfer process is proposed. Steady and periodic solutions obtained in this simplified theory are combined to a bifurcation diagram showing the solution structure of the problem. The bifurcations corresponding to the onset and cessation of the spatiotemporal patterns are investigated. Furthermore, it is shown that the transfer problem is related to pattern formation behind a propagating front.

1 Monolayer thermodynamics and substrate-mediated condensation

The present section gives a brief historical introduction to the science of surfactant monolayers, followed by a review of the theory of first-order phase transitions and spinodal decomposition. Then, the equation of state describing the monolayer in vicinity of the LE-LC phase transition is derived. Finally, the substrate-monolayer interaction is incorporated into the theory.

1.1 A brief history of surfactant monolayers

Surfactant monolayers are highly remarkable structures and their practical application actually predates its discovery by scientists by a long time. In the first century A.D., Pliny the elder observed divers dropping oil onto the water surface to calm capillary waves so that more sunlight could enter the undersea darkness [Tan10]. Many centuries later, Benjamin Franklin wrote about fishermen applying the same trick to better spot fish below the surface. He also reported an experiment where he dropped one teaspoon of oil on a lake and watched it spreading across approximately $2000\,\mathrm{m}^2$ [FBF74]. Unfortunately, he did not recognize that he had just accessed the molecular scale - at a time where molecules were still merely a theoretical concept.

He did, however, inspire Lord Rayleigh, to repeat a downscaled version of Franklin's experiment in the late nineteenth century and this marks the beginning of the systematic investigation of surfactant monolayers. Rayleigh understood that the oil would spread until a monomolecular layer is formed and used the experiment to determine the molecular length scale [Ray89, Ray99]. Indeed it is possible to estimate the size of a single molecule by comparing the volume of the oil in Franklin's spoon to the area covered by the spread film: Under the assumption of spherical molecules, the number N of molecules in a drop of volume V is proportional to V/r^3, where r denotes the unknown molecular radius. The same number of molecules can cover an area $A \sim Nr^2$ with a monomolecular film. Since N is the same before and after the spreading, one can estimate $r \approx V/A$. Since a teaspoon corresponds to a volume on the scale of milliliters, one readily obtains a molecular radius on the scale of nanometers (or micromillimetres, as they were called in Rayleigh's days). In other words, an oil droplet of radius 1 mm spreads over an area of $4.2\,\mathrm{m}^2$ which amounts to about 67 DIN A4 pages (see fig. 1.1). This provides a good visualization of how *thin* a monolayer actually is. Although the assumption of spherical molecules is, as will be explained below, only of limited value, the results are remarkably good given the simplicity of the experimental procedure. For this reason, Rayleigh's experiment is nowadays regularly repeated in secondary school science classes.

Before Rayleigh could start further experiments, important results came from a completely unexpected direction: Agnes Pockels, who - as a woman - was not allowed to attend university but who had nevertheless studied physics as an autodidact, had turned her kitchen into a laboratory where she then developed the Pockels film balance, the prototype of the Langmuir trough. Fortu-

Fig. 1.1: Cross-section of an oil-drop containing enough molecules to coat 67 pages of this thesis with a monomolecular layer[1].

nately, she, who had no access to academic circles, dared to send her results to Lord Rayleigh who recognized the value of Pockels' work and forwarded her letter to Nature [Poc91]. In this letter she reports the dependence of surface tension on the density of the monolayer:

> "The surface tension of a strongly contaminated water surface is *variable* - that is, it varies with the size of the surface." ([Poc91])

Further, she recognized that the most interesting quantity is the difference between the surface tensions of a clean water surface and one that is covered by surfactants. This quantity, that Pockels termed the "anomaly of the surface" ([Poc02]) is nowadays known as the *lateral pressure* p_{lat} or the *surface pressure* and is defined by

$$\sigma = \sigma_{\mathrm{abs}} - p_{\mathrm{lat}}, \tag{1.1}$$

where σ is the actually measured surface tension while σ_{abs} denotes the surface tension in absence of any surfactant, that is, the surface tension of the pure liquid. Using her film balance, Pockels could measure the dependence of the lateral pressure on the area A of the monolayer [Poc91, Poc93]. By this procedure, she obtained the first surface pressure isotherms $p_{\mathrm{lat}}(A)$, that can be understood as two-dimensional analogues to the pressure-volume isotherms commonly measured in three-dimensional systems.

However, neither Pockels nor Rayleigh considered the monolayers from the perspective of thermodynamics in their original publications. This important conceptual progress can be attributed to Irving Langmuir, who was later awarded the Nobel price "for his discoveries and investigations in surface chemistry" [Nob11]. Unlike his scientific predecessors he recognized that surfactant molecules are complicated structures with a head and one or more tailgroups so that they "cannot, even approximately, be regarded spherical" (page 1865 of [Lan17]). This insight allowed him to correctly interpret the isotherms in terms of phase transitions between states characterized not only by the relative position of the molecules but also by the orientation of their tailgroups.

Langmuir continued his research in the laboratory of General Electric, where Katherine Blodgett became his assistant. Blodgett successfully transfered a monolayer from the water subphase onto glass by use of a device that is nowadays known as Langmuir-Blodgett trough (see fig. 0.2) [Blo34, Blo35]. The monolayer-coated glass was highly non-reflective and thus the first practical application of Langmuir-Blodgett transfer was born [BL37].

In the late sixties, Hans Kuhn and coworkers became interested in Langmuir-Blodgett transfer, which they recognized as a powerful method to create what they used to call "organizates" ([BDF+67]). The idea was to mimic biological systems in which new properties emerge due to a distinct organization at the molecular level. To this end, they sequentially transfered monolayers

[1] I was inspired to include this example by a similar visualization in the popular science book [Tan10].

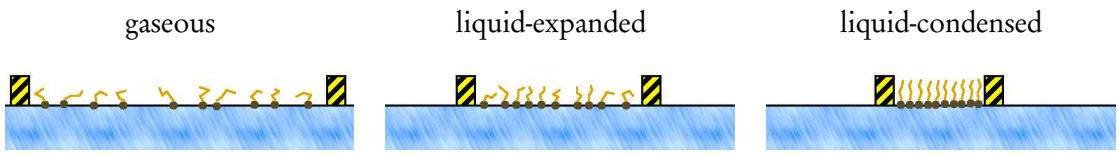

Fig. 1.2: Movable barriers at the trough allow to compress the monolayer just like one would compress a gas in a container using a piston.

of different chemicals and observed that "in this way molecular arrays of any planned order in the sequence of molecules might be constructed" ([BDF+67] page 199). By these means, surfaces could be manipulated to form functional units [KM71]. Consequently, "organizates" are to be regarded as early examples of functional nanomaterials. With their invention begins the transition to a time that can be considered more or less as "today".

1.2 Thermodynamics of surfactant monolayers

To understand the concept of lateral pressure, one has to consider that the molecules of an insoluble surfactant are essentially confined to the two-dimensional manifold given by the water surface. If the surface is bound by barriers, as is the case in a Langmuir trough, the situation is perfectly analogous to that of gas molecules confined to the volume of a container. Just like the gas exerts a force onto the container walls that leads to a measurable pressure, the surfactant molecules exert a force on the barriers. However, the boundary of a two-dimensional surface is a line, so that the lateral pressure is not a force per unit area but a force per unit length, measured in $\mathrm{N/m} = \mathrm{J/m^2}$, the unit of surface tension. The lateral pressure is not significant for low surfactant densities, because each molecule has enough area to move around freely, like in a two-dimensional ideal gas[2]. But if one of the barriers is moved inward, it has the same effect on the surfactant layer that a lowering piston would have on a three-dimensional gas in a container: compression. As the available area decreases, the molecules come closer together and begin to repel each other. Thus, the pressure rises and further compression takes more and more force. During this process, the monolayer will eventually undergo a phase transition similar to the liquefaction of vapor (see fig. 1.2). The new state is termed liquid-expanded (LE) and the transition from the gaseous to the LE state can be detected by measuring the surface tension repeatedly throughout the compression, in order to obtain an isothermal curve in a pressure-area diagram. As an example. fig. 1.3 shows the isothermal curve of DPPC at 20° C. The phase transition is evident from the strong increase of the slope at a mean molecular area of about $100\,\text{Å}^2$. As can be deduced from x-ray-diffraction experiments, the surfactant molecules in the LE phase, just like in the gaseous phase, lack short-range order, that is, their headgroups are translationally disordered and their tailgroups are conformationally

[2]This is the typical case for many substances like DPPC. However, not all monolayers expand to a gaseous state at room temperature. If they did, Franklin's teaspoon-fill of oil would not have stopped spreading at $2000\,\mathrm{m^2}$ but would have covered the entire pond. Langmuir noted on page 149 of [Lan34]: "The typical films produced on water by fatty acids and other oily substances have properties which indicate that they are 2-dimensional liquids and solids rather than gases, for they do not spread indefinitely, but the value of F becomes zero when the surface concentration σ falls to a definite value." Langmuir's F and σ correspond to p_{lat} and γ in the notation used in the present thesis.

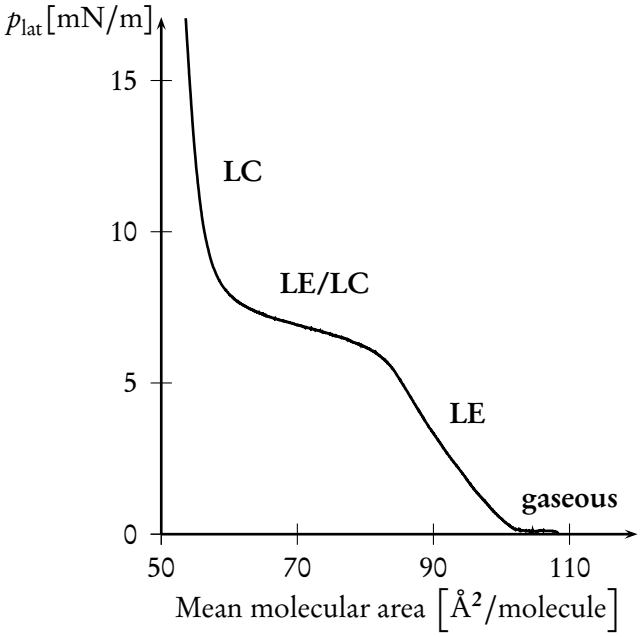

Fig. 1.3: Experimentally measured isotherm of a DPPC monolayer at 20°C. The data has been provided by Michael Hirtz (private communication).

disordered.

It is clear from fig. 1.3, that another phase transition is observed upon further compression of the LE layer: the transition to the liquid-condensed (LC) state. This transition is the most important one for the present study, since the patterns obtained in LB-transfer consist of alternating domains of monolayer in the LE and LC phases. It is the most investigated monolayer phase transition in the literature, and it is often also referred to as the *main transition*.

It is understandable, that the order of this transition has been subject of a long debate among researchers, because, as can be seen in fig. 1.3, the slope of the isotherm between about 60 and 80 Å^2 per molecule is very low but the curve is clearly not horizontal. Nevertheless, coexistence of LE and LC domains was observed *after* transfer onto substrates. The dispute could finally be resolved by direct optical observation of phase coexistence at the water surface [LSM83], proving the main transition to be of first order.

A word of caution is in order, regarding the use of the term "liquid-condensed". It turns out, that surfactant monolayers exhibit a remarkably rich phase diagram with numerous liquid-crystalline and solid-crystalline states. A clear distinction between the various different molecular configurations remained elusive as long as one had to rely on isotherm measurements only. Thus, many details of the phase diagram of monolayers have been fully accessible only after the advent of modern surface analysis tools. X-ray-diffraction revealed that the historical classification that distinguished between gaseous, LE, LC, and solid (a state even denser and less compressible than the LC state) states is too coarse to describe the monolayer accurately. In particular, the LC phase can be divided into the *tilted condensed* and the *untilted condensed* phase. Both are conformally ordered, that is, their tailgroups are aligned parallel to each other, but only in the untilted condensed phase they are vertical to the water surface. As a consequence, the tilted condensed layer can be

compressed more easily than the untilted condensed layer since the molecules can continuously decrease their tilt angle. Once the continuous transition to the untilted state is completed, further compression necessarily involves a closer packing of the headgroups. However, more detailed studies using Brewster angle microscopy (BAM) and polarized fluorescence microscopy (PFM) revealed that even the subdivision of the LC phase into tilted and untilted phases is not yet complete. All in all the regions of the phase diagram that were formerly labeled LC and S comprise at least eight different states [KMD99]. Many researchers have therefore abandoned the use of the term "liquid-condensed". Nevertheless, the old nomenclature has prevailed as standard until today in literature concerned with the main transition, where only two states, the liquid-expanded and the tilted condensed state, have to be distinguished. This standard is adopted in the present thesis.

Now that the basic phenomenology of surfactant monolayers has been introduced, one has to think about how the dependence of the surface tension on the surfactant density can be described quantitatively. This is possible in terms of a surfactant equation of state that can be derived from the theory of first order phase transitions.

1.3 First order phase transitions

In order to understand the considered pattern formation process, it is essential to know the theory of first order phase transitions. Concepts like the binodal and the spinodal impact our theory in two ways. Firstly, the main transition in the monolayer, that is, the LE-LC phase transition, is of first order. Secondly, the breakup of thin liquid films into droplets can also be described as a phase decomposition process. In order to avoid confusion, we will employ the standard notation, using the term *spinodal decomposition* for phase separation processes in the surfactant monolayer while referring to film breakup as *spinodal dewetting*.

The present section begins with a short review of the basic theory of first order phase transitions. For more details, the reader is referred to textbooks on thermodynamics such as [LL87]. It is followed by an outline of the Cahn-Hilliard equation, the de facto standard model of phase decomposition dynamics.

1.3.1 Binodal, spinodal, and the region of phase coexistence

Basic concepts

A phase transition of first order occurs when the free energy of a thermodynamical system $F(T,V,N)$, with temperature T, volume V, and particle number N, has two local minima. These minima are then necessarily divided by an energy barrier, that is, a region of concave F. This has the immediate consequence, that there is a certain region $V_\mathrm{I} < V < V_\mathrm{II}$ in which a homogeneous state is energetically disadvantageous compared to a heterogeneous state, where the system's material is divided into coexisting parts with the densities $n_\mathrm{I} = N/V_\mathrm{I}$ and $n_\mathrm{II} = N/V_\mathrm{II}$. Realizations of such heterogeneous states are commonly observed, for example, in the liquid-vapor transition of H_2O or CO_2, where the coexistence of liquid and vapor can readily be prepared experimentally.

In order to illuminate this phenomenon, we will first determine the boundaries of the coexistence region $V_\mathrm{I}, V_\mathrm{II}$ and then calculate the free energy of the heterogeneous state.

In equilibrium, the coexistence of two phases is possible if and only if pressure p, temperature T, and chemical potential μ are equal in both phases, that is, throughout the entire system. Therefore,

one can use the condition

$$\mu_{\mathrm{I}}(T, p_{\mathrm{I/II}}) = \mu_{\mathrm{II}}(T, p_{\mathrm{I/II}}) = \text{const.},$$

where $p_{\mathrm{I/II}}$ denotes the coexistence pressure, together with the Gibbs-Duhem relation $G = \sum_j \mu_j$, with free enthalpy G, to infer

$$\begin{aligned} & G_{\mathrm{I}}(T, p_{\mathrm{I/II}}) = G_{\mathrm{II}}(T, p_{\mathrm{I/II}}) \\ \Leftrightarrow\ & F_{\mathrm{I}} + p_{\mathrm{I/II}} V_I = F_{\mathrm{II}} + p_{\mathrm{I/II}} V_{\mathrm{II}} \\ \Rightarrow\ & F_{\mathrm{I}} - F_{\mathrm{II}} = p_{\mathrm{I/II}} (V_{\mathrm{II}} - V_{\mathrm{I}}). \end{aligned} \tag{1.2}$$

Here, we have used the relation $G = F + pV$ between the thermodynamic potentials. Since we also know that for $T = \text{const.}$

$$F_{\mathrm{I}} - F_{\mathrm{II}} = -\int_{V_{\mathrm{II}}}^{V_{\mathrm{I}}} \mathrm{d}V\, p, \tag{1.3}$$

we can combine the equations (1.2) and (1.3) to obtain

$$\int_{V_{\mathrm{I}}}^{V_{\mathrm{II}}} \mathrm{d}V\, p = p_{\mathrm{I/II}} (V_{\mathrm{II}} - V_{\mathrm{I}}).$$

This result allows to find the coexistence region by a simple geometrical approach: the famous *Maxwell construction*. Drawing the isotherm of the homogeneous system in a pressure-volume diagram, the coexistence pressure $p_{\mathrm{I/II}}$ corresponds to a horizontal line which is drawn in such a way that the areas A and B in fig. 1.4 are of equal size. This uniquely defines $p_{\mathrm{I/II}}$, V_{I}, and V_{II}.

The energy of the heterogeneous state is given by $F = c_{\mathrm{I}} F_{\mathrm{I}} + c_{\mathrm{II}} F_{\mathrm{II}}$, where $F_{\mathrm{I}} = F(T, V_{\mathrm{I}}, N)$ and $F_{\mathrm{II}} = F(T, V_{\mathrm{II}}, N)$ are the free energies of homogeneous systems of volume V_{I} and V_{II}, respectively, while $c_{\mathrm{I}} = N_{\mathrm{I}}/N$ and $c_{\mathrm{II}} = N_{\mathrm{II}}/N$ denote the fractions of molecules in the two phases. Since $c_{\mathrm{I}} + c_{\mathrm{II}} = 1$ and $V = c_{\mathrm{I}} V_{\mathrm{I}} + c_{\mathrm{II}} V_{\mathrm{II}}$, we can deduce the so-called *lever rule*:

$$c_{\mathrm{I}} = \frac{V_{\mathrm{II}} - V}{V_{\mathrm{II}} - V_{\mathrm{I}}}, \quad \text{and} \quad c_{\mathrm{II}} = \frac{V - V_{\mathrm{I}}}{V_{\mathrm{II}} - V_{\mathrm{I}}}.$$

Accordingly, we can write the free energy of the heterogeneous state as

$$F_{\mathrm{het}}(T, V, N) = \frac{V_{\mathrm{II}} - V}{V_{\mathrm{II}} - V_{\mathrm{I}}} F_{\mathrm{I}} + \frac{V - V_{\mathrm{I}}}{V_{\mathrm{II}} - V_{\mathrm{I}}} F_{\mathrm{II}},$$

which is obviously a straight line with the slope $\partial F_{\mathrm{het}}/\partial V = (F_{\mathrm{II}} - F_{\mathrm{I}})/(V_{\mathrm{II}} - V_{\mathrm{I}})$, connecting $F(T, V_{\mathrm{I}}, N)$ and $F(T, V_{\mathrm{II}}, N)$. Since we argued above, that the pressure $p = -\partial F/\partial V$ is constant along any isotherm in the coexistence region, we infer that the straight line F_{het} is actually tangent to F in both points $F(T, V_{\mathrm{I}}, N)$ and $F(T, V_{\mathrm{II}}, N)$. It is thus termed the *common tangent* in the literature. Due to the concavity of the free energy of the homogeneous state in between the two local minima, the tangent F_{het} is lying below F, making the heterogeneous states on the tangent energetically more favorable. This is shown graphically in fig. 1.5. This region in state-space in which the heterogeneous state has a lower overall free energy than the homogeneous state is called the *binodal region*, and it is the region where phase coexistence is possible. Its boundary, the binodal curve, is given by the loci of $V_{\mathrm{I}}, V_{\mathrm{II}}$ written as functions of another state variable such as

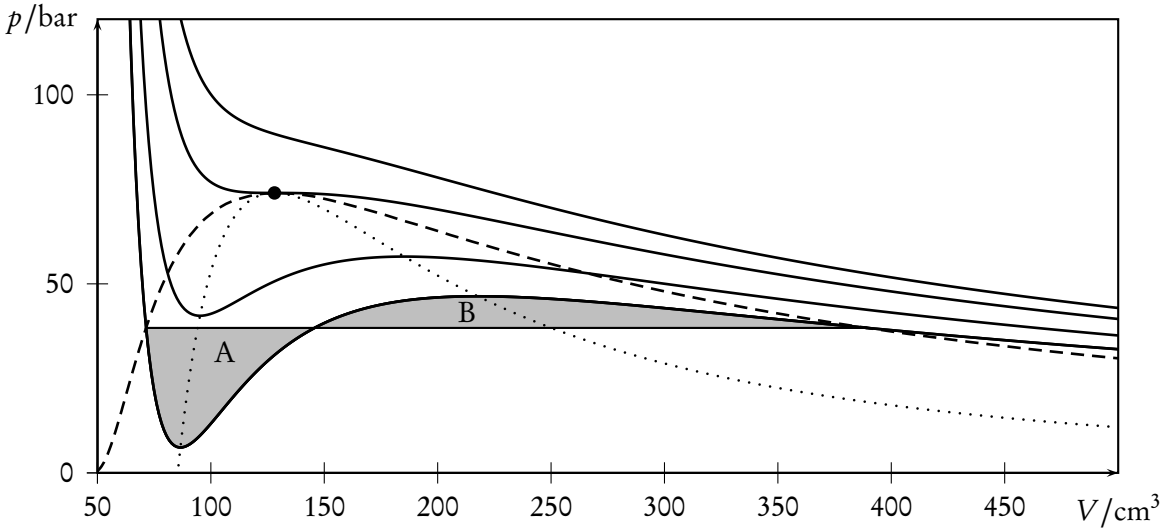

Fig. 1.4: Isothermal lines of CO_2 around the liquid-gas phase transition modeled by the van-der-Waals equation of state. The solid lines are, listed from top to bottom, isotherms calculated for $T = 320\,\mathrm{K}$, $T = T_{\mathrm{cr}} = 303.998\,\mathrm{K}$, $T = 280\,\mathrm{K}$, and $T = 260\,\mathrm{K}$. The binodal is plotted as a dashed line. It delimits the region where homogeneous states are metastable. The spinodal curve is plotted as a dotted line and it marks the boundary of the region where homogeneous states are unstable. Binodal and spinodal meet in at the critical point, which is marked by a black dot.

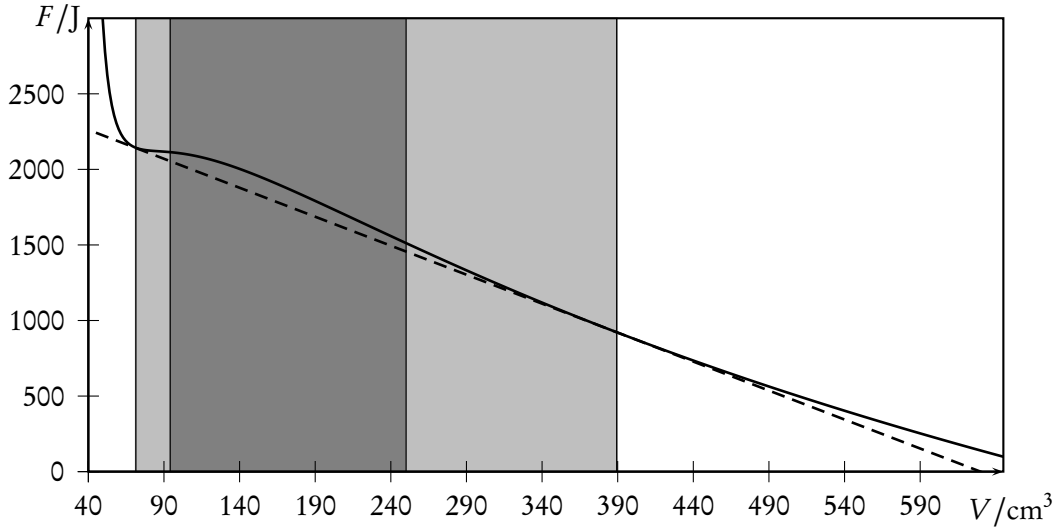

Fig. 1.5: Free energy of CO_2 at temperature $T = 260\,\mathrm{K}$ modeled by the van-der-Waals equation of state. In the binodal region, which is shown in light gray, homogeneous states are metastable, since heterogeneous states of lower free energy, lying on the common tangent (dashed line), are possible. The spinodal region is shown in dark gray.

the temperature T, yielding curves $V_{\mathrm{I}}(T), V_{\mathrm{II}}(T)$. If phase coexistence is not possible for all values of T, then the two curves $V_{\mathrm{I}}(T), V_{\mathrm{II}}(T)$ will meet in a *critical point* at a temperature T_{cr} beyond which the phases are no longer distinguishable from each other.

However, the given argument does not claim that a state within the binodal is unstable but only that it is metastable, that is, unstable to finite but not to infinitesimal perturbations. In fact, these metastable states are commonly observed, for example in form of an overheated liquid or an undercooled gas.

So, when does the homogeneous state actually become unstable? Looking at the pressure $p = -\partial F(T,V,N)/\partial V$ of the system, we note that any state with $\partial p/\partial V = -\partial^2 F/\partial V^2 > 0$, is mechanically unstable, so that the inflection points $\partial^2 F(T,V,N)/\partial V^2 = 0$, when written as functions of another state variable, such as T, mark a boundary, the so-called *spinodal curve* beyond which no homogeneous state can exist. The region within this boundary, that is the region of negatively curved $F(T,V,N)$, is called the *spinodal region*. In the next subsection, this instability is explained by use of an energetic argument.

It is clear that the spinodal region is a subset of the binodal region, since in between every two minima of the free energy there is necessarily a region of negative curvature. By the same argument, we can deduce that spinodal and binodal meet in the critical point, because the minima smoothly approach each other for $T \to T_{\mathrm{cr}}$, so that minima and inflection points finally coincide.

Throughout this thesis, we will describe the surfactant monolayer in terms of its molecular number density $n = N/V$. We therefore use the remainder of this subsection to formulate the free energy using the variable n, that is $\tilde{F}(T,V,n) := F(T,V,nV)$, and write

$$\tilde{F}(T,V,n) = f(T,n)V, \tag{1.4}$$

denoting the system's free energy density by $f(T,n)$.

The pressure of the system is then given by

$$\begin{aligned} p = -\frac{\partial F(T,V,N)}{\partial V} &= -\frac{\partial \tilde{F}(T,V,n)}{\partial V} - \frac{\partial \tilde{F}(T,V,n)}{\partial n}\frac{\partial n}{\partial V} \\ &= -\frac{\partial \tilde{F}(T,V,n)}{\partial V} + \frac{\partial \tilde{F}(T,V,n)}{\partial n}\frac{n}{V} \\ &= -\frac{\partial \tilde{F}(T,V,n)}{\partial V} + n\mu, \end{aligned}$$

where we introduce the chemical potential

$$\mu = (1/V)\frac{\partial \tilde{F}(T,V,n)}{\partial n}.$$

Inserting eq. (1.4), we find

$$\tilde{p}(T,V,n) = -f(n) + n\frac{\partial f(n)}{\partial n}. \tag{1.5}$$

In order to determine the mechanical stability of homogeneous states, one has to calculate

$$\begin{aligned}\frac{\partial p(T,V,N)}{\partial V} &= \frac{\partial \tilde{p}(T,V,n)}{\partial V} - \frac{n}{V}\frac{\partial \tilde{p}(T,V,n)}{\partial n} \\ &= -\frac{\partial^2 \tilde{F}(T,V,n)}{\partial V^2} - 2\frac{n}{V}\left(\frac{1}{V}\frac{\partial \tilde{F}(T,V,n)}{\partial n} - \frac{\partial^2 \tilde{F}(T,V,n)}{\partial n \partial V}\right) - \frac{n^2}{V^2}\frac{\partial^2 \tilde{F}(T,V,n)}{\partial n^2}.\end{aligned}$$

In case of eq. (1.4) we obtain

$$\frac{\partial^2 \tilde{F}}{\partial V^2} = 0, \qquad \frac{\partial \tilde{F}}{\partial n} = \frac{\partial f(n)}{\partial n} V, \qquad \frac{\partial^2 \tilde{F}}{\partial n \partial V} = \frac{\partial f}{\partial n}, \qquad \frac{\partial^2 \tilde{F}}{\partial n^2} = \frac{\partial^2 f}{\partial n^2} V,$$

yielding

$$\frac{\partial p(T,V,N)}{\partial V} = \frac{\partial^2 F(T,V,N)}{\partial V^2} = -\frac{n^2}{V^2}\frac{\partial^2 \tilde{F}(T,V,n)}{\partial n^2}.$$

We conclude that, no matter whether we look at the free energy in terms of the variable volume V or the variable density n, the stability is always determined by the second derivative of the corresponding free energy function.

An energetic argument for the instability of homogeneous systems within the spinodal region

The condition of mechanical stability, $\partial p(T,V,N)/\partial V < 0$, can be substantiated by a simple energetic argument which, despite its clearness, is - at least to the author's awareness - never given in the literature.

A homogeneous state is unstable when even an infinitesimal perturbation leads to a state of lower free energy. Let us assume, that an initially homogeneous system of density n_0 is perturbed with a perturbation of amplitude $\mathrm{d}n$, so that a volume portion V_+ of the fixed total volume V_0 now has the density $n_0 + \mathrm{d}n$ with infinitesimal $\mathrm{d}n$. Material conservation demands, that another portion $V_0 - V_+$ is perturbed at the same time so that it now has the density $n_0 - V_+/(V_0 - V_+)\mathrm{d}n$. Then the free energy difference between the perturbed and the initial state is given by

$$\begin{aligned}\Delta F &= V_+ f(n_0 + \mathrm{d}n) + (V_0 - V_+) f\left(n_0 - \frac{V_+}{V_0 - V_+}\mathrm{d}n\right) - V_0 f(n_0) \\ &= (V_+ - V_0) f(n_0) + V_+ \left.\frac{\partial f}{\partial n}\right|_{n_0} \mathrm{d}n + \frac{V_+}{2}\frac{\partial^2 f}{\partial n^2}\mathrm{d}n^2 \\ &\quad + (V_0 - V_+)\left[f(n_0) - \left.\frac{\partial f}{\partial n}\right|_{n_0}\frac{V_+}{V_0 - V_+}\mathrm{d}n - \frac{1}{2}\left.\frac{\partial^2 f}{\partial n^2}\right|_{n_0}\left(\frac{V_+}{V_0 - V_+}\right)^2 \mathrm{d}n^2\right] + \mathcal{O}\left(\mathrm{d}n^3\right).\end{aligned}$$

Collecting terms order by order, we see that the dn^0 and dn^1 contributions exactly cancel each other. The lowest order term of ΔF is therefore given by

$$\Delta F = \frac{V_+}{2}\left(1 + \frac{V_+}{V_0 - V_+}\right)\left.\frac{\partial^2 f}{\partial n^2}\right|_{n_0} \mathrm{d}n^2 + \mathcal{O}\left(\mathrm{d}n^3\right).$$

Since V_+ is by definition positive and less than V_0, we conclude that the sign of ΔF for infinitesimal dn is determined solely by the curvature of the free energy density in the initial state n_0. Note, that the above argument holds true also when we assume the perturbation to be limited to a subvolume $V' \subset V_0$. This means that a local infinitesimal fluctuation around n_0 will reduce the free energy of the system if and only if $\partial^2 f(n_0)/\partial n^2 < 0$. Thus, we have reproduced the stability condition given in the previous section by explicitly referring to the change of the system's free energy.

1.4 Dynamics of spinodal decomposition: The Cahn-Hilliard equation

So far we have only considered equilibrium states and investigated their stability. The actual dynamics of a system within the spinodal region is governed by the Cahn-Hilliard equation [CH58, Cah65], that describes the time evolution of the spatially varying density $\rho(\vec{x}, t)$ of the considered thermodynamical system. It can be written as a conservation law

$$\partial_t \rho(\vec{x}, t) = -\nabla \cdot \vec{J}(\vec{x}, t), \tag{1.6}$$

with the flux

$$\vec{J}(\vec{x}, t) = -\alpha \nabla \frac{\delta \mathscr{F}[\rho]}{\delta \rho(\vec{x}, t)}, \tag{1.7}$$

where α denotes a mobility factor. In the simple case of constant α, the Cahn-Hilliard equation takes the form

$$\partial_t \rho(\vec{x}, t) = \alpha \Delta \frac{\delta \mathscr{F}[\rho]}{\delta \rho(\vec{x}, t)}. \tag{1.8}$$

It is important to recognize, that the Cahn-Hilliard equation exhibits *potential dynamics*. This means that an isolated system approaches an equilibrium state, which corresponds to a local minimum of the free energy functional $\mathscr{F}[\rho]$. In the terminology of nonlinear dynamics this means that $\mathscr{F}[\rho]$ is the Lyapunov functional of the system.

This holds true for arbitrary positive definite mobility factors. To prove this, one has to consider how $\mathscr{F}[\rho]$ changes with time. A short calculation yields

$$\begin{aligned}
\partial_t \mathscr{F} &= \int_V \mathrm{d}^D x \, \frac{\delta \mathscr{F}}{\delta \rho(\vec{x})} \partial_t \rho(\vec{x}) && \Big| \text{ insert (1.8)} \\
&= \int_V \mathrm{d}^D x \, \frac{\delta \mathscr{F}}{\delta \rho(\vec{x})} \nabla \cdot \left[\alpha \nabla \frac{\delta \mathscr{F}}{\delta \rho(\vec{x})} \right] && \Big| \text{ partial integration} \\
&= \int_V \mathrm{d}^D x \, \nabla \left[\alpha \frac{\delta \mathscr{F}}{\delta \rho(\vec{x})} \nabla \frac{\delta \mathscr{F}}{\delta \rho(\vec{x})} \right] - \int_V \mathrm{d}^D x \, \alpha \left(\nabla \frac{\delta \mathscr{F}}{\delta \rho(\vec{x})} \right)^2 && \Big| \text{ Gauss' law} \\
&= \int_{\partial V} \mathrm{d}^{(D-1)} x \, \alpha \frac{\delta \mathscr{F}}{\delta \rho(\vec{x})} \nabla \frac{\delta \mathscr{F}}{\delta \rho(\vec{x})} - \int_V \mathrm{d}^D x \, \alpha \left(\nabla \frac{\delta \mathscr{F}}{\delta \rho(\vec{x})} \right)^2 .
\end{aligned}$$

Thus we have decomposed the temporal change of the free energy into a volume contribution and a boundary contribution. The value of the boundary integral depends, of course, on the specific boundary conditions of the system under consideration. In most relevant cases, such as periodic

boundary conditions or also for $\rho \to$ const. as $|\vec{x}| \to \infty$, it simply vanishes. For an isolated system, this will always be true, since in general, a system can be regarded as isolated, only if there is no energy flux through its boundaries. This leads us to the result

$$\partial_t \mathscr{F} = -\int_V \mathrm{d}^D x \underbrace{\alpha \left(\nabla \frac{\delta \mathscr{F}}{\delta \rho(\vec{x})} \right)^2}_{\geq 0} \leq 0, \tag{1.9}$$

that is, either ρ is already in an equilibrium state or it is evolving towards one.

Cahn and Hilliard proposed the following free energy functional for a general isotropic system of nonuniform composition [CH58]:

$$\mathscr{F}[\rho] = \int_V \mathrm{d}^D x \left\{ \frac{\varkappa}{2} (\nabla \rho)^2 + f_{\mathrm{hom}}(\rho) \right\}, \tag{1.10}$$

with a positive constant $\varkappa$. The idea behind this model is simple: To molecules within a subvolume $\mathrm{d}V$ of the system it makes little difference whether they are part of a homogeneous system or of an inhomogeneous system with very small density gradients. Thus, as a zeroth approximation, the system's overall free energy simply equals the sum of the free energies of each infinitesimal subvolume, $f_{\mathrm{hom}}(\rho(\vec{x}))\mathrm{d}V$. To improve the approximation, one can expand the free energy density in powers of $\nabla\rho$, keeping only the lowest orders:

$$f(\rho, \nabla\rho, \nabla^2\rho, \dots) = f_{\mathrm{hom}}(\rho) + L_i \partial_i \rho + \varkappa^{(1)}_{ij} \partial_i \partial_j \rho + \varkappa^{(2)}_{ij} \left(\partial_i \rho\right)\left(\partial_j \rho\right) + \dots$$

The tensors $\underline{\boldsymbol{\varkappa}}^{(1,2)}$ and the vector $\vec{L}$ reflect the symmetry properties of the considered material. For isotropic media, one obtains $\vec{L} = 0$ and $\underline{\boldsymbol{\varkappa}}^{(1)} = \varkappa_1 \underline{\boldsymbol{I}}$, $\underline{\boldsymbol{\varkappa}}^{(2)} = \varkappa_2 \underline{\boldsymbol{I}}$, yielding the free energy density of eq. (1.10), where $\varkappa = -\mathrm{d}\varkappa_1/\mathrm{d}\rho + \varkappa_2/2$. Any inhomogeneity of ρ results in a nonzero contribution $\varkappa(\nabla\rho)^2$ to the free energy. Thus, $\varkappa$ is a weight constant quantifying the energetic cost of spatial density fluctuations. Most importantly, it describes the line tension between domains of different thermodynamic phases and the width of the interface between two phases scales with $\sqrt{\varkappa}$ [CH58].

Inserting the free energy functional (1.10) into the Cahn- Hilliard equation (1.8), we obtain

$$\partial_t \rho(\vec{x}, t) = -\varkappa \Delta^2 \rho + \frac{\partial^2 f_{\mathrm{hom}}}{\partial \rho^2} \Delta\rho + \frac{\partial f_{\mathrm{hom}}}{\partial \rho} (\nabla\rho)^2 . \tag{1.11}$$

From our considerations in section 1.3.1 we already know qualitatively what to expect from solutions to this equation: Homogeneous systems outside of the binodal region are absolutely stable, within the binodal region they are metastable, and in the spinodal region they are unstable. Upon instability, the homogeneous state decomposes into coexisting domains of different densities $\rho_{\mathrm{I}}, \rho_{\mathrm{II}}$.

Spatially homogeneous fields $\rho = \hat{\rho} =$ const. are always stationary solutions of the Cahn-Hilliard equation. Their linear stability is readily obtained by looking at small perturbations $\zeta(x,t)$. Inserting $\rho(x,t) = \hat{\rho} + \zeta(x,t)$ into eq. (1.11), and keeping only the linear terms, we find that the time evolution of the perturbation is governed by

$$\partial_t \zeta = -\left\{ \varkappa \Delta^2 - \left. \frac{\partial^2 f_{\mathrm{hom}}}{\partial \rho^2} \right|_{\hat{\rho}} \Delta \right\} \zeta .$$

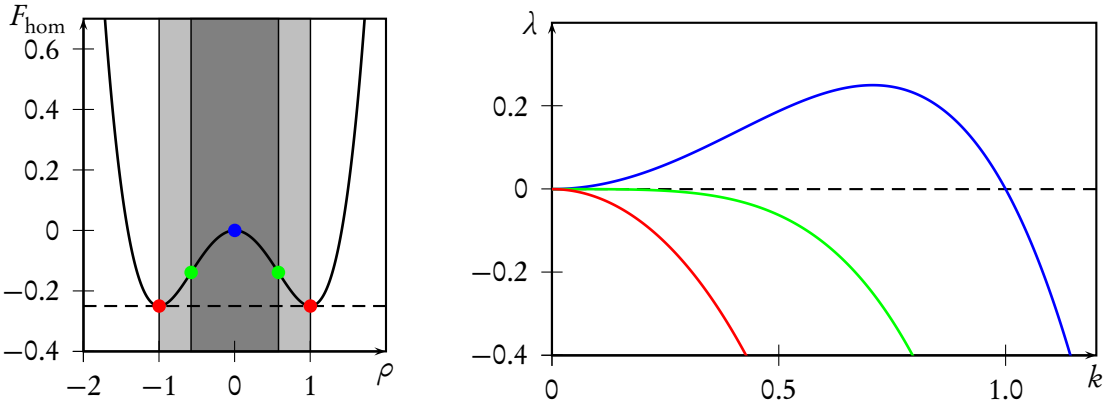

Fig. 1.6: Free energy of homogeneous solutions (left) and dispersion relations of small perturbations around these solutions (right). The binodal region is drawn in light gray while the spinodal region is coloured dark gray. For a symmetric F_{hom} the common tangent (dashed line) is simply the horizontal line connecting the minima of the free energy. Solutions from within the spinodal region, where F_{hom} is concave, are linearly unstable and have a finite band of unstable modes.

Using the ansatz $\zeta \sim \exp(\lambda t + \mathrm{i}\vec{k}\cdot\vec{x})$, one finds the dispersion relation of the perturbation, which only depends on the absolute value of the wavevector $k = |\vec{k}|$, since only even powers of ∇ are applied to ζ:

$$\lambda(k) = -k^2 \left\{ \varkappa k^2 + \left.\frac{\partial^2 f_{\text{hom}}}{\partial \rho^2}\right|_{\hat{\rho}} \right\}. \tag{1.12}$$

From this expression, it is obvious, that the stability of a homogeneous solution $\hat{\rho}$ is determined by the curvature of the free energy at $\rho = \hat{\rho}$. Physically speaking, a solution $\hat{\rho}$ is stable, as long as it is chosen from outside the spinodal region, which is defined as the region of concave f_{hom}. Otherwise, there is a finite band of modes k with $0 < k < \sqrt{(\partial^2 f_{\text{hom}}/\partial\rho^2)|_{\hat{c}}}$ which are amplified with $\lambda(k) > 0$. Dispersion relations for three different $\hat{\rho}$ in a system with a free energy of symmetric double-well shape are shown in fig. 1.6. The wavenumber k_{max}, which is maximally amplified, can be calculated from eq. (1.12) as

$$k_{\text{max}} = \sqrt{-\frac{1}{2\varkappa}\left.\frac{\partial^2 f_{\text{hom}}}{\partial \rho^2}\right|_{\hat{\rho}}}.$$

The corresponding maximal amplification is given by

$$\lambda_{\text{max}} := \lambda\left(k_{\text{max}}\right) = -\frac{3}{4}\left.\frac{\partial^2 f_{\text{hom}}}{\partial \rho^2}\right|_{\hat{\rho}}.$$

With k_{max} and λ_{max} we have obtained an estimate of the inverse time and length scales of the early stages of spinodal decomposition.

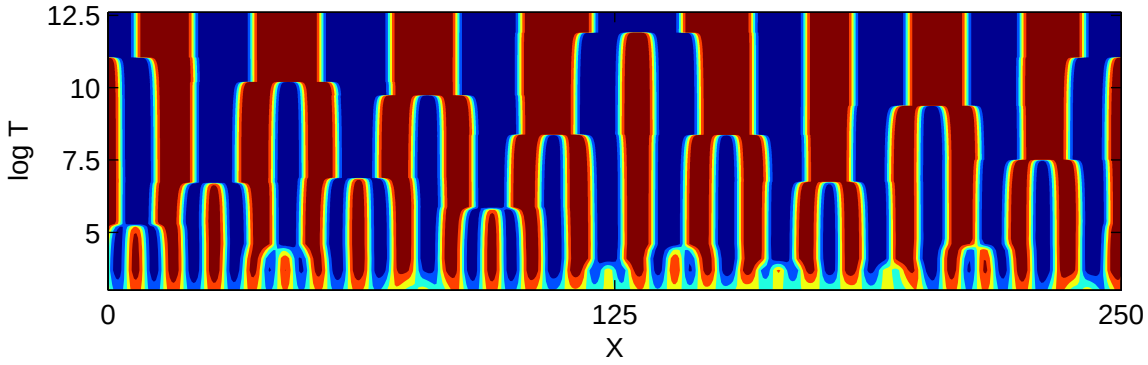

Fig. 1.7: Space-time plot of spinodal decomposition obtained from direct numerical simulation of the Cahn-Hilliard equation on a periodic domain. Red: $\rho = 1$, blue: $\rho = -1$. Parameters: Domain size $L = 250$, number of grid points $N = 512$, $\alpha = \varkappa = 1$, $\hat{\rho} = 0$.

However, after a short time, the nonlinearity of eq. 1.11 strikes and leads to a different behavior known as *coarsening* of the domains which are formed during the initial pattern formation. During this process, large domains grow larger while small domains grow smaller and finally disappear. Two mechanisms can be distinguished: Firstly, two domains can directly merge into a single larger one, thereby minimizing their overall interfacial energy. Secondly, material diffuses from the surface of small domains towards the larger ones, that is, the domains are absorbed without direct contact to other domains. This phenomenon is known as *Ostwald-ripening* [Ost00, LS61]. Direct numerical simulations in one- and two spatial dimensions show the dynamics of the coarsening process. A space-time plot of a one-dimensional solution is given in fig. 1.7. Two-dimensional simulations for different choices of the average density $\hat{\rho}$ show that the domain shape depends on the amount of available material (see fig. 1.8). The phase with the smaller overall volume will form spherical domains in order to diminish the interfacial energy. If, however, both phases have roughly the same total volume, one will rather observe labyrinthine structures. The coarsening process will continue, until finally only one domain of each phase remains, divided by the smallest possible interface.

1.5 Free-energy and lateral pressure in the vicinity of the main transition

In order to derive the equation of state of a surfactant monolayer in the vicinity to the main transition, one has to start with the formulation of the monolayer's free energy. The phenomena that we aim to describe involve the coexistence of two phases, that is, the LE and the LC phase, so that it makes sense to directly consider the general case of a non-homogeneous system with a surfactant density $\gamma(\vec{x})$ that may vary across the water surface. As has been explained in the previous section, the free energy of such systems can be written in form of the functional (1.10). Since the monolayer is confined to the water surface, the case $D = 2$ has to be considered:

$$\mathscr{F}[\gamma] = \int\int \mathrm{d}x\mathrm{d}y\, f(\vec{x}),$$

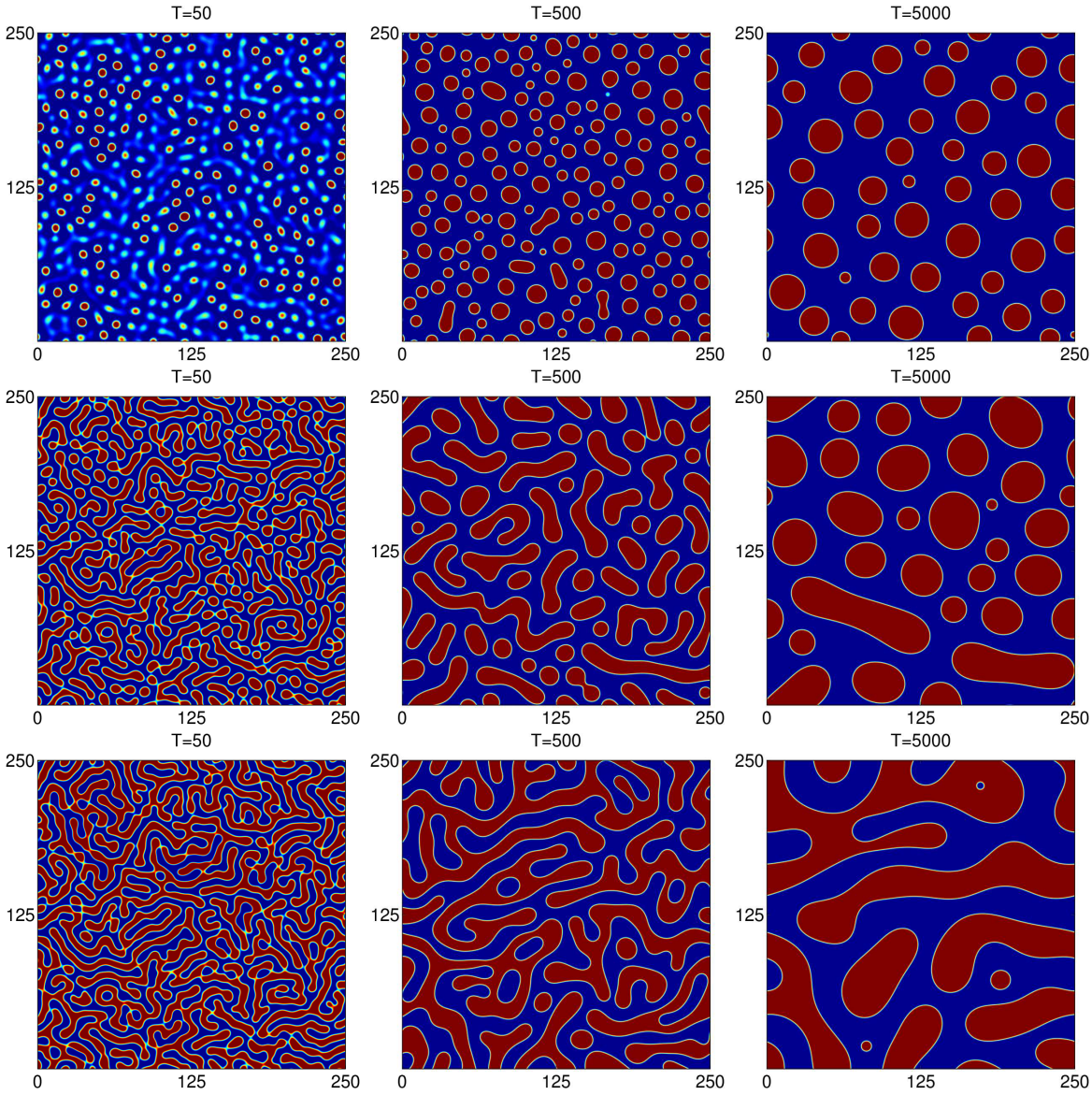

Fig. 1.8: Solutions of the Cahn-Hilliard equation on a periodic domain, as obtained from direct numerical simulation. Red means $\rho = 1$, blue means $\rho = -1$. The initial conditions were randomly perturbed homogeneous solutions. In the first row $\hat{\rho} = -0.4$, in the second row $\hat{\rho} = -0.1$, and in the third row $\hat{\rho} = 0$. In each row, time increases from left to right. The coarsening of the structures towards higher average wavelength can be clearly seen. Comparing the pictures of each column, one can see the different morphologies of the resulting patterns, going from circular domains to labyrinthine patterns as $\hat{\rho} \to 0$. Apart from $\hat{\rho}$ the same parameters as in the simulation shown in fig. 1.7 are used.

with the free energy density $f(\vec{x})$ given by

$$f(\vec{x}) = \frac{\varkappa}{2} \left(\nabla\gamma\left(\vec{x}\right)\right)^2 + f_{\text{hom}}(\gamma(\vec{x})). \tag{1.13}$$

The surfactant equation of state is now obtained by generalizing relation (1.5) to the case of spatially varying densities, yielding

$$p_{\text{lat}}\left(\vec{x}\right) = -f\left(\vec{x}\right) + \gamma\left(\vec{x}\right)\mu\left(\vec{x}\right),$$

where the chemical potential of the monolayer can be calculated by functional derivation of the free energy $\mathscr{F}$ with respect to the surfactant density γ:

$$\mu\left(\vec{x}\right) = \frac{\delta\mathscr{F}}{\delta\gamma\left(\vec{x}\right)} = -\varkappa\Delta\gamma\left(\vec{x}\right) + \left.\frac{\partial f_{\text{hom}}}{\partial\gamma}\right|_{\gamma(\vec{x})}. \tag{1.14}$$

In order to make further calculations, we have to supply an explicit formula for the free energy density of the homogeneous system f_{hom}. In the spirit of Landau's theory (see §152 of [LL87]), we approximate the free energy of the monolayer in vicinity of the main transition by a fourth-order polynomial centered around the critical density γ_{cr}:

$$f_{\text{hom}}(\gamma) = \sum_{k=0}^{4} f_k(\gamma-\gamma_{\text{cr}})^k + \mathscr{O}\left(\left(\gamma-\gamma_{\text{cr}}\right)^5\right). \tag{1.15}$$

The coefficients f_k have to be chosen in a such a way that $f_{\text{hom}}(\gamma)$ has two local minima at temperatures below the critical point, corresponding to the pure LE and the pure LC phase. For the sake of simplicity, we assume the function f_{hom} to be symmetric with respect to $\gamma = \gamma_{\text{cr}}$, so that $f_1 = f_3 = 0$, $f_2 < 0$, and $f_4 > 0$. It has to be emphasized that this assumption is no real limitation, since, around the coexistence plateau, a wide range of experimentally obtained pressure-area isotherms can be fitted reasonably well under the assumption of a symmetric f_{hom}.

It is then convenient, to write the equation of state completely in terms of $\tilde{\gamma} := \gamma - \gamma_{\text{cr}}$, yielding

$$p_{\text{lat}}(\tilde{\gamma}) = -\varkappa\left((\nabla\tilde{\gamma})^2 + \left(\tilde{\gamma}+\gamma_{\text{cr}}\right)\Delta\tilde{\gamma}\right) - f_0 + f_2\left(2\gamma_{\text{cr}}-1\right)\tilde{\gamma} + 2f_2\tilde{\gamma}^2 + 4f_4\gamma_{\text{cr}}\tilde{\gamma}^3 + \mathscr{O}\left(\tilde{\gamma}^4\right). \tag{1.16}$$

To better understand the relation between the free energy density and the lateral pressure, one can consider the simple case of homogeneous monolayers, that is, $\tilde{\gamma} = \text{const}$. For a symmetric double-well potential f_{hom}, as is shown in fig. 1.9 (a), eq. (1.16) then yields a homogeneous lateral pressure of the shape shown in fig. 1.9 (b). In general, one has to apply Maxwell's construction to obtain the horizontal part of the isothermal curve within the binodal region, in order to obtain a valid description of equilibrium states with phase coexistence, as was described in section 1.3.1.

Summarizing the above derivation, one can say that we model the monolayer as a two-dimensional real gas similar to the van-der-Waals gas. One could now ask the question, whether it is really necessary to involve the free energy of the system, because alternatively one could simply start with an equation of state suitable to describe a first-order phase transition and adjust its coefficients so that the resultant pressure would fit the experimental isotherms in the vicinity of the main transition. Actually, this would be a perfectly equivalent approach if we were only interested in the lateral pressure. But the dynamical model, which will be derived in the next chapter, also has to describe diffusion of the surfactant molecules across the water surface. The detour via the free energy then allows to formulate the corresponding diffusive flux in a way which is thermodynamically consistent with the lateral pressure.

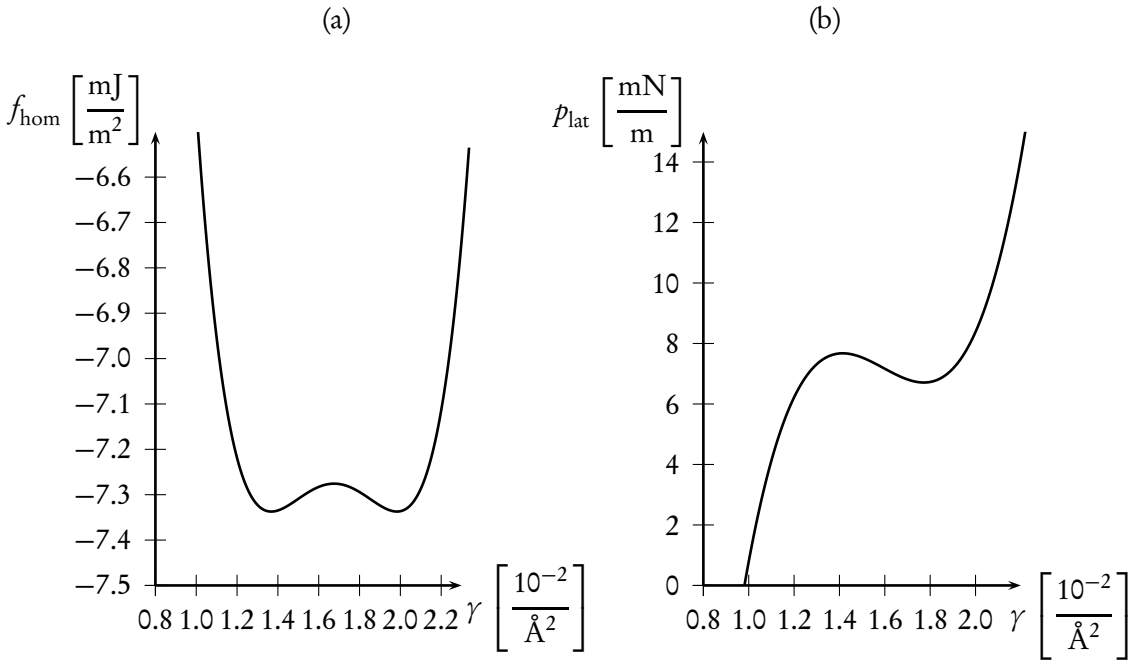

Fig. 1.9: (a) The free energy density given by eq. (1.15) and (b) the resulting lateral pressure of a homogeneous system with $\gamma = \text{const.}$ according to eq. (1.16) for $f_0 = -7.275^{-3}\,\text{J/m}^2$, $f_2 = -1.30 \times 10^{-39}\,\text{Jm}^2$, $f_4 = 6.85 \times 10^{-75}\,\text{Jm}^6$.

1.6 Substrate-mediated condensation

As has been mentioned in the introduction of this thesis, the stripe patterns obtained in Langmuir-Blodgett transfer experiments consist of alternating domains of the LE and the LC phases. It is therefore particularly remarkable, that these structures result from transfer of a monolayer which is prepared in the pure LE phase on the water surface in the Langmuir trough. This means that the lateral pressure is well below the LE-LC coexistence pressure throughout the whole transfer process (see fig. 1.10 a)). Obviously there has to be some mechanism which induces a partial condensation of the LE layer during the transfer onto the substrate. This effect is known as *substrate-mediated condensation* (SMC) in the literature and is attributed to an interaction between the substrate and the monolayer [RS92, SCR94, SR94, GR98, LBBM98, LBM00]. To be more specific, this interaction lowers the free energy of the LC phase when the monolayer comes closer to the substrate [RS92]. By this mechanism, the LC phase is energetically favored at the substrate and the condensation is facilitated. This is shown schematically in fig. 1.10 b).

The interaction can be modelled using an interaction field s whose force depends on the distance between substrate and monolayer, which in our case is just given by the thickness h of the water film in between. This field is introduced into the surfactant thermodynamics as an external field, that is, an additional contribution of order $\tilde{\gamma}$ to the free energy density f_{hom}, so that equation (1.15) is replaced by

$$f_{\text{hom}}(\tilde{\gamma}) = \sum_k f_i \tilde{\gamma}^k + s(h)\tilde{\gamma}. \tag{1.17}$$

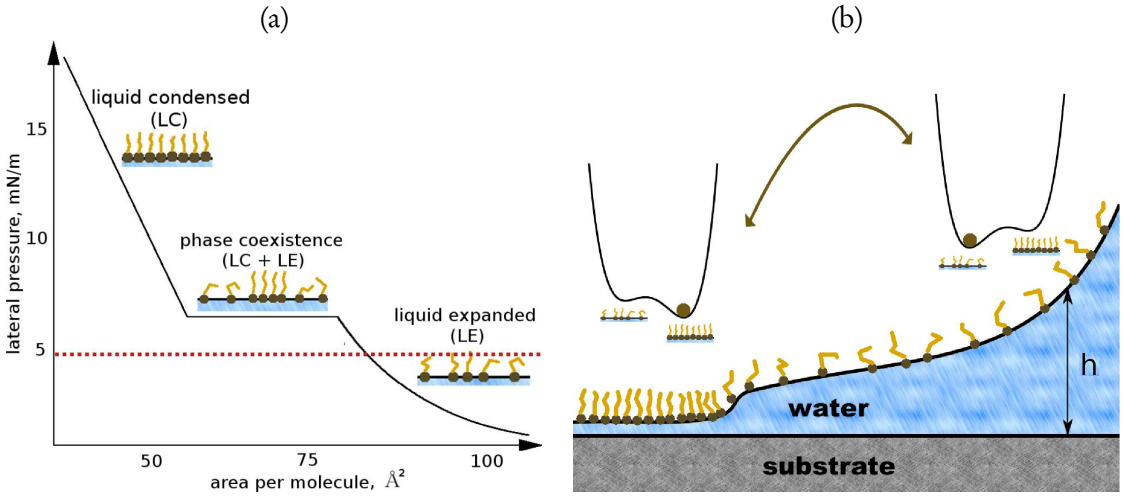

Fig. 1.10: A schematic representation of the theoretical understanding of substrate-mediated condensation (SMC). Phase-coexistence in form of alternating LE-LC-stripes is observed on the substrate after LB transfer of a purely pure LE monolayer. The red dashed line in subfigure (a) shows the transfer pressure. The condensation is facilitated by an interaction field between substrate and monolayer whose strength depends on the distance h. Close to the substrate, for small values of h, the interaction causes a tilt of the free energy toward the minimum corresponding to the LC phase as is shown in subfigure (b).

For small values of h, when the monolayer is close to the surface, the external field yields a tilt of the free energy towards its higher density minimum, that corresponds to the pure LC phase. Accordingly, the system favors the LC state energetically in the vicinity of the substrate, thereby facilitating the condensation of the monolayer.

Although SMC has been discovered almost two decades ago and its existence is experimentally well established, little is known about the nature of the responsible interaction. This means in particular, that the functional form of $s(h)$, that is, the exact dependence of the interaction strength on the distance between substrate and monolayer, is not known. Nevertheless, it has been possible to estimate at least its overall strength by measuring the pressure difference Δp_{lat} between the coexistence pressures of a monolayer floating in the trough and at the substrate. It turned out that the coexistence pressure is lowered by roughly 40 % due to SMC [SR94]. However, many details of the interaction are still unknown and remain to be investigated either by further experiments or by a microscopic theory. One can nevertheless impose a set of minimal constraints on the function $s(h)$. Since SMC facilitates condensation at the substrate, it necessarily approaches a finite negative value for vanishing h. In addition, s must quickly approach zero for increasing film height h, since SMC is never observed to occur on water films more than a few nanometers thick. By these conditions, we can at least limit the choice of $s(h)$ to a certain class of functions. Of course, for any numerical calculation, one has to provide an explicit expression for the height dependence. In this thesis, we will always assume that SMC acts on the same lengthscale as the substrate-water interaction. This means that we choose

$$s(h) = b\,\psi(h) \tag{1.18}$$

where ψ is the potential of the disjoining pressure characterizing the substrate-water interaction as will be explained in detail in the next chapter.

1.7 Pressure tensor of a non-homogeneous system

The derivation of the lateral pressure of an inhomogeneous monolayer that was outlined in the preceding section is still incomplete. In case of spatially varying density, the pressure enters the dynamics in form of a pressure *tensor* $\underline{p}^{(\mathrm{inhom})}(\vec{x})$, whose components are given by [DS82, Eva79]

$$p_{ij}^{(\mathrm{inhom})}(\vec{x}) = p_{\mathrm{lat}}(\vec{x})\delta_{ij} + \varkappa(\partial_i\gamma(\vec{x}))(\partial_j\gamma(\vec{x})).$$

The final equations of our model, that will be derived in the next chapter, will involve a term of the form $\nabla\cdot\underline{p}^{(\mathrm{inhom})}$. Then it will come in handy to know that

$$\nabla\cdot\underline{p}^{(\mathrm{inhom})} = \nabla\left[p_{\mathrm{lat}} - \varkappa(\nabla\gamma)^2\right], \tag{1.19}$$

as can be proved by the following short calculation:

$$
\begin{aligned}
&\left[\nabla\cdot\left(p_{\mathrm{lat}}\underline{\boldsymbol{I}}-\varkappa(\nabla\gamma)\otimes(\nabla\gamma)\right)\right]_i\\
&=\partial_i p_{\mathrm{hom}}+\varkappa\partial_j\left\{\left(\frac{1}{2}\gamma_{,k}\gamma_{,k}+\gamma\gamma_{,kk}\right)\delta_{ij}-\gamma_{,i}\gamma_{,j}\right\}\\
&=\partial_i p_{\mathrm{hom}}+\varkappa\left\{\gamma_{,k}\gamma_{,ik}+\gamma_{,i}\gamma_{,kk}+\gamma\gamma_{,ikk}-\gamma_{,ij}\gamma_{,j}-\gamma_{,i}\gamma_{,jj}\right\}\\
&\Big|\ \text{rename summation indices}\ j\leftrightarrow k\\
&=\partial_i p_{\mathrm{hom}}+\varkappa\gamma\gamma_{,ikk}\\
&=\left[\nabla p_{\mathrm{hom}}+\varkappa\gamma\nabla\Delta\gamma\right]_i.
\end{aligned}
$$

We see that this expression is equal to

$$
\begin{aligned}
\nabla\left[p_{\mathrm{lat}}-\varkappa(\nabla\gamma)^2\right]=&\nabla p_{\mathrm{hom}}+\varkappa\nabla\left[\frac{\varkappa}{2}(\nabla\gamma)^2+\gamma\Delta\gamma\right]-2\varkappa(\nabla\gamma)\Delta\gamma\\
=&\nabla p_{\mathrm{hom}}+\varkappa\gamma\nabla\Delta\gamma.
\end{aligned}
$$

proving our assertion. By virtue of relation (1.19), it will be possible to write the dynamical model using a *scalar* expression for the lateral pressure.

2 Derivation of the model equations

During a Langmuir-Blodgett transfer, a solid substrate is withdrawn from water. It is therefore necessary to consider how the substrate and the water interact. Therefore, this chapter begins with a section on wetting and contact lines to introduce the basic problem and terminology. In order to describe the dynamics of thin liquid films covered with monolayers of insoluble surfactants, one has to relate the flow of liquid with a free surface to another flow which occurs *within* that surface. Section 2.2 is devoted to a description of the surface geometry in very general terms. The chapter continues with the formulation of a continuity equation for insoluble surfactants confined to the curved two-dimensional liquid-vapor interface. Then, the boundary conditions at the interface, that are responsible for the coupling of the film flow and the monolayer, are derived. The films we are interested in are very thin and therefore amenable to the lubrication approximation, an approximation of the basic equations of fluid flow, the Navier-Stokes equations, for thin-film problems. This approximation has a long history and has first been applied by Reynolds (see [Rey86], especially section IV, therein). The term "lubrication approximation" stems from the fact that although it is nowadays successfully applied to describe thin liquid films with free surfaces [ODB97, CM09], it was originally meant to model liquids in a narrow space between two plates.

2.1 Wetting of substrates and the contact line problem

The mathematical description of the physics at the meniscus is intricate, because it involves phenomena close to the three-phase contact line, the line where substrate, water, and vapor meet. From the viewpoint of hydrodynamics, the contact line is problematic, because it marks the limit of the applicability of the continuum approach.

Contact lines occur whenever a substrate is partially wet, that is, whenever the substrate is not entirely covered with liquid. The simplest example from everyday life would be the rim of a raindrop on a window. The evolution of such a partial wet state depends on the properties of the involved liquid, solid, and gaseous phases. It will either spread or contract until the surfaces of the drop and the substrate meet under a particular angle, the equilibrium contact angle θ. The

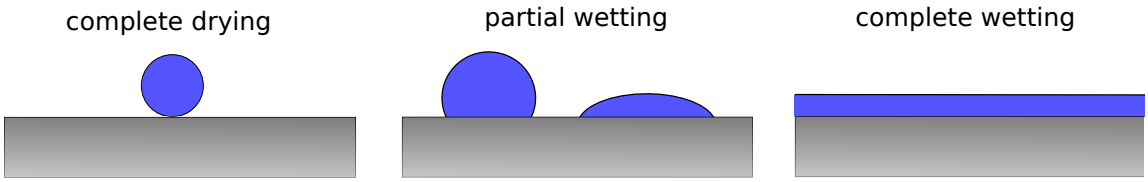

Fig. 2.1: It depends on the interfacial energies of the liquid-gas, the solid-liquid, and the solid-gas interface whether a substrate remains dry, or becomes partially or even completely wet, when brought into contact with a liquid.

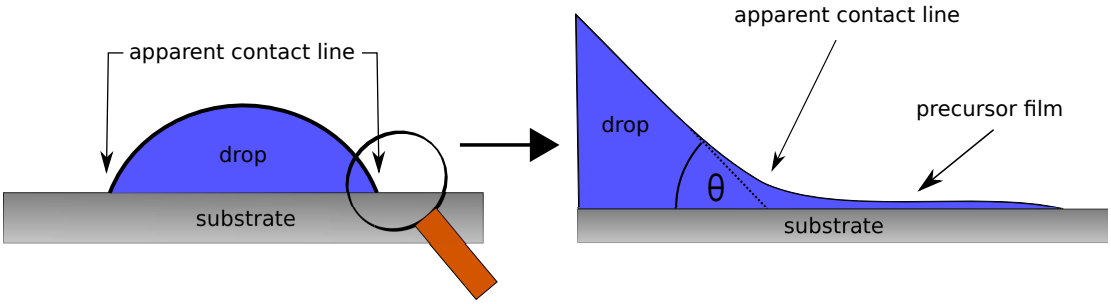

Fig. 2.2: The apparent contact line of a drop on a solid substrate. The bulk is surrounded by a microscopic precursor film.

contact angle is determined by the classical *Young-Laplace law* [You05], a relation between the interfacial energies of the gas-solid, solid-liquid, and liquid-gas interfaces, denoted by σ_{gs}, σ_{sl}, and σ_{lg}, respectively:

$$\cos\theta = \frac{\sigma_{gs} - \sigma_{sl}}{\sigma_{lg}}.$$

By definition of the *spreading coefficient* $S = \sigma_{gs} - \sigma_{lg} - \sigma_{sl}$, the Young-Laplace law can also be written as

$$S = \sigma_{lg}(\cos\theta - 1).$$

There are two extremes: $S = 0 \Leftrightarrow \theta = 0$ and $S = -2\sigma_{lg} \Leftrightarrow \theta = \pi$. In the first case, referred to as *complete wetting*, a drop on the substrate spreads out and flattens until it becomes a horizontal layer. In the second case, a drop simply rolls of the substrate, resulting in a completely dry state. All other situations, where $-2 \leq S \leq 0$, are referred to as *partial wetting*. If the involved liquid is water, the substrate is called hydrophilic if $S > -1 \Leftrightarrow \theta < \pi/2$ and hydrophobic if $S < -1 \Leftrightarrow \theta > \pi/2$. Note, that the Young-Laplace law assumes the substrate to be completely homogeneous, both chemically and topographically. This is of course an idealization, as real substrates usually exhibit some degree of roughness and random chemical inhomogeneity. The Young-Laplace law can be modified, in order to describe such phenomena (see, for example, [Cas48] or section 17.5 of [Isr11]). However, such generalizations are beyond the scope of the present thesis.

Although spreading and even sliding drops are commonly observed, they are difficult to describe mathematically. It has been shown by Huh and Scriven [HS71] that calculations using the no-slip boundary condition at solid surfaces, lead to a logarithmic divergence of energy dissipation at the three-phase contact line, making it impossible, to model a sliding droplet or similar systems with *moving* contact lines. In the literature, there are two common ways to encounter this contact line singularity. Either, one abandons the no-slip condition by introduction of a finite slip-length or one keeps the no-slip condition but assumes an ambient precursor film, covering the whole solid surface with a microscopic layer of liquid. In this thesis, we follow the latter approach, though it has to be stressed, that both lead to equivalent results [SH96].

The precursor film is not a mere mathematical trick but physical reality. Depending on the properties of the liquid and the substrate, the structure of this film can, however, vary greatly. In the case of complete wetting it has been discovered more than ninety years ago [Har19] that when a drop is brought to a dry substrate, a precursor spreads before the drop itself begins to flatten

out, as is illustrated in fig. 2.2. Thus, the apparent contact line actually moves on a prewetted substrate, covered with a precursor of typically 10 nm thickness. More details on the properties of the precursor film can be found in the reviews by de Gennes [dG85] and by Bonn et al. [BEI+09]. Even in the case of partial wetting, the substrate is covered by a precursor film, although this film is for most substrate-liquid pairs actually a submonolayer, that is, its average thickness is below the size of a single liquid molecule [BEI+09]. Nevertheless, treating this precursor film as a very thin layer of continuous liquid has proven to give remarkably good results and it has therefore become the standard approach in the literature [ODB97], [CM09].

Of course, the existence of the precursor does not remove the conceptual problem of the contact line singularity which is simply shifted to another location, that is, "the real contact line" (page 853 of [dG85]) at the rim of the precursor. However, it does no longer affect fluid dynamics close to the meniscus, which can be described by continuous hydrodynamics. Within this description, the wetting properties of the substrate enter the theory in form of an excess pressure, the *disjoining pressure* π, that alters the boundary conditions at the air-water interface. The disjoining pressure was experimentally discovered by Derjaguin and coworkers in the thirties of the twentieth century (see [Der01] and references therein). Although it is clear, that π depends on the thickness of the liquid film, several possible forms of this dependence are discussed in the literature (see [ODB97] for an overview). The most common choices are of the form

$$\pi(h) = \frac{a_3}{h^3} - \frac{a_n}{h^n} \tag{2.1}$$

with $n \in \mathbb{N}$, $n > 3$ and $a_3, a_n > 0$. The term $\sim h^{-3}$ originates from the van-der-Waals forces acting between the surfaces of the substrate and the liquid-vapor interface of the film (see chapter 13 of [Isr11]) and describes, in the case of eq. (2.1), a longrange attraction. The constant a_3 is related to the Hamaker constant A [Ham37], which is commonly used to quantify van-der-Waals interactions, by $a_3 = -A/(6\pi)$. The term h^{-n} describes a shortrange repulsive interaction. Due to this interaction, the substrate does not dry to $h = 0$ but is always covered with a precursor film whose height h_p is determined by the equation $\pi(h_p) = 0$. Thus, eq. (2.1) describes a partial wetting substrate with a precursor of height h_p. The value of n could not be determined by experiments, so far [PE08]. In the present thesis, the choices $n = 6$ [Pis01, PE08, Pis10] and $n = 9$ [MP94, Bes06] are considered.

2.2 Surface geometry

Considering physics at a sharp fluid interface, we need to take the geometry of the surface into account. For example, as will be clarified in the next section, a pressure difference between two fluid phases, say water and air, is directly related to the curvature of the interface via the Laplace condition. Furthermore, due to the presence of an inhomogeneous surfactant monolayer, spatially varying surface tension induces Marangoni forces acting tangentially to the interface. This necessitates the definition of concepts like gradients along a surface as well as fields defined *on* the two-dimensional manifold that is the interface. The textbook by Aris [Ari89] covers these geometrical aspects of interfaces in fluid flow. The following definitions and derivations up to eq. (2.7) are based on his book.

First of all, an intrinsic coordinate system of the surface has to be introduced. We denote its axes with w^α, using Greek indices $\alpha, \beta, \gamma, \dots \in \{1, 2\}$ to numerate the two directions of the surface

2-manifold. Introducing the metric tensor $\underline{\boldsymbol{a}}$ of the surface, we can link the coordinates w^α to the three-dimensional coordinate system of the surrounding space via

$$\alpha_{\alpha\beta} = g_{ij} \frac{\partial x^i}{\partial w^\alpha} \frac{\partial x^j}{\partial w^\beta}.$$

In this context, we shall use the coordinate x^i with Latin indices $i, j, k, \cdots \in \{1,2,3\}$ to denote the three directions of the surrounding space. In the following calculations, we will extensively use both two- and three-dimensional vectors. To avoid confusion, we will write a 3-vector with components a^i as $\vec{\boldsymbol{a}}^{(3)}$ while the symbol $\vec{\boldsymbol{b}}$ without superscript refers to a 2-vector with components b^α. The same convention will be used for the differential operators $\nabla = (\partial_x, \partial_y)$, $\nabla^{(3)} = (\partial_x, \partial_y, \partial_z)$, $\Delta = \nabla^2 = \partial_x^2 + \partial_y^2$, and $\Delta^{(3)} = (\nabla^{(3)})^2 = \partial_x^2 + \partial_y^2 + \partial_z^2$.

For a Cartesian coordinate system x^i the metric tensor is given by $g_{ij} = \delta_{ij}$, yielding the simplified expression

$$a_{\alpha\beta} = \frac{\partial x^i}{\partial w^\alpha} \frac{\partial x^i}{\partial w^\beta}.$$

Once the metric tensor of the 2-manifold is introduced, we are in a position to define a "derivative along the surface" in a mathematically rigorous way: the covariant derivative of a 2-vector q^α with respect to the surface coordinate w^β is denoted by a semicolon and given by

$$q^\alpha_{;\beta} = \frac{\partial q^\alpha}{\partial w^\beta} + \Gamma^\alpha{}_{\beta\gamma} q^\gamma.$$

The Christoffel symbols $\Gamma^\alpha{}_{\beta\gamma}$ in this formula describe the affine connection of the 2-manifold. They are completely defined by the metric tensor $a_{\alpha\beta}$ via the relation

$$\Gamma^\alpha{}_{\beta\gamma} = \frac{1}{2} a^{\alpha\delta} \left(a_{\gamma\delta,\beta} + a_{\beta\delta,\gamma} - a_{\beta\gamma,\delta} \right),$$

where $a^{\alpha\beta}$ are the components of $\underline{\boldsymbol{a}}^{-1}$, the inverse of the metric tensor. Here and in the remainder of this thesis, the shorthand notation $a_{,b} := \partial a / \partial b$ is frequently used in order to enhance the readability. Note, that the covariant derivative of a scalar function is identical to the usual partial derivative. Of course, any 2-vector in the surface has a corresponding 3-vector in the surrounding space. They can be linked by the hybrid tensor

$$t^i_\alpha = \frac{\partial x^i}{\partial w^\alpha},$$

so that we can find the space vector A^i to any surface vector A^α by

$$A^i = t^i_\alpha A^\alpha.$$

Moreover, keeping the index α fixed, the t^i_α are the components of the 3-vectors $\vec{\boldsymbol{t}}_1^{(3)}$ and $\vec{\boldsymbol{t}}_2^{(3)}$ which are tangent to the surface and form a local basis. Normalizing these vectors, we find the

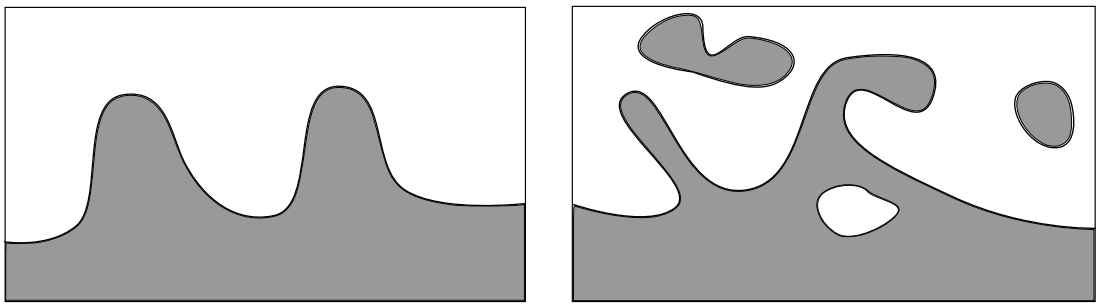

Fig. 2.3: Two systems with interfaces dividing two different media. In the left system, the interface can be well described as a function of the horizontal coordinate. If the interface has overhangs and if bubbles of one medium within the other are present, like in the right system, such a function cannot be defined and a more complicated mathematical description is needed.

unit tangent vectors $\hat{\vec{t}}_{\alpha}^{(3)}$. The unit vector normal to the surface $\hat{\vec{n}}^{(3)}$ can then be readily calculated from their cross product.

The most relevant case for the problem considered in this thesis is that of a surface which can be described as a height profile or height map in the form

$$x^3 = h\left(x^1, x^2\right).$$

Physically speaking, this means that we consider neither bubbles nor overhangs (see figure 2.3). Then, it is possible to identify the coordinates x^1, x^2 with the intrinsic coordinates of the surface w^1, w^2. One can then readily calculate the tangent vectors, the normal vector, the components of the metric tensor $\underline{\boldsymbol{a}}$ and the Christoffel symbols $\Gamma^{\alpha}{}_{\beta\gamma}$. For all explicit calculations, we use the notation $x^1 = w^1 =: x, x^2 = w^2 =: y$ and $x^3 =: z$. We find

$$\hat{\vec{t}}_x^{(3)} = \frac{1}{\sqrt{1+h_{,x}^2}} \begin{pmatrix} 1 \\ 0 \\ h_{,x} \end{pmatrix}, \qquad \hat{\vec{t}}_y^{(3)} = \frac{1}{\sqrt{1+h_{,y}^2}} \begin{pmatrix} 0 \\ 1 \\ h_{,y} \end{pmatrix}, \tag{2.2}$$

$$\hat{\vec{n}}^{(3)} = \frac{1}{\sqrt{1+h_{,x}^2+h_{,y}^2}} \begin{pmatrix} -h_{,x} \\ -h_{,y} \\ 1 \end{pmatrix}, \tag{2.3}$$

$$a_{xx} = 1+h_{,x}^2, \qquad a_{xy} = a_{yx} = h_{,x}h_{,y}, \qquad a_{yy} = 1+h_{,y}^2,$$
$$a = \det \underline{\boldsymbol{a}} = 1+h_{,x}^2+h_{,y}^2, \tag{2.4}$$

$$a^{xx} = \frac{1+h_{,y}^2}{a}, \qquad a^{xy} = a^{yx} = \frac{-h_{,x}h_{,y}}{a}, \qquad a^{yy} = \frac{1+h_{,x}^2}{a}. \tag{2.5}$$

From this, we can conclude the following form of the Christoffel symbols:

$$\Gamma^{\alpha}{}_{\beta\gamma} = \frac{h_{,\alpha\beta}h_{,\gamma}}{a} = \frac{h_{,\alpha\beta}h_{,\gamma}}{1+h_{,x}^2+h_{,y}^2}.$$

We can furthermore introduce the flow velocity of the liquid subphase at the surface as the 2-vector $\tilde{u}^{\alpha} = \mathrm{d}x^{\alpha}/\mathrm{d}t$. It is related to the three-dimensional flow velocity field u^i by

$$u^i(x,y,h(x,y)) = t^i_{\alpha}\tilde{u}^{\alpha}(x,y) + \frac{\partial x^i}{\partial t} \Leftrightarrow \vec{u}^{(3)}(x,y,h(x,y)) = \begin{pmatrix} \tilde{u}^x \\ \tilde{u}^y \\ \tilde{u}^x h_{,x} + \tilde{u}^y h_{,y} + h_{,t} \end{pmatrix}. \tag{2.6}$$

In the z-component of $\vec{u}^{(3)}$, we recognize $\mathrm{d}h/\mathrm{d}t$, so that eq. (2.6) is consistent with the definition $\vec{u}^{(3)} = \mathrm{d}\vec{x}^{(3)}/\mathrm{d}t$.

2.3 The continuity equation for insoluble surfactants

Since the considered monolayer consists of insoluble surfactant molecules, it can be described by a number density function γ defined only on the water surface. Moreover, there is no mass flux resulting from molecules which come from the bulk phases and adsorb at the surface, so that the surface is isolated from its surroundings. Due to the principle of mass conservation, we note

$$\frac{\mathrm{d}}{\mathrm{d}t}\int_{S(t)} \mathrm{d}S\,\gamma = \frac{\mathrm{d}}{\mathrm{d}t}\int_{S(t)} \mathrm{d}x\mathrm{d}y\,\sqrt{a}\,\gamma = 0.$$

Since the surface is evolving with time, the integration domain itself is a function of t so that differentiation and integration do not commute in this case. However, we can take the derivative through the integral sign if we adhere to *Reynolds' transport theorem*: Assume that we know the coordinates $\vec{w}_0$ of the surface at some fixed point in time t_0. Then we can view the coordinates at later times as the result of a transformation $\vec{w} = \vec{w}(\vec{w}_0, t)$. This means, that we can substitute the infinitesimal surface area $\mathrm{d}S = \sqrt{a(t)}\,\mathrm{d}w^1(t)\mathrm{d}w^2(t)$ at time t by $\mathrm{d}S_0 = \sqrt{a(t)}\,J(t)\mathrm{d}w_0^1\mathrm{d}w_0^2$, where $J(t)$ denotes the determinant of the Jacobi matrix $J_{ij}(t) = \partial w^i(t)/\partial w_0^j$. After the substitution, the domain of integration is the static surface S_0, so that the derivative $\mathrm{d}/\mathrm{d}t$ can readily be applied to the integrand:

$$\frac{\mathrm{d}}{\mathrm{d}t}\int\int_{S(t)} \mathrm{d}S\,\gamma(\vec{w}) = \int\int_{S_0} \mathrm{d}w_0^1\mathrm{d}w_0^2\,\frac{\mathrm{d}}{\mathrm{d}t}\left[J(t)\sqrt{a(t)}\,\gamma(\vec{w}(\vec{w}_0,t))\right].$$

The time evolution of J can be written in the form

$$\frac{\mathrm{d}J}{\mathrm{d}t} = \left(\nabla\cdot\vec{\tilde{u}}\right)J.$$

Thus, we can write

$$\begin{aligned}\frac{\mathrm{d}}{\mathrm{d}t}\int\!\!\int_{S(t)} \mathrm{d}S\,\gamma &= \int\!\!\int_{S_0} \mathrm{d}w_0^1 \mathrm{d}w_0^2 \left[J\sqrt{a}\left(\nabla\cdot\vec{\tilde{\boldsymbol{u}}}\right)\gamma + J\sqrt{a}\,\frac{\dot{a}}{2a}\gamma + J\sqrt{a}\,\gamma_{,t}\right] \\ &= \int\!\!\int_{S_0} \mathrm{d}w_0^1 \mathrm{d}w_0^2 J\sqrt{a}\left[\left(\nabla\cdot\vec{\tilde{\boldsymbol{u}}}\right)\gamma + \frac{\dot{a}}{2a}\gamma + \gamma_{,t}\right] \\ &= \int\!\!\int_{S(t)} \mathrm{d}S\left[\left(\nabla\cdot\vec{\tilde{\boldsymbol{u}}}\right)\gamma + \frac{\dot{a}}{2a}\gamma + \gamma_{,t}\right].\end{aligned}$$

Mass conservation demands that this integral vanishes for any surface $S(t)$, leading us to the continuity equation of an insoluble surfactant density [Scr60] (see also chapter 10.31 of [Ari89]):

$$\gamma_{,t} + \left(\gamma\tilde{u}^{\beta}\right)_{;\beta} + \frac{\gamma\dot{a}}{2a} = 0. \tag{2.7}$$

The presence of the term $\sim \dot{a}$ is characteristic for evolving surfaces. It can be interpreted as a source or sink of surface area due to deformation of the surface. Equation (2.7) can be generalized to take diffusion of the surfactant molecules into account. To this end, it has to be supplemented by an additional mass flux $\vec{\boldsymbol{i}}$, yielding

$$\gamma_{,t} + \left(\gamma\tilde{u}^{\beta}\right)_{;\beta} + \frac{\gamma\dot{a}}{2a} = -i^{\beta}_{;\beta}. \tag{2.8}$$

Assuming our system to be isothermal, the flux $\vec{\boldsymbol{i}}$ can be written as (see [LL91], § 59)

$$\vec{\boldsymbol{i}} = -\alpha\nabla\mu, \tag{2.9}$$

where μ is the chemical potential of the diffusing material. The first covariant derivative on the left hand side of eq. (2.8) can be calculated to

$$\begin{aligned}\left(\gamma\tilde{u}^{\beta}\right)_{;\beta} &= \left(\gamma\tilde{u}^{\beta}\right)_{,\beta} + \gamma\left[\left(\Gamma^{x}{}_{xx} + \Gamma^{y}{}_{yx}\right)\tilde{u}^{x} + \left(\Gamma^{x}{}_{xy} + \Gamma^{y}{}_{yy}\right)\tilde{u}^{y}\right] \\ &= \gamma_{,\beta}\tilde{u}^{\beta} + \gamma\tilde{u}^{\beta}_{,\beta} + \frac{\gamma}{a}\tilde{u}^{\beta}h_{,\beta}\left(h_{,xx} + h_{,yy}\right) \\ &= (\nabla\gamma)\cdot\vec{\tilde{\boldsymbol{u}}} + \gamma\nabla\cdot\vec{\tilde{\boldsymbol{u}}} + \frac{\gamma}{a}\left(\vec{\tilde{\boldsymbol{u}}}\cdot\nabla h\right)\Delta h.\end{aligned} \tag{2.10}$$

The area source term of the metric tensor is given by

$$\frac{\dot{a}}{2a} = \frac{h_{,x}h_{,xt} + h_{,y}h_{,yt}}{a}. \tag{2.11}$$

We can eliminate the partial time derivatives $h_{,xt}$ and $h_{,yt}$ in favor of the flow field u. Taking the x- and the y-derivative of the z-component of $\vec{\boldsymbol{u}}^{(3)}$ defined in eq. (2.6), we obtain

$$\begin{cases} u^z_{,x} = u^x_{,x} h_{,x} + u^x h_{,xx} + u^y_{,x} h_y + u^y h_{,xy} + h_{,xt} \\ u^z_{,y} = u^x_{,y} h_{,x} + u^x h_{,xy} + u^y_{,y} h_y + u^y h_{,yy} + h_{,yt} \end{cases},$$

$$\Rightarrow \begin{cases} h_{,xt} = u^z_{,x} - u^x_{,x} h_{,x} - u^x h_{,xx} - u^y_{,x} h_y - u^y h_{,xy} \\ h_{,yt} = u^z_{,y} - u^x_{,y} h_{,x} - u^x h_{,xy} - u^y_{,y} h_y - u^y h_{,yy} \end{cases}.$$

Replacing the time derivatives in eq. (2.11) by this result and combining it with eq. (2.10), we can recast the continuity equation (2.7) to

$$\gamma_{,t} = -\gamma_{,\beta} \tilde{u}^\beta - \gamma \tilde{u}^\beta_{,\beta} - \frac{\gamma}{a} \Big[(\nabla u^z) \cdot (\nabla h) + u^x h_{,x} h_{,yy} + u^y h_{,y} h_{,xx} - h^2_{,x} u^x_{,x} - h^2_{,y} u^y_{,y} - h_{,x} h_{,y} \left(u^y_{,x} + u^x_{,y} \right) - h_{,xy} \left(h_{,y} u^x + h_{,x} u^y \right) \Big] - i^\beta_{;\beta}. \tag{2.12}$$

With eq. (2.12), we have found the theoretical description of a diffusing monolayer at the surface of a flowing liquid. The actual flow field $\vec{\boldsymbol{u}}^{(3)}$ and the corresponding surface flow $\vec{\tilde{\boldsymbol{u}}}$ are calculated in section 2.5 by use of the lubrication approximation.

2.4 Dynamics of a liquid film

2.4.1 Boundary conditions at the air-water interface

A thin liquid-film on a substrate has two surfaces: the substrate-liquid interface and the liquid-vapor interface. As mentioned in the introduction to this chapter, no-slip and no-penetration boundary conditions are employed at the surface of the substrate. The liquid-vapor interface is more complicated, since it is a free surface, changing its shape as dictated by the flow of the liquid.

The amount of energy needed for an arbitrary deformation δS of a surface consists of two contributions. First of all, due to surface tension σ, one has to surmount work in order to change the surface area S according to

$$W_\sigma = \sigma S \rightarrow \delta E_\sigma = \sigma \delta S.$$

Secondly, a dislocation of the surface requires work against the external pressure. For a thick liquid layer, this work W_V is simply equal to the change of volume times the pressure difference between liquid and air. But for layers which are less than a few hundred nanometers thick, interactions between substrate and liquid yield an excess hydrostatic pressure, the disjoining pressure π_d [Der01].

As was explained in section 2.2, we assume that the liquid film can be described by its height profile $h(x,y)$. Therefore, a variation $h(x,y) \rightarrow h(x,y) + \delta h(x,y)$ of the interface amounts to the work

$$\delta W = \delta W_\mathrm{V} + \delta W_\sigma = \iint \mathrm{d}x\mathrm{d}y \left(p_{(\mathrm{liquid})} - p_{(\mathrm{air})} + \pi_\mathrm{d} \right) \delta h(x,y) + \sigma \delta S, \tag{2.13}$$

where $p_{(\text{liquid})}$ and $p_{(\text{air})}$ denote the pressure in the liquid film and in the surrounding air, respectively, while π_d is the disjoining pressure. Considering equilibrium situations, we demand $\delta W = 0$. The variation of the surface area δS can be written in terms of δh as

$$\delta S = \int\int \mathrm{d}x\mathrm{d}y \, \frac{\delta S}{\delta h(\vec{x})} \delta h(\vec{x}).$$

The functional derivative in this equation is evaluated to

$$\begin{aligned}
\frac{\delta S}{\delta h(\vec{x})} &= \frac{\delta}{\delta h(\vec{x})} \int\int \mathrm{d}S = \frac{\delta}{\delta h(\vec{x})} \int\int \mathrm{d}x'\mathrm{d}y' \sqrt{a} \\
&= \int\int \mathrm{d}x'\mathrm{d}y' \, \frac{1}{\sqrt{a}} \left(\nabla h(\vec{x})\right) \nabla \delta \left(\vec{x} - \vec{x}'\right) \\
&= -\nabla \cdot \left(\frac{1}{\sqrt{a}} \nabla h(\vec{x}) \right) = -\partial_i \left(1 + h_{,j}^2\right)^{-1/2} h_{,i} \\
&= \frac{h_{,i} h_{,ij} h_{,j} - (1 + h_{,j}^2) h_{,ii}}{\sqrt{a}^3} \\
&= \underbrace{-\left(\frac{\left(1 + h_{,x}^2\right) h_{,yy} - 2h_{,x} h_{,y} h_{,xy} + \left(1 + h_{,y}^2\right) h_{,xx}}{\left(1 + h_{,x}^2 + h_{,y}^2\right)^{3/2}} \right)}_{=: \varkappa_1 + \varkappa_2}.
\end{aligned} \tag{2.14}$$

The bracket in the last line of this calculation is equal to the sum of the principal curvatures $\varkappa_1$ and $\varkappa_2$, that is, twice the mean curvature, of the surface. Thus, one can write the variation of the surface area as

$$\delta S = -\int\int \mathrm{d}x\mathrm{d}y \, \delta h \, (\varkappa_1 + \varkappa_2).$$

Note, that the sum $\varkappa_1 + \varkappa_2$ is positive if the film is vaulting into the direction of the liquid, that is, for a concave water surface.

We can conclude that the equilibrium condition for the liquid film is given by

$$\int\int \mathrm{d}x\mathrm{d}y \, \left\{ \left(p_{(\text{liquid})} - p_{(\text{air})} + \pi_\text{d} \right) - (\varkappa_1 + \varkappa_2)\sigma \right\} \delta h(x, y) = 0. \tag{2.15}$$

This condition has to be met for arbitrary infinitesimal variations δh. This means, that the integrand of eq. (2.15) has to vanish, resulting in the relation

$$p_{(\text{liquid})} - p_{(\text{air})} = -\pi_\text{d} + \sigma(\varkappa_1 + \varkappa_2)$$

This equation, known as the *Laplace condition*[1], is the fundamental relation of interface physics. It predicts a pressure jump at the sharp air-liquid interface, which is determined by the surface tension, the shape of the surface, and the disjoining pressure. From this result, we can deduce

[1] Usually, the Laplace condition does not take the disjoining pressure π_d into account.

the boundary condition at the surface by noting that the viscous stresses acting upon the surfaces of both liquids have to be equal, while the non-viscous stress is given by the pressure difference between the two fluids:

$$\left(\underline{\tau}_{(\mathrm{air})} - \underline{\tau}_{(\mathrm{liquid})}\right) \hat{\vec{n}}^{(3)} = \pi_{\mathrm{d}} \hat{\vec{n}}^{(3)} - \sigma(\varkappa_1 + \varkappa_2)\hat{\vec{n}}^{(3)},$$

where $\underline{\tau}_{(\mathrm{air})}$ and $\underline{\tau}_{(\mathrm{liquid})}$ denote the stress tensors of air and liquid, respectively. In presence of an additional contact force $\vec{f}^{(3)}$ attacking at the surface, this relation can be generalized by addition of $\vec{f}^{(3)}$ to the right hand side, yielding

$$\left(\underline{\tau}_{(\mathrm{air})} - \underline{\tau}_{(\mathrm{liquid})}\right) \hat{\vec{n}}^{(3)} = \pi_{\mathrm{d}} \hat{\vec{n}}^{(3)} - \sigma(\varkappa_1 + \varkappa_2)\hat{\vec{n}}^{(3)} + \vec{f}^{(3)}. \tag{2.16}$$

So far, we have assumed the surface tension σ to be constant. In presence of surfactants, however, the surface tension will generally vary across the water surface, as has been outlined in the preceding chapter. This yields an additional force tangential to the surface (see §61 of [LL91]). Condition (2.16) thus has to be generalized to

$$\left(\underline{\tau}_{(\mathrm{air})} - \underline{\tau}_{(\mathrm{liquid})}\right) \hat{\vec{n}}^{(3)} = \pi_{\mathrm{d}} \hat{\vec{n}}^{(3)} - \sigma(\varkappa_1 + \varkappa_2)\hat{\vec{n}}^{(3)} + \nabla_S^{(3)}\sigma + \vec{f}^{(3)}, \tag{2.17}$$

where $\nabla_S^{(3)}$ is the 3-vector corresponding to the surface gradient. Its components can be calculated by use of the hybrid tensor t_α^i, but since t_α^i can only be contracted with a contravariant surface vector, we have to use the inverse metric tensor $a^{\alpha\beta}$ first, to raise the index of the covariant gradient ∂_α. Then, the components are given by $(\nabla_S^{(3)})^i = t_\alpha^i a^{\alpha\beta}\partial_\beta$ and can be calculated explicitly with help of the eqs. (2.2) and (2.5):

$$\begin{aligned}
\nabla_S^x &= \frac{\left(1 + h_{,y}^2\right)\partial_X - h_{,x}h_{,y}\partial_Y}{a}, \\
\nabla_S^y &= \frac{-h_{,x}h_{,y}\partial_X + \left(1 + h_{,x}^2\right)\partial_Y}{a}, \\
\nabla_S^z &= \frac{(\nabla h)\cdot\nabla}{a}.
\end{aligned}$$

It is reasonable to assume $\tau_{(\mathrm{air})}^{ij} \ll \tau_{(\mathrm{liquid})}^{ij}$, so that we can neglect $\underline{\tau}_{(\mathrm{air})}$ in the stress balance equation. By multiplication with $\hat{\vec{n}}^{(3)}$, $\hat{\vec{t}}_x^{(3)}$, and $\hat{\vec{t}}_y^{(3)}$, one can project the boundary condition (2.17) onto the normal and tangential directions, to obtain

$$-\hat{\vec{t}}_x^{(3)} \cdot \underline{\tau}_{(\mathrm{liquid})} \hat{\vec{n}}^{(3)} = \frac{\sigma_{,x}}{\sqrt{1 + h_{,x}^2}} + \hat{\vec{t}}_x^{(3)} \cdot \vec{f}^{(3)}, \tag{2.18}$$

$$-\hat{\vec{t}}_y^{(3)} \cdot \underline{\tau}_{(\mathrm{liquid})} \hat{\vec{n}}^{(3)} = \frac{\sigma_{,y}}{\sqrt{1 + h_{,y}^2}} + \hat{\vec{t}}_y^{(3)} \cdot \vec{f}^{(3)}, \tag{2.19}$$

$$-\hat{\vec{n}}^{(3)} \cdot \underline{\tau}_{(\mathrm{liquid})} \hat{\vec{n}}^{(3)} = \pi_{\mathrm{d}} - \sigma(\varkappa_1 + \varkappa_2) + \hat{\vec{n}}^{(3)} \cdot \vec{f}^{(3)}. \tag{2.20}$$

Here, we have used the projections of $\vec{f}^{(3)}_{(\sigma)}$:

$$\begin{aligned}
\hat{\vec{t}}^{(3)}_x \cdot \vec{f}^{(3)}_{(\sigma)} &= \frac{1}{a\sqrt{1+h_{,x}^2}} \left[\left(1+h_{,y}^2\right) \sigma_{,x} - h_{,x} h_{,y} \sigma_{,y} + h_{,x} \sigma_{,x} + h_{,x} h_{,y} \sigma_{,y} \right] \\
&= \frac{\sigma_{,x}}{a\sqrt{1+h_{,x}^2}} \underbrace{\left(1+h_{,x}^2+h_{,y}^2\right)}_{=a} = \frac{\sigma_{,x}}{\sqrt{1+h_{,x}^2}}, \\
\hat{\vec{t}}^{(3)}_y \cdot \vec{f}^{(3)}_{(\sigma)} &= \frac{\sigma_{,y}}{\sqrt{1+h_{,y}^2}}, \\
\hat{\vec{n}}^{(3)} \cdot \vec{f}^{(3)}_{(\sigma)} &= 0.
\end{aligned}$$

For the further derivation, it is useful to express the remaining $\underline{\tau}_{(\text{liquid})}$ in terms of the velocity field and pressure of the liquid. For incompressible fluids like water, one obtains (see §15 of [LL91])

$$\tau^{ij}_{(\text{liquid})} = -p\delta_{ij} + \eta \left(\frac{\partial u^i}{\partial x^j} + \frac{\partial u^j}{\partial x^i} \right),$$

with the dynamic viscosity η. The stress tensor maps the normal vector $\hat{\vec{n}}^{(3)}$ to

$$\tau^{ij}_{(\text{liquid})} \hat{n}_j = -p\hat{n}^i + \eta \left(\frac{\partial u^i}{\partial x^j} \hat{n}_j + \frac{\partial u^j}{\partial x^i} \hat{n}_j \right).$$

Expressing the three scalar products on the left hand sides of the stress balance equations (2.18)–(2.20) in terms of the pressure p and the velocity field $\vec{u}^{(3)}$, we obtain

$$-\eta \left(\frac{\partial u^i}{\partial x^j} \hat{n}_j \hat{t}^i_x + \frac{\partial u^j}{\partial x^i} \hat{n}_j \hat{t}^i_x \right) = \frac{\sigma_{,x}}{\sqrt{1+h_{,x}^2}} + \hat{\vec{t}}^{(3)}_x \cdot \vec{f}^{(3)}, \tag{2.21}$$

$$-\eta \left(\frac{\partial u^i}{\partial x^j} \hat{n}_j \hat{t}^i_y + \frac{\partial u^j}{\partial x^i} \hat{n}_j \hat{t}^i_y \right) = \frac{\sigma_{,y}}{\sqrt{1+h_{,y}^2}} + \hat{\vec{t}}^{(3)}_y \cdot \vec{f}^{(3)}, \tag{2.22}$$

$$p - \eta \left(\frac{\partial u^i}{\partial x^j} \hat{n}_j \hat{n}^i_y + \frac{\partial u^j}{\partial x^i} \hat{n}_j \hat{n}^i_y \right) = \pi_{\text{d}} - \sigma(\varkappa_1 + \varkappa_2) + \hat{\vec{n}}^{(3)} \cdot \vec{f}^{(3)}. \tag{2.23}$$

2.4.2 Evolution equation for the height profile

Since we consider a subphase consisting of water, we employ the Navier-Stokes equations subject to the incompressibility condition for its description:

$$\begin{aligned}
\rho \left(\vec{u}^{(3)} + \vec{u}^{(3)} \cdot \nabla^{(3)} \vec{u}^{(3)} \right) &= -\nabla^{(3)} p + \eta \Delta^{(3)} \vec{u}^{(3)} - \nabla^{(3)} \phi, \\
\nabla^{(3)} \cdot \vec{u}^{(3)} &= 0.
\end{aligned}$$

Note, that we allow for a conservative body force that is described by its potential ϕ. As was explained in the previous section, we impose no-slip and no-penetration boundary conditions at the substrate at $z = 0$ as well as the stress balance equation (2.17) at the water-air interface at $z = h(x,y,t)$:

$$u^x(x,y,0) = -v, \qquad u^y(x,y,0) = u^z(x,y,0) = 0,$$
$$-\underline{\tau}_{(\text{liquid})}\vec{\hat{n}}^{(3)} = \pi_d - \sigma(\varkappa_1 + \varkappa_2)\vec{\hat{n}}^{(3)} + \nabla_S^{(3)}\sigma + \vec{f}^{(3)}.$$

Since the height profile h describes the location of the water surface, it is by definition linked to the flow through the relation

$$u^z(x,y,h(x,y,t)) = \frac{\mathrm{d}h(x,y,t)}{\mathrm{d}t} \Leftrightarrow u^z(x,y,h(x,y,t)) = \frac{\partial h(x,y,t)}{\partial t} + \vec{\tilde{u}} \cdot \nabla h(x,y,t). \tag{2.24}$$

This equation can be seen as an additional boundary condition. Its meaning is clear: the surface moves along with the water flow.

The set of boundary conditions can now be used to derive a differential equation describing the time evolution of the height profile h. Exploiting incompressibility, we write

$$u^z_{,z} = -u^x_{,x} - u^y_{,y}.$$

By integration along the z-axis we find the equation

$$\int_0^{h(x,y,t)} \mathrm{d}z\, u^z_{,z} = -\int_0^{h(x,y,t)} \mathrm{d}z\, \left(u^x_{,x} + u^y_{,y}\right),$$

whose left hand side can be calculated using the no-slip condition at $z = 0$, yielding

$$u^z(x,y,h(x,y,t)) = -\int_0^{h(x,y,t)} \mathrm{d}z\, \left(u^x_{,x} + u^y_{,y}\right).$$

From eq. (2.24) follows

$$h_{,t} + \vec{\tilde{u}} \cdot \nabla h(x,y,t) = -\int_0^{h(x,y,t)} \mathrm{d}z\, \left(u^x_{,x} + u^y_{,y}\right).$$

It is now possible to "pull" the partial derivatives on the right hand side in front of the integral according to

$$\begin{aligned}
\partial_x \int_0^{g(x)} \mathrm{d}y\, f(x,y) &= \partial_x \left(F(x,g(x)) - F(x,0)\right) \\
&= \left.\frac{\partial F(x,y)}{\partial x}\right|_{y=g(x)} + \left.\frac{\partial F(x,y)}{\partial y}\right|_{y=g(x)} \frac{\partial g(x)}{\partial x} - \left.\frac{\partial F(x,y)}{\partial x}\right|_{y=0} \\
&= \int_0^{g(x)} \mathrm{d}y\, f_{,x}(x,y) + \left.\frac{\partial F(x,y)}{\partial y}\right|_{y=g(x)} \frac{\partial g(x)}{\partial x} \\
\Rightarrow \int_0^{g} \mathrm{d}y\, f_{,x}(x,y) &= \partial_x \int_0^{g(x)} \mathrm{d}y\, f(x,y) - \left.\frac{\partial F(x,y)}{\partial y}\right|_{y=g(x)} \frac{\partial g(x)}{\partial x},
\end{aligned}$$

where $F(x,y)$ denotes the primitive of $f(x,y)$ with respect to y. This procedure yields

$$h_{,t} = -\partial_x \int_0^{h(x,y,t)} \mathrm{d}z\, u^x - \partial_y \int_0^{h(x,y,t)} \mathrm{d}z\, u^y = -\nabla \cdot \int_0^{h(x,y,t)} \mathrm{d}z\, \vec{\boldsymbol{u}}, \tag{2.25}$$

the differential equation describing the time evolution of the film profile h. So far, the liquid under consideration is assumed to be nonvolatile. To include evaporation and condensation, sink and source terms have to be added to the conservative eq. (2.25). Details of the theoretical descriptions of evaporation are given later in section 3.1.3. Here, we rewrite eq. (2.25) by addition of a general non-conservative contribution q to

$$h_{,t} = -\partial_x \int_0^{h(x,y,t)} \mathrm{d}z\, u^x - \partial_y \int_0^{h(x,y,t)} \mathrm{d}z\, u^y + q = -\nabla \cdot \int_0^{h(x,y,t)} \mathrm{d}z\, \vec{\boldsymbol{u}} + q. \tag{2.26}$$

However, we still have to solve the Navier-Stokes equations for the flow field $\vec{\boldsymbol{u}}$ in order to obtain any meaningful results from eq. (2.26). Fortunately, it is possible to greatly facilitate this task by use of the lubrication approximation, an approximation of the full Navier-Stokes equations valid for thin liquid films.

2.5 Lubrication approximation

To treat the eqs. (2.26) and (2.12) within the lubrication framework, a "smallness parameter" ϵ is defined by the relation

$$\epsilon = \frac{h_0}{l_0},$$

where h_0 and l_0 are the characteristic height and length scales of the considered system. The condition $\epsilon \ll 1$ gives us a mathematical definition of the notion "thin", which is quite compatible to common sense: a system, where the typical horizontal scales are much larger than the typical vertical scales is considered thin.

The idea behind the lubrication approximation is to expand all quantities in powers of ϵ and to keep only the lowest orders, that is, the terms that dominate the physics in a thin system. To this end, the following dimensionless quantities are introduced:

$$\vec{X} = \frac{\epsilon \vec{x}}{h_0}, \quad Z = \frac{z}{h_0}, \quad T = \frac{t}{t_0}, \quad H = \frac{h}{h_0}, \quad \Gamma = \frac{\gamma}{\gamma_0}, \quad \vec{U} = \frac{t_0}{l_0} \begin{pmatrix} u^x \\ u^y \end{pmatrix}, \quad U^Z = \frac{t_0}{h_0} u^z, \quad P = \frac{t_0 \epsilon^2}{\eta} p,$$

$$\Pi = \frac{t_0 \epsilon^2}{\eta} \pi_\mathrm{d}, \quad \Phi = \frac{t_0 \epsilon^2}{\eta} \phi, \quad \mathrm{Ca} = \frac{l_0 \eta}{t_0 \sigma_0}, \quad \mathrm{Re} = \frac{\rho l_0 h_0}{\eta t_0}, \quad D = \frac{\sigma_0}{h_0 \gamma_0^2 u_0} \alpha, \quad Q = \frac{t_0}{h_0} q. \tag{2.27}$$

From the definition of $\vec{X}$ and T we can deduce the corresponding partial derivatives

$$\begin{aligned} \partial_T = t_0 \partial_t \quad &\Rightarrow \quad \partial_t = \frac{1}{t_0}\partial_T, \\ \hat{\nabla} := \begin{pmatrix} \partial_X \\ \partial_Y \end{pmatrix} = \frac{h_0}{\epsilon}\begin{pmatrix} \partial_x \\ \partial_y \end{pmatrix} \quad &\Rightarrow \quad \nabla = \frac{\epsilon}{h_0}\hat{\nabla}, \\ \partial_Z = h_0 \partial_z \quad &\Rightarrow \quad \partial_z = \frac{1}{h_0}\partial_Z. \end{aligned}$$

By using these definitions, we will now expand the Navier-Stokes equations in powers of ϵ and then finally solve them in lowest order. We obtain

$$\partial_T \vec{U} + \left(\vec{U}\cdot\hat{\nabla} + U^Z \partial_Z\right)\vec{U} = \mathrm{Re}^{-1}\left[\epsilon\hat{\Delta}\vec{U} + \frac{1}{\epsilon}\left(\partial_Z^2\vec{U} - \hat{\nabla}P - \hat{\nabla}\Phi\right)\right],$$

$$\partial_T U^Z + \left(\vec{U}\cdot\hat{\nabla} + U^Z\partial_Z\right)U^Z = \mathrm{Re}^{-1}\left[\epsilon^2\hat{\Delta}U^Z + \partial_Z^2 U^Z - \frac{1}{\epsilon^2}(\partial_Z P + \partial_Z\Phi)\right],$$

which in lowest order amount to

$$\begin{aligned} \partial_Z^2\vec{U} &= \hat{\nabla}(P+\Phi), \\ 0 &= \partial_Z(P+\Phi). \end{aligned}$$

By defining the *generalized pressure* $\bar{P} := P + \Phi$ this can be written as

$$\partial_Z^2\vec{U} = \hat{\nabla}\bar{P}, \tag{2.28}$$

$$0 = \partial_Z\bar{P}. \tag{2.29}$$

In the next step, the same treatment is applied to the boundary conditions. Beginning with the stress balance equation, we expand eqs. (2.21),(2.22), (2.23) in powers of ϵ. For this purpose, we use the expansions

$$\begin{aligned} \frac{\sigma_{,x}}{\sqrt{1+\epsilon^2 H_{,X}}} &= \left(1-\epsilon^2 H_{,X}+\ldots\right)\frac{\epsilon\sigma_0}{h_0}\hat{\sigma}_{,X} = \frac{\sigma_0}{l_0}\hat{\sigma}_{,X} + \mathcal{O}\left(\epsilon^4\right), \\ \frac{1}{\sqrt{1+\epsilon^2 H_{,X}}} &= \left(1-\epsilon^2 H_{,X}+\ldots\right)\frac{\epsilon\sigma_0}{h_0}\hat{\sigma}_{,X} = \frac{\sigma_0}{l_0}\hat{\sigma}_{,X} + \mathcal{O}\left(\epsilon^4\right). \end{aligned}$$

Further, the sum of the principal curvatures given by eq. (2.14) can be expanded as

$$\varkappa_1 + \varkappa_2 = \frac{\epsilon}{l_0}\hat{\Delta}H + \mathcal{O}\left(\epsilon^4\right).$$

By using these results, we rewrite the terms of the stress balance equations (2.21), (2.22), (2.23) as

$$\begin{aligned} \epsilon^{-1}\frac{\eta}{t_0}\vec{U}_{,Z} &= \frac{\sigma_0}{l_0}\hat{\nabla}\hat{\sigma} + \vec{f}_{(\text{tangential})}, \\ \epsilon^{-2}\frac{\eta}{t_0}P &= \epsilon^{-2}\frac{\eta}{t_0}\Pi - \epsilon\frac{\sigma_0}{l_0}\hat{\Delta}H\hat{\sigma} + \vec{f}_{(\text{normal})}. \end{aligned}$$

With the definition of the capillary number Ca (see eq. 2.27), these equations can be written as

$$-\partial_Z \vec{U} = \epsilon \mathrm{Ca}^{-1} \hat{\nabla} \hat{\sigma} + \vec{f}_{(\text{tangential})}, \tag{2.30}$$

$$P = \Pi - \epsilon^3 \mathrm{Ca}^{-1} \hat{\sigma} \hat{\Delta} H + f_{(\text{normal})},. \tag{2.31}$$

At this point it is important to note that, by keeping just the terms of lowest order in ϵ, the surface tension would completely drop out of our equations. This is not acceptable since surface tension is an essential driving force in thin film physics. In other words: Phenomenology suggests that the terms involving surface tension are of order 1. Moreover, the dynamics of surfactant monolayer and water film are coupled via the dependency of surface tension on the surfactant density. Therefore, we assume $\epsilon^3 \mathrm{Ca}^{-1} = \mathcal{O}(1)$ and $\epsilon \mathrm{Ca}^{-1} \hat{\nabla} \hat{\sigma} = \mathcal{O}(1)$.

By adding Φ to eq. (2.31), we obtain an expression for the generalized pressure $\bar{P}$:

$$\bar{P} = \Pi - \epsilon^3 \mathrm{Ca}^{-1} \hat{\sigma} \hat{\Delta} H + f_{(\text{normal})} + \Phi. \tag{2.32}$$

We know from eq. (2.29), that the second derivative of $\vec{U}$ with respect to Z is not a function of Z. By inserting eq. (2.32) into eq. (2.28) and integrating twice with respect to Z, we can thus gain the following expression for $\vec{U}$:

$$\vec{U} = \frac{1}{2} \left(\hat{\nabla} \bar{P} \right) Z^2 + \vec{g}\left(\vec{X} \right) Z + \vec{A}. \tag{2.33}$$

The value of $\vec{A}$ is determined to $\vec{A} = -\vec{V}$ due to the no-slip boundary condition at $Z = 0$. By evaluating the first derivative of eq. (2.33) with respect to Z, one obtains

$$\vec{U}_{,Z} \Big|_{Z=H} = \left(\hat{\nabla} \bar{P} \right) H + \vec{g}\left(\vec{X} \right).$$

Using this result together with the boundary condition (2.30), we conclude

$$\vec{g}\left(\vec{X} \right) = \vec{f}_{(\text{tangential})} + \epsilon \mathrm{Ca}^{-1} \hat{\nabla} \hat{\sigma} - H \nabla \bar{P}.$$

This implies

$$\vec{U} = \frac{1}{2} \left(\hat{\nabla} \bar{P} \right) Z^2 + \left[\vec{f}_{(\text{tangential})} + \epsilon \mathrm{Ca}^{-1} \hat{\nabla} \hat{\sigma} - \left(\nabla \bar{P} \right) H \right] Z - \vec{V},$$

yielding the velocity at the surface

$$\begin{aligned} \vec{\tilde{U}} = \vec{U}\left(\vec{X}, H\left(\vec{X} \right) \right) &= \frac{1}{2} \left(\hat{\nabla} \bar{P} \right) H^2 + \left[\vec{f}_{(\text{tangential})} + \epsilon \mathrm{Ca}^{-1} \hat{\nabla} \hat{\sigma} - \left(\hat{\nabla} \bar{P} \right) H \right] H - \vec{V} \\ &= -\frac{H^2}{2} \hat{\nabla} \bar{P} + \left[\vec{f}_{(\text{tangential})} + \epsilon \mathrm{Ca}^{-1} \hat{\nabla} \hat{\sigma} \right] H - \vec{V}. \end{aligned} \tag{2.34}$$

We are now in the position to perform the integration of the right hand side of the dimension-

less form of the time evolution equation (2.26) of the height profile, yielding

$$\begin{aligned} H_{,T} &= -\hat{\nabla}\cdot\int_0^H \mathrm{d}Z\,\vec{U}+Q \\ &= -\hat{\nabla}\cdot\left[\left(\hat{\nabla}\bar{P}\right)\frac{H^3}{6}+\left\{\vec{f}_{(\text{tangential})}+\epsilon\mathrm{Ca}^{-1}\hat{\nabla}\hat{\sigma}-\left(\hat{\nabla}\bar{P}\right)H\right\}\frac{H^2}{2}-\vec{V}H\right]+Q \\ &= -\hat{\nabla}\cdot\left[-\left(\hat{\nabla}\bar{P}\right)\frac{H^3}{3}+\left\{\vec{f}_{(\text{tangential})}+\epsilon\mathrm{Ca}^{-1}\hat{\nabla}\hat{\sigma}\right\}\frac{H^2}{2}-\vec{V}H\right]+Q. \end{aligned} \tag{2.35}$$

The continuity equation of the surfactant monolayer can also be simplified by use of the lubrication approximation. For this purpose, one could non-dimensionalize eq. (2.12), expand in powers of ϵ and drop all higher orders. The simpler approach, however, is to directly consider eq. (2.7) and to discuss the covariant derivatives and the area source term in the lubrication approximation. Since we have shown in section 2.2 that the Christoffel symbols are given by $\Gamma^{\alpha}{}_{\beta\gamma}=a^{-1}h_{,\alpha\beta}h_{,\gamma}$ we find the dimensionless covariant derivative of a vector $\vec{q}$ as

$$\begin{aligned} q^{\alpha}_{;\beta} &= \frac{\epsilon}{h_0}\frac{\partial q}{\partial W^A}+\left(1-\epsilon^2\left(H_{,X}^2+H_{,Y}^2\right)\right)\epsilon^3 H_{,AB}H_{\Delta}w^{\Delta}+\mathcal{O}\left(\epsilon^7\right) \\ &= \frac{\epsilon}{h_0}\frac{\partial q}{\partial W^A}+\epsilon^3 H_{,AB}H_{\Delta}q^{\Delta}+\mathcal{O}\left(\epsilon^5\right), \end{aligned}$$

where upper-case Greek letters A, B, and Δ are used to index the dimensionless coordinates $W^A\in\{X,Y\}$. We note, that the covariant derivative differs from the partial derivative only by contributions which are two or more orders in ϵ beyond the leading order. Therefore, covariant and partial differentiation can be identified within the lubrication framework.

The area source term $\gamma\dot{a}/(2a)$ can be expanded as

$$\begin{aligned} \frac{\dot{a}}{2a} &= \frac{\epsilon^2}{2t_0}\left(1-\epsilon^2\left(H_{,X}^2+H_{,Y}^2\right)\right)\left(H_{,X}H_{,XT}+H_{,Y}H_{,YT}\right)+\mathcal{O}\left(\epsilon^6\right) \\ &= \frac{\epsilon^2}{2t_0}\left(H_{,X}H_{,XT}+H_{,Y}H_{,YT}\right)+\mathcal{O}\left(\epsilon^4\right), \end{aligned}$$

so that even the lowest contribution due to temporal changes of the surface area are of order ϵ^2 and can be neglected. Thus, eq. (2.7) can be approximated by

$$\Gamma_{,T}=-\hat{\nabla}\cdot\left(\Gamma\vec{\tilde{U}}+\vec{I}\right).$$

We conclude, that within the lubrication approximation, the time evolution of a surfactant monolayer on a thin liquid film with an arbitrarily shaped surface is *not directly* affected by the surface geometry. However, there is an indirect influence, since the flow velocity $\tilde{U}$ at the surface depends on the height profile H and its derivatives. Inserting the explicit expression (2.34) for the flow velocity $\vec{\tilde{U}}$ at the surface, one obtains

$$\Gamma_{,T}=-\hat{\nabla}\cdot\left[\Gamma\left(-\frac{H^2}{2}\hat{\nabla}\bar{P}+\left[\vec{f}_{(\text{tangential})}+\epsilon\mathrm{Ca}^{-1}\hat{\nabla}\hat{\sigma}\right]H-\vec{V}\right)+\vec{I}\right]. \tag{2.36}$$

With the system of equations (2.35) and (2.36), we have now completed the derivation of the general equations governing the dynamics of a surfactant covered thin liquid film. However, we still have to link the thin film flow to the thermodynamics of the monolayer. As has been outlined in section 1 (see especially eq. (1.1), both are connected via the surface tension. To be more specific, this means, we have to include the lateral pressure p_{lat} into our model. By combination of eq. (1.1) and eq. (1.16) one obtains

$$\begin{aligned}\sigma =&\sigma_{\mathrm{abs}} - p_{\mathrm{lat}} = \sigma_{\mathrm{abs}} + f_{\mathrm{hom}} + \frac{\varkappa}{2}(\nabla\gamma)^2 + \varkappa\gamma\Delta\gamma - \gamma\frac{\partial f_{\mathrm{hom}}}{\partial\gamma}\\ =&\sigma_0\hat{\sigma}_{\mathrm{abs}} + \sigma_0 F_{\mathrm{hom}} - \sigma_0\Gamma\frac{\partial F_{\mathrm{hom}}}{\partial\Gamma} + \epsilon^2\frac{\varkappa\gamma_0^2}{h_0^2}\left[\frac{1}{2}\left(\hat{\nabla}\Gamma\right)^2 + \Gamma\hat{\Delta}\Gamma\right],\end{aligned}$$

where we define $\hat{\sigma}_{\mathrm{abs}} = \sigma_{\mathrm{abs}}/\sigma_0$ and $F_{\mathrm{hom}} := f_{\mathrm{hom}}/\sigma_0$. By introducing the dimensionless domain interface line tension K as

$$K = \frac{\gamma_0^2\sigma_0}{h_0^2\sigma_0}$$

we can express the dimensionless surface tension as

$$\hat{\sigma} = \hat{\sigma}_{\mathrm{abs}} + F_{\mathrm{hom}} - \Gamma\frac{\partial F_{\mathrm{hom}}}{\partial\Gamma} + \epsilon^2 K\left[\frac{1}{2}\left(\hat{\nabla}\Gamma\right)^2 + \Gamma\hat{\Delta}\Gamma\right]. \tag{2.37}$$

According to section 1.7, we have to use a pressure tensor instead of the scalar lateral pressure. In dimensionless form, the pressure tensor $\underline{\boldsymbol{P}}^{(\mathrm{inhom})}(\vec{\boldsymbol{X}})$ has the components

$$P_{ij}^{(\mathrm{inhom})}(\vec{\boldsymbol{X}}) = P_{\mathrm{lat}}(\vec{\boldsymbol{X}})\delta_{ij} + \epsilon^2 K(\partial_i\Gamma(\vec{\boldsymbol{X}}))(\partial_j\Gamma(\vec{\boldsymbol{X}})).$$

However, as will be explained along the following lines, the off-diagonal part of $\underline{\boldsymbol{P}}$ does not enter the equation (2.34) for the flow field $\vec{\tilde{\boldsymbol{U}}}$. To see this, we first of all have to note, that the lateral pressure enters via two different terms: the Laplace pressure in $\hat{\nabla}\tilde{P}$ and the Marangoni term $\sim\hat{\nabla}\hat{\sigma}$. In the Laplace pressure, which is itself already of third order in ϵ, the derivative term of $\underline{\boldsymbol{P}}^{(\mathrm{inhom})}$ is $\mathcal{O}(\gamma^5)$ and therefore can be safely ignored. In the Marangoni term, the lateral pressure enters in form of $\hat{\nabla}\cdot\underline{\boldsymbol{P}}^{(\mathrm{inhom})}$ and as we have proved in 1.7 this can be written as the gradient of a scalar function. Therefore, one can simply use the *scalar* expression

$$P^{(\mathrm{inhom})} = P_{\mathrm{lat}} + \varkappa\left(\hat{\nabla}\Gamma\right)^2$$

throughout all the following calculations. Substituting $P^{(\mathrm{inhom})}$ for P_{lat} in eq. (2.37) we obtain

$$\hat{\sigma} = \hat{\sigma}_{\mathrm{abs}} + F_{\mathrm{hom}} - \Gamma\frac{\partial F_{\mathrm{hom}}}{\partial\Gamma} + \epsilon^2 K\left[-\frac{1}{2}\left(\hat{\nabla}\Gamma\right)^2 + \Gamma\hat{\Delta}\Gamma\right]. \tag{2.38}$$

Besides the surface tension, the monolayer thermodynamics also influences the system by diffusion. By combination of eqs. (1.14) and (2.9), we find the dimensionless diffusive flux

$$\vec{\boldsymbol{I}} = -\epsilon A\left[-\epsilon^2 K\hat{\nabla}\hat{\Delta}\Gamma + \frac{\partial^2 F_{\mathrm{hom}}}{\partial\Gamma^2}\hat{\nabla}\Gamma\right]. \tag{2.39}$$

The equations (2.35),(2.36), (2.38), and (2.39) are the central equations describing the evolution of a surfactant-covered thin liquid film. In the following chapters, they are investigated further and applied to various different situations.

3 Monolayer covered thin liquid films on periodic domains

Before finally addressing the problem of monolayer transfer, it is advisable to first develop a good understanding of the model derived in the preceding chapter by considering less complicated situations. To this end, the present chapter begins with a section on clean water films not contaminated with surfactants. In the course of that investigation, the mechanism of film breakup is explained in terms of spinodal decomposition, thereby making use of the formalism introduced in section 1.3.1. Also, the concept of the disjoining pressure will be explained further and related to a macroscopic observable, the contact angle. The second section is then devoted to the interplay between water flow and the monolayer, with a special focus on the effect of first-order phase transitions of the surfactants. In the third and final section, the effect of surface rigidity and spontaneous curvature of the monolayer will be examined.

3.1 Clean thin liquid films

3.1.1 Spinodal dewetting

Consider a non-volatile ($Q = 0$) thin liquid film in absence of any surfactant molecules. The surface tension across its surface will be constant[1] and thus its governing equation (2.35) simplifies to[2]

$$H_{,T} = \nabla \cdot \frac{H^3}{3} \nabla \tilde{P} = \nabla \cdot \frac{H^3}{3} \nabla \left(\Pi(H) - \epsilon^3 \mathrm{Ca}^{-1} \sigma \Delta H \right). \tag{3.1}$$

Here, the system is assumed to be either infinite or periodic and the Galilean invariance has been exploited to switch to a frame where the substrate is at rest, that is, $\vec{V} = 0$. By remembering the discussion of the Cahn-Hilliard equation in section 1.4, one can see that this equation is actually a generalized Cahn-Hilliard equation of the form

$$H_{,T} = \nabla \cdot \alpha(H) \nabla \frac{\delta \mathscr{F}}{\delta H},$$

where the mobility factor is given by $\alpha(H) = H^3/3$ and the free energy $\mathscr{F}$ is defined as

$$\mathscr{F}[H] = \int\int \mathrm{d}x\mathrm{d}y \left\{ \frac{\sigma}{2} (\nabla H)^2 + \Psi(H) \right\}. \tag{3.2}$$

[1] Temperature gradients that might induce Marangoni forces are not considered here.

[2] In the following, ∇ and Δ denote the dimensionless differential operators as long as they do not need to be distinguished from their dimensionful counterparts.

Here, $\Psi(H)$ is the primitive of the disjoining pressure, that is, $\Pi = \partial\Psi/\partial H$, and can therefore be referred to as the disjoining potential. Note, that $\alpha(H)$ is non-constant but positive semi-definite, since H is by definition a positive semi-definite quantity. Thus, we know from our argument preceding eq. (1.9) that $\mathscr{F}[H]$ serves as a Lyapunov functional of the system.

By analogy, we can directly infer the stability of homogeneous solutions, that is, flat films, by consideration of the disjoining potential $\Psi(H)$ which plays the same role as $F_{\mathrm{hom}}(\rho)$ in the free energy of the Cahn-Hilliard equation (1.8): If $\partial^2\Psi/\partial H^2|_{\hat{H}} < 0$, a flat film of height $\hat{H}$ is unstable. One can therefore say that $\hat{H}$ lies within the spinodal region and its breakup into droplets is termed *spinodal dewetting*, accordingly. The extent of the binodal region, where flat films would be metastable, has to be determined iteratively employing Maxwell's construction.

To get more detailed information about the breakup of unstable homogeneous solutions, we perform a linear stability analysis around $\hat{H}$, considering small perturbations $\eta(\vec{X}, T)$. Inserting $H(\vec{X}, T) = \hat{H} + \eta(\vec{X}, T)$ into eq. (3.1) and keeping only terms linear in η, we find the linearized equation

$$\eta_{,T} = \frac{\hat{H}}{3}\Delta\left(\hat{\Pi}' - \epsilon^3 \mathrm{Ca}^{-1}\Delta H\right),$$

where the abbreviation $\hat{\Pi}' := \partial\Pi/\partial H|_{\hat{H}}$ is used. Expanding the perturbation in plane waves $\eta(\vec{X}, T) \sim \exp(\omega T + \mathrm{i}\vec{k}\cdot\vec{X})$ we obtain the dispersion relation

$$\omega(k) = -\frac{\hat{H}^3}{3}k^2\left(\hat{\Pi}' + \epsilon^3\mathrm{Ca}^{-1}k^2\right).$$

Obviously, this result is in accordance with our thermodynamic prediction, since a band of unstable modes will be found if and only if $\hat{\Pi}' < 0 \Leftrightarrow \Psi''(\hat{H}) < 0$. The extrema of the dispersion relation are determined by

$$\frac{\partial\omega}{\partial(k^2)} = -\frac{\hat{H}^3}{3}k^2\left(\hat{\Pi}' + 2\epsilon^3\mathrm{Ca}^{-1}\right) \qquad \Rightarrow \qquad \frac{\partial\omega}{\partial(k^2)} = 0 \Leftrightarrow k_{\max}^2 = -\frac{\hat{\Pi}'}{2\epsilon^3\mathrm{Ca}^{-1}}.$$

Inserting $k_{\max}$ back into $\omega(k)$ we obtain the amplification of the fastest growing mode as

$$\omega(k_{\max}) = \frac{\hat{H}^3\hat{\Pi}'^2}{12\epsilon^3\mathrm{Ca}^{-1}}.$$

The quantities $k_{\max}$ and $\omega(k_{\max})$ are inversely proportional to the typical length scale λ and time scale τ of the system in the linear regime, that is, during the onset of pattern formation. One readily calculates

$$\tau = \frac{2\pi}{\omega(k_{\max})} = \frac{24\pi\epsilon^3\mathrm{Ca}^{-1}}{\hat{H}^3\hat{\Pi}'^2},$$

as well as

$$\lambda = \frac{2\pi}{k_{\max}} = \sqrt{-\frac{8\pi^2\epsilon^3\mathrm{Ca}^{-1}}{\hat{\Pi}'}}\,.$$

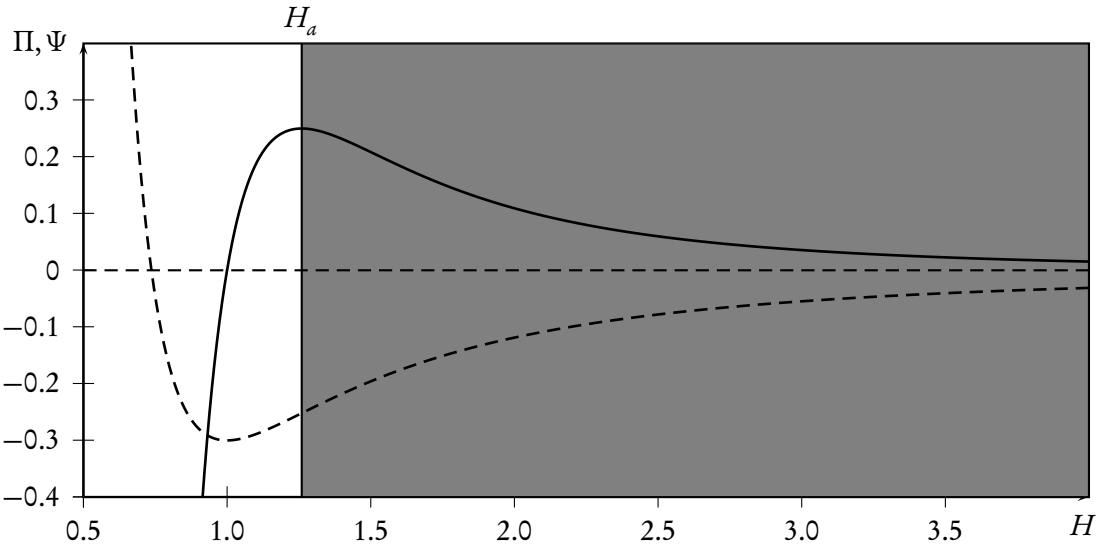

Fig. 3.1: The disjoining pressure $\Pi(H)$ (solid line) and the disjoining potential $\Psi(H)$ (dashed line). The spinodal region (gray) extends from H_a to infinity, so that homogeneous films of height $\hat{H} > H_a$ are unstable.

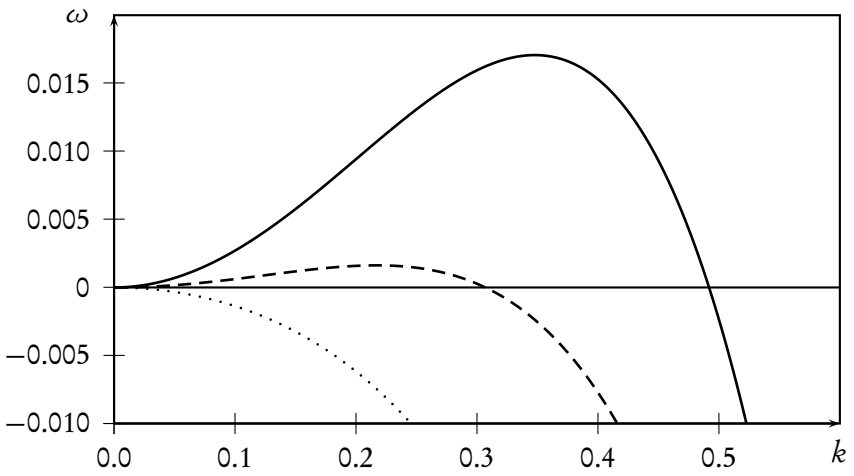

Fig. 3.2: Spectra $\omega(k)$ for perturbations of flat films of height $\hat{H} = 1.2$ (dots), $\hat{H} = 1.3$ (dashes), and $\hat{H} = 1.5183$ (solid).

Let us illuminate these results by use of a numerical example. For this purpose, we employ the disjoining pressure specified in eq. (2.1) with the exponent $n = 6$. To simplify the calculation, we choose a convenient scaling of equation eq. (3.1) by demanding $H_\mathrm{p} = \epsilon^3 \mathrm{Ca}^{-1} = 1$. This is achieved by setting

$$h_0 = h_\mathrm{p}, \qquad l_0 = h_\mathrm{p}^2 \sqrt{\frac{\sigma}{a_3}}, \qquad t_0 = \frac{h_p^5 \sigma \eta}{a_3^2}.$$

In this case, $A_3 = A_6 =: A$, so that the disjoining pressure takes the simple form

$$\Pi(H) = A\left(H^{-3} - H^{-6}\right), \tag{3.3}$$

which is shown graphically in fig. 3.1. For this particular choice of Π the spinodal region is semi-infinite, because $\Pi'(H) < 0$ for all $H > H_\mathrm{a}$, where $H_\mathrm{a} = \sqrt[3]{2} \approx 1.2599$ is the height corresponding to the maximum of $\Pi(H)$. Eigenvalue spectra $\omega(k)$ for three different values of $\hat{H}$ are plotted in fig. 3.2. Considering the homogeneous solution $\hat{H}$ corresponding to the maximum slope $\hat{\Pi}'$ of the disjoining pressure, that is, $\hat{H} = \sqrt[3]{7/2} \approx 1.5183$, we find the typical length and time scales to be $\lambda \approx 18.065$ and $\tau \approx 368.004$. This analysis is confirmed by a numerical simulation of the film-breakup. Snapshots of the numerical solution are shown in fig. 3.3. In the early stages of the time evolution, roughly 10-11 droplets are obtained along one edge of a 200×200 integration domain and it takes roughly $350 - 400$ time units to form pronounced structures.

Another kind of interesting dynamics of thin liquid films is observed when a homogeneous film is subjected to a *finite* perturbation such as a hole. The right column of fig. 3.3 shows the time evolution of a film of height $H = 2.5$ that has been pierced at a location $\vec{X}_0$. The initial condition in this case is given by

$$H(\vec{X}, 0) = \hat{H} - \frac{9}{10}\left(\hat{H} - 1\right) \operatorname{sech}^4\left(\frac{|\vec{x} - \vec{x}_0|}{20}\right).$$

A cascade-like formation of new holes that are arranged annularly around the original hole is observed. This phenomenon is actually also observed in experiments and has been termed "formation of satellite holes" [BGS+03].

3.1.2 Gravity

It is in agreement with everyday experience that thin films of water break up into droplets. Nevertheless, we also know, that if we add more and more water, we will eventually obtain a thicker film which is stable. This experimental result is obviously contradictory to our linear stability analysis, which predicts the instability of arbitrary thick films with $\hat{H} > H_a$. The reason for this contradiction is, that we have neglected gravity, so far.

This additional force can readily be included in the model equation, since our derivation in the preceding section allows for a conservative body force $\nabla\Phi$, which enters the generalized pressure eq. (2.32). Starting with the dimensionful potential energy $\phi(h) = \rho g h$ with the gravitational acceleration g, we find, according to eq. (2.27), the dimensionless expression

$$\Phi(H) = \underbrace{\frac{\epsilon^2 t_0 h_0 \rho g}{\eta}}_{=: G} H. \tag{3.4}$$

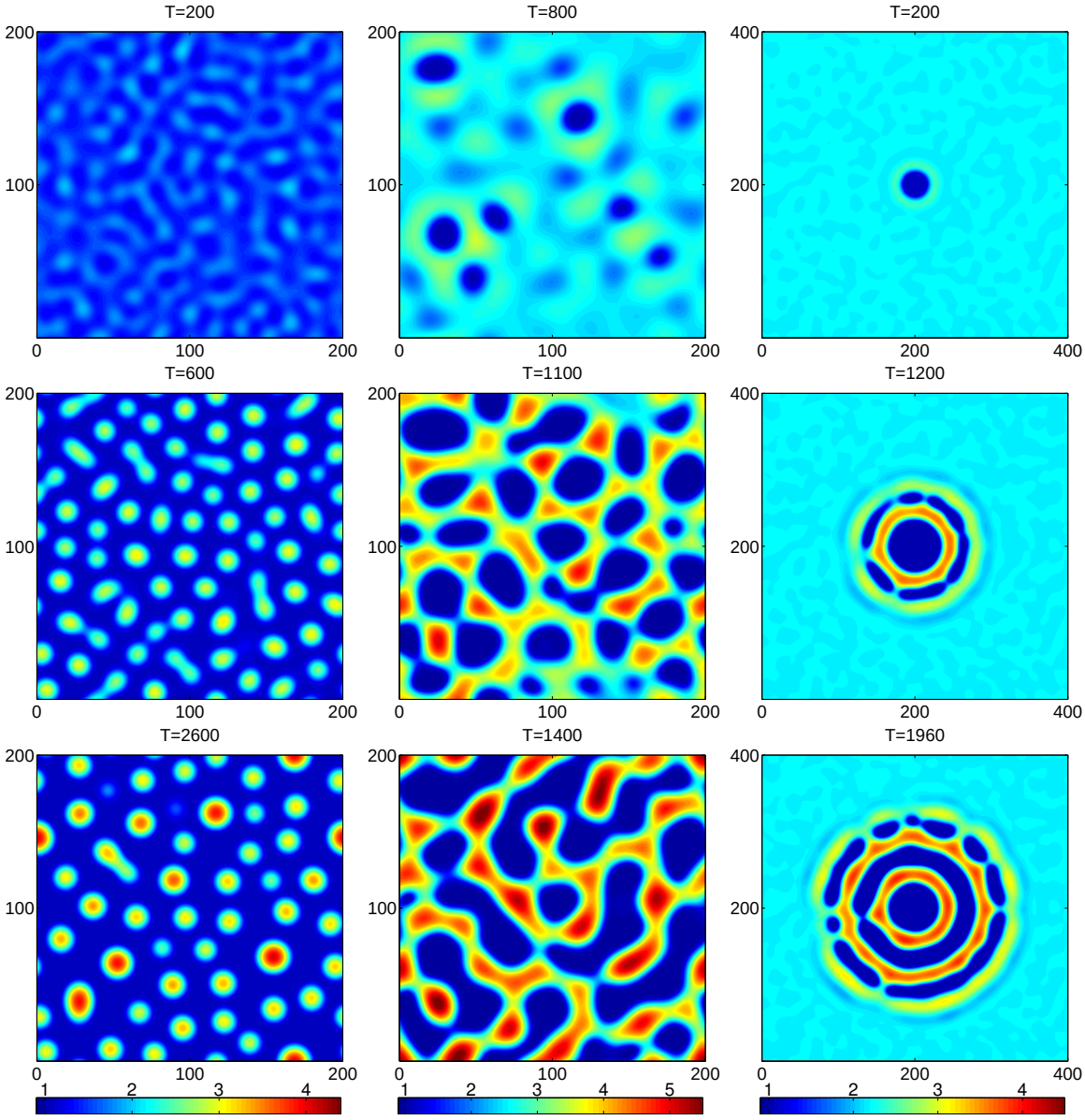

Fig. 3.3: Different dewetting scenarios of thin liquid films. The first two columns show spinodal dewetting of randomly perturbed flat films of height $\hat{H} = 1.5183$ (left column) and $\hat{H} = 2.5$ (middle column). The right column shows the formation of a cascade of holes, so called *satellite holes*, annularly arranged around an initial hole that has been pierced into a film of height $\hat{H} = 2.5$.

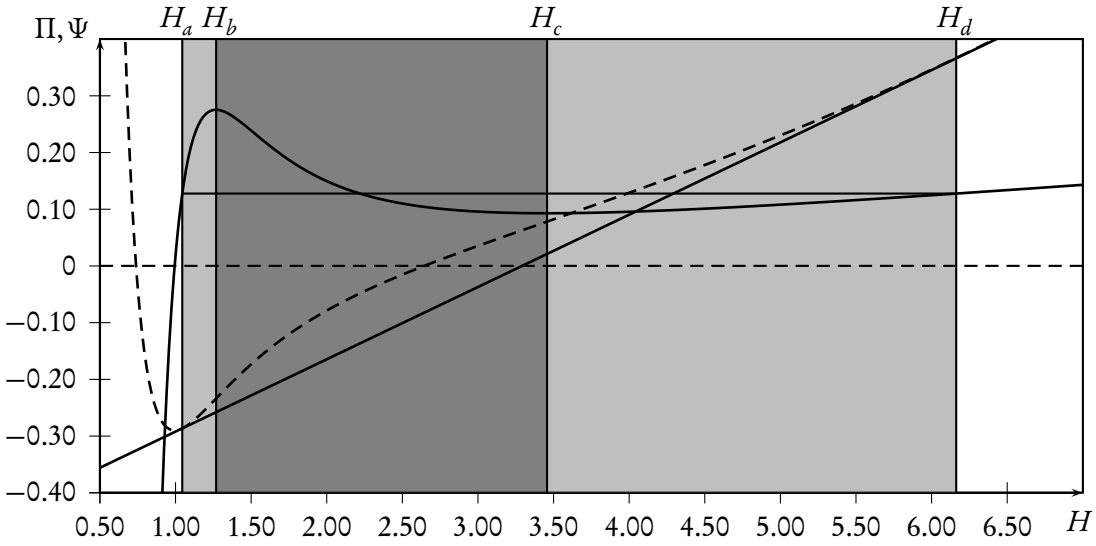

Fig. 3.4: The disjoining pressure $\Pi(H)$ (solid curve) and the disjoining potential $\Psi(H)$ (dashed curve) for the case of non-zero gravity constant G. The binodal (light gray) and spinodal (dark gray) regions can be determined like for the van-der-Waals gas. The common tangent and the horizontal line resultant from Maxwell's construction are shown as solid straight lines.

With this additional contribution, eq. (3.1) becomes

$$H_{,T} = \nabla \cdot \frac{H^3}{3} \nabla \bar{P} = \nabla \cdot \frac{H^3}{3} \nabla \left(\Pi(H) + GH - \epsilon^3 \mathrm{Ca}^{-1} \sigma \Delta H \right) \tag{3.5}$$

with the dimensionless gravitation constant G. The linear stability of flat films is then determined by the sign of $\hat{\Pi}'_G = \hat{\Pi}' + G$ and since $\Pi \to 0$ for $H \to \infty$, $\hat{\Pi}'_G$ is positive for all film heights greater than a certain $H = H_c$. Thus, gravity leads to the expected stabilization of thick films.

A further consequence of gravity is the existence of metastable solutions. This becomes obvious, when we look at eq. (3.5) from the perspective of thermodynamics. Contrary to the case without gravity, the spinodal region is now finite and extends between film heights H_b and H_c which solve $\Pi'(H) = -G$. Due to the addition of the term proportional to G, the homogeneous part of the Lyapunov functional becomes $\Psi_G(H) = \Psi(H) + GH^2/2$. It is thus possible to construct a common tangent to Ψ_G or equivalently use Maxwell's construction to find the boundaries of the binodal region. By this method, one finds a finite range of metastable solutions to the left and to the right of the spinodal region. This is shown graphically in fig. 3.4 for the case of the disjoining pressure specified in eq. (3.3). Note, that the effect of gravity is strongly exaggerated in this diagram in order to make the qualitative behavior visible. Π_G and Ψ_G are drawn for $G = 0.02$. Realistic values are several orders of magnitude smaller. Inserting $g = 9.81\,\mathrm{m/s^2}$, $h_0 = h_p = 5.5\,\mathrm{nm}$, $\epsilon = 1.0979 \times 10^{-2}$, and the typical values for water $\eta = 10^{-3}\,\mathrm{kg/(ms)}$, $\rho = 10^3\,\mathrm{kg/m^3}$ into eq. (3.4), one obtains $G \approx 3.45 \times 10^{-8}$.

3.1.3 Evaporation and condensation

Evaporation and condensation are described by the term Q in the differential equation for the film profile H. Depending on the chemical potentials of the liquid and the vapor, Q is either a sink or a source term. In the present thesis, we follow the approach of Pismen et al. [LGP02, Pis04]. By assuming the pressure in the vapor above the film to be close to the saturation pressure, Q can be written as

$$Q = -E_{\mathrm{ev}} \left(\mu_{\mathrm{l}} - \mu_{\mathrm{v}} \right), \tag{3.6}$$

where $E_{\mathrm{ev}} = \eta l_0^2 q_e / h_0^3$ is the evaporation number, that is, the dimensionless form of an effective rate constant q_e and μ_{l} and μ_{v} are the chemical potentials of the liquid and the vapor, respectively. The chemical potential of the liquid is given by the generalized pressure, that is, $\mu_{\mathrm{l}} = \tilde{P}$, whereas μ_{v} is assumed to be constant. To understand the influence of the nonconservative contribution Q, one can consider a flat film, so that the evolution equation (2.35) is reduced to

$$H_{,T} = Q = -E_{\mathrm{ev}} \left(\Pi - \mu_{\mathrm{v}} \right).$$

Thus, the film will evaporate until the equilibrium state $\Pi(H_{\mathrm{eq}}) = \mu_{\mathrm{v}}$ is reached.

Other approaches to describe evaporation exist in the literature (see, for example, [ODB97], section II.H). Probably the most common alternative to the model of Pismen et al. is the Hertz-Knudsen law (see [Bes06], chapter 8.6.7).

3.1.4 Nontrivial stationary film profiles and the Young-Laplace law in the lubrication approximation

As was explained in the preceding subsections, flat films with $H = \text{const.}$ solve the thin film equation (3.1) trivially so that there is a one parameter family of stationary solutions. Other stationary solutions can be found by the following procedure. Consider the one-dimensional version of eq. (3.1) for $H_{,T} = 0$, that is,

$$\partial_X \frac{H^3}{3} \partial_X \left(\Pi(H) - \epsilon^3 \mathrm{Ca}^{-1} H_{,XX} \right) = 0, \tag{3.7}$$

and look for solutions of this ordinary differential equation. Integration of eq. (3.7) with respect to X yields

$$\frac{H^3}{3} \partial_X \left(\Pi(H) - \epsilon^3 \mathrm{Ca}^{-1} H_{,XX} \right) = C_0.$$

For a stationary solution, the integration constant C_0 corresponds to a mean flux that vanishes in absence of any external forcing. It is then possible to divide by $H^3/3$, since H is a positive definite quantity ($H \geq H_{\mathrm{p}} > 0$). After one further integration with respect to X one obtains

$$\Pi(H) - \epsilon^3 \mathrm{Ca}^{-1} H_{,XX} = C_1 \tag{3.8}$$

To interpret the integration constant C_1, it is important to note, that eq. (3.8) can also be obtained by minimization of the Lyapunov functional given by eq. (3.2) under the side condition of mass

conservation. Seen from this perspective, the constant C_1 is the corresponding Lagrangian multiplier. One is now in the position to apply a standard approach from classical mechanics: we multiply by $H_{,X}$ and rewrite the equation in the form

$$\partial_X \left[\frac{\epsilon^3 \mathrm{Ca}^{-1}}{2} H_{,X}^2 - \Psi(H) + C_1 H \right] = 0.$$

Integrating once again with respect to X, we find,

$$\frac{\epsilon^3 \mathrm{Ca}^{-1}}{2} H_{,X}^2 - \Psi(H) + C_1 H = C_2. \tag{3.9}$$

This result can be rearranged to the form

$$H_{,X}^2 = \frac{2(\Psi(H) - C_1 H + C_2)}{\epsilon^3 \mathrm{Ca}^{-1}}. \tag{3.10}$$

Although it is in most cases not possible to solve eq. (3.10) analytically, it provides a relation $H_{,X}(H)$. This can be used to draw phase portraits of the solutions, that are completely characterized by (C_0, C_1) in the $(H, H_{,X})$-plane. One can find periodic solutions, corresponding to arrays of droplets or holes, as well as homoclinic solutions, corresponding to single droplets or holes, and heteroclinic solutions, corresponding to stationary fronts. For a presentation of such phase portraits and film profiles, the reader is referred to [TVNP01].

Here, it shall suffice to demonstrate the calculation of one particularly interesting solution: a meniscus with a constant contact angle θ. To this end, consider the boundary conditions $\lim_{X\to-\infty} H = H_\mathrm{p}$ and $\lim_{X\to\infty} H_{,X} = \theta = \text{const.}$, with asymptotic contact angle θ. Under these conditions, the integration constant C_1 obviously has to vanish, because the left hand side of equation (3.8) approaches $\Pi(H_\mathrm{p}) = 0$ for $X \to -\infty$. Taking the same limit in eq. (3.9) yields $C_2 = -\Psi(H_\mathrm{p})$. Thus, the stationary solution is determined by

$$H_{,X}^2 = \frac{2\left(\Psi(H) - \Psi(H_\mathrm{p})\right)}{\epsilon^3 \mathrm{Ca}^{-1}}.$$

Now, one has to consider the limit $X \to \infty$. From the condition that $\lim_{X\to\infty} H_{,X} = \theta > 0$, follows that H grows beyond all borders and thus $\lim_{X\to\infty} \Psi(H(X)) = 0$. Thence one obtains

$$\theta^2 = -\frac{2\Psi(H_\mathrm{p})}{\epsilon^3 \mathrm{Ca}^{-1}}. \tag{3.11}$$

This equations shows how the contact angle depends on the substrate-liquid interaction, given in terms of $\Psi(H_\mathrm{p})$, and the interfacial energy between liquid and vapor, given by $\mathrm{Ca}^{-1} \sim \sigma$. It has to be noted that the calculation of menisci becomes much more complicated as soon as one considers a moving substrate that is withdrawn with a constant velocity from a water reservoir. This problem is a topic of current research and only a few special cases are known, that are tractable at least semi-analytically [Egg04, SZA+08, BEI+09]).

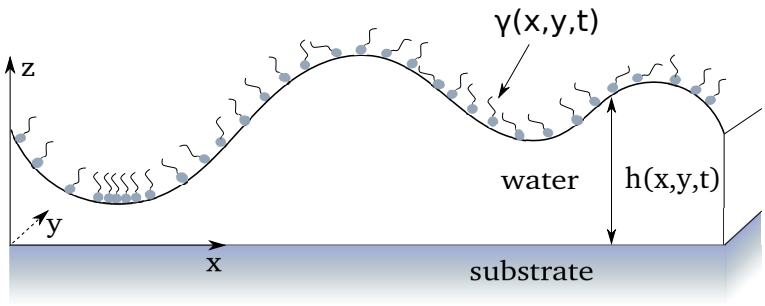

Fig. 3.5: A surfactant covered thin liquid film on a periodic domain.

As as been outline in section 2.1, the apparent contact angle can be calculated from the Young-Laplace law

$$S = \sigma_{\mathrm{lg}}(\cos\theta - 1).$$

In the domain of applicability of the lubrication approximation, θ has to be small, because the film thickness is assumed to vary only on very long scales. Therefore, one can expand $\cos\theta \approx 1 - \theta^2/2$ and obtains

$$\theta^2 = \frac{2S}{\sigma_{\mathrm{lg}}}.$$

From this result one can see that eq. (3.11) is consistent with the Young-Laplace law and that the relation between the spreading coefficient and the disjoining potential is given by $S = (\eta U_0/\epsilon^3)\Psi(H_{\mathrm{p}})$.

3.2 Monolayers in the vicinity of a first-order phase transition[3]

With the knowledge on clean thin liquid films and spinodal dewetting gathered in the preceding section, we are now in a position to address the more complicated case of a monolayer covered film. In particular, a film on a periodic domain will be considered (see fig. 3.5). Again, the stability of flat films and the dynamics of their breakup will be investigated and the results will be compared to the case of the clean film.

3.2.1 Choice of scales

In the following, it is convenient to adopt a particular choice of the scales h_0, l_0, t_0, and γ_0, which results from demanding

$$\epsilon^3 \mathrm{Ca}^{-1} = \epsilon^2 K = H_{\mathrm{p}} = 1.$$

Physically speaking, this means that we use the precursor height as the natural height scale of the system by setting $h_0 = h_{\mathrm{p}}$, yielding the same expression, eq. (3.3), for the dimensionless disjoining pressure as was used in the last section. However, due to the different scaling, the constant A is defined differently. The new definition

$$A = \frac{\gamma_0^2 \varkappa a_3}{\sigma_0^2 h_{\mathrm{p}}^4} \tag{3.12}$$

[3] This section contains an extended presentation of the results published in [KGF09].

involves a characteristic quantity of the monolayer, that is, its coefficient of domain line tension $\varkappa$. The characteristic length scale l_0 of the system is then related to the ratio of the surface tension σ_0 and the domain interface line tension $\varkappa$ as

$$l_0 = \gamma_0 \sqrt{\frac{\varkappa}{\sigma_0}} \tag{3.13}$$

and the natural time scale t_0 of the problem is obtained from the relation

$$t_0 = \frac{\gamma_0^4 \varkappa^2 \eta}{h_p^3 \sigma_0^3}. \tag{3.14}$$

With this choice of scales, ϵ obtains a direct physical meaning since

$$\epsilon = \sqrt{\frac{\sigma_0}{\gamma_0^2 \varkappa} \left(\frac{a_6}{a_3}\right)^{2/3}} \tag{3.15}$$

relates the forces acting at the monolayer covered surface, characterized by the constants σ_0, γ_0, and $\varkappa$, to the forces acting between substrate and liquid, determined by the constants a_3 and a_6.

Since we are interested in systems in the vicinity of the main transition, it is further convenient to set the number density scale γ_0 equal to the critical density, that is, $\gamma_0 = \gamma_{\mathrm{cr}}$. Correspondingly, we define the characteristic surface tension $\sigma_0 = \sigma(\gamma_{\mathrm{cr}})$ as the surface tension of water covered with a monolayer of density γ_{cr}.

The local part of the monolayer free energy density, F_{hom}, can then be written as

$$F_{\mathrm{hom}} = F_{\mathrm{cr}} + \frac{M_1}{4M_2^2} \tilde{\Gamma}^2 \left(\tilde{\Gamma}^2 - 2M_2^2\right) + S(H)\tilde{\Gamma}. \tag{3.16}$$

In this notation, $F_{\mathrm{cr}} = f_0/\sigma_0$ and $M_1 = -2\epsilon^{-2}\gamma_0^2 f_2/\sigma_0$ equals the curvature of the function F_{hom} in its center $\tilde{\Gamma} = 0$. M_2 denotes the density difference between the pure LE and LC phases, γ_{LE},γ_{LC} and the critical density γ_{cr}:

$$M_2 = \frac{|\gamma_{\mathrm{LE}} - \gamma_{\mathrm{cr}}|}{\gamma_{\mathrm{cr}}} = \frac{|\gamma_{\mathrm{LC}} - \gamma_{\mathrm{cr}}|}{\gamma_{\mathrm{cr}}}.$$

One can then relate equation (3.16) to the dimensionful expression (1.15) in terms of the coefficients f_k by

$$f_0 = \sigma_0 - \sigma_{\mathrm{abs}}, \qquad f_2 = -\frac{\epsilon^2 \sigma_0 M_1}{2\gamma_0^2}, \qquad f_4 = \frac{\epsilon^2 \sigma_0 M_1}{4\gamma_0^4 M_2^2}.$$

The resulting scaled expression for the surface tension is given by (compare eq. (2.38))

$$\hat{\sigma} = 1 - \epsilon^2 P_{\mathrm{hom}} + \left[\Gamma \Delta \Gamma - \frac{1}{2}(\nabla \Gamma)^2\right],$$

where P_{hom} is the dimensionless lateral pressure of a homogeneous system, shifted by the value of $F_{\mathrm{cr}} = \hat{\sigma}_0 - \hat{\sigma}_{\mathrm{cr}}$:

$$P_{\mathrm{hom}} = F_{\mathrm{cr}} - F_{\mathrm{hom}} + \Gamma \frac{\partial F_{\mathrm{hom}}}{\partial \Gamma} = \frac{M_1}{M_2^2} \tilde{\Gamma} \left(\tilde{\Gamma}^2 - M_2^2 \left(1 + \frac{\tilde{\Gamma}}{2}\right)\right) + S(H). \tag{3.17}$$

Analogously, the generalized pressure $\bar{P}$ takes the form

$$\bar{P} = -\left(1-\epsilon^2 P_{\text{hom}}\right)\Delta H + \Pi(H)$$

whereas $\nabla\hat{\Sigma}$ can be written in the form

$$\nabla\hat{\Sigma} = -\nabla P_{\text{hom}} + \epsilon^{-2}\Gamma\nabla\Delta\Gamma.$$

Note, that $\bar{P}$ does not contain any derivatives of Γ, due to the argument given in the end of section (2.5). Finally, one can apply the scaling to the diffusive flux given by eq. (2.39) to obtain

$$\begin{aligned}\vec{I} &= -\epsilon D\left[\nabla\Delta\Gamma + \epsilon^2\frac{\partial^2 F_{\text{hom}}}{\partial\Gamma^2}\nabla\Gamma\right]\\ &= -\epsilon D\left[-\nabla\Delta\tilde{\Gamma} + \epsilon^2 M_1\left(\frac{3}{M_2^2}\tilde{\Gamma}^2 - 1\right)\nabla\tilde{\Gamma}\right].\end{aligned}$$

The rescaled evolution equations for H and Γ are then given by

$$H_{,T} = -\hat{\nabla}\cdot\left[\frac{H^3}{3}\nabla\left\{\left(1-\epsilon^2 P_{\text{hom}}\right)\Delta H - \Pi\right\} + \frac{H^2}{2}\left(\epsilon^{-2}\Gamma\nabla\Delta\Gamma - \nabla P_{\text{hom}}\right) - H\vec{V}\right] + Q, \quad (3.18)$$

$$\Gamma_{,T} = -\nabla\cdot\left[\frac{\Gamma H^2}{2}\nabla\left\{\left(1-\epsilon^2 P_{\text{hom}}\right)\Delta H - \Pi\right\} + \Gamma H\left(\epsilon^{-2}\Gamma\nabla\Delta\Gamma - \nabla P_{\text{hom}}\right) - \Gamma\vec{V} + \vec{I}\right]. \quad (3.19)$$

Like in the case of a clean film, an important class of stationary solutions of these equations for $Q = 0$ is given by flat film profiles and homogeneous monolayers, that is, $H = \hat{H} = \text{const.}$ and $\Gamma = \hat{\Gamma} = \text{const.}$. The stability of such solutions is the topic of the following subsection.

3.2.2 Linear stability of homogeneous solution

To analyse the linear stability of stationary solutions of eqs. (3.18) and (3.19), we consider small perturbations $\eta(\vec{X}, T)$ and $\zeta(\vec{X}, T)$ solutions and insert $H(\vec{X}, T) = \hat{H} + \eta(\vec{X}, T)$ and $\Gamma(\vec{X}, T) = \hat{\Gamma} + \zeta(\vec{X}, T)$ into the eqs. (3.18),(3.19). By keeping only the linear terms the following equation for the perturbation fields is obtained:

$$\partial_T\begin{pmatrix}\eta\\ \zeta\end{pmatrix} = \mathscr{A}\begin{pmatrix}\eta\\ \zeta\end{pmatrix},$$

with the linear operator

$$\mathscr{A} = \begin{pmatrix}\mathscr{A}_{\eta\eta} & \mathscr{A}_{\eta\zeta}\\ \mathscr{A}_{\zeta\eta} & \mathscr{A}_{\zeta\zeta}\end{pmatrix}$$

whose components are given by

$$\begin{aligned}
\mathscr{A}_{\eta\eta} &= \left(\frac{\hat{H}^3}{3}\frac{\partial \Pi}{\partial H}\bigg|_{\hat{H},\hat{\Gamma}} + \frac{\hat{H}^2}{2}\frac{\partial S}{\partial H}\bigg|_{\hat{H}}\right)\Delta - \frac{\hat{H}^3}{3}\left(1-\epsilon^2 P_{\mathrm{hom}}(\hat{H},\hat{\Gamma})\right)\Delta^2,\\
\mathscr{A}_{\eta\zeta} &= \frac{\hat{\Gamma}\hat{H}^2}{2}\left(\frac{\partial^2 F_{\mathrm{hom}}}{\partial \Gamma^2}\bigg|_{\hat{\Gamma}} - \epsilon^{-2}\Delta^2\right),\\
\mathscr{A}_{\zeta\eta} &= \frac{\hat{\Gamma}\hat{H}}{2}\left[\left(\hat{H}\frac{\partial \Pi}{\partial H}\bigg|_{\hat{H}} + 2\frac{\partial S}{\partial H}\bigg|_{\hat{H}}\right)\Delta - \hat{H}\left(1-\epsilon^2 P_{\mathrm{hom}}(\hat{H},\hat{\Gamma})\right)\Delta^2\right],\\
\mathscr{A}_{\zeta\zeta} &= \left(\hat{\Gamma}^2\hat{H} + \epsilon^3 D\right)\left(\frac{\partial^2 F_{\mathrm{hom}}}{\partial \Gamma^2}\bigg|_{\hat{\Gamma}}\Delta - \epsilon^{-2}\Delta^2\right).
\end{aligned}$$

For the linearization, the partial derivatives of P_{hom} with respect to H and Γ are calculated as

$$\begin{aligned}
\frac{\partial P_{\mathrm{hom}}(H,\Gamma)}{\partial H} &= \frac{\partial S(H)}{\partial H},\\
\frac{\partial P_{\mathrm{hom}}(H,\Gamma)}{\partial \Gamma} &= -\frac{\partial F_{\mathrm{hom}}(\Gamma)}{\partial \Gamma} + -\frac{\partial F_{\mathrm{hom}}(\Gamma)}{\partial \Gamma} + \Gamma\frac{\partial^2 F_{\mathrm{hom}}(\Gamma)}{\partial \Gamma^2}\\
&= \Gamma\frac{\partial^2 F_{\mathrm{hom}}(\Gamma)}{\partial \Gamma^2},\\
\frac{\partial^2 P_{\mathrm{hom}}(H,\Gamma)}{\partial H \partial \Gamma} &= 0.
\end{aligned}$$

With the plane wave ansatz $\eta \sim \exp(\omega T + \mathrm{i}\vec{k}\cdot\vec{X})$, the application of the operator $\mathscr{A}$ yields a 2×2 matrix $\underline{\boldsymbol{A}} = \underline{\boldsymbol{A}}(k)$, whose components are polynomials of the absolute value of the wavenumber $k = |\vec{k}|$:

$$\begin{aligned}
A_{\eta\eta}(k) &= -k^2\left[\left(\frac{\hat{H}^3}{3}\frac{\partial \Pi}{\partial H}\bigg|_{\hat{H},\hat{\Gamma}} + \frac{\hat{H}^2}{2}\frac{\partial S}{\partial H}\bigg|_{\hat{H}}\right)k^2 + \frac{\hat{H}^3}{3}\left(1-\epsilon^2 P_{\mathrm{hom}}(\hat{H},\hat{\Gamma})\right)k^2\right],\\
A_{\eta\zeta}(k) &= -k^2\frac{\hat{\Gamma}\hat{H}^2}{2}\left[\frac{\partial^2 F_{\mathrm{hom}}}{\partial \Gamma^2}\bigg|_{\hat{\Gamma}} + \epsilon^{-2}k^2\right],\\
A_{\zeta\eta}(k) &= -k^2\frac{\hat{\Gamma}\hat{H}}{2}\left[\left(\hat{H}\frac{\partial \Pi}{\partial H}\bigg|_{\hat{H}} + 2\frac{\partial S}{\partial H}\bigg|_{\hat{H}}\right)k^2 + \hat{H}\left(1-\epsilon^2 P_{\mathrm{hom}}(\hat{H},\hat{\Gamma})\right)k^2\right],\\
A_{\zeta\zeta}(k) &= -k^2\left(\hat{\Gamma}^2\hat{H} + \epsilon^3 D\right)\left(\frac{\partial^2 F_{\mathrm{hom}}}{\partial \Gamma^2}\bigg|_{\hat{\Gamma}} + \epsilon^{-2}k^2\right).
\end{aligned}$$

Note, that the diffusion constant D enters $A_{\zeta\zeta}$ in form of a factor $(\hat{\Gamma}^2\hat{H} + \epsilon^3 D)$. The first term in the bracket results from the lateral pressure in the term $\sim \Delta(1-P_{\mathrm{hom}})$ in eq. (3.19). Thus, diffusion obviously amplifies the effect of the lateral pressure but does not lead to qualitatively different behavior. In fact, setting $\vec{I} = 0$ in eq. (3.19) leads only to minor quantitative changes of the following results.

The growth rates ω, which are the eigenvalues of $\underline{A}(k)$, can be calculated by use of the formula

$$\omega_{\pm} = \frac{\mathrm{Tr}\underline{A} \pm \sqrt{\left(\mathrm{Tr}\underline{A}\right)^2 - 4\det\underline{A}}}{2}. \tag{3.20}$$

The trace of $\underline{A}$ is obtained as

$$\begin{aligned}\mathrm{Tr}A = -k^2 \Bigg[& \frac{\hat{H}^3}{3}\frac{\partial\Pi}{\partial H}\bigg|_{\hat{H}} + \frac{\hat{H}^2}{2}\frac{\partial S}{\partial H}\bigg|_{\hat{H}} + \left(\hat{\Gamma}^2\hat{H} + \epsilon^3 D\right)\frac{\partial^2 F_{\mathrm{hom}}}{\partial\Gamma^2}\bigg|_{\hat{\Gamma}} \\ & + \left\{\frac{\hat{H}^3}{3}\left(1 - \epsilon^2 P_{\mathrm{hom}}\left(\hat{H},\hat{\Gamma}\right)\right) + \epsilon^{-2}\left(\hat{\Gamma}^2\hat{H} + \epsilon^3 D\right)\right\} k^2 \Bigg],\end{aligned} \tag{3.21}$$

whereas the determinant of $\underline{A}$ is given by

$$\begin{aligned}\det\underline{A} = & \frac{\hat{H}^3}{12}k^4\left(\hat{\Gamma}^2\hat{H} + 4\epsilon^3 D\right) \times \\ & \times \Bigg[\frac{\partial\Pi}{\partial H}\bigg|_{\hat{H}}\frac{\partial^2 F_{\mathrm{hom}}}{\partial\Gamma^2}\bigg|_{\hat{\Gamma}} + \left(\epsilon^{-2}\frac{\partial\Pi}{\partial H}\bigg|_{\hat{H}} + \left(1 - \epsilon^2 P_{\mathrm{hom}}\left(\hat{H},\hat{\Gamma}\right)\right)\frac{\partial^2 F_{\mathrm{hom}}}{\partial\Gamma^2}\bigg|_{\hat{\Gamma}}\right)k^2 \\ & + \epsilon^{-2}\left(1 - \epsilon^2 P_{\mathrm{hom}}\left(\hat{H},\hat{\Gamma}\right)\right)k^4\Bigg] \\ & + k^4\epsilon^3 D\frac{\partial S}{\partial H}\bigg|_{\hat{H}}\left(\frac{\partial^2 F_{\mathrm{hom}}}{\partial\Gamma^2}\bigg|_{\hat{\Gamma}} + k^4\right).\end{aligned} \tag{3.22}$$

The solution $\{\hat{H},\hat{\Gamma}\}$ is linearly stable, that is, both eigenvalues $\omega_{\pm} < 0$ for all wavenumber k, if and only if the conditions $\mathrm{Tr}\underline{A}(k) < 0$ and $\det\underline{A}(k) > 0$ are simultaneously fulfilled for all wavenumbers k.

3.2.3 The case without SMC

In a first step, one can neglect the effect of substrate-mediated condensation. The stability condition is then equivalent to

$$\begin{cases} \hat{\Pi}' & > 0, \\ \hat{F}''_{\mathrm{hom}} & > 0. \end{cases} \tag{3.23}$$

with the abbreviations $\hat{\Pi}' := (\partial\Pi/\partial H)|_{\hat{H}}$ and $\hat{F}''_{\mathrm{hom}} := (\partial^2 F_{\mathrm{hom}}/\partial\Gamma^2)|_{\hat{\Gamma}}$. The form of this condition is not a surprise if one remembers the results on spinodal decomposition from section 1.4 and the results on spinodal dewetting from the last section. If, on the one hand, the film thickness is chosen from within the spinodal region, the monolayer covered film breaks up into droplets like the clean film. If, on the other hand, the monolayer density is chosen from the spinodal region, it will decompose into a heterogeneous two-phase state. Note, that although the condition (3.23) is a combination of the corresponding conditions for the isolated subsystems film and monolayer,

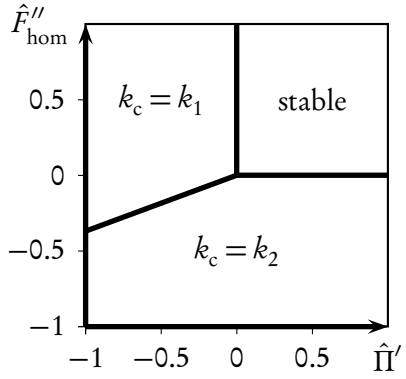

Fig. 3.6: Stability diagram of stationary homogeneous solutions in the plane of $\hat{\Pi}'$ and $\hat{F}''_{\text{hom}}$. If both derivatives are positive for a solution $\{\hat{H}, \hat{\Gamma}\}$, then it is stable. Otherwise, there is a band of unstable modes $0 < k < k_c$.

the time evolution of both subsystems is coupled form onset in the unstable case. This can be seen from the fact that the eigenvalues of $A(k_{\text{max}})$ are *not* parallel to the η and ζ directions. Whenever the condition given by eq. (3.23) is violated, there is a band of unstable modes $0 < k < k_c$, where the growth rate $\text{Re}(\omega_+)$ is positive. If both, the slope of Π and the curvature of F_{hom} are negative for the considered homogeneous solution, there will also be a band of wavenumbers with positive $\text{Re}(\omega_-)$, reaching from $k = 0$ to a maximal wavenumber smaller than k_c. In principle, the wavenumber k_{max} which is maximally amplified can be calculated from eqs. (3.20)–(3.22). The result, however, cannot be stated in a concise manner and therefore provides little new insight. Quite the contrary is true for k_c, the upper bound of the band of unstable modes k_c. It can be calculated analytically and has the form

$$k_c = \begin{cases} k_1 & \text{for} \quad \hat{\Pi}' < 0,\ \hat{F}''_{\text{hom}} > 0 \\ k_2 & \text{for} \quad \hat{\Pi}' > 0,\ \hat{F}''_{\text{hom}} < 0 \\ \max\{k_1, k_2\} & \text{for} \quad \hat{\Pi}' < 0,\ \hat{F}''_{\text{hom}} < 0 \end{cases}, \tag{3.24}$$

where k_1 and k_2 are defined as

$$k_1 = \sqrt{-\hat{\Pi}' \Big/ \left(1 - \epsilon^2 P_{\text{hom}}\left(\hat{H}, \hat{\Gamma}\right)\right)}, \qquad k_2 = \sqrt{-\hat{F}''_{\text{hom}}}. \tag{3.25}$$

A graphical representation of this result is given by figure 3.6. The lower left quadrant of the plane span by $\hat{\Pi}'$ and $\hat{F}''_{\text{hom}}$ is divided by the line

$$k_1 = k_2 \qquad \Leftrightarrow \qquad \hat{F}''_{\text{hom}} = \frac{\hat{\Pi}'}{1 - \epsilon^2 P_{\text{hom}}(\hat{\Gamma})}.$$

Parameter:	A	Ca^{-1}	M_1	M_2	ϵ	D
Value:	0.104	51.640	3.461×10^{-2}	0.177	3.724	1.163×10^{-3}

Tab. 3.1: The parameter set used in the numerical solution of eqs. (3.18) and (3.19).

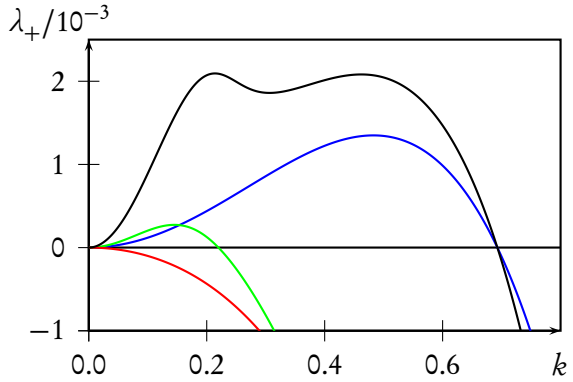

	$\hat{H}$	$\hat{\Gamma}$	$\hat{\Pi}'$	$\hat{F}''_{\mathrm{hom}}$
red	1.1	0.835	+	+
green	1.44	0.835	−	+
blue	1	1	+	−
black	1.6	1	−	−

Fig. 3.7: Eigenvalue spectra of the stability matrix of homogeneous solutions as obtained for four different sets of $\left\{\hat{H},\hat{\Gamma}\right\}$. The table on the right lists $\hat{H}$, $\hat{\Gamma}$, and the corresponding signs of $\hat{\Pi}'$ and $\hat{F}''_{\mathrm{hom}}$ that determine the stability of the solutions.

In the following, the evolution of randomly perturbed homogeneous solutions is simulated numerically. To this end, the parameter set listed in tab. 3.1 is employed[4]. The eigenvalue spectra $\omega_+(k)$ calculated with these parameters for four different sets of $\left\{\hat{H},\hat{\Gamma}\right\}$ are shown in fig. 3.7. A qualitative overview of the time evolution of two example systems with $\hat{H} = 1.44$, $\hat{\Gamma} = 0.835$ and $\hat{H} = 1.44$, $\hat{\Gamma} = 0.95$ is provided by the space-time plots and snapshots shown in fig. 3.8, that are obtained from simulations of one-dimensional domains of size $L = 500$. In the first case $\hat{\Pi}' < 0$ and $\hat{F}''_{\mathrm{hom}} > 0$, that is, the flat film is unstable with respect to spinodal dewetting whereas the monolayer is stable. Coherently, the space-time plots show how the randomly perturbed water film breaks up into an array of droplets while the monolayer stays more or less homogeneous in the beginning. The droplets coarsen, just as has been observed in the case of the clean film in section 3.1, and due to this process, more and more surfactant is gathered and concentrated in the biggest droplets. This densification eventually results in the formation of a few condensed domains that subsequently coarsen as well. In the end, there is only a single condensed domain, located on a big droplet. The behavior in the second case, where $\hat{\Pi}'$ and $\hat{F}''_{\mathrm{hom}}$ are both negative, is different, because monolayer domains form directly from the start of the simulation, due to spinodal decomposition. This time, there is enough surfactant available to form condensed domains on top of each drop. Comparing the space-time plots for the film profile H in both cases, the rapid domain formation also accelerates the formation of liquid droplets.

In the two-dimensional case, on a square domain with edge length $L = 500$, the time evolution is perfectly analogue. Figure 3.9 shows two snapshots of systems that have developed from $\hat{H} = 1.44$,

[4]The parameter values given in tab. 3.1 are not "round" because they are chosen to correspond to the values used in [KGF09], where a different set of scales is applied.

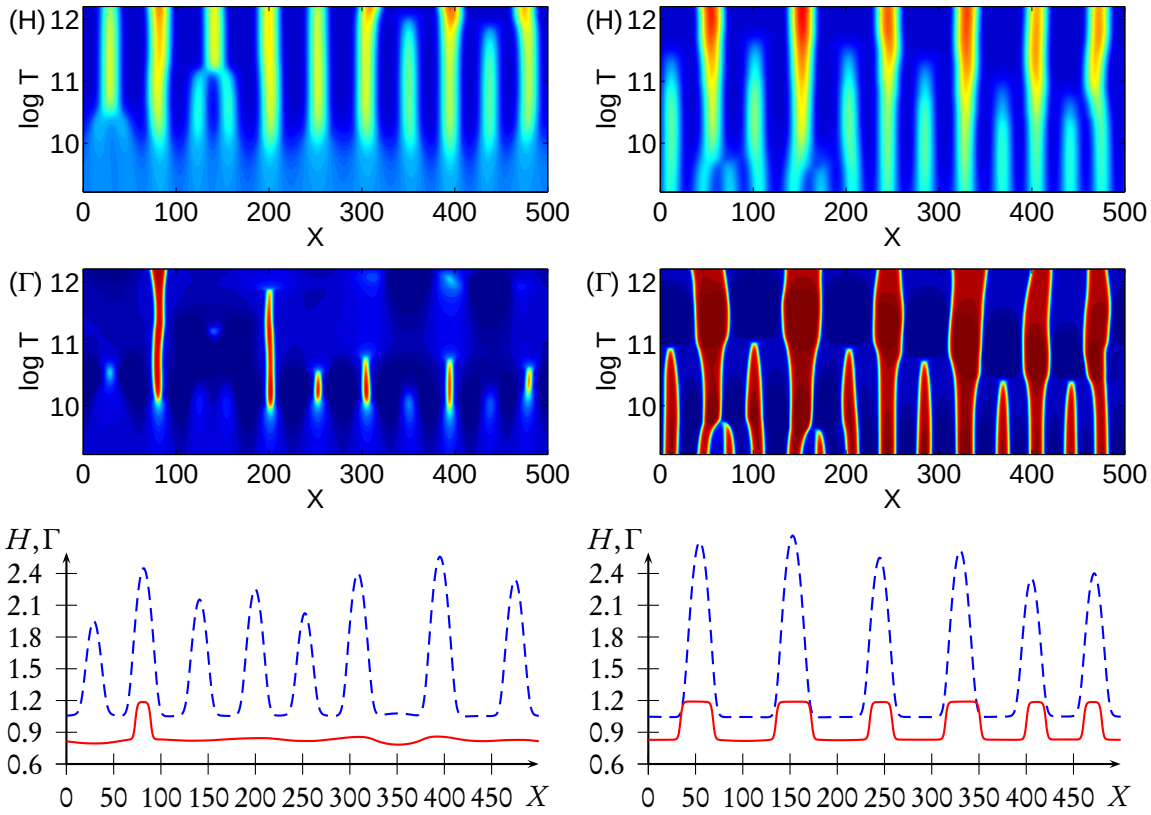

Fig. 3.8: Space-time plots of the time evolution of H and Γ after random perturbation of homogeneous states. Left column: $\hat{H} = 1.44$, $\hat{\Gamma} = 0.835$. Right column: $\hat{H} = 1.44$, $\hat{\Gamma} = 0.95$. At the bottom of both columns the final state of the profiles of H (blue dashes) and Γ (red solid line) at the end of the simulation is displayed.

$\hat{\Gamma} = 0.835$ and $\hat{H} = 1.44$, $\hat{\Gamma} = 1$. In the first case, only a few drops are covered with condensed domains, due to the limited available surfactant. In the second case, there is enough surfactant to cover half of the water surface with condensed domains. The value $\hat{\Gamma} = 1$ corresponds to the critical density, that is, the center of the spinodal region and one should therefore expect the formation of labyrinthine domains, analogously to what has been observed for the Cahn-Hilliard equation in the case $\hat{\rho} = 0$ (see fig. 1.8). As can be seen from fig. 3.9, the labyrinth structure is indeed present and it results also in the existence of some elongated droplets that follow the shape of the monolayer pattern (see for example the center of fig. 3.9 (b)).

The results of the linear stability analysis as well as of the numerical simulations in one and two spatial dimensions show that surfactant covered thin liquid films in the vicinity of a phase transition of the monolayer are subject to a combination of spinodal decomposition and spinodal dewetting. Although the stability condition given by equation (3.23) is simply a superposition of the respective conditions of an isolated thin film and an isolated monolayer, the evolution of the subsystems is coupled from onset.

3.2.4 The case with SMC

When substrate-mediated condensation is taken into account, the stability condition given by eq. (3.23) has to be supplemented by a further inequality, and it becomes

$$\begin{cases} \hat{\Pi}' & > 0, \\ \hat{F}''_{\mathrm{hom}} & > 0 \\ L(\hat{H},\hat{\Gamma}) & > 0, \end{cases} \tag{3.26}$$

with

$$L(H,\Gamma) = \frac{\hat{H}^3}{3}\frac{\partial \Pi}{\partial H}\bigg|_{\hat{H}} + \frac{\hat{H}^2}{2}\frac{\partial S}{\partial H}\bigg|_{\hat{H}} + \left(\hat{\Gamma}^2\hat{H} + \epsilon^3 D\right)\hat{\Gamma}\frac{\partial^2 F_{\mathrm{hom}}}{\partial \Gamma^2}\bigg|_{\hat{\Gamma}}. \tag{3.27}$$

All of the three values $\hat{\Pi}'$, $\hat{F}''_{\mathrm{hom}}$, and $L(\hat{H},\hat{\Gamma})$ are completely determined by the choice of the two quantities $\hat{H},\hat{\Gamma}$. One can therefore visualize the stability condition in the $\hat{H}$-$\hat{\Gamma}$-plane. If there is no SMC, that is, $S = 0$, the condition for L can only be violated if at least one of the conditions for $\hat{\Pi}'$ or $\hat{F}''_{\mathrm{hom}}$ is violated, anyway. In that case, the regions in $\hat{H}$-$\hat{\Gamma}$-plane that correspond to unstable states are just given by the overlapping spinodal regions of the monolayer and the thin film (see fig. 3.10 (a)). For nonvanishing S, there is another region of unstable states whose boundary is given by the curve defined by $L(\hat{H},\hat{\Gamma}) = 0$. In that case, it depends on the details of the function $S(H)$, whether or not formerly stable states are rendered unstable by SMC. As has been explained in section 1.6, the exact form of S is unknown. However, the eqs. (3.26) and (3.27) are valid for arbitrary S and they can be used to investigate the consequences of the various possible choices. In the following, two example cases are presented. If the height dependence of the substrate-monolayer interaction is exponential, that is, of the form $S(H) = -\alpha\exp(-\beta H)$ with $\alpha,\beta > 0$, then $\partial S/\partial H > 0 \,\forall\, H$. This means, that $L(\hat{H},\hat{\Gamma})$ can again only be negative if either $\hat{\Pi}'$ or $\hat{F}''_{\mathrm{hom}}$ are negative. Consequently, the curve $L = 0$ lies within the overlapping spinodal regions of the film and the monolayer as is shown in fig. 3.10 (b). In the remainder of this thesis, $S(H)$ is always

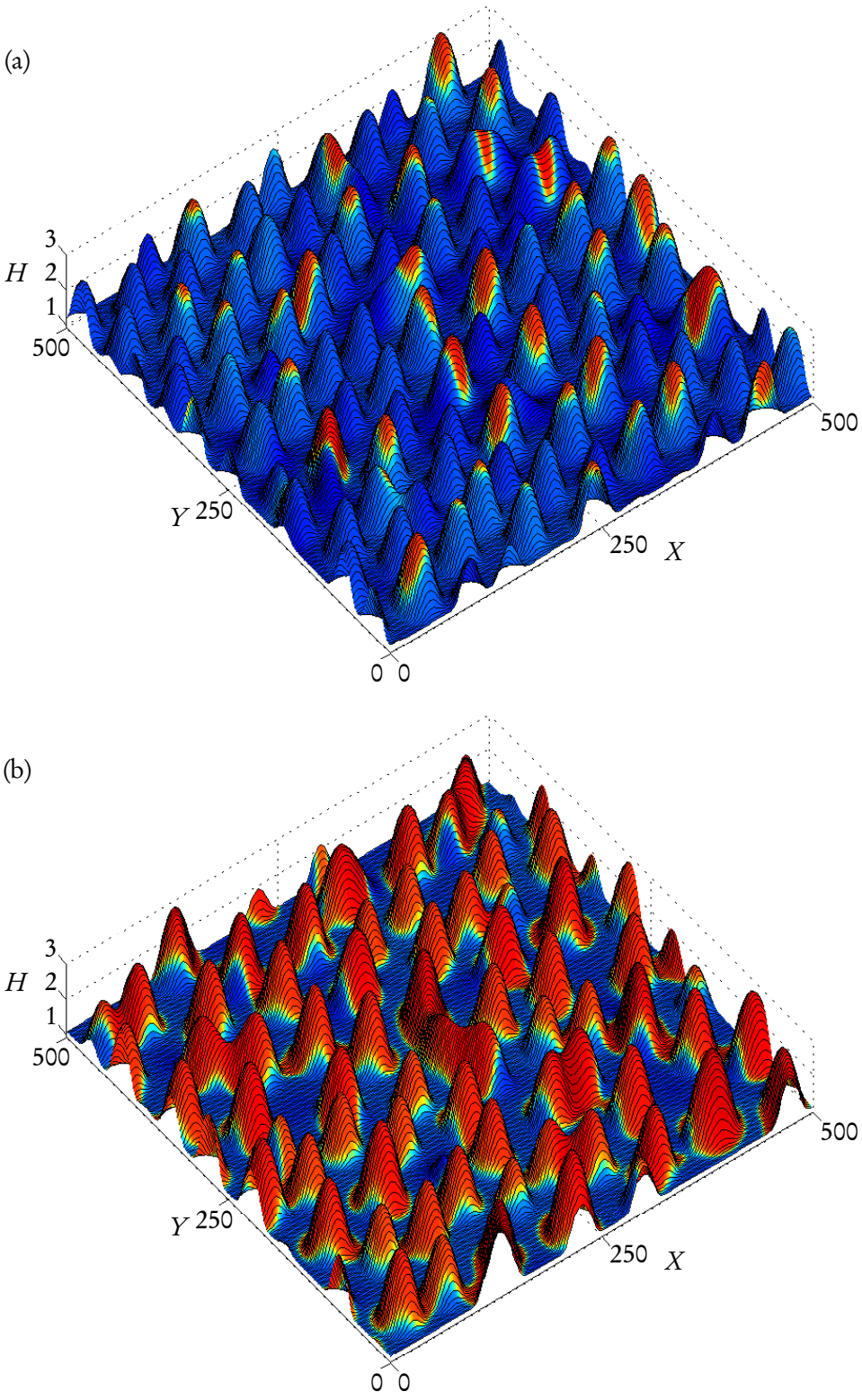

Fig. 3.9: Snapshots from the simulation of randomly perturbed homogeneous states on a two-dimensional domain: (a) $\hat{H} = 1.44$, $\hat{\Gamma} = 0.835$; (b) $\hat{H} = 1.44$, $\hat{\Gamma} = 1$. The height profile H is shown in pseudo-3D whereas the surfactant density Γ is encoded in the color. Blue corresponds to the LE phase, red to the LC phase.

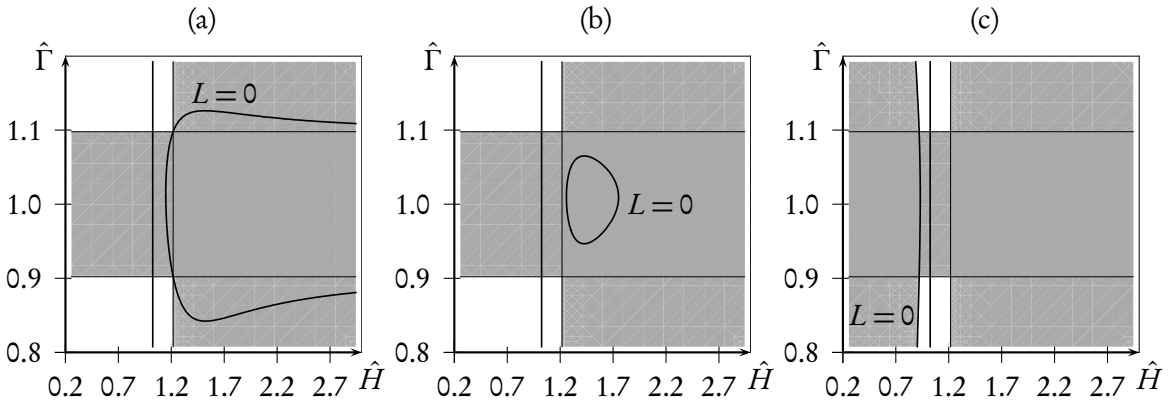

Fig. 3.10: Stability diagrams for different choices of the SMC function $S(H)$. (a) $S(H)=0$, (b) $S(H)=-0.9\exp(-0.1H)$, (c) $S(H)=10\Psi(H)$. All other parameters are set to the values specified in tab. 3.1. The vertical lines at $H=1$ and $H=\sqrt[6]{3}\approx 1.201$ indicate the precursor film height and the height corresponding to $\Pi'(H)=0$, respectively. The horizontal lines indicate the boundaries of the spinodal region of the monolayer determined by $F''_{\mathrm{hom}}(\Gamma)=0$.

assumed to be related to the substrate-liquid interaction characterized by the disjoining potential $\Psi(H)$, that is,

$$S(H)=B\Psi(H) \tag{3.28}$$

with a positive coupling constant B (see discussion in section 1.6). For this choice, the resulting region of unstable states is larger than the combined spinodal regions. However, the new unstable states all lie in a practically irrelevant region, because $\partial S/\partial H$ is then only negative for $H<H_{\mathrm{p}}$, that is, for films thinner than the precursor thickness (see fig. 3.10 (c)).

3.3 Dynamics of a thin liquid film with surface rigidity and spontaneous curvature[5]

The model developed in chapter 2 is based on the assumption of perfectly mobile interfaces. In reality, surfactant mono- and multilayers are rigid to some extent, depending on the chemical and thermodynamical properties of the used substances. Thus, any deformation of a surfactant covered liquid surface takes an additional amount of work in order to bend the surface layer. This energy can be quantified in terms of a *bending rigidity* and is measurable by x-ray scattering experiments [DBAB+05, MDLS04]. These experiments show that the rigidity depends strongly on the used surfactant species and its thermodynamic phase. One further property of surfactant layers is that they can exhibit *spontaneous curvature* due to the different chemical properties of the head- and tailgroups of the molecules [Saf94]. If the equilibrium distance between the tailgroups differs from the equilibrium distance between the headgroups, the layer will obviously have to curve in

[5] This section contains an extended presentation of the results published in [KGWF11].

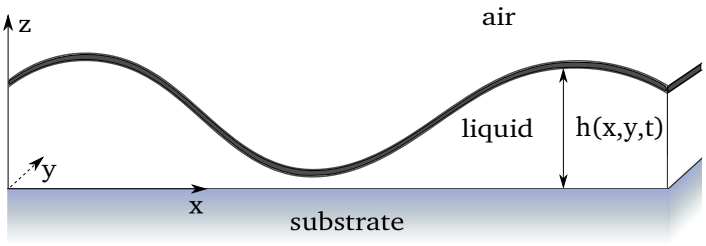

Fig. 3.11: Schematic drawing of a thin liquid film with a rigid surface layer. The shape of the film is described by $h(\vec{x}, t)$, while the surface layer is assumed to be homogeneous and away from any phase transition.

order to reach its energetic optimum. There will also be a resistance against any deformation of the subphase surface because such a deformation necessarily leads to a deviation from that optimal state. It is reasonable to assume that these effects are even more pronounced if the liquid support of such a surfactant layer becomes a very thin film, as is the case for example in all kinds of coating processes - including, of course, LB transfer - so that interfacial influences become increasingly important.

The lubrication approximation of the dynamics of thin liquid films outlined in chapter 2 can be generalized by incorporation of the bending rigidity and the spontaneous curvature of a surface layer. Following this approach, one finds that the surface rigidity gives rise to a pair of antagonistic effects: while short wavelength fluctuations are suppressed by the bending rigidity, the spontaneous curvature can lead to instabilities at intermediate wavelengths. This is particularly interesting, because the usually observed instabilities of thin films involve a band of unstable modes reaching from $k = 0$ to some maximal wavenumber $k_{\max}$. The longwave nature of these instabilities is a consequence of mass conservation, symmetry, and the highest order (four) of the occurring derivatives. Due to mass conservation, the right hand side of the differential equations describing the system is the divergence of a flux. Thus, the lowest order term in the eigenvalue spectrum $\omega(\vec{k})$ is of order $\vec{k}$, so that $\omega(\vec{0}) = \vec{0}$. Due to symmetry, only even powers of $\vec{k}$ occur in $\omega(\vec{k})$, that is, $\omega(\vec{k}) = \omega(k)$. Because the term of the highest order of k needs to have a negative coefficient in a physically meaningful theory, and only terms of order k^2 and k^4 are available, a band of unstable modes necessarily needs to start at $k = 0$.

When surface rigidity is taken into account, a term with a sixth derivative has to be added to the differential equations describing the film. This yields the possibility to have the terms of order k^2 and k^6 with negative coefficients and the term of order k^4 with a positive coefficient, a combination that can result in the existence of a band of unstable modes beginning with a nonzero wavenumber. However, the system is still mass conservative. Therefore, the single mode $k = 0$ will be neutrally stable in any case.

By the end of this section, it will be possible to estimate the effect of surface rigidity on the pattern formation in Langmuir-Blodgett transfer, which turns out to be negligible. However, our model is not limited to the application to that particular problem, and the generalization achieved in this section may serve as the basis of further research on more rigid monolayers.

The work presented in this section is a based on ideas by Wulf, Gurevich, and Friedrich [Wul08], which are here extended to take spontaneous membrane curvature into account. Furthermore, the

model is generalized to the two-dimensional case and a first numerical investigation is performed.

3.3.1 Surface rigidity

In the spirit of Helfrich, the energy E_r of a rigid interfacial layer can be written as a sum of integrals over the mean curvature and the Gaussian curvature of the surface [Hel73, Saf94]. Denoting the two principal curvatures of the surface by $\varkappa_1$, $\varkappa_2$, and its spontaneous curvature by $\varkappa_0$, one can express E_r as

$$E_r = \frac{k_c}{2}\int \mathrm{d}S\,(\varkappa_1+\varkappa_2-\varkappa_0)^2 + \frac{k_g}{2}\int \mathrm{d}S\,\varkappa_1\varkappa_2.$$

The positive material constants k_c and k_g are the bending rigidity and the modulus of the Gaussian curvature, respectively. According to the Gauss-Bonnet theorem, the result of the second integral, the total curvature, is a topological quantity, dependent only on the genus p of the considered surface S (see chapter 9 of [Lee97]). Thus, E_r can be written as

$$E_r = \frac{k_c}{2}\int \mathrm{d}S\,(\varkappa_1+\varkappa_2-\varkappa_0)^2 + 2\pi k_g(1-p). \tag{3.29}$$

Here, only thin films which are entirely covered by a homogeneous surfactant layer without any defects are considered. This is a valid assumption for single component monolayers that are not in the vicinity of a phase transition. Consequently, the surface topology remains constant and does not impact the evolution of the surfactant covered film. To connect the interfacial energy E_r to the dynamics of the subphase one has to consider that the surface rigidity yields an additional contribution to the force balance at the interface, resulting in a modified version of equation (2.15):

$$\delta W = \int\int \mathrm{d}x\mathrm{d}y \left\{ p - \sigma(\varkappa_1+\varkappa_2) + \pi_d + \frac{\delta E_r}{\delta h}\right\}\delta h. \tag{3.30}$$

As follows from eq. (3.29), the functional derivative of E_r for constant topology, that is, in the case of $\delta p/\delta h = 0$, is given by

$$\frac{\delta E_r}{\delta h} = \frac{k_c}{2}\int\int \mathrm{d}x\mathrm{d}y\,\frac{\delta\sqrt{a}}{\delta h}(\varkappa_1+\varkappa_2-\varkappa_0)^2 + k_c\int\int \mathrm{d}x\mathrm{d}y\,\sqrt{a}\,(\varkappa_1+\varkappa_2-\varkappa_0)\frac{\delta(\varkappa_1+\varkappa_2)}{\delta h}. \tag{3.31}$$

Here, a denotes the determinant of the surface metric as defined in eq. (2.4). To evaluate the first term in this equation, we calculate the functional derivative of $\sqrt{a}$ as

$$\frac{\delta\sqrt{a}}{\delta h} = \frac{1}{2}a^{-1/2}\frac{\delta a}{\delta h} = a^{-1/2}(\nabla h)\cdot\nabla\delta^{(2)}\left(\vec{x}-\vec{x}'\right).$$

This expression is part of an integrand, so that the nabla operator acting on the delta function can be treated by use of partial integration. Thus, we calculate

$$\int\int \mathrm{d}x\mathrm{d}y\,\frac{\delta\sqrt{a}}{\delta h}(\varkappa_1+\varkappa_2-\varkappa_0)^2 = -\nabla\cdot\left\{a^{-1/2}(\nabla h)(\varkappa_1+\varkappa_2-\varkappa_0)^2\right\}. \tag{3.32}$$

To explicitly calculate the variational derivative of the sum of the principal curvatures, we use the differential geometric identity $\varkappa_1 + \varkappa_2 = -\nabla \cdot \hat{\vec{n}}^{(3)}$, which allows us to write

$$-\frac{\delta(\varkappa_1+\varkappa_2)}{\delta h} = \nabla \cdot \frac{\delta \hat{\vec{n}}^{(3)}}{\delta h}.$$

At this point, it is convenient to carry out the variational derivative component-wise, whereupon the unit normal can be rewritten as $\hat{\vec{n}}^{(3)} = a^{-1/2}\vec{n}^{(3)}$ with $\vec{n}^{(3)} = (-h_{,x}, -h_{,y}, 1)$ (see eq. (2.3)). The z-component does not play any role in the following calculation, as the differential operators are purely two-dimensional.

$$\partial_\alpha \frac{\delta \hat{n}_\alpha}{\delta h} = \partial_\alpha \frac{\delta}{\delta h} a^{-1/2} n_\alpha \tag{3.33}$$

$$= -\partial_\alpha \frac{1}{2} a^{-3/2} \frac{\delta a}{\delta h} n_\alpha + \partial_\alpha a^{-1/2} \frac{\delta n_\alpha}{\delta h}. \tag{3.34}$$

The variational derivatives of a and $\hat{\vec{n}}^{(3)}$ can be evaluated separately, yielding the expressions

$$\frac{\delta a}{\delta h} = \left(2h_{,x}\partial_x + 2h_{,y}\partial_y\right)\delta^{(2)}\left(\vec{x}-\vec{x}'\right) = 2(\partial_\alpha h)\partial_\alpha \delta^{(2)}\left(\vec{x}-\vec{x}'\right),$$

$$\frac{\delta \vec{n}^{(3)}}{\delta h} = \begin{pmatrix} -\partial_x \\ -\partial_y \\ 0 \end{pmatrix} \delta^{(2)}\left(\vec{x}-\vec{x}'\right) \Leftrightarrow \frac{\delta n_\alpha}{\delta h} = -\delta_{\alpha\beta}\partial_\beta \delta^{(2)}\left(\vec{x}-\vec{x}'\right).$$

By inserting these results into eq. (3.34), we can finally write

$$\left[\nabla \cdot \frac{\delta \hat{\vec{n}}^{(3)}}{\delta h}\right]_\alpha = -\partial_\alpha \left\{a^{-3/2}\left(\partial_\beta h\right) n_\alpha \partial_\beta + a^{-1/2}\partial_\alpha\right\}\delta^{(2)}\left(\vec{x}-\vec{x}'\right), \tag{3.35}$$

and are now ready to return to vector notation for the rest of our calculation. Equation (3.35) can be rewritten as

$$\nabla \cdot \frac{\delta \hat{\vec{n}}^{(3)}}{\delta h} = -\nabla \cdot \left(\frac{\hat{\vec{n}}^{(3)}}{a}\left[(\nabla h)\cdot\nabla\delta^{(2)}\left(\vec{x}-\vec{x}'\right)\right]\right) - \nabla \cdot \left(a^{-1/2}\nabla\delta^{(2)}\left(\vec{x}-\vec{x}'\right)\right)$$

$$= -\left[\left(\nabla \cdot \frac{\hat{\vec{n}}^{(3)}}{a}\right)(\nabla h) + (\Delta h)\frac{\hat{\vec{n}}^{(3)}}{a} + \left(\nabla a^{-1/2}\right)\right]\cdot\nabla\delta^{(2)}\left(\vec{x}-\vec{x}'\right)$$

$$- \left[\frac{\hat{\vec{n}}^{(3)}}{a}\cdot(\nabla h) + a^{-1/2}\right]\Delta\delta^{(2)}\left(\vec{x}-\vec{x}'\right). \tag{3.36}$$

By inserting eq. (3.36), the complete second integral in eq. (3.31) becomes

$$\begin{aligned}
&\int\int \mathrm{d}x\mathrm{d}y\,\sqrt{a}\,(x_1+x_2-x_0)\frac{\delta(x_1+x_2)}{\delta h}\\
&=\int\int \mathrm{d}x\mathrm{d}y\,\left(-\nabla\cdot\hat{\vec{n}}^{(3)}-x_0\right)\sqrt{a}\,\left[\left(\nabla\cdot\frac{\hat{\vec{n}}^{(3)}}{a}\right)(\nabla h)+(\Delta h)\frac{\hat{\vec{n}}^{(3)}}{a}+\left(\nabla a^{-1/2}\right)\right]\cdot\nabla\delta^{(2)}\left(\vec{x}-\vec{x}'\right)\\
&\quad+\int\int \mathrm{d}x\mathrm{d}y\,\left(-\nabla\cdot\hat{\vec{n}}^{(3)}-x_0\right)\left[\frac{\hat{\vec{n}}^{(3)}}{\sqrt{a}}\cdot(\nabla h)+1\right]\Delta\delta^{(2)}\left(\vec{x}-\vec{x}'\right).
\end{aligned}$$

To evaluate this expression, we apply partial integration to remove the differential operators acting on the delta functions. Once this is done, the remaining integrals can be calculated trivially:

$$\begin{aligned}
&\int\int \mathrm{d}x\mathrm{d}y\,\sqrt{a}\,(x_1+x_2-x_0)\frac{\delta(x_1+x_2)}{\delta h}\\
&=-\nabla\cdot\left\{\left(-\nabla\cdot\hat{\vec{n}}^{(3)}-x_0\right)\left[\sqrt{a}\left(\nabla\cdot\frac{\hat{\vec{n}}^{(3)}}{a}\right)(\nabla h)+(\Delta h)\frac{\hat{\vec{n}}^{(3)}}{\sqrt{a}}+\sqrt{a}\left(\nabla a^{-1/2}\right)\right]\right\}\\
&\quad+\Delta\left\{\left(-\nabla\cdot\hat{\vec{n}}^{(3)}-x_0\right)\left[\frac{\hat{\vec{n}}^{(3)}}{\sqrt{a}}\cdot(\nabla h)+1\right]\right\}.
\end{aligned}\tag{3.37}$$

The functional derivative of E_r with respect to h is then obtained by inserting eqs. (3.32) and (3.37) into eq. (3.31):

$$\begin{aligned}
\frac{\delta E_\mathrm{r}}{\delta h}=k_\mathrm{c}\nabla\cdot\Bigg\{&\left(\nabla\cdot\hat{\vec{n}}^{(3)}+x_0\right)\Bigg[a^{1/2}\left(\nabla\cdot\frac{\hat{\vec{n}}^{(3)}}{a}\right)(\nabla h)+\frac{2(\Delta h)\hat{\vec{n}}^{(3)}-\left(\nabla\cdot\hat{\vec{n}}^{(3)}+x_0\right)(\nabla h)}{2a^{1/2}}\\
&-\frac{(\nabla h)(\Delta h)}{a}\Bigg]-\nabla\left(a^{-1}\left(\nabla\cdot\hat{\vec{n}}^{(3)}+x_0\right)\right)\Bigg\}.
\end{aligned}\tag{3.38}$$

To derive the time evolution equation for the film profile, one can now follow precisely the same steps as in section 2.4, with the only difference that $\delta E_\mathrm{r}/\delta h$ is taken into account. Thus, we expand the functional derivative (3.38) in powers of the smallness parameter ϵ, obtaining

$$\begin{aligned}
\frac{\delta E_\mathrm{r}}{\delta h}=\frac{k_\mathrm{c}}{2}\hat{\nabla}\cdot\Bigg\{&\frac{2\epsilon}{l_0^3}\hat{\nabla}\hat{\Delta}H-\frac{\epsilon\varkappa_0^2}{l_0}\hat{\nabla}H-\frac{4\epsilon^2\varkappa_0}{l_0^2}\left[(\hat{\Delta}H)\hat{\nabla}H-\frac{1}{2}\hat{\nabla}(\hat{\nabla}H)^2\right]+\frac{5\epsilon^3}{l_0^3}(\hat{\Delta}H)^2\hat{\nabla}H\\
&-\frac{\epsilon^3}{l_0^3}\hat{\nabla}\left[3(\hat{\Delta}H)(\hat{\nabla}H)^2+2(\hat{\nabla}H)\cdot\hat{\nabla}(\hat{\nabla}H)^2\right]\Bigg\}+\mathcal{O}\left(\epsilon^4\right).
\end{aligned}$$

By inserting this result into equation (3.30) and expanding the remaining terms in powers of ϵ as well, one obtains, after dropping terms of higher order in ϵ, the following formula, which is a generalization of eq. (2.31):

$$-P+\Pi=\bar{\mathrm{Ca}}_{\mathrm{I}}^{-1}\hat{\Delta}H+\bar{\mathrm{Ca}}_{\mathrm{II}}^{-1}\hat{\Delta}^2H,$$

where two new "capillary numbers" are defined as

$$\bar{\mathrm{Ca}}_{\mathrm{I}}^{-1}=\frac{\epsilon^3}{U_0\mu}\left(\sigma-\frac{k_{\mathrm{c}}x_0^2}{2}\right)\quad\text{and}\quad\bar{\mathrm{Ca}}_{\mathrm{II}}^{-1}=\frac{\epsilon^3}{U_0\mu}\frac{k_{\mathrm{c}}}{2l_0^2}. \tag{3.39}$$

With this result at hand, one can follow the remaining steps of the derivation outlined in section 2.4 to obtain the time evolution equation

$$\partial_T H=-\nabla\cdot\left\{\frac{H^3}{3}\nabla\left[\bar{\mathrm{Ca}}_{\mathrm{I}}^{-1}\Delta H-\bar{\mathrm{Ca}}_{\mathrm{II}}^{-1}\Delta^2H-\Pi(H)\right]\right\}, \tag{3.40}$$

where we have again dropped the hat above the dimensionless differential operators as they do not have to be distinguished from their dimensionful counterparts, anymore. It is a noteworthy result that the thin film dynamics does not depend on the sign of the spontaneous curvature, but only on its absolute value.

Typical values for the bending modulus and the spontaneous curvature are $k_{\mathrm{c}}\approx 10^{-19}\,\mathrm{J}$ [DBAB+05, MDLS04] and $|x_0|\approx 10^7\,\mathrm{m}^{-1}$ - $10^9\,\mathrm{m}^{-1}$ [KCF+05], respectively. One can thus roughly estimate $k_{\mathrm{c}}x_0^2/2\approx 10^{-5}\,\mathrm{J/m^2}$ - $10^{-1}\,\mathrm{J/m^2}$. Comparing this range of values to the surface tension of water in absence of any surfactant, $\sigma_{\mathrm{abs}}\approx 72\times 10^{-2}\,\mathrm{J/m^2}$, we note that the contribution due to spontaneous curvature can be of the same order of magnitude or even larger. The latter implies that spontaneous curvature can lead to a *negative effective surface tension*. Assuming $l_0\approx 10^{-7}\,\mathrm{m}$ - $10^{-6}\,\mathrm{m}$ one can further estimate $k_{\mathrm{c}}/(2l_0^2)\approx 10^{-7}\,\mathrm{J/m^2}$ - $10^{-5}\,\mathrm{J/m^2}$. Thus, $\bar{\mathrm{Ca}}_{\mathrm{II}}^{-1}$ will in most cases be orders of magnitude smaller than $\bar{\mathrm{Ca}}_{\mathrm{I}}^{-1}$.

3.3.2 Linear stability of flat films

To compare the dynamics of a thin liquid film with a rigid surface layer to that of a clean film, the linear stability of the former is investigated in the present section and then compared to the results listed in section 3.1. By looking at small perturbations $\eta(\vec{X},T)$ of a homogeneous film of thickness $\hat{H}$, that is, $H(\vec{X},T)=\hat{H}+\eta(\vec{X},T)$, linearization of eq. (3.40) yields

$$\eta(\vec{X},T)_{,T}=-\frac{\hat{H}^3}{3}\left[\left.\frac{\partial\Pi}{\partial H}\right|_{\hat{H}}\Delta+\mathrm{Ca}_{\mathrm{I}}^{-1}\Delta^2+\mathrm{Ca}_{\mathrm{II}}^{-1}\Delta^4\right]\eta(\vec{X},T).$$

Employing the plane wave ansatz $\eta\sim\mathrm{e}^{\mathrm{i}\vec{k}\cdot\vec{X}-\omega T}$, one obtains the dispersion relation

$$\omega(k)=-\frac{\hat{H}^3}{3}k^2\left[\hat{\Pi}'+\bar{\mathrm{Ca}}_{\mathrm{I}}^{-1}k^2+\bar{\mathrm{Ca}}_{\mathrm{II}}^{-1}k^4\right]. \tag{3.41}$$

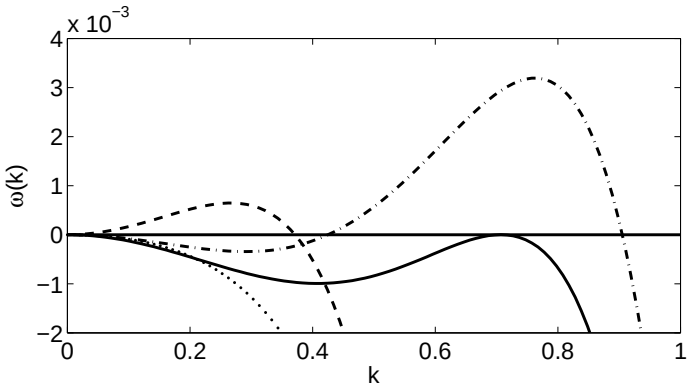

Fig. 3.12: Dispersion relation $\omega(k)$ for four different parameter sets: $\bar{\mathrm{Ca}}_{\mathrm{I}}^{-1} = -0.1$, $\bar{\mathrm{Ca}}_{\mathrm{II}}^{-1} = 0.1$, and $\hat{\Pi}' = 0.025$ (solid line); $\bar{\mathrm{Ca}}_{\mathrm{I}}^{-1} = -0.1$, $\bar{\mathrm{Ca}}_{\mathrm{II}}^{-1} = 0.1$, and $\hat{\Pi}' = 0.0148$ (dash-dotted line); $\bar{\mathrm{Ca}}_{\mathrm{I}}^{-1} = 0.1$, $\bar{\mathrm{Ca}}_{\mathrm{II}}^{-1} = 0.1$, and $\hat{\Pi}' = -0.0157$ (dashed line); and $\bar{\mathrm{Ca}}_{\mathrm{I}}^{-1} = 0.1$, $\bar{\mathrm{Ca}}_{\mathrm{II}}^{-1} = 0.1$, and $\hat{\Pi}' = 0.0148$ (dotted line). Source: [KGWF11].

This result complies with the physical intuition that, for a vanishing spontaneous curvature, the bending rigidity will damp short wavelength fluctuations and thus has a stabilizing influence. However, if $\mathrm{Ca}_{\mathrm{I}}^{-1}$ takes negative values, this leads to an instability for intermediate wavenumbers: For negative $\mathrm{Ca}_{\mathrm{I}}^{-1}$ and $\hat{\Pi}' = \mathrm{Ca}_{\mathrm{I}}^{-2}/(4\mathrm{Ca}_{\mathrm{II}}^{-1})$ the eigenvalue $\omega(k_{\mathrm{cr}})$ of mode $k_{\mathrm{cr}} = \sqrt{-\mathrm{Ca}_{\mathrm{I}}^{-1}/(2\mathrm{Ca}_{\mathrm{II}}^{-1})}$ crosses the imaginary axis. For $0 < \hat{\Pi}' < \mathrm{Ca}_{\mathrm{I}}^{-2}/(4\mathrm{Ca}_{\mathrm{II}}^{-1})$ and $\mathrm{Ca}_{\mathrm{I}}^{-1} < 0$ there is a band of unstable modes k with $k_1 < k < k_2$ and

$$k_{1,2} = \sqrt{\frac{-\bar{\mathrm{Ca}}_{\mathrm{I}}^{-1} \mp \sqrt{\bar{\mathrm{Ca}}_{\mathrm{I}}^{-2} - 4\bar{\mathrm{Ca}}_{\mathrm{II}}^{-1}\hat{\Pi}'}}{2\bar{\mathrm{Ca}}_{\mathrm{II}}^{-1}}}\,, \tag{3.42}$$

so that $k_1 = 0$ for negative $\hat{\Pi}'$ and arbitrary values of $\mathrm{Ca}_{\mathrm{I}}^{-1}$. The wavenumber corresponding to the maximum of $\omega(k)$, that is, the most unstable mode, is given by

$$k_{\max} = \sqrt{\frac{-\bar{\mathrm{Ca}}_{\mathrm{I}}^{-1} + \sqrt{\bar{\mathrm{Ca}}_{\mathrm{I}}^{-2} - 3\bar{\mathrm{Ca}}_{\mathrm{II}}^{-1}\hat{\Pi}'}}{3\bar{\mathrm{Ca}}_{\mathrm{II}}^{-1}}}\,, \tag{3.43}$$

with

$$\begin{aligned}\omega(k_{\max}) = &-\frac{\hat{H}^3}{81\bar{\mathrm{Ca}}_{\mathrm{II}}^{-2}}\left(-\bar{\mathrm{Ca}}_{\mathrm{I}}^{-1} + \sqrt{\bar{\mathrm{Ca}}_{\mathrm{I}}^{-2} - 3\bar{\mathrm{Ca}}_{\mathrm{II}}^{-1}\hat{\Pi}'}\right)\\ &\times\left(6\bar{\mathrm{Ca}}_{\mathrm{II}}^{-1}\hat{\Pi}' - \bar{\mathrm{Ca}}_{\mathrm{I}}^{-2} + \bar{\mathrm{Ca}}_{\mathrm{I}}^{-1}\sqrt{\bar{\mathrm{Ca}}_{\mathrm{I}}^{-2} - 3\bar{\mathrm{Ca}}_{\mathrm{II}}^{-1}\hat{\Pi}'}\right).\end{aligned} \tag{3.44}$$

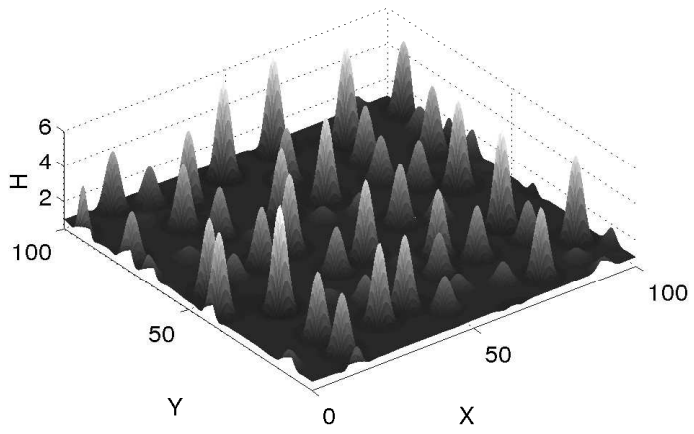

Fig. 3.13: Snapshot from a numerical simulation of film breakup with $\mathrm{Ca}_{\mathrm{I}}^{-1} = -0.1$ and $\mathrm{Ca}_{\mathrm{II}}^{-1} = 0.1$. Source: [KGWF11].

A numerical simulation of a randomly perturbed flat film with $\mathrm{Ca}_{\mathrm{I}}^{-1} = -0.1$ and $\mathrm{Ca}_{\mathrm{II}}^{-2} = 0.1$ was carried out using the disjoining pressure specified in eq. (3.3). The simulated situation is then precisely corresponding to the dash-dotted line in figure 3.12. The longterm evolution of the thin film is very similar to that of the clean film. Initially flat, the film quickly breaks up into small droplets which then undergo a process of coarsening, as is commonly observed after film rupture. A snapshot of a simulation on a periodic two-dimensional square domain of size 100×100 is shown is fig. 3.13.

3.3.3 The shape of a drop covered with a rigid layer

In this section, we want to address the question how the shape of the droplets is affected by a nonzero surface rigidity. For this purpose, stationary state solutions of eq. (3.40) on a periodic one dimensional domain are considered. These are obtained numerically by relaxation, that is, direct numerical simulation of a system that relaxes toward the stationary state.

When a stationary state is obtained for one set of parameters, that state is used as the initial condition for a subsequent run with slightly different parameters. Thus, the overall volume of liquid within the integration domain remains constant throughout a whole parameter scan.

In the first scan, $\bar{\mathrm{Ca}}_{\mathrm{II}}^{-1}$ is held constant while $\bar{\mathrm{Ca}}_{\mathrm{I}}^{-1}$ is varied from 0 to -0.1 and the domain size is $L = 100$. The obtained shape of the droplet depends sensitively on $\bar{\mathrm{Ca}}_{\mathrm{I}}^{-1}$, as can be seen in on the left of fig. 3.14. The drop becomes steeper and develops more and more pronounced undershoots below the precursor height $H = 1$ as the parameter is decreased. During a second parameter scan, $\bar{\mathrm{Ca}}_{\mathrm{I}}^{-1} = 0.1$ is fixed while $\bar{\mathrm{Ca}}_{\mathrm{II}}^{-1}$ is varied from 0 to 50, as is shown on the right of fig. 3.14. The domain size in this run is $L = 400$.

These results indicate that the scaled bending modulus $k_c/(2l_0^2)$ needs to be 10-100 times higher than the effective surface tension in order to change the shape of the droplet significantly.

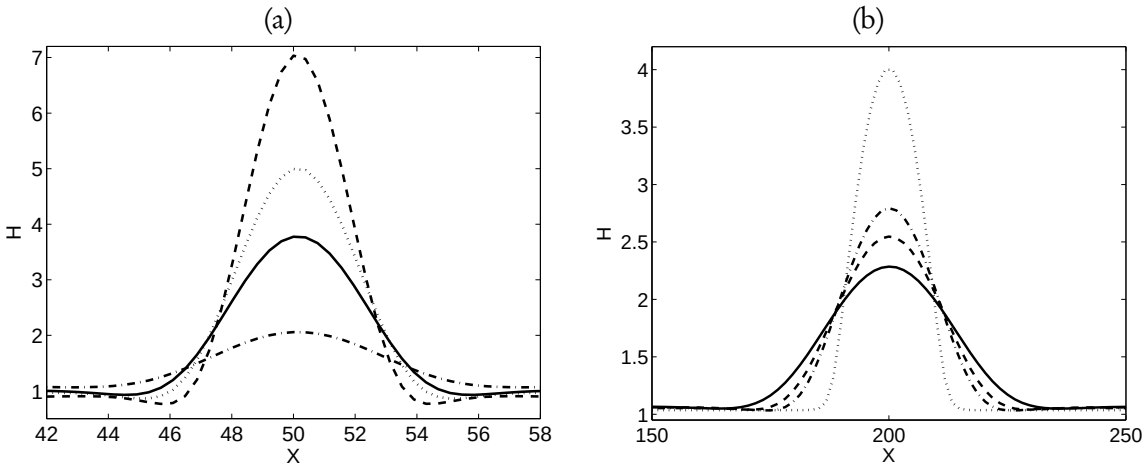

Fig. 3.14: Different shapes of droplets obtained for various choices of the capillary numbers $\mathrm{Ca}_{\mathrm{I}}^{-1}, \mathrm{Ca}_{\mathrm{II}}^{-1}$. (a) $\mathrm{Ca}_{\mathrm{II}}^{-1} = 0.1$ in all four cases, $\mathrm{Ca}_{\mathrm{I}}^{-1} = 0$ (dash-dotted line); $\mathrm{Ca}_{\mathrm{I}}^{-1} = -0.05$ (solid line); $\mathrm{Ca}_{\mathrm{I}}^{-1} = -0.07$ (dotted line); $\mathrm{Ca}_{\mathrm{I}}^{-1} = -0.1$ (dashed line). The image shows a closeup of a stationary state on a periodic domain of size $L = 100$. (b) $\mathrm{Ca}_{\mathrm{I}}^{-1} = 0.1$ in all four cases, $\mathrm{Ca}_{\mathrm{II}}^{-1} = 0$ (dotted line); $\mathrm{Ca}_{\mathrm{II}}^{-1} = 10$ (dash-dotted line); $\mathrm{Ca}_{\mathrm{II}}^{-1} = 30$ (dashed line); $\mathrm{Ca}_{\mathrm{II}}^{-1} = 50$ (solid line). The image shows a closeup of a stationary state on a periodic domain of size $L = 400$. Source: [KGWF11].

3.3.4 Estimation of the effect on the formation of LE-LC stripe patterns[6]

Now that surface rigidity has been included in the lubrication theory model of monolayer covered thin liquid films, one can estimate its effect on the formation of the stripe-patterns that we are going to investigate in the following chapters. During the pattern formation, the monolayer is either in the LE or in the LC phase. Significant bending rigidity is experimentally observed only after the transition from LC to a solid (S) state and spontaneous curvature is negligible. Even if the monolayer were entirely in the S phase, which is much more rigid than the LC phase, a DPPC monolayer has a bending rigidity of $k_c \leq 3 \times 10^{-20}\,\mathrm{J}$ [DBB90]. With $l_0 \approx 10^{-7}\,\mathrm{m}$ one can estimate that in this case $k_c/2l_0^2 \approx 10^{-5}\,\mathrm{J/m^2}$. This value is three orders of magnitude smaller than the surface tension of water and it is therefore safe to neglect it in the considered regime close to the main transition. Nevertheless, for other problems that involve materials with rigidities of a few hundred $k_\mathrm{B}T$ or more, it is necessary to include the terms $\sim \mathrm{Ca}_{\mathrm{II}}^{-1}$ derived here in order to obtain accurate results.

[6]The estimation outlined in this subsection has been published in [KGF11] on pages 2–3.

4 Transfer onto homogeneous substrates[1]

The basic differential equations for the description of surfactant covered thin liquid films with monolayers close to a first order phase transition have been derived and investigated in the last two chapters. Now, the model will be applied to the problem of Langmuir-Blodgett transfer. This can be achieved by a suitable choice of boundary conditions. The transfer process is then investigated numerically in order to obtain the dependence of the stripe pattern formation on the main control parameter, the transfer velocity V. The chapter is then concluded with a section on the influence of the subphase temperature on the stripe formation, a problem that has been investigated experimentally by Harder et al., very recently [Har11].

4.1 Choice of parameters

In the following calculations the scaling outlined in section 3.2.1, so that the central equations are given by eqs. (3.18) and (3.19). The Hamaker constant, a_3 that quantifies the substrate-liquid interaction, is set to a typical value of $a_3 = 1/(12\pi) \times 10^{-20}\,\mathrm{J}$ (see [Bes06], section 8.6.6). Further, the precursor height is assumed to be $h_\mathrm{p} \approx 5.8\,\mathrm{nm}$, yielding, according to eq. (3.12), the dimensionless Hamaker constant $A = 6.5 \times 10^{-2}$. The critical number density of the main-transition is taken to be $\gamma_\mathrm{cr} = 1.539 \times 10^{18}\,\mathrm{m}^{-2}$, corresponding to the center of the coexistence plateau of the isotherm shown in fig. 1.3. From the same data, one can estimate $\sigma_\mathrm{cr} \approx 0.9\sigma_\mathrm{abs} = 65.48\,\mathrm{mN/m}$. The isotherm is then reasonably well approximated by using the parameters $M_1 = 50$ and $M_2 = 0.2$. By this choice $\Gamma_\mathrm{LE} = 0.8$ and $\Gamma_\mathrm{LC} = 1.2$. The surfactant domain line tension is assumed to be $\varkappa = 5 \times 10^{-52}\,\mathrm{Jm}^4$. With these values, the characteristic time and length scales can be calculated by use of eqs. (3.13) and (3.14). They are given by $t_0 = 25.23\,\mu\mathrm{s}$ and $l_0 = 134.49\,\mathrm{nm}$. This yields the smallness parameter $\epsilon = 4.31 \times 10^{-2}$. Diffusion is not considered, that is, $\vec{I} = 0$, due to the argument given in section 3.2.2. The evaporation parameters used in the simulation are given by $E_\mathrm{ev} = 0.45$ and $\mu_\mathrm{v} = 5 \times 10^{-4}$, amounting to an effective rate constant $q_\mathrm{e} = 4.93 \times 10^{-9}\,\mathrm{m^2 s/kg}$. The SMC coupling constant is set to $B = 1500$, corresponding to a lateral pressure shift of $\delta p_\mathrm{lat} = S(H_\mathrm{p})\sigma_0 = -3AB\sigma_0/10 \approx -3.6\,\mathrm{mN/m}$. This means, that the coexistence lateral pressure at the substrate is roughly 50% lower than for the floating monolayer.

4.2 Boundary and initial conditions

Since we are interested in the region where the substrate-mediated condensation takes place, our reference frame will be located around the meniscus, the region where the substrate touches the surface of the water bath in the Langmuir trough. In our model system, we consider a finite domain $X \in [0, L]$, whose right boundary is connected to the water reservoir which ensures a

[1] This chapter contains an extended presentation of results published in [KGFC10] and [KGF11].

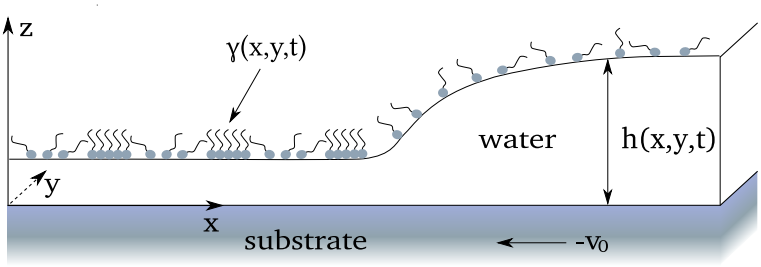

Fig. 4.1: Schematic drawing of a surfactant-laden meniscus. Source: [KGF11].

constant film-height at $X = L$ (see fig. 4.1). The solid substrate is withdrawn from the bath into the negative X-direction, thereby carrying water into the domain. A balance between the supply of fresh water and evaporation leads to the formation of a meniscus which is at rest in our reference frame but moving relatively to the substrate.

The water bath itself is assumed to be covered with a surfactant monolayer of constant density, corresponding to the pure LE phase, which is perpetually carried along with the water towards the contact line at the end of the meniscus. When the layer comes close enough to the solid, the substrate-mediated condensation sets in and leads - within a certain parameter range - to the formation of LC domains.

Ideally, the left boundary of the system would simply be perfectly permeable, so that the material would just leave the domain to the left. For equations like eqs. (2.35) and (2.36), such non-reflective boundary conditions are complicated to implement. The simpler approach, which we are following here, is to demand the first and second derivative of H and Γ to vanish at $X = 0$. Thorough testing has shown that this choice leads to an effective non-reflectiveness of the left boundary, since there are only very small boundary effects which are limited to the close vicinity of the integration domain. Running simulations on three different domain sizes $L = 1200$, 2400 and 3600, no influence of the left boundary on the pattern formation at the meniscus was observed.

The above considerations lead to the following choice of boundary conditions [2]:

$$\Gamma(L) = \Gamma_L, \qquad \Gamma_{,XX}(L) = 0 = \Gamma_{,X}(0) = \Gamma_{,XX}(0) \tag{4.1}$$

$$H(L) = H_L, \qquad H_{,XX}(L) = 0 = H_{,X}(0) = H_{,XX}(0). \tag{4.2}$$

In all two-dimensional calculations, the boundary conditions in Y-direction are chosen to be periodic.

It should be noted at this point, that our approach using the boundary conditions given by eqs. (4.1) and (4.2), yields a very simple model of a moving contact line. However, as always this simplicity comes at a price: Our model contains the meniscus height H_L as a parameter. In reality, H_L is a quantity that cannot be controlled by the experimenter operating the Langmuir-Blodgett transfer device. It rather results from the actual transfer hydrodynamics. As has been mentioned in subsection 3.1.4 it is - even in absence of surfactants - a highly nontrivial problem to determine

[2] Similar boundary conditions are used by Doumenc and Guerrier in the investigation of a closely related physical problem: the drying of a solution in a meniscus in contact with a moving substrate [DG10].

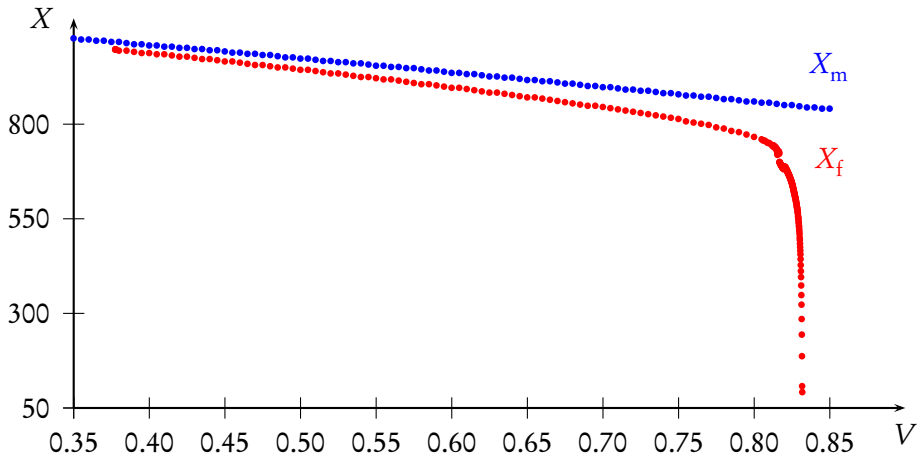

Fig. 4.2: Position of the contact line and of the front where the new domains are formed against pull velocity V. One can clearly see, that the front detaches from the contact line at $V \approx 0.83$.

the shape of a meniscus and the dynamical contact angle observed at a moving substrate. Our approach requires to choose H_L according to the following argument: The monolayer on the water reservoir in the trough is assumed to be of constant density. This is experimentally realized, since the Langmuir trough can be set up to automatically adjust the movable barriers to keep a constant lateral pressure throughout the whole transfer. Close to the contact line, however, where the dynamical process behind the pattern formation is taking place, the surfactant density varies locally. Thus, the contact line has to be sufficiently far away from the right boundary, so that we can safely assume the monolayer to be approximately constant at that point. Since the value H_L determines the height and implicitly also the horizontal distance of the contact line to the right boundary, we have to choose H_L, so that this assumption is justified. Here, we set the surfactant density at the right boundary to $\Gamma_L = 0.835$ and the film height is set to $H_L = 2.5$. The initial conditions are

$$\begin{aligned} \Gamma(\vec{X},0) &= \Gamma_L + (\Gamma_{cr} - \Gamma_L)\left(1 - \tanh\frac{X - 0.94L}{L/140}\right), \\ H(\vec{X},0) &= H_p + (H_L - H_p)\exp\left(-\frac{(L-X)^2}{500}\right), \end{aligned}$$

that is, we use a kink-like density function going from $\Gamma_{cr} + \Gamma_L \approx \Gamma_{LC}$ to Γ_L for the surfactant and a Gaussian water drop centered at $X = L$ for H. Both initial conditions are also slightly perturbed by addition of random noise of amplitude 0.1. However, this specific choice is not essential for our results, since it does not affect the long-time evolution of the system. It takes only very short simulation time until the film profile takes the shape of an almost entirely stationary meniscus. The shape of this meniscus is determined by the balance of evaporation and the supply of fresh water that depends on H_L and the advection velocity V. Figure 4.2 shows the horizontal extent of the meniscus, that is, the position of the contact line, as a function of V.

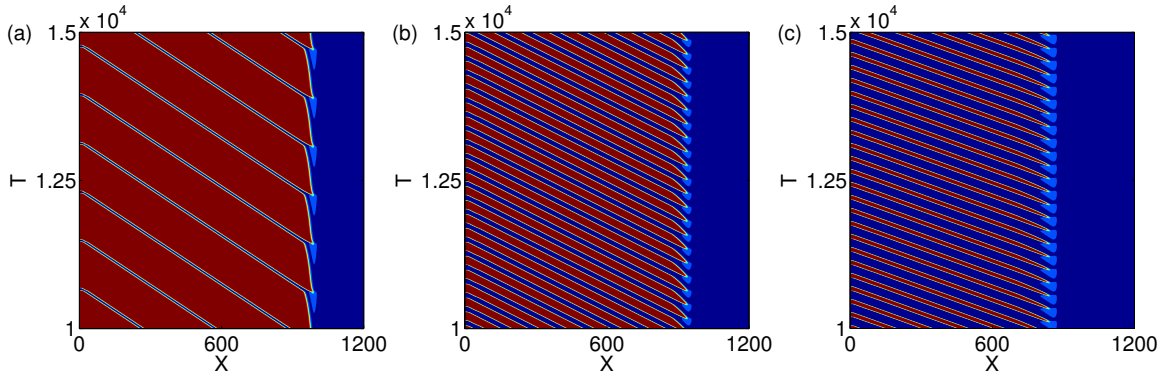

Fig. 4.3: Space-time plots of the one-dimensional numerical simulation of the monolayer transfer process using three different transfer velocities: (a) $V = 0.385$, (b) $V = 0.500$, and (c) $V = 0.700$. Only the monolayer density is shown. Blue indicates the liquid-expanded phase, red corresponds to the liquid-condensed parts of the monolayer. Source: [KGF11]

4.3 The one-dimensional case

Using the initial and boundary conditions described in the preceding section, we solved eqs. (2.35) and (2.36) in the one-dimensional case numerically for different transfer velocities V. In this parameter scan, different operation regimes of the system are found. For small velocities the substrate is coated with a homogeneous LC monolayer. Increasing the velocity beyond a critical value $V_{\mathrm{cr,l}} \approx 0.38$, the homogeneous transfer becomes unstable and a periodic spatiotemporal pattern is created. This pattern consists of alternating domains of the LE and the LC phase (see figure 4.4). These domains are created at the contact line and detach from it, as soon as they have reached the full density of the LC phase. This behavior can be seen in the space-time plots shown in fig. 4.3.

The overall wavelength as well as the ratio of the width of the LE and LC stripes depends on the transfer velocity, as is shown in fig. 4.4. For small velocities, one obtains broad LC domains divided by very narrow LE stripes. Upon increase of V, the LC domains become narrower while the LE stripes grow, until equally sized domains of both phases are transferred for $V \approx 0.52$. For even higher velocities, the LE domains become broader and broader, until eventually an upper velocity bound $V_{\mathrm{cr,u}} \approx 0.83$ is reached, beyond which the transfer becomes purely homogeneous again, coating the whole substrate with a LE monolayer. In the remainder of this thesis, the range $(V_{\mathrm{cr,l}}, V_{\mathrm{cr,u}})$ will be referred to as the *patterning range*.

Due to the fact that $k(V)$ is non-monotonous there are pairs of patterns with equal k but different V. At first glance, the two patterns comprising such a pair are roughly inverse to each other. However, a closer examination reveals that they differ in detail. This can be seen by comparison of the two profiles shown in fig. 4.5. Their wavelength $\lambda \approx 200$ is equal but they exhibit different structure. If they were perfectly inverse to each other, the LE domains in fig. 4.5 (a) would be of the same size as the LC domains in fig. 4.5 (b). In reality, the former are narrower than the latter. As will be shown in the following chapter, this fact will have measurable consequences for the transfer onto prepatterned substrates.

Away from the contact line, the surfactant domains are subject to coarsening and the pattern is

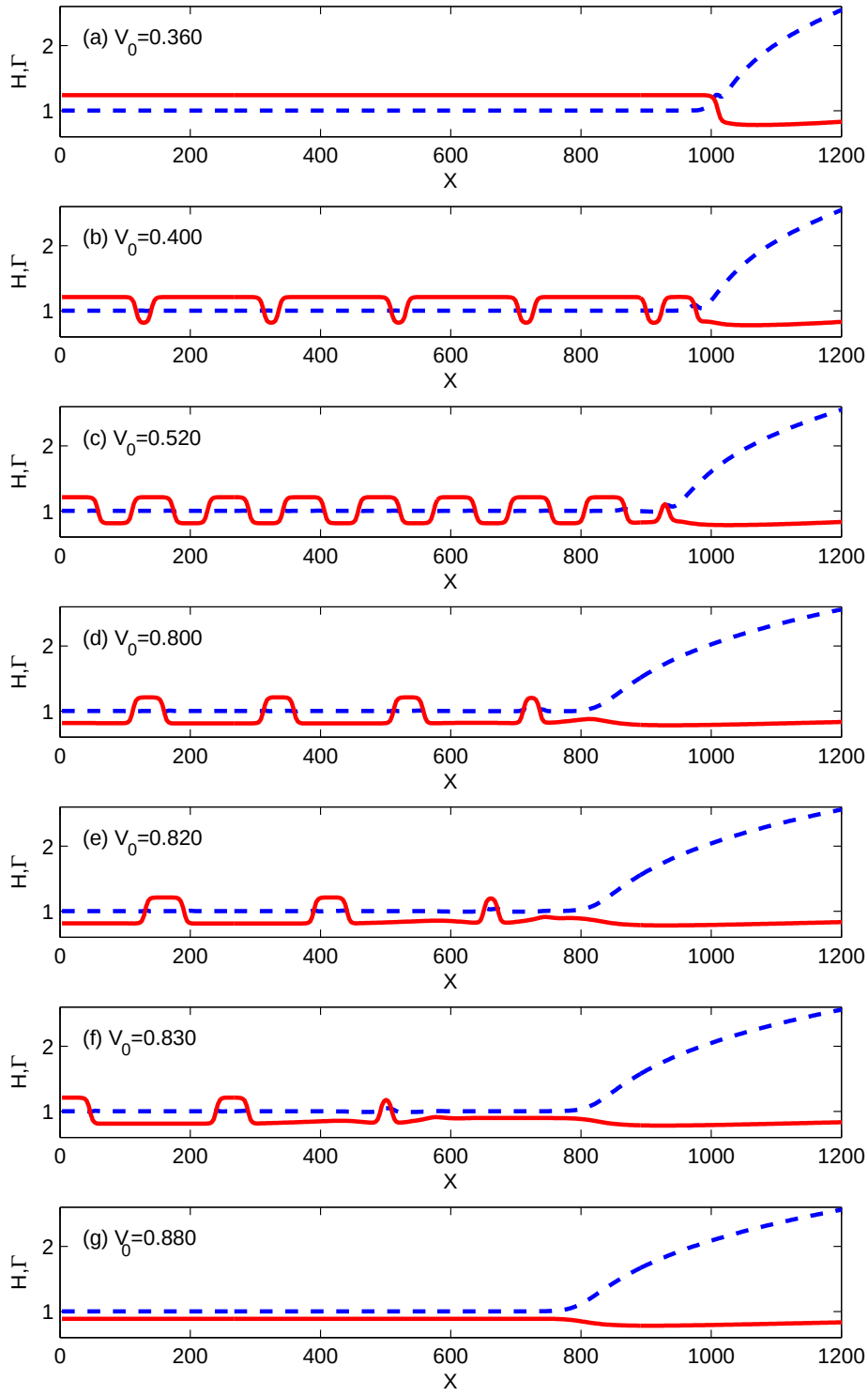

Fig. 4.4: Snapshots from one-dimensional computations of monolayer transfer with seven different velocities. The solid red line is the density of the monolayer whereas the dashed blue line is the height profile of the water film. The letters (a-g) correspond to the labels in fig. 4.6.

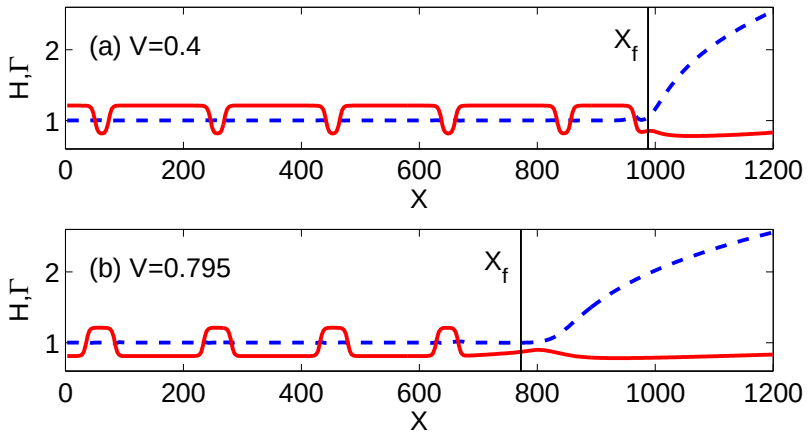

Fig. 4.5: Patterns of equal wavelength, $\lambda \approx 200$, obtained from one-dimensional simulations at different velocities V on a homogeneous substrate: (a) $V = 0.4$ and (b) $V = 0.795$. The solid red line corresponds to monolayer density Γ, while the blue dashes represent the height profile. H. The patterns are *almost* inverse to each other. The solid vertical lines indicate the location X_f where new domains are created. Source: [KGF11]

slightly distorted while moving downstream. Instead of looking at the resultant spatial structures, one can focus on the density oscillations at the location X_f at the contact line, where the new domains are created (see fig. 4.5). Naturally, this location depends on V, as the meniscus is more and more elongated with increasing velocity (see fig. 4.2). The surfactant density at the position X_f is then sampled as a time series $s(T) := \Gamma(X_\mathrm{f}, T)$. By making use of tools from signal analysis to define an instantaneous phase $\phi_s(T)$ of the "signal" $s(T)$. To this end, the Hilbert transform $s_\mathrm{H}(T)$ of $s(T)$ is calculated and used to construct the analytic signal

$$\zeta(T) = s(T) + \mathrm{i}s_\mathrm{H}(T) := C(T)\exp\left(\mathrm{i}\phi_s(T)\right).$$

By this method, the signal is continued into the complex plane. The outlined procedure can be regarded as a generalization of the continuation of the sine and cosine functions to the exponential function [PRK03]. The frequency of the domain formation can finally be obtained as

$$\omega = \langle \mathrm{d}\phi_s/\mathrm{d}T \rangle, \tag{4.3}$$

where the brackets $\langle \ldots \rangle$ denote the time average. As the velocity V is known, the frequency can be translated into a wavelength $\lambda = 2\pi V/\omega$ and into a wavenumber $k = \omega/V$. The calculation of ω and k was implemented in MATLAB.

The velocity dependence can be summarized in a diagram displaying the wavenumber k as a function of the transfer velocity (see fig. 4.6). At the low-velocity boundary of the patterning range, the curve $k(V)$ seems to start from infinite wavelengths, that is, $k = 0$. This can of course not be proven by a numerical simulation but it can nevertheless be made plausible that the system in fact exhibits an infinite period bifurcation by consideration of a simplified model that is explained later in chapter 6. The curve then increases toward a maximum at $V \approx 0.53$ beyond which the wavenumber decreases slowly and almost linearly with increasing velocity. Close to $V_\mathrm{cr,u}$,

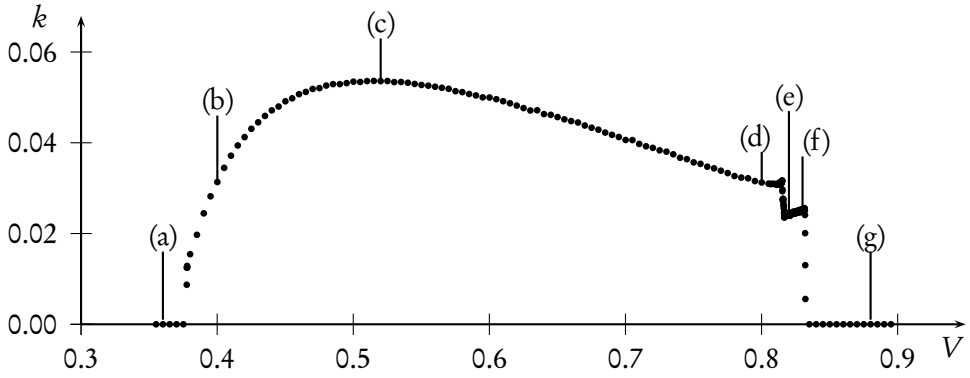

Fig. 4.6: Wavenumber k against transfer velocity V of patterns transferred onto homogeneous substrates obtained from one-dimensional computations. The curve is non-monotonous, so that the same k can be obtained for high and for low V.

at $V \approx 0.815$, the curve suddenly drops by a significant amount of ≈ 0.006 within a velocity interval of merely 0.003. The solutions from this interval cannot be assigned a single wavelength or frequency, as can be seen from the non-equidistant domains in the space-time plot shown in fig. 4.7 (a). To understand this, one has to take a closer look at the domain formation at the meniscus. New domains evolve from small bumps in the density Γ. In the considered velocity range around $V = 0.815$, not a single bump but a sequence of two or even three bumps detaches from the contact line (see fig. 4.7 (b)). As they grow, the small domains compete for the available material and, because they are close together, only a single domain of the sequence prevails. Sometimes, it is the first bump that succeeds, sometimes it is the second. This leads to variations in the distance between two subsequent domains. Therefore, the wavenumbers in the considered velocity interval have to be interpreted as time-averages in the sense of eq. (4.3). After the sudden drop, the curve $k(V)$ settles to a plateau that ends abruptly with a second steep drop which goes to $k = 0$ at $V = V_{\mathrm{cr,u}}$. Although it is impossible to obtain periodic solutions beyond this point, one observes very long transients before the system finally settles to homogeneous LE transfer.

It is noteworthy, that the meniscus remains almost static during the formation of the periodic monolayer structure. Only a tiny oscillation of the meniscus is observed whenever a new LC domain is created. Also a very small droplet detaches along with each newly created domain, but it evaporates quickly. All in all, the numerical results indicate that the dynamics of the water film plays only a minor role in the formation of the nanochannel lattices. This will be the starting point of a deeper theoretical analysis presented in chapter 6.

Instead of the transfer velocity V, one could also use the lateral pressure on the water reservoir as a control parameter. This quantity enters the model in form of the boundary condition Γ_L. Figure 4.8 shows the wavenumbers of patterns that are obtained from transfer at $V = 0.4$ for various values of Γ_L that can be converted into pressures $P_{\mathrm{hom}}(\Gamma_L)$ by use of eq. (3.17). The curve $k(P_{\mathrm{lat}}(\Gamma_L))$ is similar to the curve $k(V)$ shown in fig. 4.6 except that the patterns obtained at low lateral pressures are equivalent to those obtained at high velocities and vice versa. Thus, $P_{\mathrm{hom}}(\Gamma_L)$ and V can be seen as equivalent control parameters. In the following we will nevertheless focus on the transfer velocity as the main control parameter.

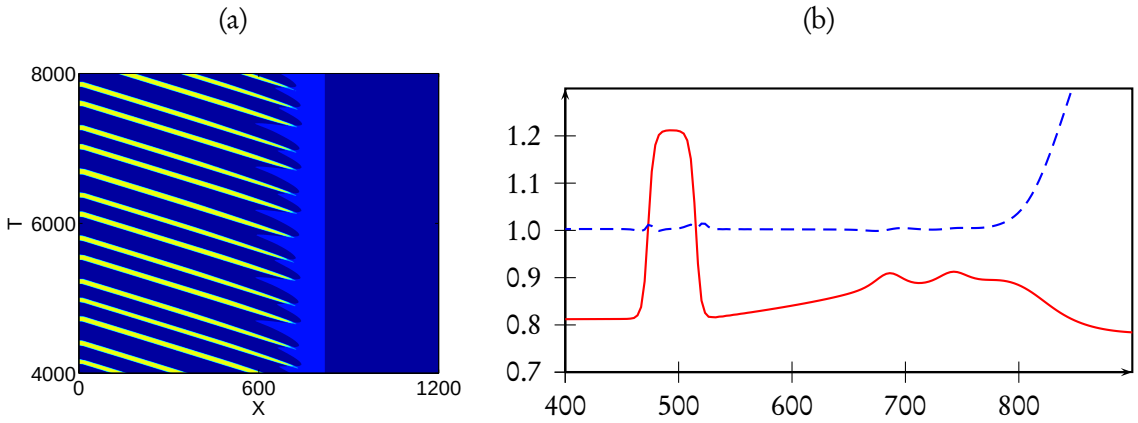

Fig. 4.7: Pattern formation at $V = 0.816$. The space-time plot (a) of the surfactant density Γ shows that the domains are not equidistant. A closeup of the contact line region (b) shows a sequence of bumps in Γ (red line). These bumps grow and compete for the available material. The blue dashes indicate the profile of the water film.

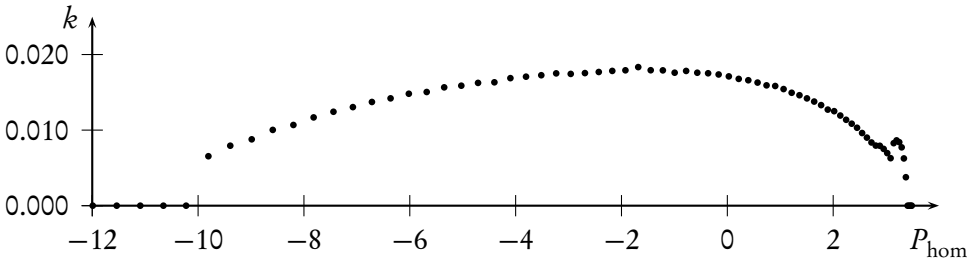

Fig. 4.8: Wavenumbers of the observed patterns obtained from a simulation of transfer at $V = 0.4$ against the lateral pressure on the water reservoir. $P_{\mathrm{hom}} = 0$ corresponds to the lateral pressure of a homogeneous monolayer with $\Gamma = \Gamma_{\mathrm{cr}}$.

4.4 The two-dimensional case

For most transfer velocities ($0.47 \lesssim V \lesssim 0.8$), the two-dimensional solutions look exactly like what one would expect from naively extrapolating the one-dimensional results: stripes parallel to the contact line correspond to the alternating domains of the one-dimensional solutions. However, the zoo of possible patterns is much richer in the two-dimensional case, although the interesting new structures appear only in narrow velocity ranges close to the lower and upper bound of the patterning range ($V_{\mathrm{cr,l}}, V_{\mathrm{cr,u}}$). For the corresponding velocities, the formation of parallel stripes is not stable: First, a few stripes are produced, but then the regularity breaks down and instead disordered patterns of holes and drops are obtained close to $V_{\mathrm{cr,l}}$ and $V_{\mathrm{cr,u}}$, respectively. Interestingly, for $0.38 \lesssim V \lesssim 0.46$ the disordered structures are themselves only transient and mark a transition to stripes perpendicular to the contact line. Figure 4.9 provides an overview of the various kinds of patterns that are obtained depending on the transfer velocity. For velocities lower than $V = 0.38$, a homogeneous LC layer is transfered. In the beginning of the patterning range, at $0.38 \lesssim V \lesssim 0.405$, fringes develop at the rim of the condensed layer close to the contact line. These fringes grow and elongate but before they can become stripes, their tip is constricted to a circular domain, breaks away, and is carried along with the moving substrate. With increasing velocity, a few of these fringes begin to eject larger and larger domains. At a certain velocity $V \approx 0.405$, these large domains merge into solid stripes perpendicular to the contact line. For velocities $0.410 \lesssim V \lesssim 0.455$ a direct transition from the formation of stripes parallel to the contact line to perpendicular stripes is observed, so that there is no intermediate state where fringes and circular LE domains can be observed. Such a transition is shown in fig. 4.10. If the wavelength of the perpendicular stripes is incommensurate with the size of the domain, the system cannot reach its optimal state and interesting defect structures are created (see fig. 4.11, left column). For velocities $V \lesssim 0.46$ that are at the boundary between the transfer of perpendicular and parallel stripes, one obtains intermediate structures which do not settle to either orientation. Instead, the patterns in these solutions seem to have a certain preferred angle ϑ, that is, stripes meeting the contact line under an angle of $\pi/2 \pm \vartheta$ are repeatedly created. Due to symmetry reasons, the system is indifferent to the sign of the deviation from the right angle, and therefore it takes a long time until a pattern with one orientation wins the competition and covers the complete domain (see fig. 4.11, right column). For $0.47 \lesssim V \lesssim 0.7$ stripes parallel to the contact line are transfered. Their structure shows the same dependence on the velocity as the one-dimensional solutions (see figs. 4.4 and 4.6). When $V \approx 0.82$, that is, for velocities close to $V_{\mathrm{cr,u}}$, the stripes become unstable again and break up into circular LC domains. However, these domains are still more or less aligned along periodic lines parallel to the contact line. For $V \gtrsim 0.83$ the formation of LC domains ceases completely and the substrate is covered with a homogeneous LE layer.

4.5 Comparison to experimental data

The numerically obtained curve $k(V)$ (see fig. 4.6) can be compared to similar diagrams obtained from experiments [CLH$^+$07, HFC08, CLZ$^+$06, LGFC05, Gle00]. Like in the theoretical model, the formation of stripes is observed experimentally in a certain velocity range. The qualitative agreement is striking: For low velocities, pattern with very large periods are observed. Then, for intermediate V, the minimal spatial periodicity is achieved. At the high velocity end of the patterning range, the periodicity increases again and finally, the range ends abruptly. Alas, the

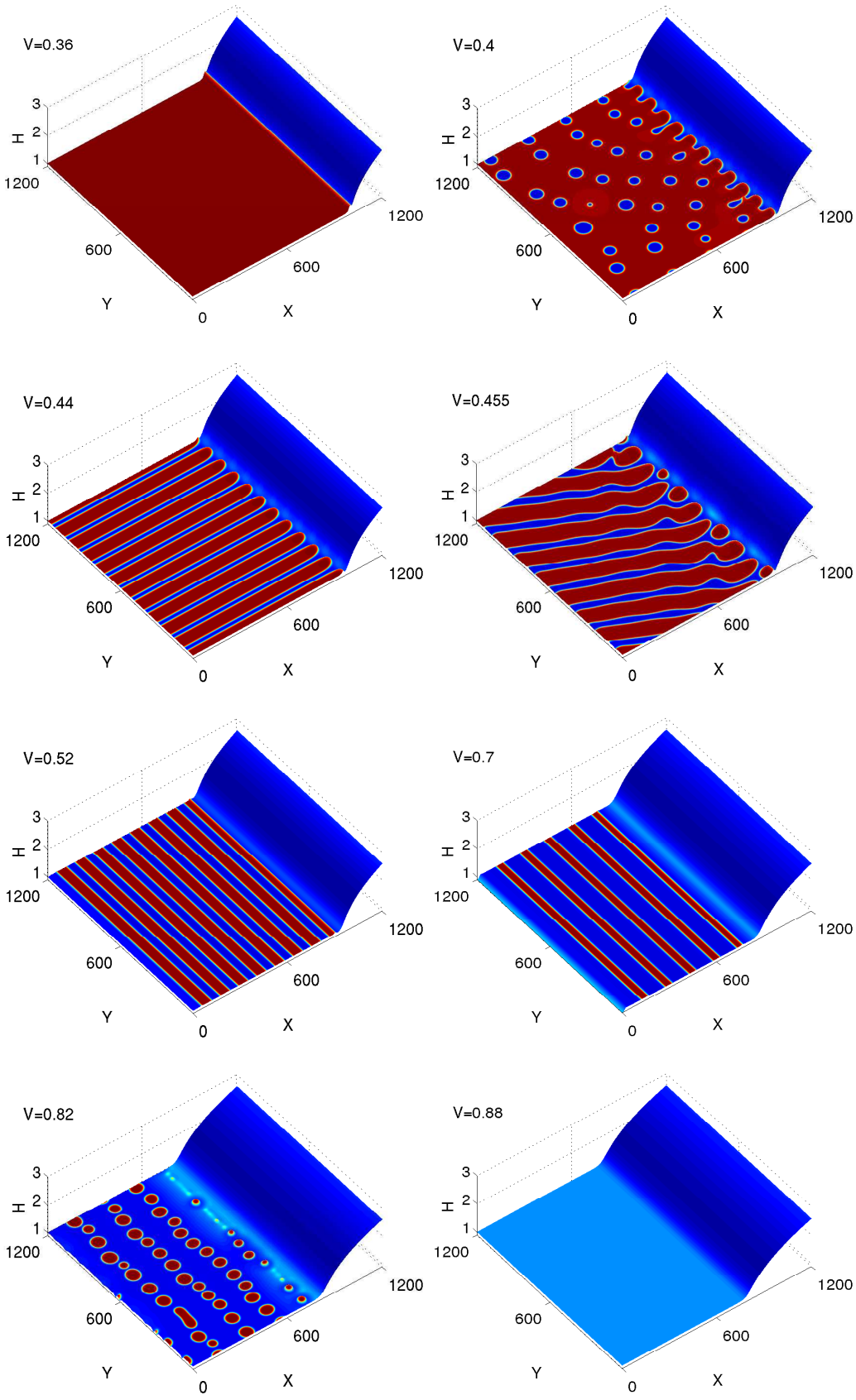

Fig. 4.9: The different regimes of transfer in the spatially two-dimensional case.

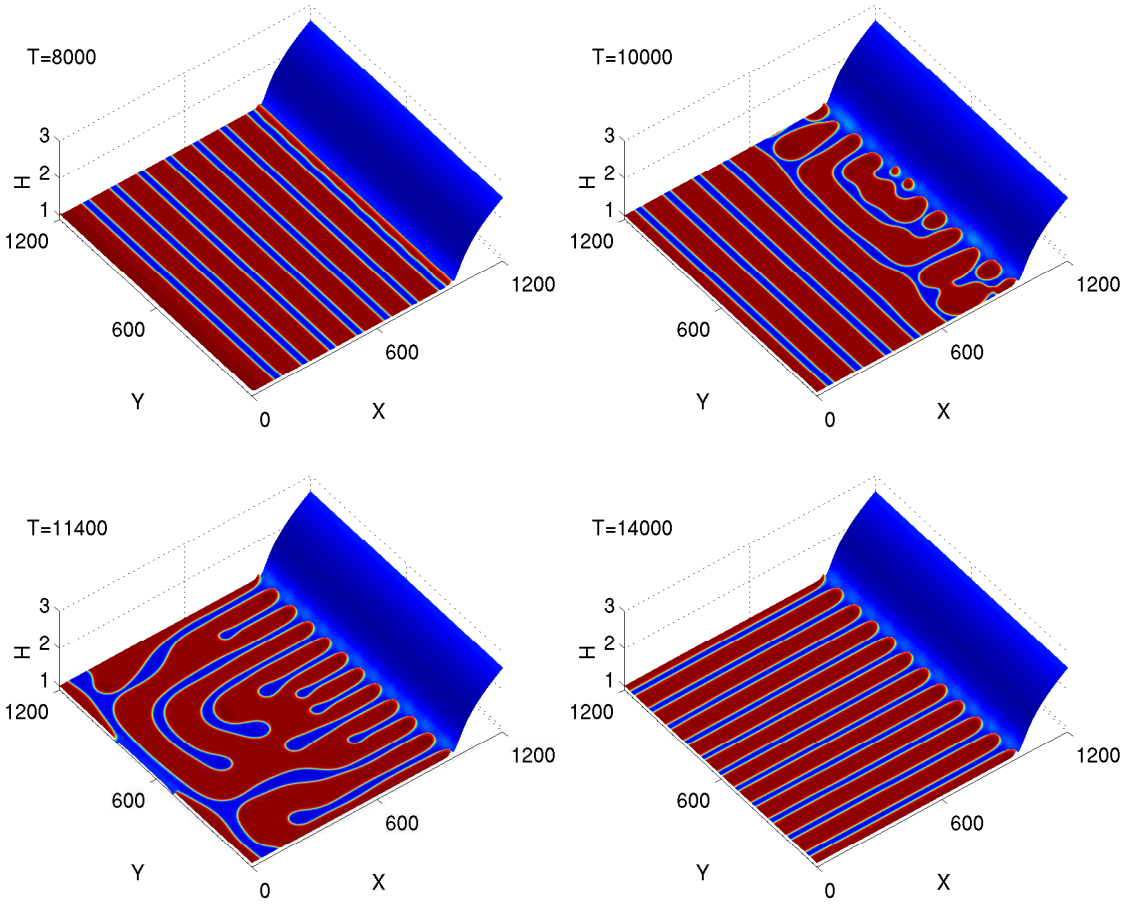

Fig. 4.10: The transition between stripes parallel to the contact line to stripes perpendicular to the contact line as observed at $V = 0.44$.

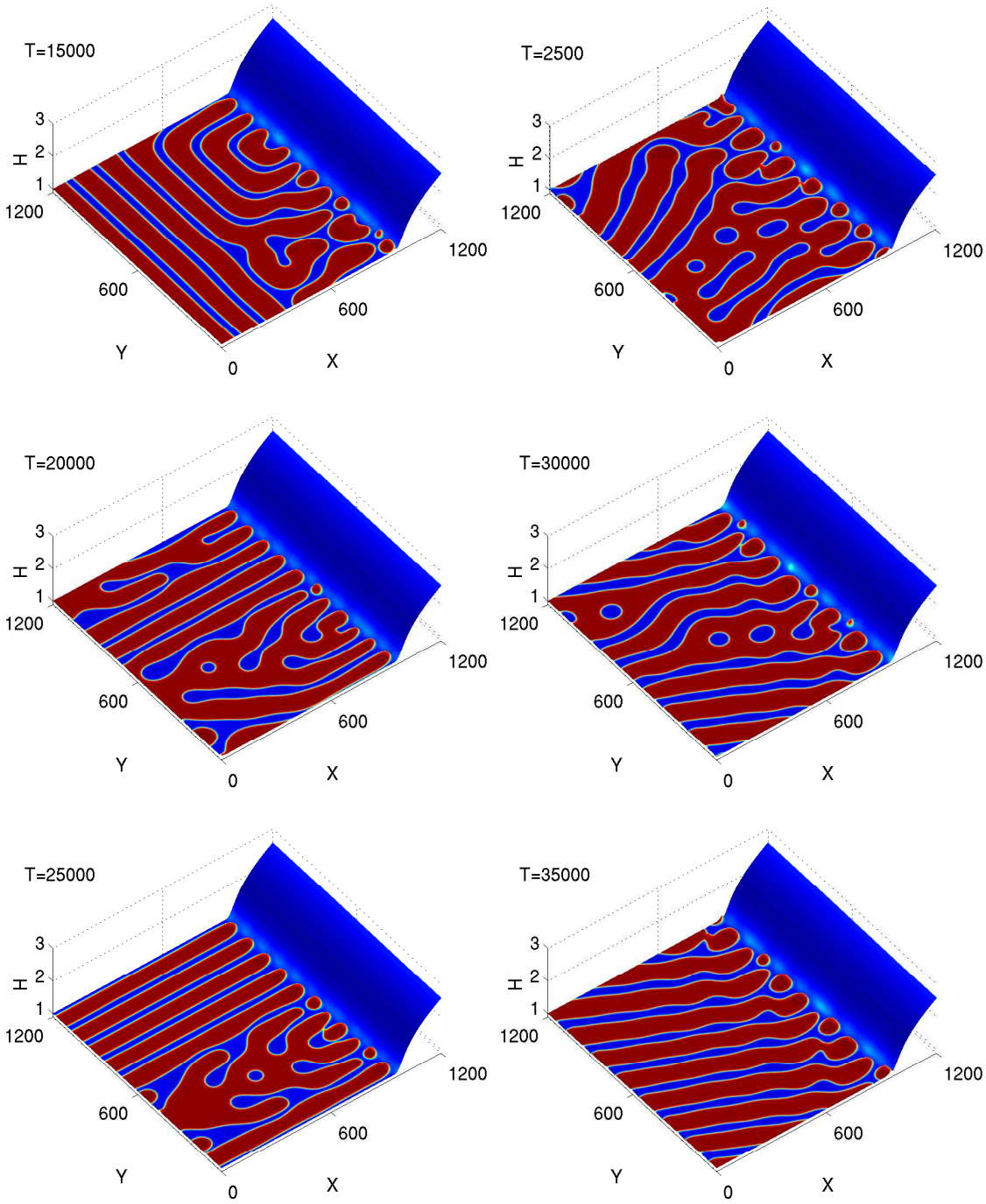

Fig. 4.11: Left column: Interesting defect structures can be observed if the domain size is not commensurate with the period length of the stripe pattern. This is shown here for $V = 0.45$. Right column: For $V = 0.455$, the competition between stripes parallel and perpendicular to the contact line results in a structure with inclined stripes.

number of data points in the experimental plots is very limited, ranging from 6–8 different velocity values. As can be seen in fig. 4.6, the curve $k(V)$ changes significantly within a small velocity interval at both ends of the patterning range. To resolve such details, experiments with 20–30 data points would be desirable.

The situation is better when the velocity is held constant while the monolayer density or equivalently the lateral pressure is considered as the control parameter. Lenhert et al. present a plot with the periodicities of stripe patterns obtained at $v = 8\,\mathrm{mm/min}$ and 25 different lateral pressures ranging from 0 to 5 mN/m [LGFC05]. The form of the curve $k(P_{\mathrm{hom}})$ from the theory (see fig. 4.8) and from the experiment are in good qualitative agreement.

As the model calculations correctly predict, the formation of stripes perpendicular to the contact line are observed for low velocities, close to the left boundary of the patterning range. Chen et al. present a phase diagram showing which patterns are obtained for several different values of the lateral pressure and the transfer velocity [CLZ+06].

Clearly, it is difficult to achieve quantitative agreement. This difficulty stems from the fact that the calculation involves a number of material parameters that are not known exactly from the experiments, such as the domain line tension $\varkappa$, the exact form of the disjoining pressure Π, and the SMC function S. Nevertheless, the theory is able to reproduce the qualitative behavior of the experimental system. Another experimental test that also agrees with the theory very well is discussed in the following section.

4.6 Temperature dependence of the pattern formation

The formation of the LE-LC stripe patterns is directly connected to the thermodynamics of the surfactant monolayer. One can therefore expect the transfered patterns to depend on the temperature τ of the subphase. Any change of τ will change the isothermal curve and the extent of the coexistence region (this is shown in fig. 1.4 for the van-der-Waals gas). In particular, a temperature greater than the critical temperature obviously rules LE-LC coexistence out, so that pattern formation is possible only for lower τ. A systematic experimental study of the temperature dependence of the stripe patterns has recently been performed by Harder [Har11]. In a series of measurements, the LB transfer was carried out at different temperatures between 20°C and 26°C while the lateral pressure on the trough was kept constant at $p_{\mathrm{lat}} = 2\,\mathrm{N/m}$. At constant transfer velocity, an increase of the period length of the stripes was observed with increasing temperature. This can be seen in fig. 4.12, where AFM images of stripe patterns obtained at different temperatures between 21.5°C and 25.5°C are shown. For temperatures higher than 25.5°C, stripe patterns could no longer be observed. However, they reappeared when the lateral pressure was increased to 4 N/m. Furthermore, the morphology of the patterns seems to depend strongly on the temperature. As is shown in the present section, these tendencies can be confirmed by theoretical calculations.

4.6.1 Modelling of the temperature influence

To describe the thermodynamic conditions at different subphase temperatures, the coefficients f_i in the free energy density f_{hom}, introduced in section 1.5, have to be understood as functions of τ. However, to facilitate the comparison to the experiment, the coefficients were chosen to yield a qualitative fit to isothermal curves obtained experimentally by Harder [Har11], rather than defining the functions $f_i(\tau)$. The resultant coefficients and the corresponding model isotherms

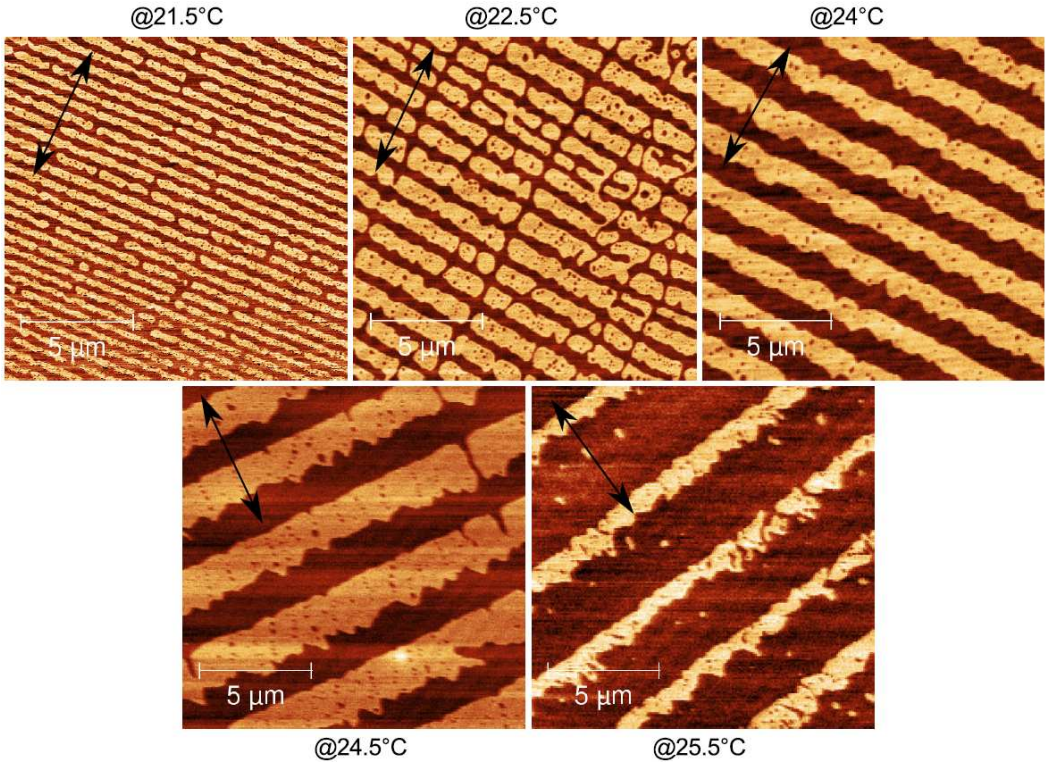

Fig. 4.12: AFM images of stripe patterns obtained during transfer at different temperatures. Source: [Har11].

	$f_0/(10^{-3}\mathrm{Jm}^{-2})$	$f_2/(10^{-39}\mathrm{Jm}^2)$	$f_4/(10^{-75}\mathrm{Jm}^6)$	M_1	M_2	Γ_L	δP_lat
20°C	−7.275	−1.3	7	50.071	0.1980	0.690	0.000
22°C	−8.100	−1.0	7	38.617	0.1737	0.6718	1.260
25°C	−9.000	−0.7	7	26.962	0.1453	0.6548	2.635
27°C	−9.900	−0.4	7	15.407	0.1098	0.6404	4.000

Tab. 4.1: Coefficients of the free energy density f_hom, chosen to model isothermal curves at $\tau =$ 20°,C, 22°C, and 25°C. Figure 4.13 shows the resultant curves.

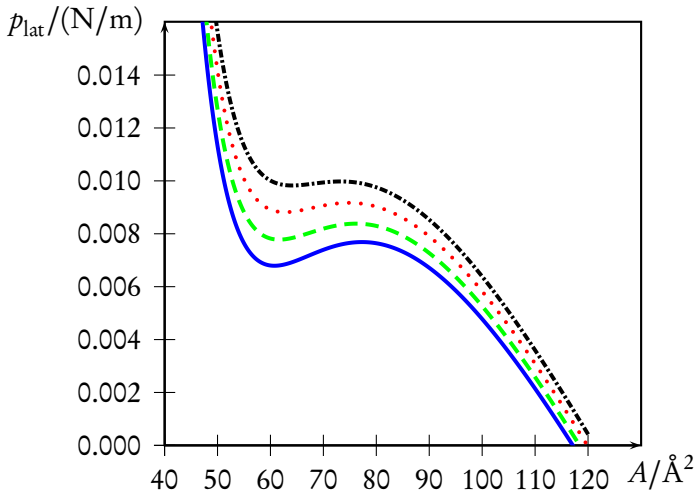

Fig. 4.13: Model isotherms for four different temperatures: $\tau = 20°\mathrm{C}$ (solid line), $\tau = 22°\mathrm{C}$ (dashed line), $\tau = 25°\mathrm{C}$ (dotted line), and $\tau = 27°\mathrm{C}$ (dash-dotted line).

for three different temperatures are shown in tab. 4.1 and fig. 4.13, respectively.

Using these three parameter sets, one-dimensional simulations of monolayer transfer were performed for velocities in the range $0.38 \leq V \leq 0.85$. Like in the experiment, the lateral pressure in the surfactant reservoir should be the same in all calculations. To this end, the boundary condition Γ_{L} at the right side of the integration domain has been adjusted so that $p_{\mathrm{lat}}(\Gamma_{\mathrm{L}}) = 6\,\mathrm{mN/m}$ for all four temperatures. Furthermore, the equation of state (3.17) has to be augmented by an additive correction $P_{\mathrm{hom}} \to P_{\mathrm{hom}} + \delta P_{\mathrm{hom}}$ with

$$\delta P_{\mathrm{hom}} = \frac{\sigma_{\mathrm{cr}}(\tau) - \sigma_{\mathrm{cr}}(20°\mathrm{C})}{\sigma_{\mathrm{cr}}(20°\mathrm{C})}$$

because the scaling of the surface tension and the lateral pressure is based on the reference surface tension $\sigma_0 = \sigma_{\mathrm{cr}}(20°\mathrm{C})$. Except for the M_1, M_2, Γ_L, and δP_{hom}, which are chosen according to tab. 4.1, the parameters listed in 4.1 are employed.

4.6.2 The temperature dependence of the surface tension of water

As has been explained above, a change of the lateral pressure is connected to a change of surface tension, but one has to consider also that the surface tension of water is a function of temperature even in absence of surfactants. However, this dependence is rather weak and can be described by Eötvös' empirical formula [Eö86]

$$\sigma(\tau) = \frac{k}{V_{\mathrm{mol}}^{2/3}} (\tau_{\mathrm{cr}} - \tau) \tag{4.4}$$

where $k = 2.1 \times 10^{-7}\,\mathrm{J/(K\,mol^{-2/3})}$ is the Eötvös constant and V_{mol} is the molar volume of the liquid. The surface tension vanishes at the critical temperature $\tau = \tau_{\mathrm{cr}}$, above which liquid and vapour can no longer be distinguished.

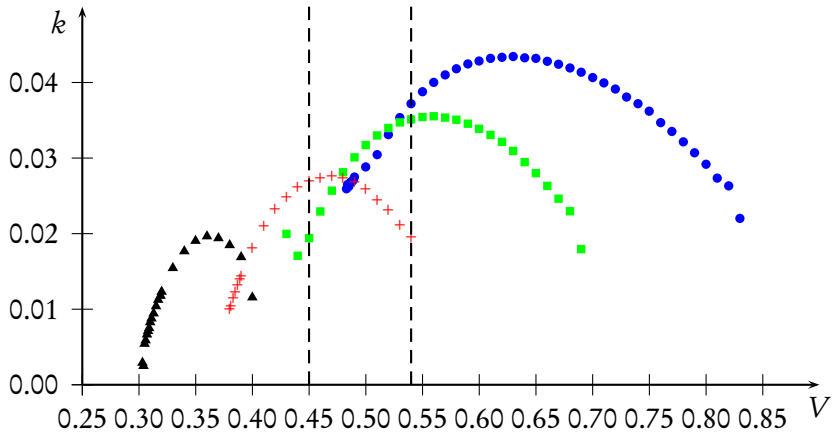

Fig. 4.14: Wavenumber k against the transfer velocity V for transfer at three different temperatures: $\tau = 20°\mathrm{C}$ (blue circles), $\tau = 22°\mathrm{C}$ (green squares), $\tau = 25°\mathrm{C}$ (red crosses), and $\tau = 27°\mathrm{C}$ (black triangles).

For water, the surface tensions at 20°C and 25°C are given by $\sigma(20°\mathrm{C}) = 72.75\,\mathrm{mN/m}$ and $\sigma(25°\mathrm{C}) = 71.97\,\mathrm{mN/m}$, respectively. Thus, the surface tension changes by $\delta\sigma = 0.78\,\mathrm{mN/m}$. This amounts to a relative change given by

$$\frac{\delta\sigma_{\mathrm{abs}}}{\sigma_{\mathrm{abs}}(20°\mathrm{C})} = -\frac{0.78\,\mathrm{mN/m}}{72.75\,\mathrm{mN/m}} \approx -1.07\%.$$

On the other hand, the lateral pressure at $\tau = 25°\mathrm{C}$, measured in the coexistence region, is about 6 mN/m higher compared to the pressure at 20°C. This yields a relative change of

$$\frac{-\delta p_{\mathrm{lat}}}{\sigma_{\mathrm{abs}}(20°\mathrm{C})} \approx -0.084 = -8.4\%.$$

Comparing $\delta\sigma$ to the change of the lateral pressure for the same temperature difference, one can conclude that both effects lower the surface tension but that the major contribution is given by δp_{lat}. Therefore, $\delta\sigma$ is neglected in the following calculations.

4.6.3 Results and comparison to the experiment

The wavenumbers of the stripe patterns obtained in the numerical simulation of the transfer at four different temperatures are shown in fig. 4.14. For each of the chosen temperatures a patterning range is found. The position and extent of the patterning range strongly depends on the temperature: It is shifted toward lower V and becomes significantly narrower as the temperature increases. This is understandable from thermodynamic considerations, because the region of phase coexistence becomes smaller and smaller as τ approaches the critical temperature τ_{cr}, so that the patterning range eventually has to disappear completely for $\tau \approx \tau_{\mathrm{cr}}$. For the majority of transfer velocities the wavenumber of the pattern decreases with increasing temperature, as can be seen by looking at the intersections of the curves in fig. 4.14 with a vertical line. Figure 4.15 shows patterns obtained for $V = 0.54$ at three different temperatures. Only for velocities scarcely above

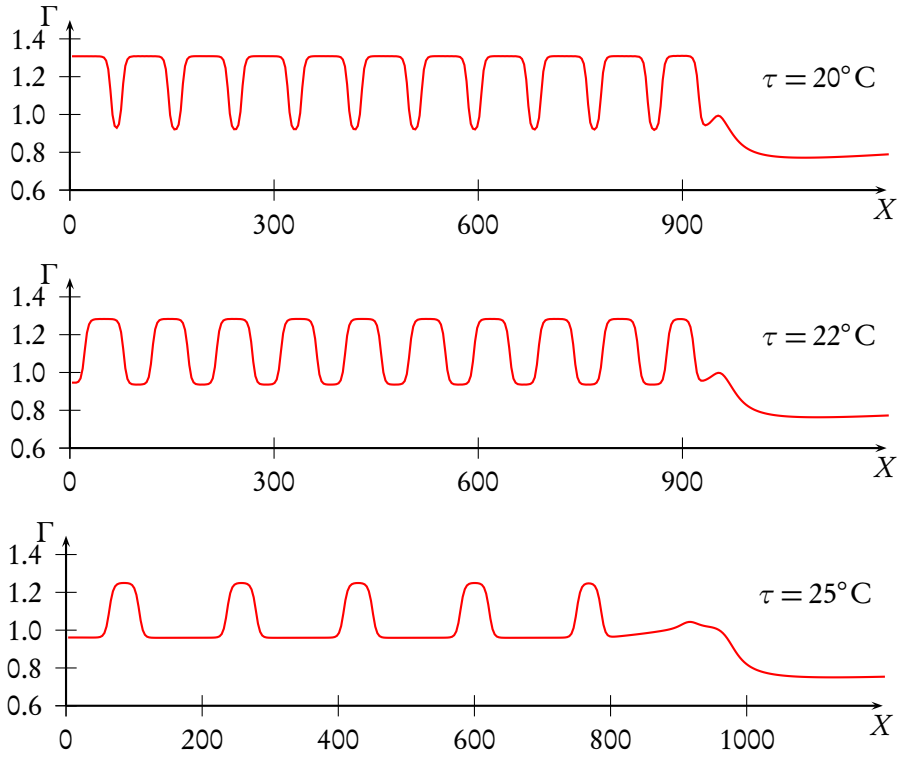

Fig. 4.15: Density profiles of monolayers transferred with transfer velocity $V = 0.54$ for three different temperatures (see fig. 4.14). High and low values correspond to liquid-condensed and liquid-expanded domains, respectively.

the lower boundary of the patterning range does an increase of temperature result in an increase of the wavenumber. However, for these velocities one cannot expect stable stripes parallel to the contact line, because of the instability with respect to perpendicular stripes (see section 4.4).

Note, that a change of $\approx 5°\mathrm{C}$ is sufficient to shift the patterning range completely from the right to the left of a constant velocity. The left vertical line in fig. 4.14 marks $V = 0.45$ and lies left of the patterning range at 20°C and right of the patterning range at 27°C. This behavior can actually be observed in the experiment [Har11]: Applying a surface pressure of 2 mN/m and a withdrawal speed of $v = 60\,\mathrm{mm/min}$, a homogeneous LC layer is transfered at temperatures below 21.5°C. Under these conditions, v is lower than the minimal patterning velocity. Between 21.5°C and 24.5°C, the same transfer velocity lies within the patterning range and consequently stripe patterns are formed. The pattern formation ceases for subphase temperatures exceeding 25.5°C, because under these conditions, v is greater than the maximal patterning velocity.

From these considerations, it is clear that it is also possible to switch between the formation of stripes parallel to the contact line to perpendicular stripes by adjusting the subphase temperature. To obtain perpendicular stripes at a given velocity V, one has to set the temperature to a value for which V is close to the left boundary of the patterning range. Consider for example again the velocity $V = 0.45$ in fig. 4.14. At 25°C the velocity is almost in the center of the patterning range so that regular stripes parallel to the contact line are transfered. In order to switch to

perpendicular stripes, one can lower the temperature to about 22°C, so that V lies almost at the lower boundary of the patterning range. Again, the experiments by Harder support this picture: At constant velocities, the tendency to form perpendicular stripes or rectangles increases with decreasing temperature [Har11].

5 Transfer onto prepatterned substrates[1]

Now that the basic model of monolayer transfer has been established in the previous chapter, the present chapter is devoted to a possible control mechanism that allows to deliberately modify the pattern formation process. It is well known that prepatterned substrates provide a flexible means to control wetting and dewetting processes [GHLL99, QXX+99, SOG+02, CGO06]. Chemically or topographically prepatterned, the substrate exhibits heterogeneous wetting properties and thereby enforces an extrinsic pattern upon a covering liquid layer. A particularly interesting scenario emerges if, as is the case in the monolayer transfer experiments considered in this thesis, the liquid itself exhibits pattern formation *intrinsically*, yielding regular or irregular structures even on homogeneous substrates. This gives rise to the formation of a final pattern resulting from a competition between the extrinsic structure imposed by the substrate and the intrinsic structure that is formed naturally in the system.

In this chapter, we focus on the effect of *periodically* prepattened substrates on the pattern formation process. Specifically, we will consider a prestructure which is periodic in the direction perpendicular to the contact line, as is schematically shown in fig. 5.1. This leads to a periodic forcing at the contact line, where the LC domains are generated. We shall find synchronization of various orders between this forcing and the pattern formation process at the contact line, leading to the production of patterns of higher complexity than the patterns obtained on homogeneous substrates.

5.1 Modelling prepatterned substrates

All the properties of the considered substrates are contained in the disjoining pressure Π. To model a prestructure, we supplement the expression for the disjoining pressure by a modulating

[1]This chapter contains an extended presentation of the results published in [KGF11].

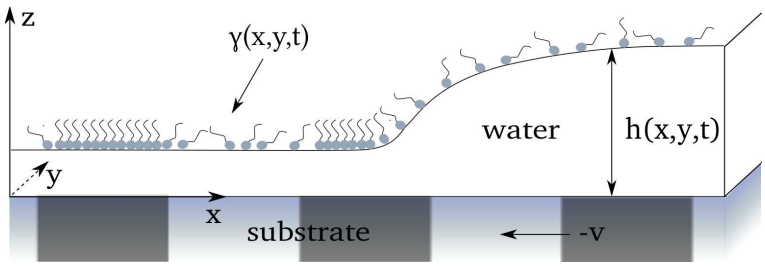

Fig. 5.1: Schematic drawing of a surfactant-covered meniscus on a periodically prepatterned substrate.

factor $m(\vec{x})$:

$$\pi(h,\vec{x}) = m(\vec{x})\left(\frac{a_3}{h^3} - \frac{a_6}{h^6}\right).$$

In this general formulation, the function $m(\vec{x})$ can be of arbitrary form. However, focussing on periodic prestructures, we choose the modulation

$$m(\vec{x}) = 1 + \rho\xi(x + vt),$$

which only depends on the x-coordinate, moves along with the substrate, and has the form of a kink-antikink train

$$\xi(x) = \tanh\left(\frac{10\,\mathrm{tri}(x/l_\mathrm{p})}{\varkappa_\mathrm{p}}\right)$$

with the periodic triangle function

$$\mathrm{tri}(x) = 1 - 2\left|\{x\} - \frac{1}{2}\right|,$$

where $\{x\} := x \mod 1$ denotes the fractional part of x. By this choice, we consider a modulation with amplitude ρ and wavelength l_p. The case of a homogeneous substrate is retrieved for $\rho \to 0$. The sharpness of the contrast between the minima and maxima of the modulation is determined by the constant $\varkappa_\mathrm{p}$: the width of the interfacial regions kink and antikink regions is roughly proportional to $\sqrt{\varkappa_\mathrm{p}}$. It has to be noted, that $\varkappa_\mathrm{p}$ may not be chosen too small, lest the assumption of slow variation in x- and y-direction, which forms the basis of lubrication theory, is violated. Here, we use $\varkappa_\mathrm{p} = 1$.

Applying the same scaling scheme used in chapter 4, we obtain the disjoining pressure as

$$\Pi(H,X) = A\left(1 + \rho\bar{\xi}(X + VT)\right)H^{-3}\left(1 - H^{-3}\right),$$

where ξ can be written in terms of the scaled quantities $X = x/l_0$ and $L_\mathrm{p} = l_\mathrm{p}/l_0$ as

$$\xi = \tanh\left(\frac{10\,\mathrm{tri}\left(X/L_\mathrm{p}\right)}{\varkappa_\mathrm{p}}\right).$$

Due to the spatial variation of the properties of the substrate, the substrate-monolayer interaction also varies spatially. This is automatically included in the model due to the definition of $S(H)$ according to eq. (3.28).

5.2 Controlled formation of more complex patterns

In the following, periodically prepatterned substrates with three different wavelengths, $L_\mathrm{p} = 200$, 300, and 400, each for wetting contrast amplitudes between $\rho = 0.001$ and $\rho = 0.01$, will be investigated. Note, that all three prepattern wavelengths are on the same order of magnitude as the natural wavelengths of the system. By this choice the periodic forcing is only slightly detuned with respect to the natural oscillatory behavior at the meniscus.

Fig. 5.2: Synchronization plateaus obtained from one-dimensional simulations of transfer onto a prepatterned substrate with $L_p = 400$ and $\rho = 6 \cdot 10^{-3}$.

The effect of the prepattern is first investigated in the one-dimensional system. The frequency ω of the domain formation is calculated with the method outlined in section 4.3, that is, by analysis of the density fluctuations at a fixed location X_f. The prepatterned substrate moves underneath this location with the velocity V and thus the spatially periodic modulation of the disjoining pressure translates into a time-periodic perturbation or forcing at $X = X_f$. The forcing frequency is given by $\Omega = 2\pi V / L_p$.

For non-vanishing ρ the wettability contrast of the moving substrate affects the oscillations at the meniscus, going along with a change of the wavelength of the produced pattern. The most striking feature of the patterns formed under these circumstances is the existence of synchronization regions, that is, velocity regions wherein the pattern synchronizes with the substrate. This synchronization yields commensurate frequencies, so that $\omega/\Omega = n : m$ with integer n, m. Figure 5.2 shows a plot of the frequency ration ω/Ω against the transfer velocity. In the plot, the synchronization is evident from the pronounced plateaus at 1 : 1, 2 : 1, 5 : 2, and 3 : 1. Further, it is noteworthy, that the patterning range is extended beyond $V = 0.83$, the upper limit on homogeneous substrates.

In a different representation, it is possible to directly relate the frequency ω that is obtained in presence of the prepattern to the frequency ω_0 that would be obtained on a homogeneous substrate ($\rho = 0$). This is interesting, because the frequency ω_0 observed in the unperturbed system can be regarded as the natural frequency of the pattern formation process. To make the connection between ω and ω_0, one can use the ratio Ω/ω_0 instead of the transfer velocity V as the abscissa. The resulting diagram then usually has the appearance of a staircase with one "step" for each $n : m$ synchronization region [PRK03]. However, in the case considered here, this approach has two disadvantages. Firstly, velocities $V > 0.83$, for which patterns are only obtained on prepatterned substrates, could not be included in the diagrams, since for them $\omega_0 = 0$. Secondly, it has already been mentioned in explanation of the differences between figs. 4.5 (a) and (b), that patterns obtained for higher V differ from those obtained for lower V, even if they have exactly the same period. Due to these differences, the synchronization plateaus of the low and the high transfer velocity regimes do not match perfectly. Instead, one obtains two staircases, one for low and one for high V, as is shown in figure 5.3. Therefore, we will keep the V representation throughout the remainder of this chapter.

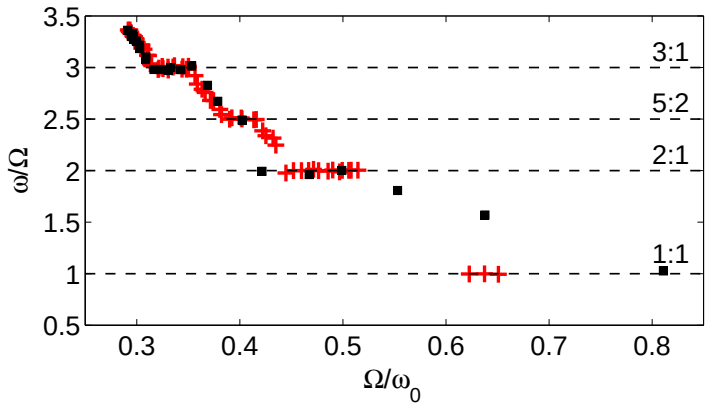

Fig. 5.3: Staircase obtained from one-dimensional simulations of transfer onto a prepatterned substrate with $L_p = 400$ and $\rho = 6 \times 10^{-3}$, after elimination of the transfer velocity in favor of the natural frequency scale Ω/ω_0. Red crosses indicate patterns obtained for velocities higher than 0.52, black squares correspond to lower V.

As one would intuitively expect, the synchronization effects become stronger with increasing amplitude ρ. Consequently, the frequency plateaus broaden as the wetting contrast is enhanced. In order to visualize this dependence one can draw the synchronization regions in a ρ-V diagram as is shown for the three different L_p in fig. 5.4. Such diagrams can be understood as follows: For each value of ρ, a horizontal line can be drawn and wherever it passes through a shaded region, a synchronization plateau would be observed in a k-V diagram like fig. 5.2. Due to their appearance, the shaded regions have been termed *Arnold tongues*, in honor of Vladimir I. Arnold (see [PRK03]) . Although the tongues necessarily originate from the abscissa, they are very narrow for small values of ρ, making it increasingly hard to extract their position and width from the numerical data. The dashed lines in fig. 5.4 represent an estimation of how the tongues connect to the $\rho = 0$ axis. The points, where the tongues meet the V-axis can be determined by considering the wavenumber $k_0(V)$ obtained at $\rho = 0$. Generally, an $n : m$ Arnold tongue meets the V-axis at the velocity corresponding to the $n : m$ ratio of the intrinsic wavenumber k_0 and the forcing wavenumber k. This velocity can be easily determined graphically, by looking at the intersections of a horizontal line at $k_0 = kn/m$ with the curve $k_0(V)$. Figure 5.5 illustrates the graphical procedure for the examples of $1 : 1$ and $3 : 2$ synchronization with $L_p = 200$.

Now that the synchronization behavior has been quantified, we turn to the question what the transfered patterns actually look like. Figure 5.6 shows snapshots of transfer processes that are simulated using a periodic wettability contrast of wavelength $L_p = 400$ and amplitude $\rho = 0.005$. In comparison to the case of homogeneous substrates (see fig. 4.4 in the previous chapter), transfer onto prepatterned substrates obviously yields patterns of higher complexity. Generally, the obtained patterns can be classified into two groups. For velocities which belong to one of the synchronization plateaus, the transfered structure is periodic. Figure 5.6 (a) for example shows a periodic train of domain pairs produced by $2 : 1$ synchronization. If the chosen velocity instead lies outside the plateaus, a non-periodic train of domains is obtained (see figure 5.6 (b)). Hence, the substrate is covered with a stripe pattern that does not repeat itself. By eye, it is generally difficult to distinguish a non-synchronous pattern from a synchronous pattern with higher values

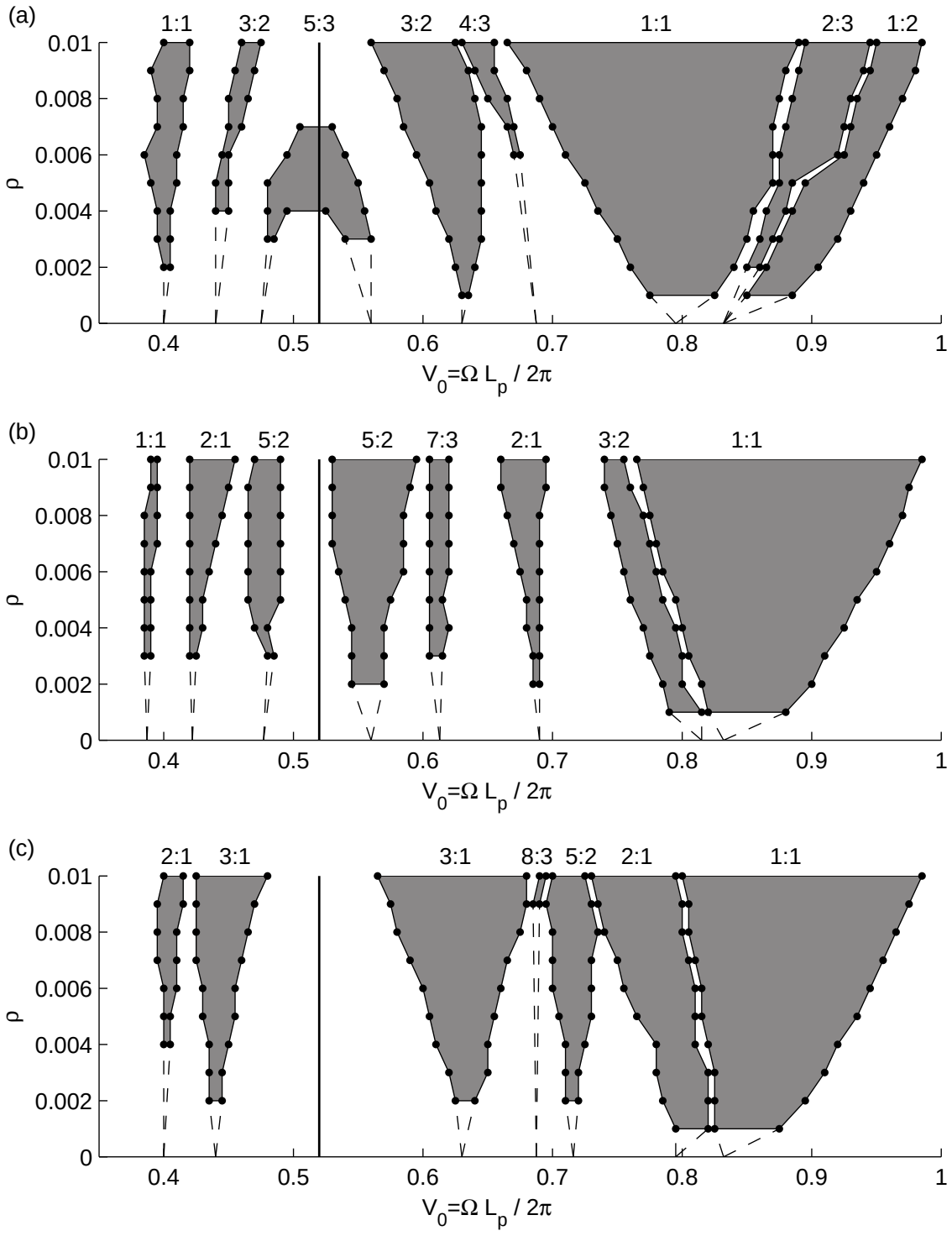

Fig. 5.4: Arnold tongues resulting from one-dimensional computations for prepatterned substrates with (a) $L_p = 200$, (b) $L_p = 300$, and (c) $L_p = 400$. The dashed lines show how the Arnold tongues are expected to go to $\rho = 0$ (see caption of figure 4.6). The vertical solid line in each diagram indicates the velocity corresponding to the maximum of the intrinsic frequency ω_0.

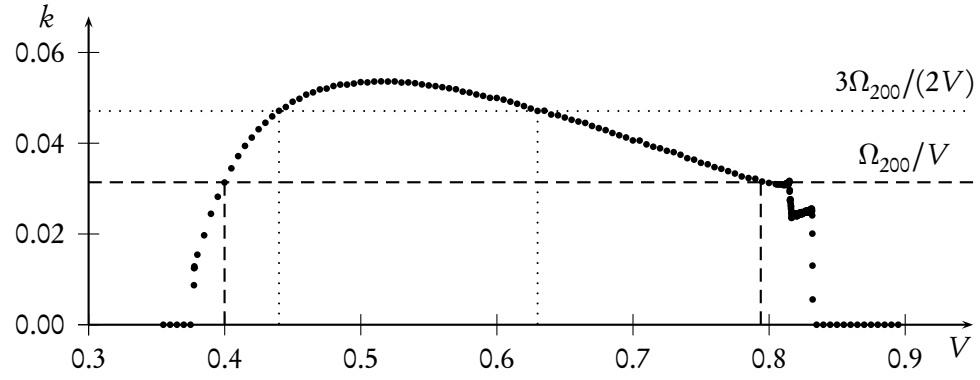

Fig. 5.5: Wavenumber k against transfer velocity V of patterns transferred onto homogeneous substrates obtained from one-dimensional computations. The origins of the Arnold tongues in figure 5.4 below can be determined from the intersection points of the curve with horizontals at the corresponding $n : m$ ratio. This is shown here for 1 : 1 and 3 : 2 synchronization with $L_\mathrm{p} = 200$.

of n and m as can be seen by comparison of figures 5.6 (b) and 5.6 (c). For the system under consideration, this difficulty is even enhanced since, as has been mentioned above, the domains are subject to coarsening from the moment they detach from the contact line. The coarsening is obvious in figure 5.6 (d), where the leftmost, that is oldest, pair of domains already differs visibly from the rightmost pair which has just been formed at the meniscus.

Like on homogeneous substrates, for most velocities from the patterning range, the solutions obtained in two-dimensional simulations of transfer onto prepatterned substrates are analogous to the corresponding one-dimensional profiles. Thus, stripes arranged parallel to the contact line correspond to the one-dimensional domains. Their periodicity and their reaction to the prepattern matches the one-dimensional solutions. Two snapshots of numerically simulated transfer onto a prepatterned substrate with $L_\mathrm{p} = 400$ and $\rho = 6 \times 10^{-3}$ are shown in fig. 5.7.

As has been explained in section 4.4, there exists a velocity range close to the lower boundary of the patterning range, where the formation of stripes arranged parallel to the contact line is competing with a stationary pattern of perpendicular stripes. The following section is devoted to the question how this competition is affected by the presence of a prepattern that favours the orientation parallel to the contact line.

5.3 Effect of the prepattern on the orientation transition

During transfer onto homogeneous substrates, a transition from stripes parallel to the contact line to perpendicular stripes was observed for velocities between a lower bound, $V_\mathrm{cr,l} \approx 0.38$, and an upper bound, $V_\mathrm{cr,u} \approx 0.47$. On prepatterned substrates, these perpendicular stripes are stable only for small wetting contrast ρ. To illustrate this, we consider the solution obtained for $\rho = 0$, $V = 0.44$, that is, a stable, stationary pattern of stripes perpendicular to the contact line obtained on a homogeneous substrate. This solution is then used as the initial condition for computations

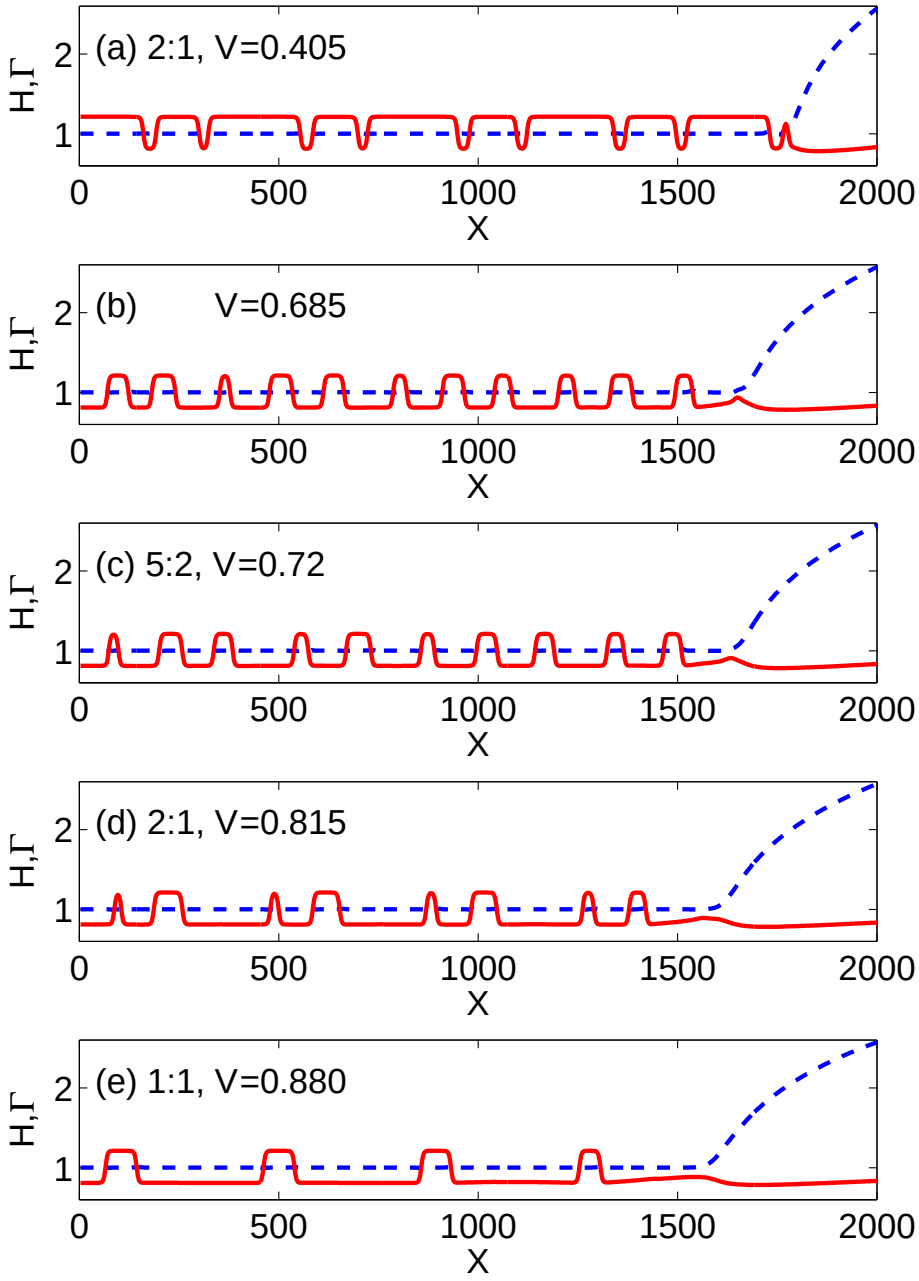

Fig. 5.6: One-dimensional patterns obtained during transfer with five different velocities on a prepatterned substrate with $L_p = 400$ and $\rho = 5 \cdot 10^{-3}$. The velocities in the (a) and (c-f) are chosen from different $n : m$ synchronization regions, while (b) shows a pattern obtained at a velocity from between the right $3:1$ and $2:1$ regions.

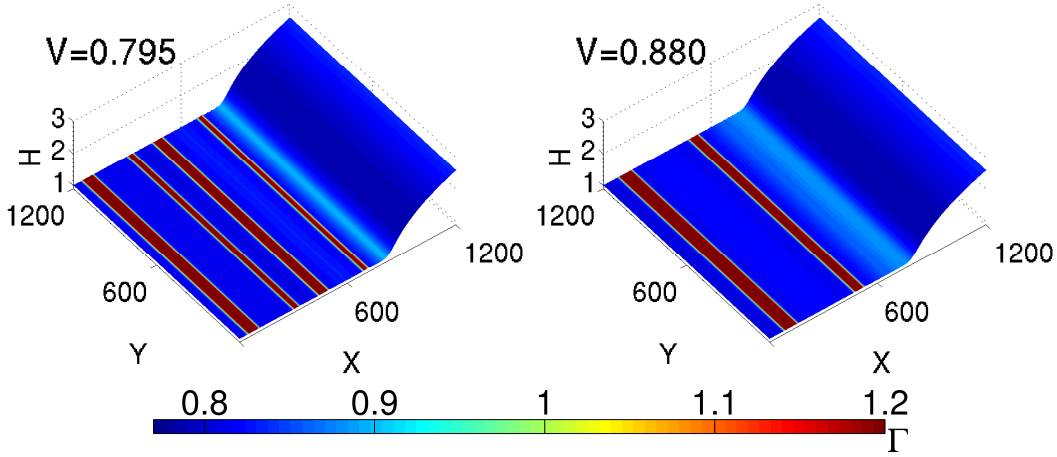

Fig. 5.7: Two-dimensional patterns obtained on a prepatterned substrate with $L_p = 400$ and wetting contrast $\rho = 6 \times 10^{-3}$. The film profile is shown in pseudo-3D while the monolayer density Γ is color-coded.

with non-zero ρ. In these simulations, the wetting contrast is not activated instantaneously across the whole domain. Instead, the region with $\rho > 0$ is moving in from the right boundary of the integration domain with the transfer velocity V, thereby mimicking transfer onto a substrate which is divided into an homogeneous and a prepatterned part. This means, that the monolayer is first transferred onto a homogeneous substrate, where it forms stripes perpendicular to the contact line. Then, at $T = 0$, the contact line reaches the prepatterned part of the substrate. Figure 5.8 shows how the wetting contrast impacts the initially regular stripe pattern. For small amplitudes such as $\rho = 2 \cdot 10^{-3}$, the stripes persist but are periodically undulated across the X-direction. For higher values of ρ the stripes break up into well-arranged arrays of LE domains, aligned like beads on a string parallel to the contact line. For even higher amplitudes $\rho \approx 7 \times 10{-}3$, these linearly arranged LE domains alternate with solid LE stripes. Finally, for very strong wetting contrasts $\rho \gtrsim 10^{-2}$, the extrinsic structure of the prepattern is completely enforced upon the system, resulting in a regular L_p-periodic structure.

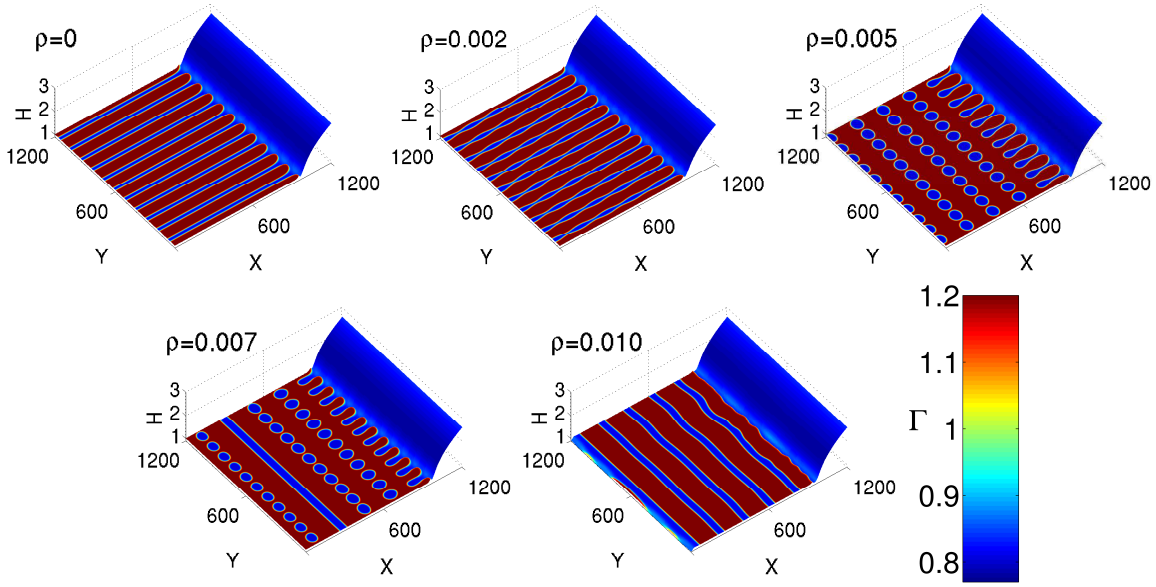

Fig. 5.8: Snapshots of two dimensional solutions for various values of wetting contrast ρ. The velocity was $V = 0.44$ in all runs. For this velocity, transfer of stripes perpendicular to the contact line is stable on homogeneous substrates.

6 Towards a reduced model of monolayer transfer

Due to the complexity of the experimental system, the theory developed in the preceding chapters contains many different physical contributions: The hydrodynamics of the water film, the thermodynamics of the surfactant monolayer, the substrate-water interaction characterized by the disjoining pressure Π, the substrate-monolayer interaction described by the SMC field S, and also evaporation of the liquid. It is therefore probably the most important result of the numerical analysis of the model, that the essential mechanism behind the LE-LC pattern formation was identified: It is basically a phase decomposition process occurring under the influence of an external field. In order to gain a deeper understanding of the nature of the observed phenomena, it would therefore be advantageous to write down a *reduced* model, that contains nothing but the essential contributions. This reduction is indeed possible for our model and allows for a deeper analysis of the problem. In particular, the bifurcations corresponding to the onset and loss of spatiotemporal periodicity can be investigated.

This progress relies on a number of theoretical tools that will be introduced in the first two sections of this chapter, where first necessary prerequisites from the theory of global bifurcations are recollected and then the method of numerical continuation is outlined. The reduced model will then be introduced in the third section of this chapter, followed by a thorough investigation of its bifurcation behavior. In the fourth and final section of this chapter, it will be shown that the oscillatory instability of the transfer process can also be understood in terms of front propagation into an unstable state.

6.1 Bifurcations and the slaving principle

One of the most striking features of the pattern formation in Langmuir-Blodgett transfer systems is the onset and the eventual loss of spatiotemporal periodicity, depending on the chosen transfer velocity. Studying such qualitative changes in the dynamics upon variation of parameters is essential for the understanding of any nonlinear system. The importance of this topic has been recognized more than hundred years ago and since then continuously attracted the attention of great minds such as Henri Poincaré, Aleksandr Andronov, and Vladimir Arnold, to name only a few, whose work evolved into the mathematical theory of *bifurcations* which is nowadays an integral part of nonlinear dynamics classes. For a survey of bifurcation theory, the reader is referred to the introductory textbooks [AFHF10, Str00]. The mathematically minded reader might prefer the presentation in [GH86, Wig90].

For system with a large number of degrees of freedom, the importance of bifurcation theory stems from the slaving principle [Hak04]: If a systems with many degrees of freedom becomes unstable due to a parameter change, the slaving principle can be invoked to describe the dynamics of the system in terms of order parameter equations taking into account only the slow critical

modes that have just become unstable due to the parameter change and that determine the dynamics of the quickly decaying stable modes. For temporally deterministic systems this is qualitatively equivalent to the center manifold theorem which states that the amplitudes $\vec{y}$ of the stable modes are functions of the amplitudes of the central modes $\vec{x}$ whose eigenvalues lie on the imaginary axis: $\vec{y}(t) = \vec{h}(\vec{x}(t))$ (see for example sections 6.2 and 6.8 in [AFHF10].

As local bifurcations are extensively treated in the introductory textbooks, the presentation here focuses on the homoclinic bifurcation, also known as saddle-loop bifurcation (SL bifurcation), that belongs to the class of *global* bifurcations and occurs in the reduced model system as is shown in section 6.3.2. The term *global* refers to the fact, that they involve larger regions of the phase space and not just the neighborhood of a single fixed point. Other examples of global bifurcations are the saddle-node bifurcation of periodic orbits (SNP bifurcation) and the saddle-node infinite-period bifurcation (SNIPer bifurcation).

In this section, the properties of homoclinic bifurcations will be briefly reviewed, following the presentation in chapter 6.1 of [GH86] and chapter 8.4 of [Str00]. Due to their nonlocality, global bifurcations are more difficult to detect and to identify than their local counterparts. However, for many of these bifurcations, characteristic scaling laws are known that describe the behavior close to the bifurcation point. If experimental or numerical data can be shown to agree with these scaling laws, one has obtained very good evidence for a certain bifurcation scenario. For example, in the case of a homoclinic bifurcation, the period of the limit cycle diverges as it becomes eventually a homoclinic orbit. The different phase portraits before and after a homoclinic bifurcation are shown in fig. 6.1. Close to the bifurcation, the system is dramatically slowed down when it passes nearby the saddle point, so that the time it takes to travel around the rest of the cycle becomes negligible.

One can then consider, how the trajectory behaves in the neighborhood of the saddle point. If the system is close enough to the saddle point, so that it can be described by linearized equations, one obtains

$$\begin{aligned} \dot{x} &= \lambda_u x \\ \dot{y} &= -\lambda_s y, \end{aligned}$$

where x and y are the directions of the unstable and stable manifold, respectively. Now consider a trajectory, which passes through a point close to the saddle point, for example $(\mu, 1)$ with $\mu \ll 1$. In the linear regime, this trajectory is given by

$$\vec{r}(t) = \begin{pmatrix} \mu e^{\lambda_u t} \\ e^{-\lambda_s t} \end{pmatrix}.$$

Thus, it is clear that the trajectory will depart from the saddle point to some given distance $x = x_1$ in a time that can be readily calculated to

$$x(t) = x_1 \Leftrightarrow \mu e^{\lambda_u t} = x_1 \Rightarrow t = \frac{\ln x_1}{\lambda_u} - \frac{\ln \mu}{\lambda_u}. \tag{6.1}$$

As was mentioned before, the period length T of the cycle is determined by the time it takes for the system to get away from the saddle point. Thus, one can infer the characteristic scaling of the

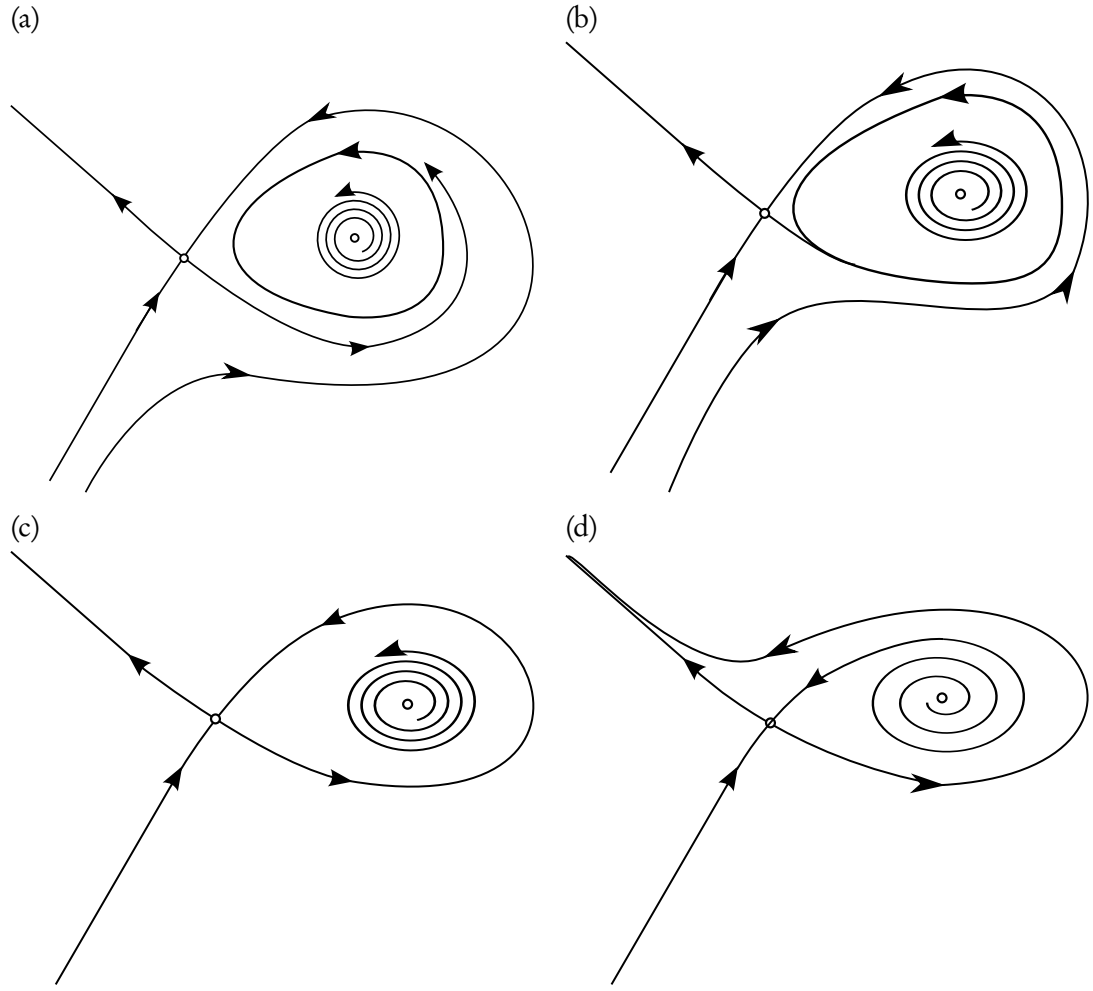

Fig. 6.1: Phase portraits around a homoclinic bifurcation: (a) For $\mu < \mu_c$, where μ denotes the control parameter and μ_c is the value of the parameter at the bifurcation point, a stable limit cycle is close to a saddle point. (b) As μ increases to $\mu \lesssim \mu_c$, the cycle comes closer to the saddle point. (c) For $\mu = \mu_c$, the cycle touches the saddle point and becomes a homoclinic orbit. (d) For $\mu > \mu_c$, the homoclinic orbit is broken.

Bifurcation	Period	Amplitude
Supercritical Hopf	$\mathcal{O}(1)$	$\sim \sqrt{\mu - \mu_c}$
SNP	$\mathcal{O}(1)$	$\mathcal{O}(1)$
SNIPer	$\sim \frac{1}{\sqrt{\mu - \mu_c}}$	$\mathcal{O}(1)$
Homoclinic	$\sim \ln(\mu - \mu_c)$	$\mathcal{O}(1)$

Tab. 6.1: The different scaling behavior of periods and amplitudes close to the bifurcation point for the supercritical Hopf and the homoclinic bifurcation. Source: [Str00].

period length from eq. (6.1) as

$$T \sim -\frac{\ln \mu}{\lambda_u}. \tag{6.2}$$

A more detailed version of the above argument can be found in [Gas90], where a homoclinic bifurcation in a chemical system is investigated. Table 6.1 lists the characteristic scaling laws for the global homoclinic, SNP, and SNIPer bifurcations. For comparison, the scaling behavior of a supercritical Hopf bifurcation is listed as well.

6.2 Continuation methods

The short introduction to continuation methods presented in this section follows the representation in the lecture notes by Doedel [Doe10]. Consider a set of n nonlinear differential equations $\dot{f}_i = G_i(f_1, \ldots, f_n)$. Using vector notation, the equations can be written in the form

$$\dot{\vec{u}} = \vec{G}(\vec{u})$$

with $\vec{u}, \vec{G} \in \mathbb{R}^n$. In order to understand the complete solution structure of these equations, one needs to know its stable *and* unstable solutions. Of course, the latter are not accessible by direct numerical integration since the numerical treatment necessarily involves fluctuations. To find stable and unstable stationary solutions, one can set all time derivatives to zero and solve the resulting system of nonlinear equations

$$\vec{G}(\vec{u}) = \vec{0}.$$

The generic way to solve such systems numerically is to apply Newton's method [Pre99]: Starting with an initial guess $\vec{u}^{(0)}$ one iteratively solves

$$\vec{G}_{\vec{u}}\left(\vec{u}^{(\nu)}\right) \Delta\vec{u}^{(\nu)} = -\vec{G}\left(\vec{u}^{(\nu)}\right) \qquad \text{with} \qquad \left(\vec{G}_{\vec{u}}\right)_{ij} = \frac{\partial G_i}{\partial u_j}$$

for the ν-th increment $\Delta\vec{u}^{(\nu)}$, to find the improved solution

$$\vec{u}^{(\nu+1)} = \vec{u}^{(\nu)} + \Delta\vec{u}^{(\nu)}.$$

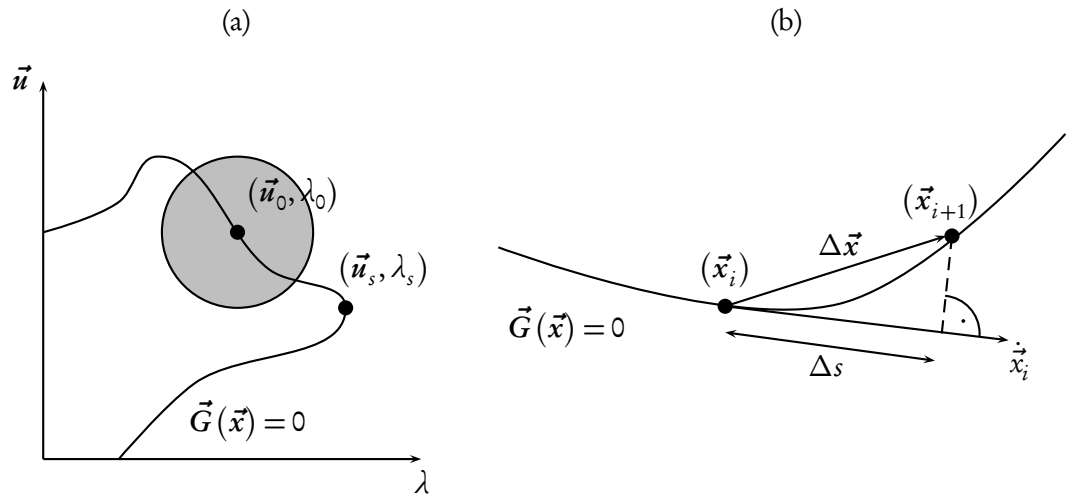

Fig. 6.2: (a) Under certain conditions (see text) the implicit function theorem guarantees the existence of a solution family $(\vec{u}(\lambda), \lambda)$ in the environment of a known solution $(\vec{u}_0, \lambda_0)$. At the saddle-node bifurcation $(\vec{u}_s, \lambda_s)$ the solution family has to be parameterized by one of the components of $\vec{u}$. (b) A geometrical representation of pseudo-arclength continuation.

The procedure is repeated until the desired accuracy is reached, that is, until $\vec{G}(\vec{u})$ is close enough to zero. Although Newton's method is famous for its rapid convergence, it is limited by its strong dependence on the initial condition. If $\vec{u}^{(0)}$ is not close enough to a solution, the method may not converge at all. This weakness is amended by the use of continuation methods which provide a systematic way to find a good initial guess.

The basic idea is the following: If the set of equations one aims to solve involves a parameter $\lambda \in \mathbb{R}$ and if one knows *one* solution $\vec{u}_0$ for a particular value $\lambda = \lambda_0$, that is,

$$\vec{G}(\vec{u}_0; \lambda_0) = \vec{0},$$

then $(\vec{u}_0, \lambda_0)$ might belong to a *solution family* or *branch*. If one could calculate the tangential direction of the branch in the $n+1$ dimensional space of $(\vec{u}, \lambda)$, a small step into this direction should provide a good initial guess for Newton's method to find another nearby solution on the same branch. By this approach, the complete solution family can be traced.

It is noteworthy, that this method can also be used to find solutions to complicated equations by introduction of an *artificial* parameter. For this purpose, one writes the parameter λ in front of the most problematic terms of the equation. If it is possible to solve the simplified equation obtained for $\lambda = 0$, this solution can be used as the starting point of a continuation to $\lambda = 1$, a solution to the original equation.

The mathematical foundation of continuation is given by the implicit function theorem: Consider a mapping

$$\begin{aligned} \vec{G} &: \mathbb{R}^n \times \mathbb{R} \to \mathbb{R}^n \\ &(\vec{u}, \lambda) \mapsto \vec{G}(\vec{u}, \lambda) \end{aligned}$$

with $\vec{G}(\vec{u}_0, \lambda_0) = \vec{0}$ at a point $(\vec{u}_0, \lambda_0)$. If

- $\vec{G}_{\vec{u}}(\vec{u}_0, \lambda_0)$ is non-singular and
- $\vec{G}$ and $\vec{G}_{\vec{u}}$ are smooth, that is, $\vec{G} \in \mathscr{C}^1$,

then there exists a *unique* and *smooth* function $\vec{u}(\lambda)$ with $\vec{G}(\vec{u}(\lambda), \lambda) = 0$ and $\vec{u}(\lambda_0) = \vec{u}_0$ in an environment of λ_0 (see fig. 6.2 (a)). The proof of this important theorem can be found in any textbook covering multivariate calculus, such as [FK97].

By virtue of the implicit function theorem, a solution branch can be locally parametrized by the parameter λ. However, outside the environment of $(\vec{u}, \lambda)$ the matrix $\vec{G}_{\vec{u}}$ might become singular. A very common scenario is the occurrence of a turn of the solution branch. In that case, the branch has a tip $(\vec{u}_s, \lambda_s)$ in which the tangential direction is perpendicular to the λ-axis (see fig. 6.2 (a)), so that there is a one direction along which $\vec{G}$ remains constant: $\dim \mathrm{Ker}\, \vec{G}_{\vec{u}}(\vec{u}_s, \lambda_s) = 1$. However, this is not a problem if $\vec{G}_\lambda(\vec{u}_s, \lambda_s) \notin \mathrm{Im}\, \vec{G}_{\vec{u}}(\vec{u}_s, \lambda_s)$, because then it is possible to parameterize the branch around the tip by one of the components of $\vec{u}$ by interchanging one row of $\vec{G}_{\vec{u}}$ with $\vec{G}_\lambda$. In that case, the tip is called a *saddle-node bifurcation* or also a *fold*.

Continuation around such a fold is possible by use of the *pseudo-arclength algorithm* invented by Keller [Kel77]. In this approach, the solution branch is approximately parametrized by its arclength s. Consider the $n+1$-dimensional vector $\vec{x} := (\vec{u}, \lambda)$ and assume a solution $\vec{x}_i$ as well as the corresponding tangential unit vector $\dot{\vec{x}}_i := (\mathrm{d}\vec{x}/\mathrm{d}s)_i$ is known. Then the pseudo-arclength algorithm then a neighboring solution $\vec{x}_{i+1}$ for which the increment $\Delta\vec{x} := (\vec{x}_{i+1} - \vec{x}_i)$ projected on the tangential direction $\dot{\vec{x}}_i$ has the length Δs (see fig. 6.2 (b) for a geometrical representation). This is achieved by solving the $n+1$-dimensional system of equations

$$\begin{pmatrix} \vec{G}(\vec{u}_{i+1}, \lambda_{i+1}) \\ (\vec{x}_{i+1} - \vec{x}_i) \cdot \dot{\vec{x}}_i - \Delta s \end{pmatrix} = \begin{pmatrix} \vec{0} \\ 0 \end{pmatrix},$$

with the tangential vector $\dot{\vec{x}}_i$ which is normalized so that $\|\dot{\vec{x}}_i\| = 1$. By applying Newton's method, this amounts to the iterative solution of

$$\begin{pmatrix} \vec{G}_{\vec{x}}(\vec{x}_{i+1}^{(\nu)}) \\ \dot{\vec{x}}_i^{\mathrm{T}} \end{pmatrix} \Delta\vec{x}^{(\nu)} = - \begin{pmatrix} \vec{G}\left(\vec{x}_{i+1}^{(\nu)}\right) \\ \left(\vec{x}_{i+1}^{(\nu)} - \vec{x}_i\right) \cdot \dot{\vec{x}}_i - \Delta s \end{pmatrix},$$

where the superscript "T" denotes the transpose. If $\vec{x}_{i+1}$ has been calculated with the desired accuracy one can proceed to calculate the next direction vector, $\dot{\vec{x}}_{i+1}$, by solving

$$\begin{pmatrix} \vec{G}_{\vec{x}}(\vec{x}_{i+1}) \\ \dot{\vec{x}}_i^{\mathrm{T}} \end{pmatrix} \dot{\vec{x}}_{i+1} = \begin{pmatrix} \vec{0} \\ 1 \end{pmatrix}.$$

Ideally, the tangent vector $\dot{\vec{x}}_0$ corresponding to the first solution should be known in order to start the pseudo-arclength continuation. In practice this information is usually not available, since the details of the branch are unknown *before* the continuation has been performed. However, as

long as the starting solution $\vec{x}_0$ is not a fold, it is not a problem to simply start with the "wrong" tangent vector $\dot{\vec{x}} = (\vec{0}, \epsilon \Delta s)$, with a small quantity ϵ. Once the algorithm has found the second solution on the branch it will automatically calculate the correct tangent $\dot{\vec{x}}_1$.

For the calculation that is presented in the following section, the pseudo-arclength algorithm has been implemented in MATLAB using the same discretization that is also used in the direct numerical simulations, that is, finite differences on equidistant grid points. Alternatively one could use ready-made continuation software like AUTO[1] which are highly optimized. The decision in favor of an own implementation has been made to ensure perfect interoperability between the solutions obtained by continuation and by direct numerical simulations, that is given when every details of both calculations is known.

6.3 The reduced model

6.3.1 The model equation

In contrast to his colleagues who work on real experiments, a theoretical physicists enjoys the freedom to switch single physical effects in a model on or off at will. This can be exploited to reduce a complicated set of equations to a simpler one which still exhibits the desired properties. In our case, the aim is to find the simplest model which describes the formation of stripes at a receding contact line, including the transition from parallel to perpendicular orientation.

Numerical simulations of the model system used in the chapters 4 and 5 show that, once it is formed, the meniscus remains almost static during the transfer process (see section 4.3). This suggests, that the dynamics of the height profile H might not be essential to the process. This is indeed confirmed by numerical tests: Freezing the meniscus completely by setting $H_{,T} = 0$ does not inhibit the pattern formation. Thus, after this first elimination, one is left with the equation

$$\Gamma_{,T} = -\nabla \cdot \left(\frac{\Gamma H^2}{2} \nabla \left(\left(1 - \epsilon^2 P_{\text{hom}}\right) \Delta H - \Pi \right) + \Gamma H \left(\epsilon^{-2} \Gamma \nabla \Delta \Gamma - \nabla P_{\text{hom}} \right) - \vec{V} \Gamma \right),$$

where the functions $H(\vec{X})$ and $\Pi(H(\vec{X}))$ have become space-dependent parameters. In this situation, the gradient of the generalized pressure, that is, the term $\sim \Gamma H^2$, is rather small because the meniscus has developed to a shape which minimizes this contribution. The Marangoni forces and the advection due to the moving substrate can therefore be identified as the most important terms. Thus, a further reduction to the equation

$$\begin{aligned} \Gamma_{,T} &= -\nabla \cdot \left(\Gamma H \left(\epsilon^{-2} \Gamma \nabla \Delta \Gamma - \nabla P_{\text{hom}} \right) - \vec{V} \Gamma \right) \\ \Leftrightarrow \Gamma_{,T} &= -\nabla \cdot \left(-\Gamma H \epsilon^{-2} \nabla \left(\Gamma \Delta \Gamma - \frac{1}{2} (\nabla \Gamma)^2 + \epsilon^2 P_{\text{hom}} \right) \right) + \vec{V} \cdot \nabla \Gamma \end{aligned} \tag{6.3}$$

is possible. By comparison to the eqs. (1.6) and (1.7), one can see that eq. (6.3) is a generalized Cahn-Hilliard equation with the mobility factor $\alpha = \Gamma H \epsilon^{-2}$. Even when the mobility α is set to one, the qualitative pattern formation phenomena explained in chapter 4 can still be found. Thus, the model has been reduced to the following theoretical picture: Due to SMC, the meniscus shape

[1] `http://indy.cs.concordia.ca/auto/`

is translated into a space dependent free energy resulting in a space-dependent lateral pressure. The meniscus can therefore be seen as a smooth step function connecting two regions of different free energy densities: The water bath, on which the monolayer is not yet subject to SMC, and the substrate, where the free energy is tilted by an amount of $S(H_p)$ (see eq. (3.16)). Carried along with the moving substrate, material is perpetually driven across the boundary between these two regions and becomes subject to the external field S. Stable in the one region, unstable in the other, the initially homogeneous system decomposes into domains *at* the boundary, that is in our case given by the contact line. Thus, the whole process of stripe-pattern formation in Langmuir-Blodgett transfer can be understood as a phase decomposition process under influence of an external field that changes significantly in the vicinity of the contact line.

Motivated by the above findings, it seems advisable to study a prototypical model equation describing pattern formation in systems where phase decomposition occurs due to advection across a boundary where parameters change significantly. A suitable model is given by a modified version of the Cahn-Hilliard equation. Consider a concentration field $c(\vec{X}, T)$ whose time evolution is governed by

$$c_{,T} = -\nabla \cdot \left[-\nabla \left(-\Delta c + \frac{\partial F}{\partial c} \right) + \vec{V} c \right] \tag{6.4}$$

with the free energy density

$$F(c) = -\frac{c^2}{2} + \frac{c^4}{4} + \mu \zeta(\vec{X}) c. \tag{6.5}$$

These equations describe the dynamics of spinodal decomposition as has been outlined in section 1.4, but they also include a space dependent external field whose amplitude is given by the constant μ. The strength of this field varies along the X-direction as

$$\zeta(X) = -\frac{1}{2} \left(1 + \tanh \left(\frac{X - X_s}{l_s} \right) \right). \tag{6.6}$$

According to this choice, $\zeta \approx 0$ for $X < X_s$ and $\zeta \approx 1$ for $X > X_s$. Further, advection with a constant velocity V is included in the model, and $V > 0$ is assumed to describe transfer of material from the region of untilted free energy to the region where the external field facilitates condensation[2]. In the following, we refer to the model given by eqs. (6.4)–(6.6) as the "reduced model", while the model used in chapters 4 and 5 is referred to as the "full model".

A direct numerical simulation of the reduced model is performed on a one dimensional domain of size $L = 100$ using the parameters $X_s = 10, l_s = 2$, and $\mu = 0.5$. The boundary conditions are chosen analogous to eq. (4.1):

$$c(0) = c_0, \qquad c_{,XX}(0) = c_{,X}(L) = c_{,XX}(L) = 0.$$

Like in the case of the full model, periodic stripes are obtained within a certain velocity range. For the simplified model this patterning range is between $V \approx 0.024$ and $V \approx 0.0575$. For other velocities, the transfer is completely homogeneous, but the homogeneous layer for $V \lesssim 0.0242$ is of high density while it is of low density for $V \gtrsim 0.0575$.

[2]By this choice, transfer occurs from left to right, whereas it was from right to left in the simulations presented in the chapters 4 and 5. Physically, the choice of the direction does not effect the system at all, due to symmetry.

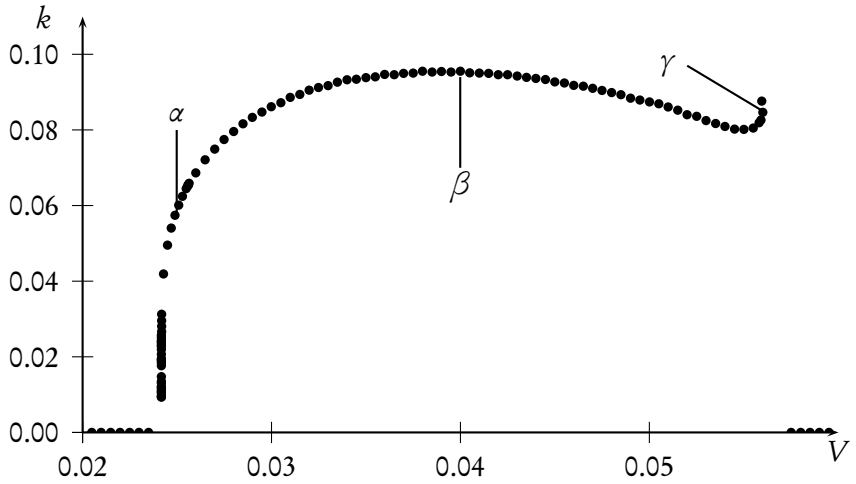

Fig. 6.3: Wavenumbers of the patterns observed in simulations of the modified Cahn-Hilliard equation against the transfer velocity. The Greek letters α–γ correspond to the same letters in fig. 6.5.

The wavenumber k of the stripes depends on the transfer velocity V as is shown in fig. 6.3. This dependence resembles the corresponding relationship between k and V of the full model (compare fig. 4.6). Close to the left boundary of the patterning range, the curve $k(V)$ is extremely steep. In fact, it will be shown in section 6.3.2, that the bifurcation leading to the onset of periodicity at $V \approx 0.024$ is an infinite period bifurcation and the period diverges logarithmically at the bifurcation point. The right end of the patterning range is difficult to locate exactly, because the solutions in that region exhibit very long transient behavior and because of the nature of the corresponding bifurcation that is investigated in section 6.3.3. When the reduced model is simulated in two dimensions, the very same structures that have been described in section 4.4 are obtained. Figure 6.4 shows the transition between stripes parallel to the contact line and perpendicular stripes (compare fig. 4.10 that shows the analogous behavior in the full model).

To complement the results of the direct numerical simulation, stationary solutions are calculated using the method of pseudo-arclength continuation that has been outlined in section 6.2. A solution has to be supplied as a starting point of the continuation. For this purpose, a time simulation is performed for $V = 0.2$, that is, a velocity for which $c(\vec{X}, T)$ relaxes to a stationary state. That stationary state is then used as the first solution of the continuation process. A branch going through this solution is then traced into both directions. In a second step, the linear stability of the stationary states is investigated. Writing eq. (6.4) in the form

$$c_{,T} = \mathscr{L}[\nabla, V]c \tag{6.7}$$

with a nonlinear operator $\mathscr{L}$, infinitesimal perturbations $\eta = c - \hat{c}$, where $\hat{c}$ is a stationary solution, are governed by the linearized equation

$$\eta_{,T} = \mathscr{L}'[\nabla, V]\Big|_{\hat{c}} \eta$$

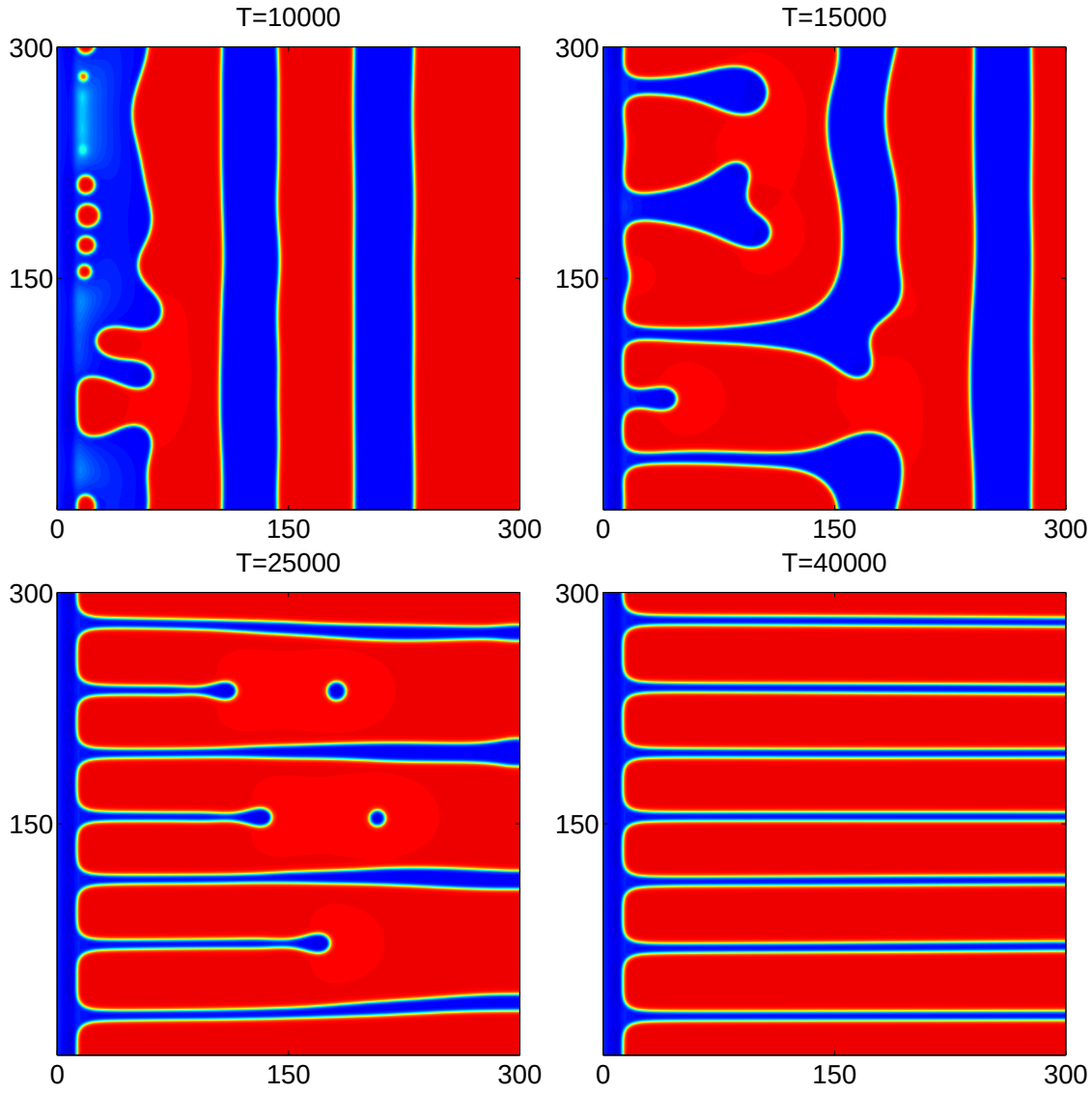

Fig. 6.4: The transition between stripes parallel to the "contact line" and perpendicular stripes obtained in a simulation of the reduced model based on the Cahn-Hilliard equation. For comparison, see fig. 4.10 showing the analogous transition in a simulation of the full model.

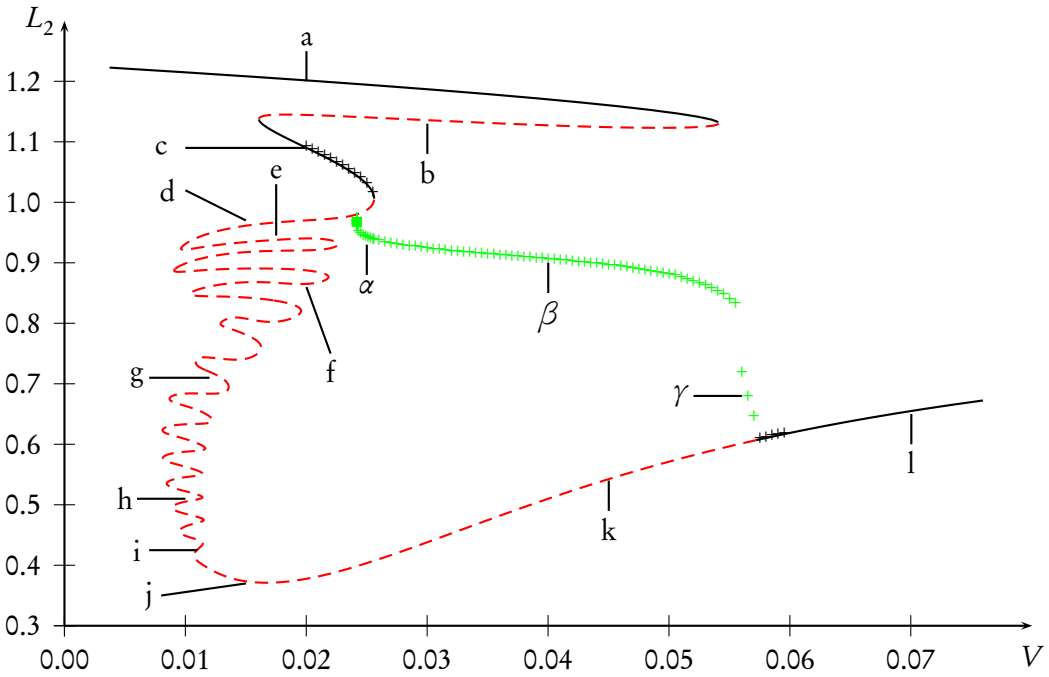

Fig. 6.5: L_2 norms of stationary and time-periodic solutions against transfer velocity V. The solid and dashed lines are obtained by numerical continuation and mark the stable and unstable parts of the branch, respectively. The crosses correspond to solutions obtained by direct numerical simulation. The solutions corresponding to the points marked with the letters (a–l) are shown in fig. 6.6. The Greek letters α–γ correspond to the letters in fig. 6.3.

with the *linear* operator $\mathscr{L}'$ which is equal to the Frechet-derivative of $\mathscr{L}$ evaluated for the solution $\hat{c}$. It is given by

$$\left.\mathscr{L}'\right|_{\hat{c}} = -\Delta^2 + \left(3\hat{c}^2 - 1\right)\Delta + (12\hat{c}\nabla\hat{c} - V)\nabla + 6\left(\hat{c}\Delta\hat{c} + (\nabla\hat{c})^2\right). \tag{6.8}$$

The stationary states are not homogeneous and therefore $\mathscr{L}'_c$ is space dependent. Moreover, $\mathscr{L}'_c$ is not self-adjoint so that its eigenfunctions and eigenvalues are complex, in general. Here, they are calculated numerically using MATLAB. By this procedure, the stability of each solution on the branch is determined.

We are now in the position to draw a bifurcation diagram containing the combined information gathered from the direct numerical simulation and the continuation. Because of the high dimensionality of the system - its continuous version is infinite dimensional, its discretized version has the dimension of the grid - the L_2-norm

$$L_2[c] = \sqrt{\frac{1}{L}\int_0^L \mathrm{d}X\, c^2(X)}$$

is used to classify the solutions. Figure 6.5 shows a plot where the branch of stationary states is drawn together with the branch of periodic solutions corresponding to the results from the direct numerical simulations. The branch of the stationary solution exhibits 26 folds. However, only in the saddle-node bifurcations at $(V = 0.0541, L_2 = 1.133)$, $(V = 0.0161, L_2 = 1.137)$, and $(V = 0.0256, L_2 = 1.006)$ stable and unstable states meet. At the other folds, more and more eigenvalues cross the imaginary axis, but there is already at least one eigenvalue with a positive real part. Twelve stationary profiles from different parts of the bifurcation diagram are shown in fig. 6.6. The uppermost part of the branch consists of stable solutions of the type shown in fig. 6.6 (a). The profile c directly goes from its boundary value $c = -0.9$ to a higher value $c \approx 1.23$. The variation of the external field strength around $X_s = 10$ yields merely a small undulation of the profile. Along the unstable part of the branch, where solutions of the type shown in fig. 6.6 (b) are found, the position of the step from low to high c is continuously shifted to X_s. There, stable solutions of the type shown in fig. 6.6 (c) are found. In the context of LB transfer, these solutions can be associated with homogeneous transfer of a condensed layer. Following the branch further, the step is shifted away from X_s to the right until the solutions become unstable again in the saddle-node bifurcation at $(V = 0.0256, L_2 = 1.006)$. Note, that there is exactly one eigenvalue with a positive real part along the part of the branch between the two bifurcations at $(V = 0.0256, L_2 = 1.006)$ and $(V = 0.00964, L_2 = 0.924)$, so that the points of the branch are simple saddle points in that region. As can be seen from the solutions shown in fig. 6.6 (d–i), every following turn of the branch corresponds to the formation of a localized bump that is formed at X_s and then moves to the right as the next bump forms. Similar behavior is known from the investigation of other model equations of pattern formation, such as the Swift-Hohenberg equation [SH77]. There, solutions with different numbers of localized structures are observed for one control parameter value, just as different numbers of bumps are observed here for one transfer velocity. However, usually these localized structures are investigated in periodic systems or systems where the boundary conditions on the left and on the right are identical, so that the solutions are homoclines. Due to the wiggly appearance of the bifurcation diagrams

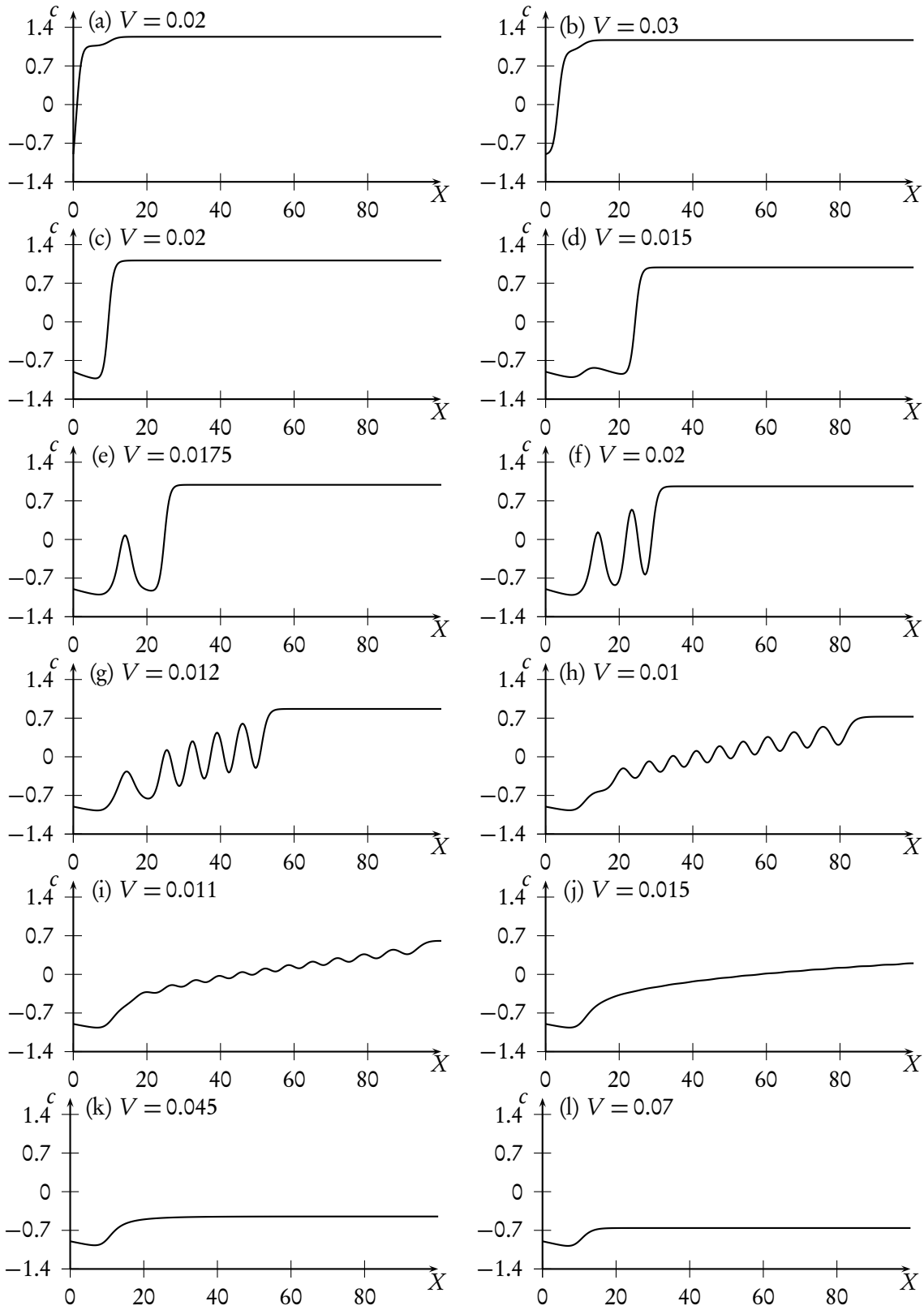

Fig. 6.6: Steady solutions of the reduced model equations from different parts of the solution branch. The labels a–l correspond to the labels in fig. 6.5. Only the profiles (a,c,l) are stable.

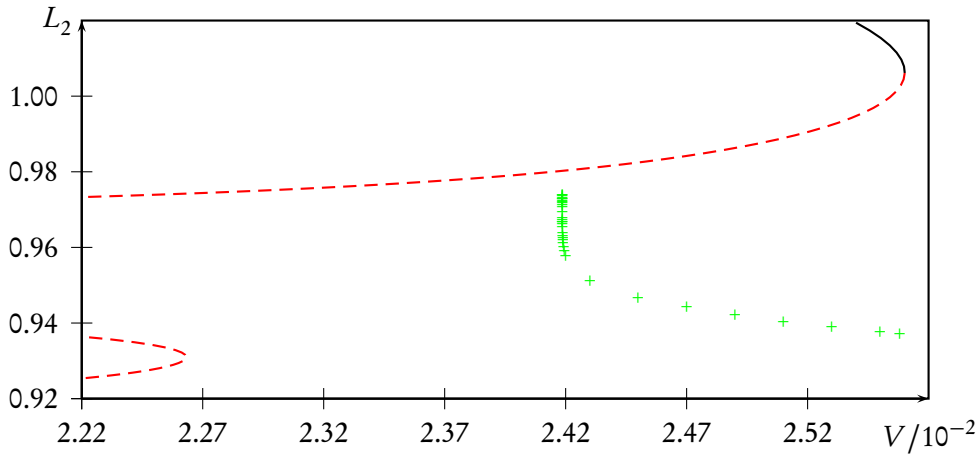

Fig. 6.7: Closeup showing the homoclinic bifurcation of the branch of periodic solutions (green crosses) from the branch of unstable stationary solutions (red dashes).

the phenomenon has been termed *homoclinic snaking* [BK06, BK07, Kno08]. Consequently, the behavior observed here could be called *heteroclinic snaking* as the trains of localized bumps connect a low and a high value of c. The snaking ends when the whole domain is filled with localized structures, as is shown in fig. 6.6 (i). The amplitude of the bumps becomes smaller and smaller as one follows the branch further so that the profile finally becomes smooth. At the same time, the slope of c decreases and its value at the right boundary $X = L$ drops significantly (see fig. 6.6 (j–k)). Finally, at $(V = 0.05719135, L_2 = 0.607)$, a Hopf bifurcation takes place beyond which the branch is linearly stable. Figure 6.6 (l) shows the type of solution that is found for higher velocities. These solutions can be associated with the homogeneous transfer of an expanded layer in the context of LB transfer.

By averaging of the L_2-norms of the time periodic solutions obtained from direct numerical simulations with respect to time, they can be plotted into the bifurcation diagram in fig. 6.5. Their branch emerges from $(V = 0.0242, 0.980)$, a point where no change in linear stability occurs, and ends at the location of the Hopf bifurcation at $(V = 0.0572, L_2 = 0.607)$. In the following two sections these two points will be investigated more closely.

6.3.2 Onset of pattern formation

Figure 6.7 shows a closeup of the bifurcation point at which the time periodic solutions emerge. Since no eigenvalue of the linearization operator crosses the imaginary axis in the relevant region of the branch of stationary solutions, the bifurcation has to be global. With a large number of direct numerical simulations in the vicinity of the critical velocity it is possible to determine the scaling behavior of the period length of the solutions. In the velocity range $0.0242 \lesssim V \lesssim 0.0256$, the branch of periodic solutions coexists with two other stable branches (see fig. 6.5) and it depends on the initial condition onto which branch the simulation settles. Therefore, it is necessary to follow the branch of the periodic solutions very carefully. One has to start with a profile obtained in the region $V > 0.0256$, and then decrement the velocity in small steps in a series of simulation runs, whereupon each run uses the final state of the previous run as its initial condition. Close to the bifurcation point, the velocity decrement ΔV has to be chosen

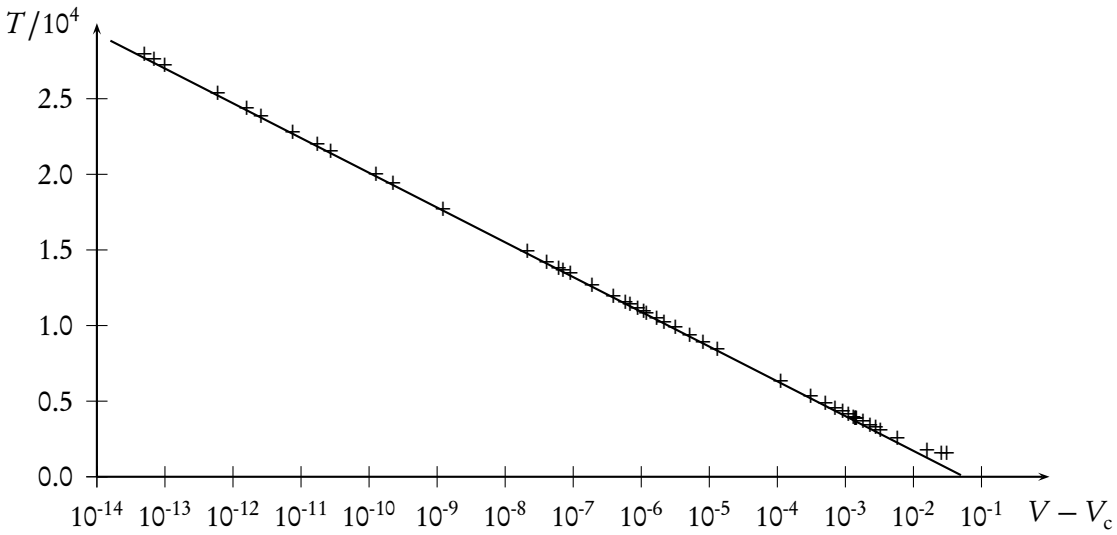

Fig. 6.8: Logarithmic dependence of the period length on the distance to the bifurcation point. The crosses denote the period length obtained from direct numerical simulations close to the bifurcation point V_c. The straight line corresponds to $T = -2880 - 998.191(V - V_c)$ and shows the theoretically predicted scaling behavior.

smaller and smaller, because even tiny ΔV yield a significant change of the period length of the solutions. Using the outlined approach, the critical velocity can be determined up to twelve significant digits: $V_c = 0.0241868087724$. Figure 6.8 shows a logarithmic plot of the period lengths T of the solutions against the distance from the bifurcation point $V - V_c$. Clearly, T diverges logarithmically as V_c is approached. According to section 6.1, this scaling behavior indicates a homoclinic bifurcation. This can be tested further by use of eq. (6.2). In case of a homoclinic bifurcation, the slope of $T(V - V_c)$ in a logarithmic plot should be equal to the negative inverse of the eigenvalue of the unstable mode at the saddle point. The eigenvalue of the stationary solution is given by $\lambda_u = 1.00181 \times 10^{-3}$, yielding a slope of $-\lambda_u^{-1} = -998.191$. A straight line straight line $T = -2880 - 998.191(V - V_c)$ is drawn in fig. 6.8. The offset of 2880 cannot be calculated within a linear theory, but it can be estimated from a fit. Obviously, the scaling behavior fits the theoretical expectation very well. Thus, the bifurcation leading to the onset of the periodic behavior has successfully been identified as a homoclinic bifurcation.

6.3.3 Cessation of pattern formation

The branch of the periodic solutions ends around the point $(V = 0.0572, L_2 = 0.607)$, where according to the linear stability analysis, a Hopf bifurcation occurs. Actually, this bifurcation is the last in a series of many consecutive Hopf bifurcations as can be seen from the eigenvalue spectra close to the bifurcation point (see fig. 6.9). This explains the occurrence of very long transients as is observed around the critical velocity of the bifurcation: Several modes decay very slowly around this point. Furthermore, the presence of so many eigenvalues close to the imaginary axis limits the applicability of an asymptotic theory to a very narrow range of velocities. Nevertheless, the

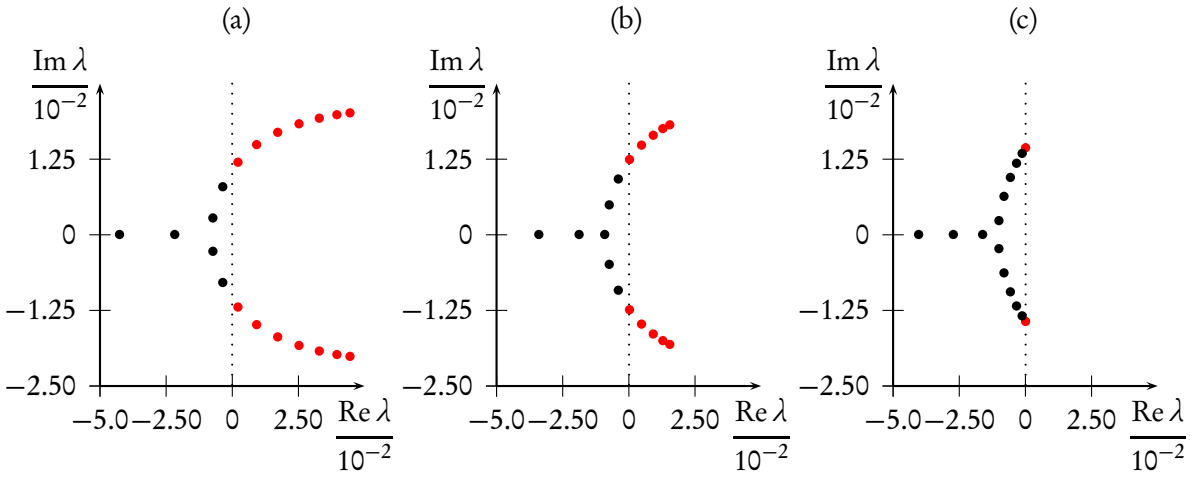

Fig. 6.9: Eigenvalues of the linearization operator of stationary states close to the Hopf bifurcation at the right end of the patterning range. (a) $V = 0.043295$, (b) $V = 0.050109$, (c) $V = 0.057191$. Black and red dots denote eigenvalues with negative and positive real part, respectively. Only the twenty eigenvalues with the largest real parts are shown.

bifurcation can be investigated perturbatively by means of standard tools from bifurcation analysis in order to determine whether the bifurcation is sub- or supercritical. Close to the bifurcation point $V = V_c$, the solution can be written as

$$c(X,T) = \hat{c}(X) + \underbrace{\xi(T)\phi(X)e^{i\omega_c T} + \Psi_2(X,T)e^{2i\omega_c T} + \text{c.c.} + \Psi_0(X,T)}_{=:\eta(X,T)}, \tag{6.9}$$

where $\hat{c}(X)$ denotes the stationary solution at the bifurcation point and $\xi(T)$ denotes the complex amplitude of the one critical mode that becomes unstable by the bifurcation. Note, that this approach is based on a separation of timescales and that T is assumed to be a "slow time", so that $\partial_T \xi \sim \epsilon\xi$ (see chapter 2.2 of [Kur03]). The complex eigenfunction of the mode belonging to ξ is denoted by $\phi(X)$ and the imaginary part of the corresponding eigenvalue is the frequency ω_c. The functions $\Psi_0(X,T)$ and $\Psi_2(X,T)$ describe contributions due to the harmonics $e^{0\cdot i\omega_c T}$ and $e^{2i\omega_c T}$. Considering a perturbation η so that $c = \hat{c} + \eta$, the evolution equation (6.7) can be expanded as

$$\partial_T \eta = \mathscr{L}'_c \eta + \frac{1}{2}\mathscr{L}''_c \eta\eta + \frac{1}{3!}\mathscr{L}'''_c \eta\eta\eta + \ldots, \tag{6.10}$$

where the operators $\mathscr{L}'_c$, $\mathscr{L}''_c$, and $\mathscr{L}'''_c$ denote the Frechet derivatives of the nonlinear operator defined in eq. (6.7) evaluated at $\hat{c}$. The operator $\mathscr{L}'_c$ depends on the control parameter V (see eq. (6.8)). Close to the bifurcation point, it can be approximated by

$$\mathscr{L}'_c(V_{cr} + \epsilon) = \mathscr{L}'_c(V_c) + \underbrace{\epsilon \left.\frac{\partial \mathscr{L}'}{\partial V}\right|_{V=V_c}}_{=:\mathscr{L}'_\epsilon}.$$

By inserting expression (6.9) into eq. (6.10) the following equation is obtained:

$$\begin{aligned}
&\dot{\xi}(T)\phi e^{i\omega_c T} + i\omega_c \xi(T)\phi e^{i\omega_c T} + \frac{\partial \Psi_2(X,T)}{\partial T} e^{2i\omega_c T} + 2i\omega_c \Psi_2(X,T) e^{i\omega_c T} + \text{c.c.} + \frac{\partial \Psi_0(X,T)}{\partial T} \\
&= \left(\mathscr{L}'_{cr} + \epsilon \mathscr{L}'_{\epsilon}\right)\left(\xi(T)\phi e^{i\omega_c T} + \Psi_2(X,T)e^{2i\omega_c T} + \text{c.c.} + \Psi_0(X,T)\right) \\
&\quad + \frac{1}{2}\mathscr{L}''_{cr}\left(\xi(T)\phi e^{i\omega_c T} + \Psi_2(X,T)e^{2i\omega_c T} + \text{c.c.} + \Psi_0(X,T)\right)^2 \\
&\quad + \frac{1}{6}\mathscr{L}'''_{cr}\left(\xi(T)\phi e^{i\omega_c T} + \Psi_2(X,T)e^{2i\omega_c T} + \text{c.c.} + \Psi_0(X,T)\right)^3 .
\end{aligned} \tag{6.11}$$

In the following, the arguments X, T are suppressed to enhance the readability. The different orders of $e^{i\omega_c T}$ can be treated separately. The resulting equation for $e^{i\omega_c T}$ reads

$$\dot{\xi}\phi + i\omega_c \xi \phi = \xi \mathscr{L}'_c \phi + \epsilon \xi \mathscr{L}'_{\epsilon}\phi + \xi \mathscr{L}''_c \phi \Psi_0 + \xi^* \mathscr{L}''_c \phi^* \Psi_2 + \frac{1}{2}\xi|\xi|^2 \mathscr{L}'''_c \phi\phi\phi^*,$$

where the asterisk denotes complex conjugation. By using the eigenvalue equation $\mathscr{L}'_c \phi = i\omega_c \phi$ at the bifurcation point, this equation becomes

$$\dot{\xi}_1 \phi = \epsilon \xi \mathscr{L}'_{\epsilon}\phi + \xi \mathscr{L}''_c \phi \Psi_0 + \xi^* \mathscr{L}''_c \phi^* \Psi_2 + \frac{1}{2}\xi|\xi|^2 \mathscr{L}'''_c \phi\phi\phi^*. \tag{6.12}$$

For $e^{2i\omega_c T}$, the equation

$$\frac{\partial \Psi_2}{\partial T} + 2i\omega_c \Psi_2 = \mathscr{L}'_c \Psi_2 + \frac{1}{2}\xi^2 \mathscr{L}''_c \phi\phi$$

is obtained. The time derivative of Ψ_2 can be eliminated adiabatically [Hak04] and the amplitude Ψ_2 can be expressed in terms of ξ as $\Psi_2 = X_2 \xi^2$, where X_2 denotes a function living in the same space as the eigenfunction ϕ and ξ^2 is the corresponding coefficient. Then, one is left with the solvability condition

$$\left(2i\omega_c - \mathscr{L}'_c\right) X_2 = \frac{1}{2}\mathscr{L}''_c \phi\phi.$$

For $e^{0 \cdot i\omega_c T}$, the equation reads

$$\frac{\partial \Psi_0}{\partial T} = \mathscr{L}'_c \Psi_0 + \frac{1}{2}\mathscr{L}''_c \Psi_0 \Psi_0 + |\xi|^2 \mathscr{L}''_c \phi\phi^*.$$

Again, the time derivative is eliminated and Ψ_0 is rewritten as $\Psi_0 = X_0|\xi|^2$. Therefore, the term $\sim \Psi_0^2$ is of order $|\xi|^4$ and is negligible. This yields

$$\mathscr{L}'_c X_0 = -\mathscr{L}''_c \phi\phi^*.$$

To obtain an evolution equation for ξ, the state vectors have to be projected. As the operator $\mathscr{L}'_c$ is not self-adjoint, its eigenfunctions do not obey an orthogonality relation. Instead, the components of the modes have to be calculated by projection on the eigenfunctions of the adjoint eigenvalue problem

$$\mathscr{L}'^{\dagger}_c \phi^{\dagger} = \lambda^* \phi^{\dagger}.$$

Here, $\mathscr{L}_c'^{\dagger}$ is the adjoint of $\mathscr{L}_c'$ and its eigenvectors are denoted by $\phi^{\dagger}$[3]. By use of the scalar product

$$\langle\phi|\psi\rangle = \int_0^L \mathrm{d}X\, \phi^*(X)\psi(X),$$

eq. (6.12) is then projected onto $\phi^{\dagger}$, the mode of the adjoint operator $\mathscr{L}'^{\dagger}$ belonging to the eigenvalue $\lambda^* = -\mathrm{i}\omega_c$. This yields

$$\begin{aligned}\dot{\xi}\langle\phi^{\dagger}|\phi\rangle &= \epsilon\xi\langle\phi^{\dagger}|\mathscr{L}_{\epsilon}'\phi\rangle + \left(\langle\phi^{\dagger}|\mathscr{L}_c''\phi X_0\rangle + \langle\phi^{\dagger}|\mathscr{L}_c''\phi^* X_2\rangle + \frac{1}{2}\langle\phi^{\dagger}|\mathscr{L}_c'''\phi\phi\phi^*\rangle\right)\xi|\xi|^2 \\ \Leftrightarrow \qquad \dot{\xi} &= \epsilon a_1\xi + a_2\xi|\xi|^2 \end{aligned} \tag{6.13}$$

with the complex coefficients

$$a_1 = \frac{\langle\phi^{\dagger}|\mathscr{L}_{\epsilon}'\phi\rangle}{\langle\phi^{\dagger}|\phi\rangle} \tag{6.14}$$

and

$$a_2 = \frac{\langle\phi^{\dagger}|\mathscr{L}_c''\phi X_0\rangle + \langle\phi^{\dagger}|\mathscr{L}_c''\phi^* X_2\rangle + \frac{1}{2}\langle\phi^{\dagger}|\mathscr{L}_c'''\phi\phi\phi^*\rangle}{\langle\phi^{\dagger}|\phi\rangle}. \tag{6.15}$$

Equation (6.13) is the normal form of a supercritical Hopf bifurcation. It is an ordinary differential equation for the complex amplitude of the mode ϕ. The dynamics of ξ is defined by the complex coefficients a_1, a_2. If $\mathrm{Re}\,\epsilon a_1 < 0$, the mode is linearly damped and the system is stable. If $\mathrm{Re}\,\epsilon a_1 > 0$, the system is unstable and a periodic solution of the form $\xi = R\mathrm{e}^{\mathrm{i}\omega_c T}$ with the radius

$$R = \sqrt{-\epsilon\frac{\mathrm{Re}\,a_1}{\mathrm{Re}\,a_2}}\,.$$

exists. This solution is stable, if $\mathrm{Re}\,a_2 < 0$ and unstable if $\mathrm{Re}\,a_2 > 0$ (see chapter 2.2 of [Kur03]).

In our case, the derivatives of the operator $\mathscr{L}_c$ acting on arbitrary states ϕ, ψ, and χ are given by eq. (6.8) and

$$\begin{aligned}\mathscr{L}_c''\phi\psi &= 6(\hat{c}\psi\Delta\phi + \psi\phi\Delta\hat{c} + \hat{c}\phi\Delta\psi + 2\hat{c}(\nabla\psi)\cdot(\nabla\phi) + 2\psi(\nabla\hat{c})\cdot(\nabla\phi) + 2\phi(\nabla\hat{c})\cdot(\nabla\psi)), \\ \mathscr{L}_c'''\phi\psi\chi &= 6(\chi\psi\Delta\phi + \chi\phi\Delta\psi + \psi\phi\Delta\chi + 2\chi(\nabla\psi)\cdot(\nabla\phi) + 2\psi(\nabla\chi)\cdot(\nabla\phi) \\ &\qquad + 2\phi(\nabla\chi)\cdot(\nabla\psi)), \\ \mathscr{L}_{\epsilon}'\phi &= -\nabla\phi.\end{aligned}$$

The vectors ϕ, $\phi^{\dagger}$, X_0, and X_2 as well as the coefficients a_1 and a_2, can be calculated from the discretized versions of $\mathscr{L}_c'$, $\mathscr{L}_c''$, and $\mathscr{L}_c'''$. This discretization is performed in the same way as in the direct numerical simulation of the problem, that is, by finite differences. The needed scalar

[3] Note, that $\phi\dagger$ is not simply given by $(\phi^{\mathrm{T}})^*$, in this case.

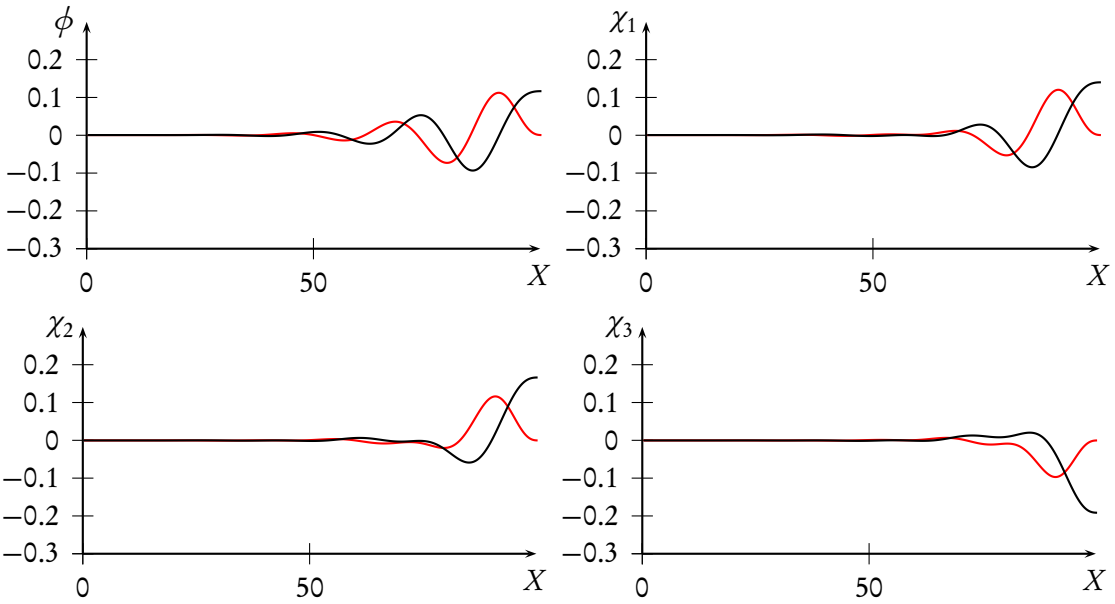

Fig. 6.10: The four modes corresponding to the eigenvalues with the largest real parts. The mode ϕ becomes unstable at the bifurcation point, while the modes χ_1, χ_2, χ_3 are stable. The modes χ_i show the tendency to form large bumps close to the right boundary.

products are calculated as

$$\begin{aligned}
\langle\phi|\phi^\dagger\rangle &= -3.09440\times10^{-2} - 2.62900\times10^{-2}\mathrm{i},\\
\langle\phi^\dagger|\mathscr{L}'_\epsilon\phi\rangle &= 9.89909\times10^{-3} - 6.22986\times10^{-3}\mathrm{i},\\
\langle\phi^\dagger|\mathscr{L}''_c\phi X_0\rangle &= 4.92086\times10^{-6} + 8.96302\times10^{-5}\mathrm{i},\\
\langle\phi^\dagger|\mathscr{L}''_c\phi^* X_2\rangle &= -4.65628\times10^{-5} - 1.52648\times10^{-4}\mathrm{i},\\
\langle\phi^\dagger|\mathscr{L}'''_c\phi\phi\phi^*\rangle &= -4.10991\times10^{-6} + 3.62869\times10^{-5}\mathrm{i}.
\end{aligned}$$

Inserting the results into the eqs. (6.14) and (6.15), one obtains

$$\begin{aligned}
a_1 &= -8.64531\times10^{-2} + 2.74777\times10^{-1}\mathrm{i}\\
a_2 &= 1.53569\times10^{-3} + 1.45445\times10^{-4}\mathrm{i}.
\end{aligned}$$

Note, that $\epsilon = V - V_c$ is negative in the unstable region because the stationary solutions are unstable for velocities *below* V_c. Accordingly, the product ϵa_1 has a positive real part for $V < V_c$. Calculating the radius R from the numerical values of a_1 and a_2, one obtains the purely imaginary result

$$R = 7.50305\mathrm{i}\sqrt{|\epsilon|}$$

in the unstable region. From this result one can conclude that the bifurcation is *not* a supercritical Hopf bifurcation. The behavior of the solutions close to the bifurcation point shows in fact no trace of a stable limit cycle. Starting a simulation at $V = 0.05719133$, a velocity that lies only 2×10^{-8} below V_c, a long phase of slow exponential growth of the unstable mode is observed,

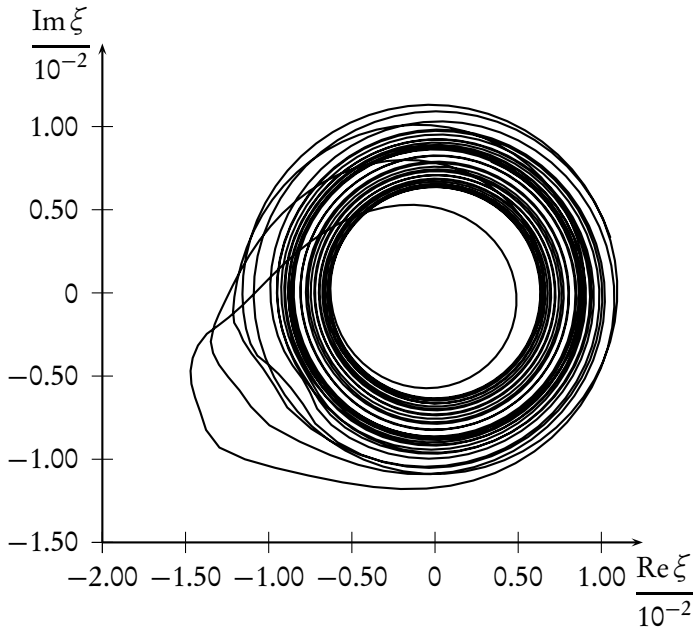

Fig. 6.11: Phase plot showing the projection of the dynamics at $V = 0.05719133$ onto the unstable mode. Spiraling behavior alternates with large excursions. For clarity of the representation only a time interval of $\Delta T = 15000$ from a longer simulation is shown.

corresponding to the very small real part of the eigenvalue close to the bifurcation. The unstable mode ϕ has the shape of an almost sinusoidal wave traveling to the right whereas the amplitude grows slowly from left to right (see fig. 6.10). The regime of linear growth ends abruptly and further modes are excited. This goes along with the formation of larger bumps or even complete domains with $c \approx 1$ close to the right boundary of the integration domain. These bumps leave the integration domain quickly to the right and the dynamics settles back to the linear behavior for some time. Sooner or later, however, the formation of a larger bump occurs again. By projection of the solution onto the unstable mode ϕ, the complex amplitude ξ can be calculated and a phase plot can be drawn, as is shown in fig. 6.11. The linear phases of the dynamics corresponds to slowly growing spirals. The formation of bumps can be seen from the excursion from these planar spirals that follow an obviously higher dimensional trajectory that eventually comes back to the plane and begins to follow a spiral again. The absolute value of the amplitude, $|\xi|$, is shown in fig. 6.12. From these results the following picture emerges: The stationary solutions become unstable spirals due to a subcritical Hopf bifurcation. Nonlinearly, the spiral motion is caught by a higher-dimensional structure due to the influence of the stable modes which are next to the imaginary axis. A possible scenario involving two pairs of complex conjugate eigenvalues $\lambda_{1,2} = -\gamma \pm \mathrm{i}\omega$ and $\lambda_{3,4} = \lambda \pm \mathrm{i}\alpha$ with $\lambda, \gamma, \alpha, \omega > 0$ and $\lambda \neq \gamma$ is given by Leonid Shilnikov's quasi-chaotic spiral-attractor (case 3 in [OS92], see also chapter 6.5 of [GH86]).

6.4 Is it pattern formation behind a propagating front?

Switching from the comoving reference frame to a fixed laboratory frame, one can imagine the location of the domain formation to be a propagating front which closely follows the contact line.

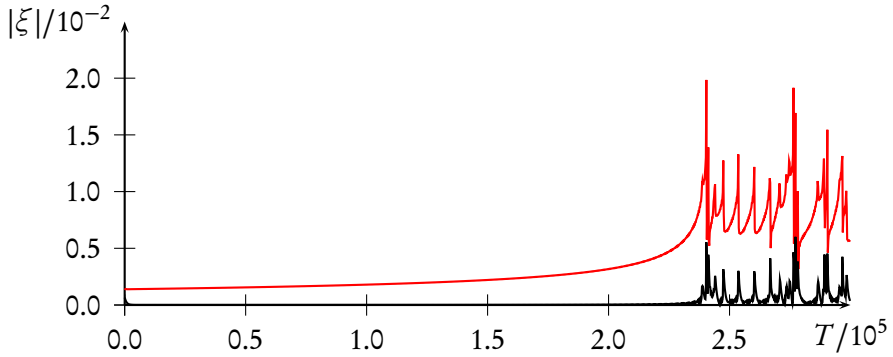

Fig. 6.12: Absolute values of the amplitudes of the unstable mode ϕ (red line) and the first stable mode χ_1 (black line) mode calculated by projection of the dynamics at $V = 0.05719133$. The peaks correspond to the excursions in the phase plot shown in fig. 6.11.

This idea is especially appealing, since it is possible to calculate front velocities analytically. It also provides an intuitive explanation of the detachment of X_f from the contact line: When the pull velocity exceeds the front velocity, the meniscus escapes the front.

However, there are also some limitations of the proposed picture. First of all, the analytical results for front propagation are based on the assumption, that the front moves into a homogeneous unstable or metastable state. This is not given in our case, since the front moves into the meniscus region which is determined by the boundary conditions at $X = 0$ and which is clearly non-homogeneous. Nevertheless, the stationary states that develop for velocities $V \approx V_{\mathrm{c,u}}$ are almost constant at the rear end. If this almost constant value corresponds to an unstable or metastable state, one can - at least approximately - calculate a front velocity.

In a different context, patterns formed in the wake of propagating fronts in solutions of the Cahn-Hilliard equation have been investigated recently [Kre09, FW09, FW11]. The calculation of the front velocity is based on the marginal-stability criterion [vS03]. Consider the leading edge of the front, where it only slightly deviates from the homogeneous state, so that it is well described by the linearized version of the evolution equations. The linear equations can be solved by a superposition of plane waves with wavenumber k and amplitude $\tilde{c}(k)$ in the form

$$c(X,T) = \int_{-\infty}^{\infty} \mathrm{d}k\, \tilde{c}(k) \mathrm{e}^{\mathrm{i}(kX - \omega(k)T)},$$

where $\omega(k)$ is the dispersion relation of the linearized system and $\tilde{c}(k)$ Assuming the existence of a finite front velocity V_f, it is possible to perform a Galilei transform to a comoving reference frame:

$$c(X,T) = \int_{-\infty}^{\infty} \mathrm{d}k\, \tilde{c}(k) \mathrm{e}^{\mathrm{i}(kX + kV_\mathrm{f}T - \omega(k)T)}. \tag{6.16}$$

Integrals like eq. (6.16) can be evaluated using the *saddle point approximation* if the exponent is sufficiently large. This is convenient in our case, as we are interested in the asymptotic behavior for $T \to \infty$. First, the integrand is continuated analytically by allowing a complex argument, $k \in \mathbb{C}$. The integral along the real axis in eq. (6.16) is then equal to a contour integral in the complex

plane. Due to Cauchy's theorem, this contour can be deformed arbitrarily in the region where the integrand is analytic. In presence of a saddle point[4] k_0, this can be exploited to approximatively calculate the integral. If the contour is deformed so that it passes through the saddle point and does so in direction of steepest descent, then the largest contributions of the integrand are located around the saddle point itself. Thus, the integral can be approximated by its value at k_0.

Here, it is not necessary to carry out the integration. Instead it suffices to know that the integral will be dominated by the contribution around the saddle point. We therefore look for wavenumber k_0 with

$$\left.\frac{\partial \omega}{\partial k}\right|_{k_0} = V_\mathrm{f}. \tag{6.17}$$

Since the leading edge of the front is stationary in the comoving frame, its envelope will be stationary, so that there is neither growth nor decay, that is,

$$\mathrm{Im}[\omega(k_0) - k_0 V_\mathrm{f}] = 0. \tag{6.18}$$

Equations (6.17) and (6.18) are the conditions from which k_0 and V_f can be calculated.

Now that the theory of front propagation into unstable states has been outlined for general $\omega(k)$, we are in the position to consider the particular case of our reduced model. Linearization of equation (6.4) in a comoving frame yields

$$\omega(k) = \mathrm{i}\left(k^4 + \hat{F}_{,cc} k^2\right).$$

Searching for the saddle point k_0, we differentiate ω with respect to k and obtain

$$\begin{aligned}\frac{\partial \omega}{\partial k} &= 2\mathrm{i}\left(2k^3 + \hat{F}_{,cc} k\right) \\ &= 2\mathrm{i}\left[2\left(k_\mathrm{r}^3 + 3\mathrm{i}k_\mathrm{r}^2 k_\mathrm{i} - 3k_\mathrm{r}k_\mathrm{i}^2 - \mathrm{i}k_\mathrm{i}^3\right) + \hat{F}_{,cc}\left(k_\mathrm{r} + \mathrm{i}k_\mathrm{i}\right)\right],\end{aligned} \tag{6.19}$$

where we introduce $k_\mathrm{r} = \mathrm{Re}\, k$ and $k_\mathrm{i} = \mathrm{Im}\, k$. Condition (6.17) can then be written as two equations, treating the real part and the imaginary part of equation (6.19) separately:

$$-6k_\mathrm{r}^2 k_\mathrm{i} + 2k_\mathrm{i}^3 - \hat{F}_{,cc} k_\mathrm{i} = V_\mathrm{f}/2, \tag{6.20}$$

$$2k_\mathrm{r}^3 - 3k_\mathrm{r}k_\mathrm{i}^2 + \hat{F}_{,cc} k_\mathrm{r} = 0. \tag{6.21}$$

From eq. (6.21) we find three solutions for k_r:

$$k_\mathrm{r} = 0, \qquad k_\mathrm{r} = \pm\sqrt{3k_\mathrm{i}^2 - \frac{\hat{F}_{,cc}}{2}}\,.$$

First, we consider the nonzero solutions and insert $k_\mathrm{r} = \pm\sqrt{\ldots}$ into the condition (6.18):

$$\omega_i(k_\mathrm{r} = \pm\sqrt{\ldots}, k_\mathrm{i}) - k_\mathrm{i} V_\mathrm{f} = 0 \Leftrightarrow -8k_\mathrm{i}^4 + 2\hat{F}_{,cc} k_\mathrm{i}^2 - \frac{\hat{F}_{,cc}^2}{4} - k_\mathrm{i} V_\mathrm{f} = 0. \tag{6.22}$$

[4] There are no minima and maxima within a function's region of analyticity.

Now, the velocity V_f can be expressed in terms of k_i. By inserting $k_r = \pm\sqrt{\dots}$ into equation (6.20) one obtains

$$V_f = 4k_i\left(\hat{F}_{,cc} - 8k_i^2\right). \tag{6.23}$$

This result can be inserted into equation (6.22) to yield

$$k_i^2 = \frac{\hat{F}_{,cc}}{24}\left(1 \pm \sqrt{7}\right).$$

Depending on the sign of $\hat{F}_{,cc}$, we have to distinguish two cases:

$$k_i = \begin{cases} \pm\sqrt{\dfrac{\hat{F}_{,cc}}{24}\left(1+\sqrt{7}\right)} & \text{for} \quad \hat{F}_{,cc} > 0 \\ \pm\sqrt{\dfrac{\hat{F}_{,cc}}{24}\left(1-\sqrt{7}\right)} & \text{for} \quad \hat{F}_{,cc} < 0. \end{cases}$$

In the final step of the calculation, we insert this result for k_i into equation (6.23) and obtain the front velocity as

$$V_f = \begin{cases} \pm\dfrac{2}{3}\hat{F}_{,cc}^{3/2}\left(2-\sqrt{7}\right)\sqrt{\dfrac{\sqrt{7}+1}{6}} & \text{for} \quad \hat{F}_{,cc} > 0, \\ \pm\dfrac{2}{3}|\hat{F}_{,cc}|^{3/2}\left(2+\sqrt{7}\right)\sqrt{\dfrac{\sqrt{7}-1}{6}} & \text{for} \quad \hat{F}_{,cc} < 0. \end{cases} \tag{6.24}$$

Now we have to consider the other solution of eq. (6.21), that is, $k_r = 0$:

$$\omega_i(k_r = 0, k_i) - k_i V_f = k_i^4 - \hat{F}_{,cc}k_i^2 - k_i V_f. \tag{6.25}$$

Inserting $k_r = 0$ into (6.20) yields

$$V_f = 2k_i\left(2k_i^2 - \hat{F}_{,cc}\right). \tag{6.26}$$

Substituting this result for V in equation (6.25), one obtains

$$-3k_i^4 + \hat{F}_{,cc}k_i^2 = 0.$$

The solutions k_i of this equation are

$$k_i = 0, \qquad k_i = \pm\sqrt{\frac{\hat{F}_{,cc}}{3}} \quad \text{for} \quad \hat{F}_{,cc} > 0.$$

There are no nonzero solutions if $\hat{F}_{,cc} < 0$ because k_i is real. For $k_i = 0$ the front velocity is $V_f = 0$ according to eq. (6.26). For $k_i = \pm\sqrt{\hat{F}_{,cc}/3}$ one obtains

$$V_f = \pm\frac{2}{3\sqrt{3}}\hat{F}_{,cc}^{3/2}.$$

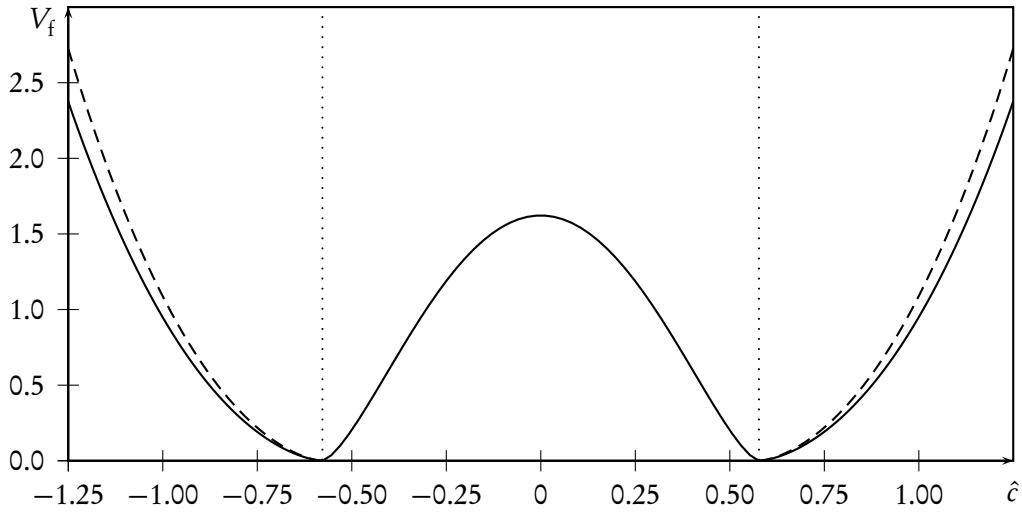

Fig. 6.13: The calculated front velocities as functions of the homogeneous state $\hat{c}$. The dotted vertical lines mark the boundary of the spinodal region, where $\hat{F}_{,cc} < 0$. The solid curve shows the velocity given by eq. (6.24). The dashed curve is the velocity given by eq. (6.26) that only exists outside of the spinodal region.

By inserting the particular choice given by eq. (6.5) for the free energy density F, the dependence of the different calculated front velocity on the homogeneous state has the shape shown in fig. 6.13. Note, that the validity of the calculated front velocities depends on the sign of $\hat{F}_{,cc}$, that is, on the sign of the curvature of the free energy density. This sign is also decisive with respect to the stability of the homogeneous state $\hat{c}$, as spinodal decomposition sets in if $\hat{F}_{,cc} < 0$. Only the velocities

$$V_f = \pm\frac{2}{3}|\hat{F}_{,cc}|^{3/2}\left(2+\sqrt{7}\right)\sqrt{\frac{\sqrt{7}-1}{6}}$$

are therefore relevant for front propagation into an *unstable* state. Here, only the absolute value of V_f is important to answer the question whether or not the front can keep up with the moving contact line. Now we consider the situation close to the Hopf bifurcation at the right end of the patterning regime. Away from the contact region, the profiles obtained by continuation are almost completely flat (see fig. 6.6 (k)) and can thus be approximately regarded as homogeneous with $c = c_L = \text{const.}$, where c_L denotes the value of c at the right boundary of the integration domain. Figure 6.14 (a) shows the values c_L of the stationary solutions obtained by continuation as a function of the pull velocity V_f. With this information, it is possible to establish a direct relation between the pull velocity V_f and the front velocity V_f in form of the function $V_f(c_L(V))$. Of course, the front can only keep up with the contact line as long as $V_f > V$. Figure 6.14 (b) shows the plot of $V_f(c_L(V))$ together with the bisecting line $V_f = V$. Both lines intersect at $V = 0.0575$, a value that differs by less than 0.6% from the exact location of the Hopf bifurcation as determined from the linear stability analysis of the stationary solutions. Given the approximations involved in the calculation outlined above, the achieved level of agreement is considerable and leads to

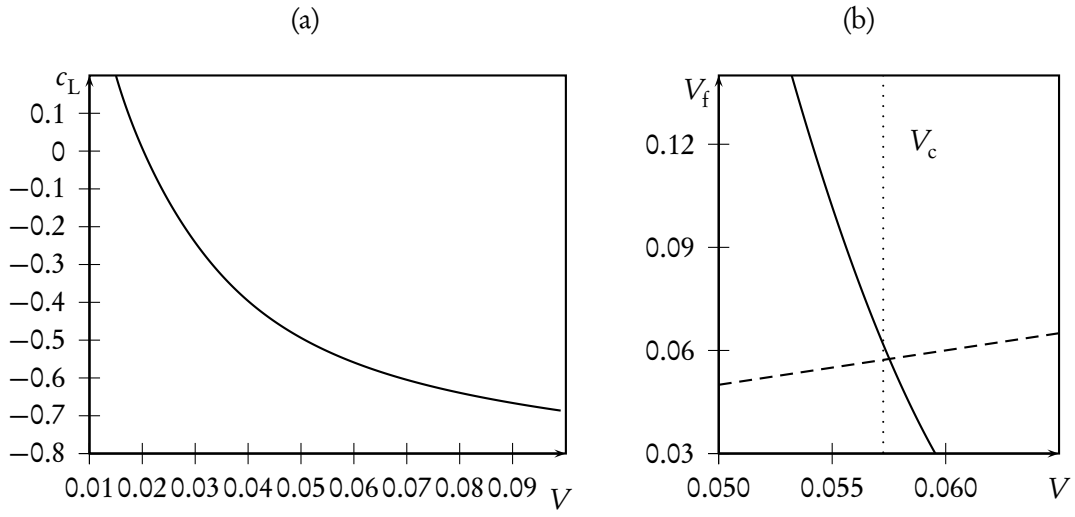

Fig. 6.14: (a) The value of $c_L = c(L)$ of the stationary states obtained by continuation against the pull velocity V. (b) The relation between the front velocity and the pull velocity, $V_f(c_L(V))$. The intersection with the bisecting line $V_f = V$ marks the point beyond which the contact line escapes the front. The dotted vertical line shows the location of the Hopf bifurcation at the right boundary of the patterning range.

the conclusion that it is indeed justified to conceive the pattern formation process at the moving contact line as pattern formation in the wake of a propagating front.

Conclusions & Outlook

As has been shown in the present thesis, the formation of LE-LC stripe patterns in Langmuir-Blodgett transfer of surfactant monolayers can be described theoretically by means of two coupled partial differential equations describing the monolayer density and the height profile of the water subphase.

The model has been developed on the basis of lubrication theory and includes, besides the hydrodynamics of the water film and the wetting properties of the substrate, a thermodynamic relation between the surfactant density and the surface tension that is quantified in terms of an equation of state. It constitutes the first dynamical model of surfactant covered thin liquid films that takes a surfactant phase transition into account [KGF09].

First, the model has been tested outside the Langmuir-Blodgett scenario. A thin liquid film covered with a surfactant layer close to the main-transition was considered on a periodic domain. The main results of this study are the stability conditions given by eqs. (3.23) and (3.26) as well as the dependence of the wavelengths involved in the pattern formation on the material properties that is summarized in the eqs. (3.24) and (3.25). Furthermore, a model to describe thin films covered by rigid monolayers has been developed. It takes into account a bending rigidity as well as a spontaneous curvature of the surface layer. Central results of this work are given by the eqs. (3.42)–(3.44) that summarize the results of the linear stability analysis of flat films covered with rigid surface layers. Furthermore, it is a noteworthy result of the derivation, that only the absolute value of the spontaneous curvature, irrespective of its sign, plays a role for thin liquid films [KGWF11].

In the next step, the model was applied to the problem of Langmuir-Blodgett transfer [KGFC10]. To this end, the evolution equations for H and Γ were subjected to suitable boundary conditions and solved numerically. This investigation showed the existence of a certain range of velocities, the patterning range, for which trains of alternating LE-LC stripes are obtained. The dependence of the wavenumber of the obtained patterns on the velocity is shown in fig. 4.6. In the two-dimensional case, a variety of different patterns has been obtained in the simulations, where the predominant structures are stripes parallel and perpendicular to the contact line (see fig. 4.9). Usually the perpendicular stripes form in the late stage of a simulation and are preceded by the formation of a number of parallel stripes as is shown in fig. 4.10.

In response to very recent experiments [Har11] the dependence of the pattern formation on the temperature of the subphase has been investigated theoretically. To this end, the shift of the isotherm due to a temperature shift has been included in the model and the patterning range has been determined for different temperatures. The central result, that the patterning range shrinks and moves to lower velocities as the temperature increases, is summarized in fig. 4.14. This behavior is in accordance with the experimental findings.

To investigate a possible control mechanism that allows the purposeful fabrication of more complicated patterns, the transfer onto chemically prepatterned substrates has been simulated [KGF11]. The spatially varying wetting properties of the substrate are modeled by inclusion

of a spatial modulation in the disjoining pressure. As has been shown in section 5.2, periodic prepatterns can be used to yield synchronization of various orders between the periodic domain formation at the meniscus and the periodic forcing due to the moving substrate. This behaviour can be seen from the pronounced plateaus in fig. 5.2 and the staircase structure of fig. 5.3. As a result of a large number of transfer simulations at different velocities and for different wetting contrast amplitudes the corresponding Arnold tongues could be determined (see fig. 5.4). In the two-dimensional case, the influence of a periodic pattern oriented parallel to the contact line on the formation of perpendicular stripes was investigated in section 5.3. As a result, intermediate structures consisting of a combination of circular and stripe-like domains were found (see fig. 5.8).

Finally, a reduced model of monolayer transfer has been proposed. It is based on the Cahn-Hilliard equation, includes a spatially varying free energy density, and is subject to nonperiodic boundary conditions. By a combination of direct-numerical simulation and continuation methods, the bifurcation diagram shown in fig. 6.5 has been obtained. The diagram shows stable and unstable stationary solutions as well as the branch of periodic solutions that corresponds to the stripe pattern formation. The bifurcation leading to the onset of pattern formation for small velocities could be identified as a global homoclinic bifurcation. At the other end of the patterning range a subcritical Hopf bifurcation takes place. A calculation based on a two-scale expansion in the vicinity of the bifurcation point and the slaving principle showed that there is no stable limit cycle in the unstable region. The dynamics close to the bifurcation point is governed by a higher-dimensional attractor (see fig. 6.11). In section 6.4, the transfer problem was approached from a completely different perspective: The formation of stripes behind the moving contact line was conceived as pattern formation behind a propagating front. This idea has been substantiated by a calculation that accurately predicts the upper bound of the patterning range by seeking the velocity at which the meniscus outruns the front.

As can be seen from the results listed here, many questions regarding the pattern formation in Langmuir-Blodgett transfer have been answered. However, the number of answers is, as usual, exceeded by a number of new questions that have arisen in the course of the research summarized in the present thesis. In the following, possible directions of future research are proposed.

Although the limited knowledge on SMC is sufficient to explain the pattern formation during the transfer process, the nature of the condensation phenomenon has to be investigated further, as the current understanding is unsatisfactory. The results of the analysis presented in section 3.2.4 might be helpful to this research, which should be a joint effort of theoreticians and experimenters. The former should aim at a microscopic model of SMC while the latter should develop new ways to measure the effect with higher accuracy.

The investigation of rigid surface layers in section 3.3 was limited to layers with constant topology. Considering the case of a multiphase layer, where only one phase has a significant rigidity, topological contributions to the Helfrich functional given by eq. (3.29) have to be taken into account. Further research is necessary to understand how this would affect the dynamics of a liquid film covered by such a layer.

In chapter 5, chemical prepatterns were discussed. Another important class of prepatterns is comprised by topographic prestructures. These can be taken into account by use of a modified generalized pressure of the form [KBH00, KH01]

$$\bar{P}(H,\vec{X}) = \sigma\Delta\left(H(\vec{X},T) + S_{\text{topo}}(\vec{X})\right) - \Pi(H),$$

where the function $S_{\text{topo}}(\vec{X})$ describes the height profile of the substrate. By inserting this expression for $\bar{P}$ into the model equations derived in this thesis, transfer onto topographically prepatterned substrates could be readily simulated. With this method one could investigate the impact of surface defects as well as of deliberately created topographic prestructures on the pattern formation at the contact line. Furthermore, random topographies could be implemented to take surface roughness into account.

By reduction of the transfer problem to a simplified model equation, it was possible to investigate the instabilities leading to the onset of the observed pattern formation. However, a further detailed analysis of the bifurcation at the upper boundary of the patterning range is necessary to identify the nature of the observed higher-dimensional attractor. To this end, one could extend the calculation presented in section 6.3.3 by addition of one or more of the stable modes to the ansatz given in eq. (6.9). Moreover, as has been shown in section 4.4, there is also a number of secondary instabilities, most prominently the transition from stripes parallel to the contact line to perpendicular stripes. Understanding these secondary instabilities would be a first and necessary step in order to understand how patterns of higher complexity might arise. This topic is particularly interesting, because the transition between the parallel and the perpendicular orientation is a common, yet unexplained, phenomenon in various dewetting experiments involving complex fluids like nanoparticle suspensions, surfactant solutions or monolayers, and polymer blends or solutions [DBD+97, DBD+00, YS05, BLN+06]. Many of these systems can be understood as decomposition processes located at the contact line. Thus, the reduced system derived in chapter 6 might serve as a prototypical model equation to describe these various problems and represents a first step towards the development of a universal theory that treats these problems in a common framework. To treat such problems as pattern formation behind propagating fronts, as has been outlined in section 6.4, is a particularly promising method. Future work should address whether also the lower boundary of the patterning range might be determined by use of this approach.

The formation of stripe patterns in Langmuir-Blodgett transfer has proven to be a remarkably complex phenomenon that can only be understood by a combination of concepts from hydrodynamics, thermodynamics, non-equilibrium pattern formation, and bifurcation theory. However, the present thesis shows that the essential dynamics can indeed be captured by a mathematical model. Its purpose is fulfilled, if it provides guidance for the future theoretical and experimental research on this fascinating topic.

A Methods used in direct numerical simulations

> Computers are useless. All they can do is give you answers.
>
> *(Pablo Picasso)*

All direct numerical simulations presented in this thesis are performed using the method of lines. This means, that we use spatial discretization of the right hand side of the time evolution equations to turn the set of partial differential equations into a larger set of *ordinary* differential equations, one for each function and grid point. These are then solved explicitly, using an embedded Runge-Kutta algorithm of fourth and fifth order, allowing for adaptive time stepping.

Depending on the specific problem one is interested in, the spatial discretization can be performed in different ways. For periodic problems, it is convenient to employ the pseudo-spectral method using Fourier modes to calculate derivatives [Boy00] . Looking at monolayer transfer, one has to consider an open system, with a steady throughput of material. In this case, the boundary conditions are necessarily non-periodic. To implement the resulting nontrivial boundaries one could still use a pseudo-spectral method but instead of Fourier modes, a suitable set of basis functions that by themselves obey the boundary conditions has to be supplied. A common approach is to use linear combinations of Chebyshev polynomials as basis functions, as is explained, for example, in chapter 6 of [Boy00]. A very flexible and straightforward alternative is provided by the method of finite differences, where derivatives are simply approximated by differential quotients. Then, arbitrary boundary conditions can be imposed by use of virtual grid points. The accuracy of finite difference methods depends on the number of grid points that are taken into account for the calculation of the derivative at each grid point. Although pseudo-spectral methods have been used in the original investigation of the thin film dynamics in the vicinity of a surfactant phase transition [KGF09], all computations presented in this thesis use finite differences.

A.1 Finite differences

The finite difference method is based on the approximation of derivatives by means of difference quotients. The idea is clarified by looking at the first derivative of a function $f(x)$. By use of a Taylor expansion, we can write the value of f at position $x+\Delta x$ as

$$f(x+\Delta x)=f(x)+\frac{\partial f(x)}{\partial x}\Delta x+\mathcal{O}\left(\Delta x^2\right).$$

From this, we can immediately deduce

$$\frac{\partial f(x)}{\partial x}=\frac{f(x+\Delta x)-f(x)}{\Delta x^2}+\mathcal{O}(\Delta x).$$

Provided Δx is small enough, the higher order terms can be dropped leaving us with a first approximation of the derivative. Analogously, the Taylor expansion can be used to formulate

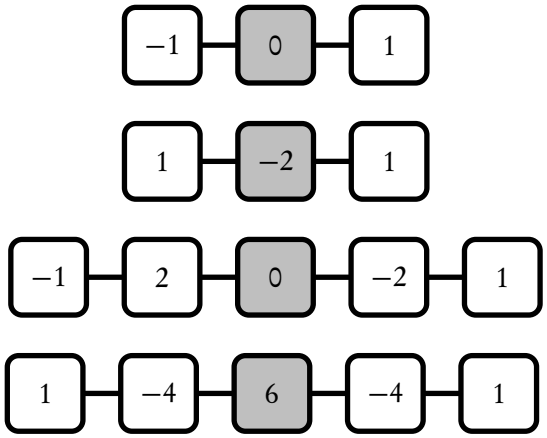

Fig. A.1: Stencils of finite differences approximating the first, second, third, and fourth derivative (from top to bottom).

approximative difference formulas for derivatives of arbitrary order. The accuracy can be increased to any desired level by combination of several Taylor series yielding formulas involving $f(x \pm \Delta x), f(x \pm 2\Delta x), \ldots$. If an equation is discretized by use of an equidistant grid with spacing Δx, this means, that the accuracy can be increased by including the values of f at more and more grid points.

Since finite difference are the most common way to discretize differential equations and therefore ubiquitous in the literature, we will simply write down the formulas up to the fourth derivative without going into the details of their derivation. With the shorthand notation $f_i := f(x_i)$ these can be written as

$$\left.\frac{\partial f}{\partial x}\right|_{x_i} = \frac{-f_{i-1} + f_{i+1}}{2\Delta x} + \mathcal{O}\left(\Delta x^2\right), \tag{A.1}$$

$$\left.\frac{\partial^2 f}{\partial x^2}\right|_{x_i} = \frac{f_{i-1} - 2f_i + f_{i+1}}{\Delta x^2} + \mathcal{O}\left(\Delta x^2\right), \tag{A.2}$$

$$\left.\frac{\partial^3 f}{\partial x^3}\right|_{x_i} = \frac{-f_{i-2} + 2f_{i-1} - 2f_{i+1} + f_{i+2}}{2\Delta x^3} + \mathcal{O}\left(\Delta x^2\right), \tag{A.3}$$

$$\left.\frac{\partial^4 f}{\partial x^4}\right|_{x_i} = \frac{f_{i-2} - 4f_{i-1} + 6f_i - 4f_{i+1} + f_{i+2}}{\Delta x^4} + \mathcal{O}\left(\Delta x^2\right). \tag{A.4}$$

To facilitate the memorization of finite difference formulas like eqs. (A.1) to (A.4), they are commonly represented graphically in form of stencils as is shown in fig. A.1.

The finite difference formulas can be generalized to two or more dimensions in the obvious way. The two dimensional Laplacian is approximated by the sum of the finite difference approximations of the second derivatives in x- and y-direction, yielding

$$\left.\Delta f(\vec{x})\right|_{x_{i,j}} = \frac{f_{i-1,j} + f_{i,j-1} - 4f_{i,j} + f_{i+1,j} + f_{i,j+1}}{\Delta x^2} + \mathcal{O}\left(\Delta x^2\right), \tag{A.5}$$

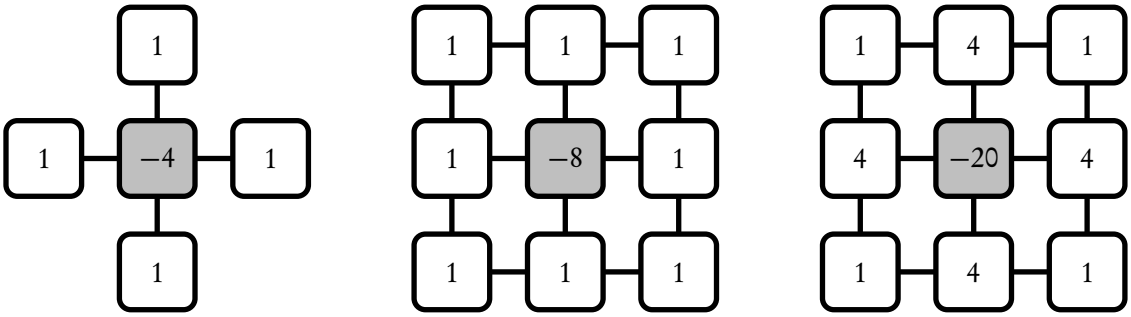

Fig. A.2: Three different approximations of the two dimensional Laplacian. The stencils on the left and in the middle are both of order $(\Delta x)^2$, but they have different symmetry properties. The middle version comes closest to the rotational symmetry of the continuous Laplacian. The stencil on the right approximates the Laplacian up to $\mathcal{O}(\Delta x)^4$.

where $f_{i,j} = f(x_i, y_j)$. Although this approximation is perfectly correct up to terms $\mathcal{O}(\Delta x)^2$, other discretizations with the same order of accuracy are possible. For example,

$$\Delta f(\vec{x})\Big|_{x_{i,j}} = \frac{f_{i-1,j-1} + f_{i-1,j} + f_{i-1,j+1} + f_{i,j-1} - 8f_{i,j} + f_{i,j+1} + f_{i+1,j-1} + f_{i+1,j} + f_{i+1,j+1}}{3\Delta x^2} + \mathcal{O}\left(\Delta x^2\right)$$

comes closer to the rotational symmetry of the continuous Laplacian, at the price of having to access almost twice as many grid points as for the approximation given by eq. (A.5). A fourth order approximation of the Laplacian is given by the following formula

$$\Delta f(\vec{x})\Big|_{x_{i,j}} = \frac{f_{i-1,j-1} + 4f_{i-1,j} + f_{i-1,j+1} + 4f_{i,j-1} - 20f_{i,j} + 4f_{i,j+1} + f_{i+1,j-1} + 4f_{i+1,j} + f_{i+1,j+1}}{6\Delta x^2} + \mathcal{O}\left(\Delta x^4\right).$$

The stencils of these three different discretizations of the Laplacian are shown in fig. A.2. Of course, the listed central finite differences cannot be used to calculate derivatives at the boundaries of a non-periodic domain. However, this is no serious problem as alternative finite difference formulas can be derived that use only terms to the left- or right of the grid point where the derivative is calculated. Consequently, these formulas are termed *left- and rightsided finite differences*. The corresponding stencils of the first and second derivatives and of the Laplacian are shown in fig. A.3 and A.4.

Implementation of the boundary conditions

Derivatives of functions can be fixed at the boundaries by use of virtual grid points. These points lie outside of the integration domain, left and right from the actual boundaries and they have no physical significance by themselves. In the simulations of the transfer process in the complete and in the reduced model that are presented in the chapters 4, 5, and 6, either f and f'' or f' and f''

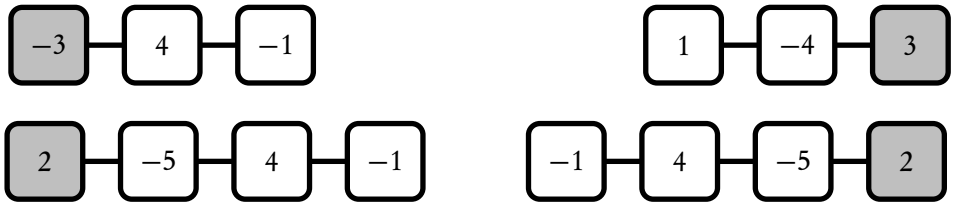

Fig. A.3: Stencils of the second order left- and rightsided finite difference approximations to the first (top) and second (bottom) derivative. They can be used to calculate derivatives at the boundaries of the domain without referring to any point outside of the grid.

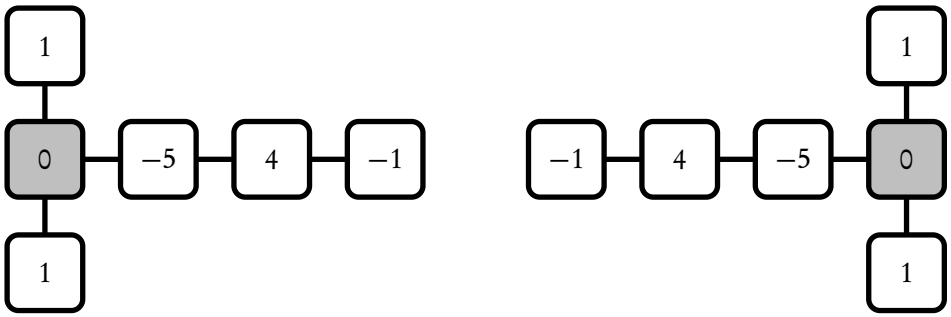

Fig. A.4: Boundary stencils of the second order two-dimensional Laplacian, where left- and rightsided finite differences are used to approximate $\partial/\partial x$.

are kept constant. Using the second order finite differences defined in eqs. (A.1) and (A.2), the condition $f = \alpha$, $f' = \beta$ can be realized at either side by setting

$$\begin{aligned} f_0 &= \Delta x^2 \beta + 2\alpha + f_2, & \text{or} \qquad & f_{N-1} = \Delta x^2 \beta + 2\alpha + f_{N-3}, \\ f_1 &= \alpha, & & f_{N-2} = \alpha. \end{aligned}$$

Here, the two outermost grid points 0 and $N-1$ are the virtual grid points that ensure the boundary condition to be fulfilled at the points 1 and $N-2$, respectively. Analogously, the condition $f' = \alpha$, $f'' = \beta$ is implemented by use of

$$\begin{aligned} f_0 &= 2\Delta x \alpha + f_2, & \text{or} \qquad & f_{N-1} = 2\Delta x \alpha + f_{N-3}, \\ f_1 &= \Delta x \alpha - \frac{1}{2}\Delta x^2 \beta + f_2, & & f_{N-2}, = \Delta x - \frac{1}{2}\delta x^2 + f_{N-3}. \end{aligned}$$

Again, the grid points 0 and $N-1$ are virtual. Corresponding formulas for arbitrary boundary conditions can be derived by solving the linear equations following from the finite differences given by eq. (A.1)–(A.4).

A.2 Time integration: Runge-Kutta-Fehlberg

In the following, the Runge-Kutta method is explained briefly. For a more detailed introduction, the reader is referred to [Pre99]. A Runge-Kutta algorithm of order s is an explicit integration

0					
c_2	a_{21}				
c_3	a_{31}	a_{32}			
$\vdots$	$\vdots$		$\ddots$		
c_2	a_{s1}	a_{s2}	$\dots$	$a_{s,s-1}$	
	b_1	b_2	$\dots$	b_{s-1}	b_s

Tab. A.1: The butcher tableau summarizes the coefficients of the Runge-Kutta formulas (A.6) and (A.7).

0						
1/5	1/5					
3/10	3/40	9/40				
3/5	3/10	−9/10	6/5			
1	−11/54	5/2	−70/27	35/27		
7/8	1631/55296	175/512	575/13824	44275/110592	253/4096	
	37/378	0	250/621	125/594	0	512/1771
	2825/27648	0	18575/48384	13525/55296	2771/14336	1/4

Tab. A.2: Butcher tableau of the embedded Runge-Kutta scheme of orders 4 and 5 [Pre99].

algorithm that calculates the solution $\vec{y}_{n+1}$ at time $(n+1)\cdot\Delta t$ from the solution $\vec{y}_n$ at time $n\cdot\Delta t$ via

$$\vec{y}_{n+1} = \vec{y}_n + \Delta t \sum_{i=1}^{s} b_i \vec{k}_i \tag{A.6}$$

where the k_i are calculated as

$$\begin{aligned}
\vec{k}_1 &= f(t_n, \vec{y}_n) \\
\vec{k}_2 &= f(t_n + c_2\Delta t, \vec{y}_n + a_{21}\Delta t\vec{k}_1) \\
\vec{k}_3 &= f(t_n + c_3\Delta t, \vec{y}_n + a_{31}\Delta t\vec{k}_1 + a_{32}\Delta t\vec{k}_2) \\
&\vdots \\
\vec{k}_s &= f(t_n + c_s\Delta t, \vec{y}_n + a_{s1}\Delta t\vec{k}_1 + a_{s2}\Delta t\vec{k}_2 + \cdots + a_{s,s-1}\Delta t\vec{k}_s)
\end{aligned} \tag{A.7}$$

Different choices of the coefficients a_{ij}, b_i, and c_i are possible. A particular choice can be summarized in a *Butcher tableau* (see tab. A.1). Throughout this thesis, an embedded Runge-Kutta scheme is used. The term "embedded" means, that two versions of $\vec{y}_{n+1}$ are calculated by use of common coefficients. One version, $\vec{y}^{(4)}_{n+1}$, is of fourth, the other, $\vec{y}^{(5)}_{n+1}$, of fifth order. One can limit the error of the calculation by setting a maximal tolerance $\epsilon_{\max}$ for the difference $\epsilon = |\vec{y}^{(5)}_{n+1} - \vec{y}^{(4)}_{n+1}|$. If the tolerance is exceeded, the calculation is repeated with a smaller time step Δt that is calculated

as

$$\Delta t_{\text{new}} = 0.95 \left(\frac{\epsilon_{\max}}{\epsilon} \right)^{1/4}.$$

On the other hand, one can also *increase* the time step as long as $\epsilon < \epsilon_{\max}$. To this end, a new time step

$$\Delta t_{\text{new}} = 0.95 \left(\frac{\epsilon_{\max}}{\epsilon} \right)^{1/5}$$

is set after every time step when the last calculated ϵ is tolerable. By this approach, the optimal time step is chosen throughout the complete computation. The parameter set used in this thesis is taken from [Pre99] and summarized in the Butcher tableau A.2. Since we are considering vectors $\vec{y}$ with components $y_{n,i}$ where the index i denotes the grid point, the error ϵ may in some cases vary significantly across the spatial integration domain. To enforce a certain accuracy at each grid point, the maximal discrepancy

$$\epsilon = \max_{i \in [0,N-1]} \left\{ |y^{(5)}_{n+1,i} - y^{(4)}_{n+1,i}| \right\}, \tag{A.8}$$

is used as a measure of the error and compared to the tolerance $\epsilon_{\max}$.

A.3 Parallel computation using graphics devices

Explicit numerical simulation of two dimensional pattern forming systems involving spatial derivatives of fourth or higher order suffer from severe time-step restrictions. The reason for this is given by the Courant-Friedrichs-Levy (CFL) criterion (see chapter 9 of [Boy00]). A straight-forward way to accelerate the computation is to execute calculations parallely on different processing units.

The two-dimensional simulations presented in sections 1.4, 3.1.1, and 6.3 are computed on a graphical processing unit (GPU). The underlying code is based on the CUDA framwork provided by the graphics device manufacturer NVIDIA. In recent years, graphics adapters have become an increasingly attractive alternative for parallel computation on the desktop scale. Although standard personal computers provide four central processing units (CPUs) which can also be used for parallel computations, a graphics device is a piece of hardware that is especially designed for parallel operations. Thus, modern graphics devices which are aimed at the consumer market provide up to 512 cores. However, this impressive number has to be relativized, when compared to the common number of four CPUs, since the tact frequency of each of the cores on the graphics device is only a fraction of the typical $\approx$ 2GHz frequency of a CPU. Accordingly, as a rule of thumb, GPU parallelization is highly efficient if used to perform a large number of very simple operations in parallel.

It has to be mentioned, that by the time of the writing of this thesis, manufacturers like NVIDIA have become aware of the possibility to "abuse" their hardware for scientific purposes. Therefore, more and more products which are directly aimed at this new market become commercially available. However, for the computations presented in this thesis, a GeForce480 is used, that is, a device primarily optimized for entertainment and not a scientific instrument. Nevertheless, in comparison to the single core calculations, the CUDA parallelized versions of the direct numerical simulation codes were between 14–17 times faster. Due to the fact that scientific computation of graphics devices is still a young topic, there is only few literature available. The most important sources are directly provided by the manufacturer [Mic09, CUD10, Har].

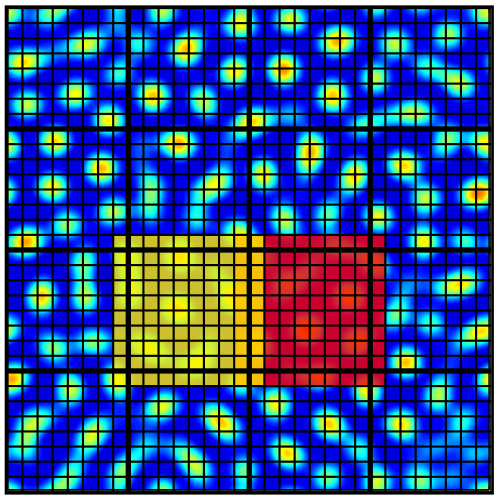

Fig. A.5: Schematic picture of a two-dimensional grid with 32×32 points that is divided into 4×4 blocks of edge length 8. The blocks are processed independently of each other. Overlapping parts of the domain are loaded into the shared memory of the blocks to allow for calculation of finite difference at the block boundaries. This is indicated for two blocks by the colors.

In spite of the obvious advantages of GPU usage, one has to bear in mind, that a graphics adapter is a highly specialized device. If a program is not carefully adapted to the peculiarities of the hardware, the advantage gained by the parallel computation is lost. Another disadvantage of GPU programming is the limited possibility to perform calculations with double precision. Although newer devices are in principle capable to do such calculations, they come at the price of a significant loss of efficiency. Whether or not this is a serious limitation depends, however, on the specific problem one is interested in. For the numerical simulation of pattern forming systems, single precision is usually sufficient[1].

Maybe the most important difference between programming for a CPU and programming for a GPU is the memory layout: The graphics device is designed to primarily work with its own memory and is extremely slow in accessing the RAM of its host computer. It is therefore necessary to keep the data transfer between RAM and graphics memory to a minimum. All data which is needed for the actual computation has to be stored directly on the graphics device. But even the internal memory usage of the graphics device has to be optimized for efficient computation, since it is organized in different layers which have dramatically different access times. The program is organized in sequential and parallel parts. If needed, the program is forked into a large number of parallel processes, so-called *threads*. The global memory is available to all threads. However, accessing it takes some time. To amend this problem, threads are bundled into blocks and each thread within one block has access to a common shared memory, which can be processed much faster than the global memory.

For numerical calculations of partial differential equations with finite differences, this compu-

[1]Before the CUDA-based code was written, all model equations have been simulated on single CPU cores with double precision. A comparison of the results with the later performed CUDA simulations showed no visible difference.

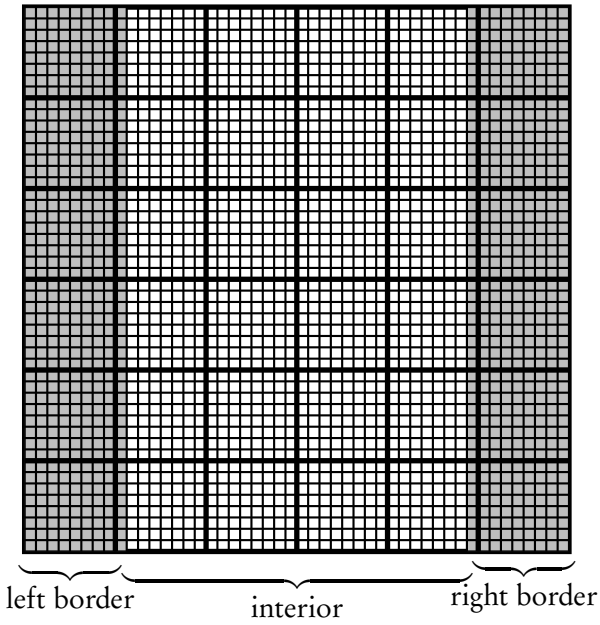

Fig. A.6: If non-periodic boundary conditions apply in x-direction, the left and right column of blocks has to be treated differently as no points outside the grid are available to calculate the finite differences at the outermost points.

tational paradigm is very suitable, since the increment of the solution at any grid point depends only on the value at the grid point itself and a number of neighboring points. Due to this locality, the integration domain can simply be split up into blocks which can be operated upon completely independent of each other. Consider, for example, an integration domain discretized by 32×32 grid points. This domain can be split into 4×4 square blocks of edge length 8 as shown in fig. A.5. Each of these domain blocks will then be processed by one thread block. In order to optimize performance, it is essential, that the blocks do not need to communicate with each other. However, to calculate derivatives at grid points at the boundary of one block one needs to access values belonging to the domain of a neighboring block. To circumvent any inter-block communication, each block loads all needed data into its shared memory, that is, all grid points of its original domain plus all grid points needed to calculate derivatives at the boundaries. This means, that the parts of the physical domain, which are loaded into the shared memories of the blocks overlap, as is shown in fig. A.5, where each 8×8 thread block loads a 10×10 chunk of the domain into its shared memory. If non-periodic boundary conditions apply in x-direction, the domain can be separated in to three parts: one column of blocks on each side of the domain constitutes the border, while the remaining blocks form the interior (see fig. A.6). The blocks belonging in the interior can be treated exactly as in the case of periodic boundary conditions. In the bordering blocks, however, the derivatives at the outermost grid points cannot be calculated by central finite differences as there are no points available outside of the grid. Depending on the purpose, one can either calculate the derivatives there by use of left- and rightsided finite differences or not calculate them at all if they are fixed by the boundary conditions, anyway. The blocks of the bordering rows and of the interior also use a different layout of the shared memory. A block in the left-

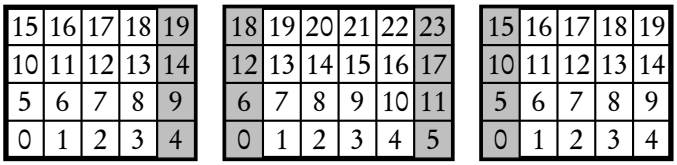

Fig. A.7: Shared memory layout of blocks of 4×4 threads, working on the left, in the center, and on the right of the domain. The shaded fields contain data from the outside of the block.

and right border needs only one additional column of grid points to calculate finite differences of second order. A central block has to access one column on each side. The different layouts are shown in fig. A.7. They have to be taken into account whenever certain grid points have to be accessed.

A further important point concerns the calculation of the maximal error ϵ according to eq. (A.8). To determine the maximum of a set of data points, a serial program would simply scan through all points from start to end and seek the maximum. This algorithm cannot be parallelized directly. Instead, one has to use a *reduction algorithm* [Har]. To find the maximum of a large set of numbers, the set is divided into two subsets. A number of parallel threads then processes the data in the following way: The ith thread reads the ith number of the first subset and compares it to the ith number of the second subset. If the latter is greater than the former, the thread overwrites the ith number with it. When all threads are done, the maximal number of the whole set is now necessarily included within the first subset. The procedure is then repeated, taking the halved set as input. Thus, the set can iteratively be reduced until only one number remains that is identical to the maximum of the initial set. Although slight modifications allow to use reduction for arbitrary grid sizes, it is applied here only to grids with 2^n, $n \in \mathbb{N}$ points.

Bibliography

> Happy indeed is the scientist who not only has the pleasures which I have enumerated, but who also wins the recognition of fellow scientists and of the mankind which ultimately benefits from his endeavors.
>
> *(Irving Langmuir)*

[AFHF10] J. Argyris, G. Faust, M. Haase, and R. Friedrich. *Die Erforschung des Chaos*. Springer Berlin / Heidelberg, 2010.

[Ari89] R. Aris. *Vectors, tensors and the basis equations of fluids mechanics*. Dover, New York, 1989.

[BDF+67] H. Bücher, K. H. Drexhage, M. Fleck, H. Kuhn, D. Möbius, F. P. Schäfer, J. Sondermann, W. Sperling, P. Tillmann, and J. Wiegand. Controlled transfer of excitation energy through thin layers. *Molecular Crystals*, 2:199–230, 1967.

[BEI+09] D. Bonn, J. Eggers, J. Indekeu, J. Meunier, and E. Rolley. Wetting and spreading. *Rev. Mod. Phys.*, 81(2):739–805, 2009.

[Bes06] M. Bestehorn. *Hydrodynamik und Strukturbildung*. Springer Berlin / Heidelberg, 2006.

[BGS+03] J. Becker, G. Grün, R. Seemann, H. Mantz, K. Jacobs, Klaus R. Mecke, and Ralf Blossey. Complex dewetting scenarios captured by thin-film models. *Nature Materials*, 2(1):59–63, 2003.

[BK06] J. Burke and E. Knobloch. Localized states in the generalized Swift-Hohenberg equation. *Phys. Rev. E*, 73(5):056211, 2006.

[BK07] J. Burke and E. Knobloch. Homoclinic snaking: Structure and stability. *Chaos*, 17(3):037102, 2007.

[BL37] K. B. Blodgett and I. Langmuir. Built-up films of barium stearate and their optical properties. *Phys. Rev.*, 51(11):964–982, 1937.

[BLN+06] T. P. Bigioni, X.-M. Lin, T. T. Nguyen, E. I. Corwin, T. A. Witten, and H. M. Jaeger. Kinetically driven self assembly of highly ordered nanoparticle monolayers. *Nature Materials*, 5(4):265–270, 2006.

[Blo34] K. B. Blodgett. Monomolecular films of fatty acids on glass. *Journal of the American Chemical Society*, 56(2):495–495, 1934.

[Blo35] K. B. Blodgett. Films built by depositing successive monomolecular layers on a solid surface. *Journal of the American Chemical Society*, 57(6):1007–1022, 1935.

[Boy00] J. P. Boyd. *Chebyshev and Fourier Spectral Methods 2nd Edition*. Dover, New-York, 2000.

[Cah65] J. W. Cahn. Phase separation by spinodal decomposition in isotropic systems. *J. Chem. Phys.*, 42(1):93–99, 1965.

[Cas48] A. B. D. Cassie. Contact angles. *Discuss. Faraday Soc.*, 3:11–16, 1948.

[CGO06] A. Checco, O. Gang, and B. M. Ocko. Liquid nanostripes. *Phys. Rev. Lett.*, 96(5):056104, 2006.

[CH58] J. W. Cahn and J. E. Hilliard. Free energy of a nonuniform system. I. interfacial free energy. *J. Chem. Phys.*, 28(2):258–267, 1958.

[CH93] M. C. Cross and P. C. Hohenberg. Pattern formation outside of equilibrium. *Rev. Mod. Phys.*, 65(3):851–1112, 1993.

[CLH+07] X. Chen, S. Lenhert, M. Hirtz, N. Lu, H. Fuchs, and L. F. Chi. Langmuir-Blodgett patterning: A bottom-up way to build mesostructures over large areas. *Acc. Chem. Res.*, 40(6):393–401, 2007.

[CLZ+06] X. Chen, N. Lu, H. Zhang, M. Hirtz, L. Wu, H. Fuchs, and L. Chi. Langmuir-Blodgett patterning of phospholipid microstripes: Effect of the second component. *The Journal of Physical Chemistry B*, 110(15):8039–8046, 2006.

[CM09] R. V. Craster and O. K. Matar. Dynamics and stability of thin liquid films. *Rev. of Mod. Phys.*, 81(3):1131–1198, 2009.

[CUD10] NVIDIA CUDA C programming guide version 3.2, 2010. (`http://developer.download.nvidia.com/compute/cuda/3_2_prod/toolkit/docs/CUDA_C_Programming_Guide.pdf`; visited on May 5th, 2011).

[DBAB+05] J. Daillant, E. Bellet-Amalric, A. Braslau, T. Charitat, G. Fragneto, F. Graner, S. Mora, F. Rieutord, and B. Stidder. Structure and fluctuations of a single floating lipid bilayer. *Proceedings of the National Academy of Sciences of the United States of America*, 102(33):11639–11644, 2005.

[DBB90] J. Daillant, J. J. Benattar, and L. Bosio. X-ray reflectivity study of monolayers of amphiphilics at the air-water interface. *Journal of Physics: Condensed Matter*, 2(S):SA405, 1990.

[DBD+97] R. D. Deegan, O. Bakajin, T. F. Dupont, G. Huber, S. R. Nagel, and T. A. Witten. Capillary flow as the cause of ring stains from dried liquid drops. *Nature*, 389(6653):827–829, 1997.

[DBD+00] R. D. Deegan, O. Bakajin, T. F. Dupont, G. Huber, S. R. Nagel, and T. A. Witten. Contact line deposits in an evaporating drop. *Phys. Rev. E*, 62(1):756–765, 2000.

[Der01] B. V. Derjaguin. Untersuchungen des Spaltdruckes dünner Filme, deren Entwicklung, Ergebnisse und zu lösende aktuelle Probleme. *Colloid & Polymer Science*, 253(6):492–499, 1975.

[dG85] P. G. de Gennes. Wetting: statics and dynamics. *Rev. Mod. Phys.*, 57(3):827–863, 1985.

[DG10] F. Doumenc and B. Guerrier. Drying of a solution in a meniscus: A model coupling the liquid and the gas phases. *Langmuir*, 26(17):13959–13967, 2010.

[Doe10] E. J. Doedel. Lecture notes on numerical analysis of nonlinear equations, 2010. (`http://cmvl.cs.concordia.ca/auto/notes.pdf`; visited on May 1st, 2011).

[DS82] H. T. Davis and L. E. Scriven. Stress and structure in fluid interfaces. *Adv. Chem. Phys.*, 49:357–454, 1982.

[Eö86] R. Eötvös. Ueber den Zusammenhang der Oberflächenspannung der Flüssigkeiten mit ihrem Molecularvolumen. *Ann. Phys.*, 263(3):448–459, 1886.

[Egg04] J. Eggers. Hydrodynamic theory of forced dewetting. *Phys. Rev. Lett.*, 93(9):094502, 2004.

[ES90] D. M. Eigler and E. K. Schweizer. Positioning single atoms with a scanning tunnelling microscope. *Nature*, 344(6266):524–526, 1990.

[Eva79] R. Evans. The nature of the liquid-vapour interface and other topics in the statistical mechanics of non-uniform, classical fluids. *Adv. Phys.*, 28(2):143–200, 1979.

[FBF74] B. Franklin, W. Brownrigg, and Mr. Farish. Of the stilling of Waves by means of Oil. extracted from Sundry Letters between Benjamin Franklin, ll. d. f. r. s. William Brownrigg, m. d. f. r. s. and the Reverend Mr. Farish. *Philosophical Transactions (1683–1775)*, 64:445–460, 1774.

[FK97] H. Fischer and H. Kaul. *Mathematik für Physiker 1*. Teubner, Stuttgart, 1997.

[FW09] E. M. Foard and A. J. Wagner. Enslaved phase-separation fronts in one-dimensional binary mixtures. *Phys. Rev. E*, 79(5):056710, 2009.

[FW11] E. M. Foard and A. J. Wagner. Survey of morphologies formed in the wake of an enslaved phase-separation front in two dimensions. 2011, arXiv:0805.3745v1 [cond-mat.soft].

[Gas90] P. Gaspard. Measurement of the instability rate of a far-from-equilibrium steady state at an infinite period bifurcation. *The Journal of Physical Chemistry*, 94(1):1–3, 1990.

[GCF00] M. Gleiche, L. F. Chi, and H. Fuchs. Nanoscopic channel lattices with controlled anisotropic wetting. *Nature*, 403:173–175, 2000.

[GH86] J. Guckenheimer and P. Holmes. *Nonlinear Oscillations, Dynamical Systems, and Bifurcations of Vector Fields*. Applied Mathematical Sciences. Springer-Verlag, New York, second printing, reviced and corrected edition, 1986.

[GHLL99] H. Gau, S. Herminghaus, P. Lenz, and R. Lipowsky. Liquid morphologies on structured surfaces: From microchannels to microchips. *Science*, 283(5398):46–49, 1999.

[Gle00] M. Gleiche. *Verfahren zur Herstellung periodischer Strukturen durch Benetzungsinstabilitäten*. Phd thesis, Westfälische Wilhelms-Universität, Münster, 2000.

[GR98] K. Graf and H. Riegler. Molecular adhesion interactions between Langmuir monolayers and solid substrates. *Colloids and Surfaces A: Physicochemical and Engineering Aspects*, 131(1-3):215–224, 1998.

[Hak04] H. Haken. *Synergetics - Introduction and Advanced Topics*. Springer Berlin / Heidelberg, 2004.

[Ham37] H. C. Hamaker. The London–van der Waals attraction between spherical particles. *Physica*, 4(10):1058–1072, 1937.

[Har] M. Harris. Optimizing parallel reduction in CUDA. (`http://developer.download.nvidia.com/compute/cuda/1_1/Website/projects/reduction/doc/reduction.pdf`; visited May 7th, 2011).

[Har19] W. B. Hardy. III. the spreading of fluids on glass. *Philosophical Magazine Series 6*, 38(223):49–55, 1919.

[Har11] H. Harder. Diploma thesis, Universität Potsdam, Institut für Physik und Astronomie, 2011.

[Hel73] W. Helfrich. Elastic properties of lipid bilayers: Theory and possible experiments. *Z. Naturforsch.*, 28 c:693–703, 1973.

[HFC08] M. Hirtz, H. Fuchs, and L. F. Chi. Influence of substrate treatment on self-organized pattern formation by Langmuir-Blodgett transfer. *The Journal of Physical Chemistry B*, 112(3):824–827, 2008.

[HKT+05] J. Huang, F. Kim, A. R. Tao, S. Connor, and P. Yang. Spontaneous formation of nanoparticle stripe patterns through dewetting. *Nature Materials*, 4(12):896–900, 2005.

[HS71] C. Huh and L. E Scriven. Hydrodynamic model of steady movement of a solid/liquid/fluid contact line. *Journal of Colloid and Interface Science*, 35(1):85–101, 1971.

[Isr11] J. N. Israelachvili. *Intermolecular and Surface Forces*. Academic Press, 2011.

[KBH00] S. Kalliadasis, C. Bielarz, and G. M. Homsy. Steady free-surface thin film flows over topography. *Physics of Fluids*, 12(8):1889–1898, 2000.

[KCF+05] E. E. Kooijman, V. Chupin, N. L. Fuller, M. M. Kozlov, B. de Kruijff, K. N. J. Burger, and P. R. Rand. Spontaneous curvature of phosphatidic acid and lysophosphatidic acid. *Biochemistry*, 44(6):2097–2102, 2005.

[Kel77] H. B. Keller. *Numerical solution of bifurcation and nonlinear eigenvalue problems*, pages 359–384. Academic Press, New York, 1977.

[KGF09] M. H. Köpf, S. V. Gurevich, and R. Friedrich. Thin film dynamics with surfactant phase transition. *EPL (Europhysics Letters)*, 86(6):66003, 2009.

[KGF11] M. H. Köpf, S. V. Gurevich, and R. Friedrich. Controlled nanochannel lattice formation utilizing prepatterned substrates. *Phys. Rev. E*, 83(1):016212, 2011.

[KGFC10] M. H. Köpf, S. V. Gurevich, R. Friedrich, and L. F. Chi. Pattern formation in monolayer transfer systems with substrate-mediated condensation. *Langmuir*, 26(13):10444–10447, 2010.

[KGWF11] M. H. Köpf, S. V. Gurevich, T. Wulf, and R. Friedrich. Dynamics of a thin liquid film with surface rigidity and spontaneous curvature. *Phys. Rev. E*, 83(4):040601, 2011.

[KH01] S. Kalliadasis and G. M. Homsy. Stability of free-surface thin-film flows over topography. *Journal of Fluid Mechanics*, 448:387–410, 2001.

[KM71] H. Kuhn and D. Möbius. Systems of monomolecular layers - assembling and physicochemical behavior. *Angew. Chem. Int. Ed. Engl.*, 10(9):620–637, 1971.

[KMD99] V. M. Kaganer, H. Möhwald, and P. Dutta. Structure and phase transitions in Langmuir monolayers. *Rev. Mod. Phys.*, 71(3):779–819, 1999.

[Kno08] E. Knobloch. Spatially localized structures in dissipative systems: open problems. *Nonlinearity*, 21(4):T45–T60, 2008.

[Kre09] A. Krekhov. Formation of regular structures in the process of phase separation. *Phys. Rev. E*, 79(3):035302, 2009.

[Kur03] Y. Kuramoto. *Chemical Oscillations, Waves, and Turbulence*. Dover, New York, 2003.

[Lan17] I. Langmuir. The constitution and fundamental properties of solids and liquids. II. Liquids. *Journal of the American Chemical Society*, 39(9):1848–1906, 1917.

[Lan34] I. Langmuir. Mechanical properties of monomolecular films. *Journal of the Franklin Institute*, 218(2):143–171, 1934.

[LBBM98] S. Leporatti, F. Bringezu, G. Brezesinski, and H. Möhwald. Condensed phases of branched-chain phospholipid monolayers investigated by scanning force microscopy. *Langmuir*, 14(26):7503–7510, 1998.

[LBM00] S. Leporatti, G. Brezesinski, and H. Möhwald. Coexistence of phases in monolayers of branched-chain phospholipids investigated by scanning force microscopy. *Colloids and Surfaces A: Physicochemical and Engineering Aspects*, 161(1):159–171, 2000.

[Lee97] J. M. Lee. *Riemannian Manifolds: An introduction to curvature*, volume 176. Springer New York, 1997.

[LGFC05] S. Lenhert, M. Gleiche, H. Fuchs, and L. F. Chi. Mechanism of regular pattern formation in reactive dewetting. *ChemPhysChem*, 6(12):2495–2498, 2005.

[LGP02] A. V. Lyushnin, A. A. Golovin, and L. M. Pismen. Fingering instability of thin evaporating liquid films. *Phys. Rev. E*, 65(2):021602, 2002.

[LGS+10] L. Li, P. Gao, K. C. Schuermann, S. Ostendorp, W. Wang, C. Du, Y. Lei, H. Fuchs, L. De Cola, K. Müllen, and L. F. Chi. Controllable growth and field-effect property of monolayer to multilayer microstripes of an organic semiconductor. *Journal of the American Chemical Society*, 132(26):8807–8809, 2010.

[LL87] L. D. Landau and E. M. Lifschitz. *Statistische Physik, Teil 1*. Akademie Verlag, Berlin, 1987.

[LL91] L. D. Landau and E. M. Lifschitz. *Hydrodynamik*. Akademie Verlag, Berlin, 1991.

[LS61] I. M. Lifshitz and V. V. Slyozov. The kinetics of precipitation from supersaturated solid solutions. *Journal of Physics and Chemistry of Solids*, 19(1-2):35–50, 1961.

[LSM83] M. Lösche, E. Sackmann, and H. Möhwald. A fluorescence microscopic study concerning the phase diagram of phospholipids. *Berichte der Bunsengesellschaft für physikalische Chemie*, 87(10):848–852, 1983.

[MDLS04] S. Mora, J. Daillant, D. Luzet, and B. Struth. X-ray surface scattering investigation of Langmuir films: Phase transitions and elastic properties. *EPL (Europhysics Letters)*, 66(5):694, 2004.

[Mic09] P. Micikevicius. 3D finite difference computation on GPUs using CUDA. In *Proceedings of 2nd Workshop on General Purpose Processing on Graphics Processing Units*, pages 79–84, Washington, D.C., 2009. ACM.

[MP94] V. S. Mitlin and N. V. Petviashvili. Nonlinear dynamics of dewetting: kinetically stable structures. *Physics Letters A*, 192(5-6):323–326, 1994.

[Nob11] Nobelprize.org. The nobel prize in chemistry 1932., 2011. (`http://nobelprize.org/nobel_prizes/chemistry/laureates/1932/`; visited on April 20th, 2011).

[ODB97] A. Oron, S. H. Davis, and S. G. Bankoff. Long-scale evolution of thin liquid films. *Rev. Mod. Phys.*, 69(3):931–980, 1997.

[OS92] I. M. Ovsyannikov and L. P. Shil'nikov. Systems with a homoclinic curve of multidimensional saddle-focus type, and spiral chaos. *Mathematics of the USSR-Sbornik*, 73(2):415–443, 1992.

[Ost00] W. Ostwald. Über die vermeintliche Isomerie des roten und gelben Quecksilberoxyds und die Oberflächenspannung fester Körper. *Z. Phys. Chem.*, 34:495, 1900.

[PE08] L. M. Pismen and J. Eggers. Solvability condition for the moving contact line. *Phys. Rev. E*, 78(5):056304, 2008.

[Pis01] L. M. Pismen. Nonlocal diffuse interface theory of thin films and the moving contact line. *Phys. Rev. E*, 64(2):021603, 2001.

[Pis04] L. M. Pismen. Spinodal dewetting in a volatile liquid film. *Phys. Rev. E*, 70(2):021601, 2004.

[Pis10] L. M. Pismen. Chemocapillary instabilities of a contact line. *Phys. Rev. E*, 81(2):026307, 2010.

[Poc91] A. Pockels. Surface tension. *Nature*, 43:437–439, 1891.

[Poc93] A. Pockels. Relations between the surface-tension and relative contamination of water surfaces. *Nature*, 48:152–154, 1893.

[Poc02] A. Pockels. Ueber das spontane Sinken der Oberflc̈henspannung von Wasser, wässerigen Lösungen und Emulsionen. *Annalen der Physik*, 313(8):854–871, 1902.

[Pre99] W. H. Press. *Numerical Recipes in C*. University Press, Cambridge, 1999.

[PRK03] A. Pikovsky, M. Rosenblum, and J. Kurths. *Synchronization - A universal concept in nonlinear sciences*. Cambridge University Press, Cambridge, 2003.

[QXX+99] D. Qin, Y. Xia, B. Xu, H. Yang, C. Zhu, and G. M. Whitesides. Fabrication of ordered two-dimensional arrays of micro- and nanoparticles using patterned self-assembled monolayers as templates. *Adv. Mater.*, 11(17):1433–1437, 1999.

[Ray89] Lord Rayleigh. Measurements of the amount of oil necessary in order to check the motions of camphor upon water. *Proceedings of the Royal Society of London*, 47:364–367, 1889.

[Ray99] Lord Rayleigh. Investigations in capillarity: The size of drops.the liberation of gas from supersaturated solutions, colliding jets, the tension of contaminated water-surfaces. *Philosophical Magazine Series 5*, 48(293):321–337, 1899.

[Rey86] O. Reynolds. On the theory of lubrication and its application to Mr. Beauchamp Tower's experiments, including an experimental determination of the viscosity of olive oil. *Philosophical Transactions of the Royal Society of London*, 177:157–234, 1886.

[RS92] H. Riegler and K. Spratte. Structural changes in lipid monolayers during the Langmuir-Blodgett transfer due to substrate/monolayer interactions. *Thin Solid Films*, 210–211(Part 1):9–12, 1992.

[Saf94] S. A. Safran. *Statisitical Thermodynamics of Surfaces, Interfaces, and Membranes*. Frontiers in Physics. Addison-Wesley, Reading, Massachusetts, 1994.

[Scr60] L. E. Scriven. Dynamics of a fluid interface equation of motion for newtonian surface fluids. *Chem. Eng. Sci.*, 12(2):98–108, 1960.

[SCR94] K. Spratte, L. F. Chi, and H. Riegler. Physisorption instabilities during dynamic Langmuir wetting. *Europhysics Letters*, 25(3):211–217, 1994.

[SH77] J. Swift and P. C. Hohenberg. Hydrodynamic fluctuations at the convective instability. *Phys. Rev. A*, 15(1):319–328, 1977.

[SH96] M. A. Spaid and G. M. Homsy. Stability of newtonian and viscoelastic dynamic contact lines. *Phys. Fluids*, 8(2):460–478, 1996.

[SOG+02] H. Shimoda, S. Oh, H. Geng, R. Walker, X. Zhang, L. McNeil, and O. Zhou. Self-assembly of carbon nanotubes. *Adv. Mater.*, 14(12):899–901, 2002.

[SR94] K. Spratte and H. Riegler. Steady state morphology and composition of mixed monomolecular films (Langmuir monolayers) at the air/water interface in the vicinity of the three-phase line: Model calculations and experiments. *Langmuir*, 10(9):3161–3173, 1994.

[Str00] S. H. Strogatz. *Nonlinear Dynamics and Chaos*. Westview Press, 2000.

[SZA+08] J. H. Snoeijer, J. Ziegler, B. Andreotti, M. Fermigier, and J. Eggers. Thick films of viscous fluid coating a plate withdrawn from a liquid reservoir. *Phys. Rev. Lett.*, 100(24):244502, 2008.

[Tan10] C. Tanford. *Ben Franklin Stilled the Waves*. Oxford University Press, New York, 2010.

[THY08] A. R. Tao, J. Huang, and P. Yang. Langmuir-Blodgettry of nanocrystals and nanowires. *Acc. Chem. Res.*, 41(12):1662–1673, 2008.

[TVNP01] U. Thiele, M. G. Velarde, K. Neuffer, and Y. Pomeau. Film rupture in the diffuse interface model coupled to hydrodynamics. *Phys. Rev. E*, 64(3):031602, 2001.

[vS03] W. van Saarloos. Front propagation into unstable states. *Physics Reports*, 386(2-6):29–222, 2003.

[Wig90] S. Wiggins. *Introduction to Applied Nonlinear Dynamical Systems and Chaos*. Springer Verlag New York, 1990.

[Wul08] T. Wulf. *Theorie zur Streifenbildung in Langmuir-Blodgett Transfersystemen*. Diploma thesis, Westfälische Wilhelms-Universität, Münster, January 2008.

[You05] T. Young. An essay on the cohesion of fluids. *Philosophical Transactions of the Royal Society of London*, 95:65–87, 1805.

[YS05] H. Yabu and M. Shimomura. Preparation of self-organized mesoscale polymer patterns on a solid substrate: Continuous pattern formation from a receding meniscus. *Advanced Functional Materials*, 15(4):575–581, 2005.

Danksagung

Die Vollendung einer Doktorarbeit markiert das Ende eines langen Weges. In den letzten drei bis dreieinhalb Jahren habe ich vieles gelernt, was sich in der vorliegenden Arbeit hoffentlich niedergeschlagen hat. Das meiste davon verdanke ich all den Menschen, die mich während dieser Zeit unermüdlich unterstützt haben. Ihnen möchte ich an dieser Stelle meinen Dank aussprechen:

- Herrn Prof. Dr. Rudolf Friedrich für die Möglichkeit an einer so spannenden Aufgabe zu arbeiten, für die kontinuierliche Unterstützung während der gesamten Zeit und nicht zuletzt für das große Vertrauen.
- Herrn Prof. Dr. Andreas Heuer für die Bereitschaft das Zweitgutachten zu erstellen.
- Frau Dr. Svetlana Gurevich für unendlich viele gute Ratschläge und die ständige Bereitschaft mir mit ihrem Fachwissen zur Seite zu stehen.
- Frau Prof. Dr. Lifeng Chi und Herrn Dr. Dr. Michael Hirtz für Diskussionen über die Experimente zur Streifenbildung.
- Der Deutschen Forschungsgemeinschaft für die finanzielle Unterstützung und nicht zuletzt für die Möglichkeit, meine Arbeit auf verschiedensten internationalen Fachtagungen zu präsentieren.
- All denjenigen WWU-externen Wissenschaftlern, die mir bei Diskussionen zahlreiche wichtige Anregungen gegeben oder mich in anderer Weise wirkungsvoll unterstützt haben:
  - Dr. Hans Riegler (MPIKG Potsdam), einem der Entdecker der SMC, der mir das Phänomen aus erster Hand erklären konnte.
  - Dr. Jürgen Reiche und Prof. Dr. Svetlana Santer (beide Universität Potsdam) für die experimentellen Ergebnisse und die Zusammenarbeit bezüglich der Temperaturabhängigkeit der Streifenbildung.
  - Prof. Dr. Uwe Thiele (Loughborough University) dafür, dass er mich auf die Kontinuierungsmethode aufmerksam gemacht hat, sowie für zahlreiche Diskussionen über das vereinfachte Modell.
  - Prof. Dr. Edgar Knobloch (University of California, Berkeley) für die Unterstützung eines Antragsvorhabens sowie für zahlreiche wertvolle Literaturhinweise.
  - Prof. Dr. Len Pismen (Technion, Haifa) auf dessen Anregung hin ich die Untersuchung der Oberflächensteifigkeit durchgeführt habe.
- Der während der drei langen Jahre meiner Promotionsphase mehrfach wechselnden Belegschaft des Büros 412, also Tobias Sudmann, Jaïr Wuilloud, Bastian Drees, Dirk Sandbrink, Umut Deniz Özugurel und Anna Lusiewicz, für die dauerhaft angenehme Arbeitsatmosphäre.

- Den Schaddiplomanden, deren Existenz zu einer schönen Wortschöpfung führte.
- Max Theodor Kuchel nach dessen pünktlichem Einläuten der Mittagsrunde man die Uhr stellen kann. Ihm verdanke ich mein leibliches Wohl sowie die Information, dass Biber keine Raubtiere sind.
- Meinen Korrekturlesern Michael Wilczek, Svetlana Gurevich und Cornelia Petrović. Ihnen sei folgender Satz gewidmet:

  "Valdimir Arnold determinded the minimima of a diffifult expample mensicus."

- Meiner Familie für die andauernde Unterstützung in allen Lebensbereichen.
- Meiner Freundin Cornelia Petrović für ihre Unterstützung und Liebe, aus der ich immer, aber insbesondere auch in den letzten Wochen der Promotionsphase, Kraft schöpfen konnte.